Exploring Gas-Phase Ionic Liquid Aggregates by Mass Spectrometry and Computational Chemistry

Andrew P. Gray

THE UNIVERSITY *of* EDINBURGH

Doctor of Philosophy

The University of Edinburgh

2011

Declaration

This work is my own and where this is not so, credit has been duly given. This thesis has not been previously submitted, in whole or in part, for any degree at this or any other university.

Andrew Peter Gray

November 2011

Acknowledgements

I would like to take this chance to express my gratitude to the wide number of people who have helped me during my post-graduate studies and made my time in Edinburgh incredibly memorable and enjoyable. I would like to thank my supervisor, Prof. Eleanor Campbell, for all of her kind help, support and guidance during these years. While I was not initially one of your students, I am extremely grateful that I ended up with you and your welcoming research group. Special thanks go to Dr. Bridgette Duncombe for the opportunity to continue my studies at Edinburgh and for all the support along the way. Thanks also go to Prof. Paul Madden and Dr. Philip Camp who also acted as supervisors and I am very appreciative for their guidance.

My thanks go to all of the people who taught me about mass spec. and helped overcome the glitches and hiccups. To Dr. Pat Langridge Smith and Dr. Logan MacKay, thank you for letting us set up camp in your lab and helping to rediscover an ion signal at some difficult times. To all of the remaining SIRCAMS members, especially Dr. Stefan Weidt, Dr. Jenna Scotcher and Dr. Adam Stokes, thank you for your help with all aspects of mass spectrometry, for making me welcome while sharing your lab and offices and also for letting me be part of your group meetings. I am very thankful to Dr. Perdita Barran for introducing me to the joys of mass spectrometry and allowed the use of her resources at many points during this work. To Dr. Martin De Cecco, thank you for your generous experimental help and Yana Berezovskaya, thank you for your time and patience with both mass spectrometry and the Russian language. I am also very grateful to Prof. Martin McCoustra for allowing the use of the experimental PADI source and the assistance of his student Katherine MacKay. A special thank you must be said to the ever helpful and resourceful Alan Taylor and to Michael Burton for his brilliant work during his summer project.

I would like to thank Dr. Patricia Hunt, Dr. Andrew Turner and Dr. Patricia Richardson for their continued help and advice with computational chemistry. To

Prof. Polly Arnold and Dr. Jason Love, thank you for the use of your facilities for synthesis and to Prof. Tom Welton and Dr. Jason Hallett for your help during synthesis and procurement of other ionic liquids. My thanks go to Dr. Benjamin Roach for everything while we were under the supervision of Bridgette and Alla Kirkun for her generosity, kindness and artistic gifts. Thanks must also be given to the University of Edinburgh, EaStChem and the EPSRC for giving me the opportunity to happily spend this time studying in Edinburgh.

A special thank you is reserved for the members of the Eleanor Campbell Research Group. Thank you for the scientific advice during discussions, presentations and meetings and also for teaching me about nanocarbon through the superb science performed within the group. Dr. Andrei Gromov, Dr. Oleg Nerushev, Dr. Olof Johansson, Johan Ek Weis, Gordon Henderson, Chaweewan Sapcharoenkun, Kirsten Strain, Adrianna Złoczewska and Andreas Molle, you have my complete gratitude. Thank you for giving me such a warm welcome and wonderfully friendly home during these years in particular for all of the delicious fika, patience with my quizzes and entertaining group outings.

Finally, I would like to thank my family especially my parents, Morag and Peter, and my brother, Donald. You have always supported me throughout my education, travelling and life in general for which I am incredibly grateful. Thank you all!

Abstract

Ionic liquids (IL) are salts which are liquid at low temperatures, typically with melting points under 100 ˚C. In recent years ILs have been treated as novel solvents and used in a wide variety of applications such as analytical and separation processes, electrochemical devices and chemical syntheses. The properties of many ILs have been extensively studied; these studies have primarily focused on the investigation of key physical properties including viscosity, density and solubility. This thesis presents mass spectrometry (MS) and computational data to investigate the intrinsic interactions between a small number of IL ions and also their interactions with contaminants.

MS was used to study gas-phase aggregates of three ILs based on the 1-butyl-3-methylimidazolium ($C4mim^+$) cation. The influence of different ion sources was investigated on C4mimCl. Conventional electrospray ionisation (ESI) and nano-ESI techniques were compared with recently developed sonic-spray ionisation (SSI) and plasma assisted desorption ionisation (PADI). SSI was found to be beneficial to the formation of larger aggregates while PADI was significantly less efficient. Gas-phase structures of the singly charged cationic aggregates of C4mimCl were characterised with the aid of collision induced dissociation (CID) and density functional theory (DFT) calculations. Additionally, CID and DFT gave consistent results for the relative stability of the C4mimCl aggregates, showing a good agreement between experiment and theory.

Mixed solutions of C4mimCl with a range of metal chloride salts were used to form aggregates incorporating both IL and metal chlorides. LiCl, NaCl, KCl, CsCl, $MgCl_2$ and $ZnCl_2$ were all combined with C4mimCl. Magic number characteristics were observed for a number of pure IL and mixed aggregates. Many of the mixed species were characterised using MS and DFT calculations. In particular, the relative stabilities were determined and the structures of the aggregates were calculated. It was found that the metal ions would normally act as a core for the aggregates with the stability determined by the metal-chlorine binding strength and the steric

hindrance of the aggregates. It was necessary to exploit pseudopotentials as opposed to all-electron basis sets for the larger aggregates and aggregates containing heavy atoms.

While water is a very effective contaminant for ILs it was not possible to observe gas-phase IL aggregates incorporating this despite using multiple methods. Additionally the presence of protonated aggregates was likewise not observed throughout the range of experiments. Possible structures where these features would be incorporated were studied with DFT to obtain some insight into their lack of formation.

Abbreviation List

APCI	Atmospheric-Pressure Chemical ionisation
BASIL	Biphasic Acid Scavenging utilising Ionic Liquids
BSSE	Basis Set Superposition Error
BuS	Butyl Side Conformation
C4mim	1-butyl-3-methylimidazolium
CAC	Critical Aggregation Concentration
CCE	Characteristic Collision Energy
CGTF	Contracted Gaussian Type Function
CI	Configuration Interaction
CID	Collision Induced Dissociation
C*n*mim	1-alkyl-3-methylimidazolium where *n* = alkyl chain length
DFT	Density Functional Theory
EASI	Easy Ambient Sonic-Spray Ionisation
ECP	Effective Core Potential
ESI	Electrospray ionisation
FrB	Front Butyl Conformation
FrM	Front Methyl Conformation
FTICR	Fourier Transform Ion Cyclotron Resonance
FTIR	Fourier Transform Infrared spectroscopy

GGA	Generalised Gradient Approximation
GTO	Gaussian Type Orbital
HDX	Hydrogen Deuterium Exchange
HF	Hartree-Fock
IL	Ionic Liquid
LanL	Los Alamos National Laboratory
LC	Liquid chromatography
LCAO	Linear Combination of Atomic-like Orbitals
LCQ	Thermo Finnigan LCQ Classic mass spectrometer
LDA	Local Density Approximation
MALDI	Matrix-Assisted Laser Desorption Ionisation
MCP	Microchannel plate
MD	Molecular Dynamics
MeS	Methyl Side Conformation
MP	Møller-Plesset perturbation theory
MS	Mass Spectrometry
m/z	Mass-to-charge ratio
NCE	Normalized Collision Energy
NMR	Nuclear Magnetic Resonance
PADI	Plasma-Assisted Desorption Ionisation

PP	Pseudopotential
QIT	Quadrupole ion trap
QTOF	Waters Micromass QTOF1 mass spectrometer
RTIL	Room Temperature Ionic Liquid
SCF	Self-Consistent Field
SIMS	Secondary Ion Mass Spectrometry
SSI	Sonic spray ionisation
STO	Slater Type Orbital
SY	Survival Yield
TIC	Total ion chromatogram
TOF	Time-of-Flight
VOC	Volatile Organic Compound

Contents

Chapter 1: Introduction

1.1 Ionic Liquids

The study of species in solution dominates chemistry. However, only a limited number of different liquids are commonly used such as water, hexane, 2-propanol and dimethylformamide.[1] The drive towards more environmentally friendly chemistry by industry and academia has lead to a re-examination of solvents in particular due to the quantity used and their volatility.[2] Ionic liquids (IL) have been suggested and used to replace traditional solvents in a wide variety of areas including synthetic chemistry.[3] This has been successfully done and in some cases the IL was found to have beneficial effects on the chemical processes by providing different chemical environments.[2,3] These ILs are salts consisting of cations and anions which have low melting points. Typically an arbitrary cut-off of 100 ˚C is used to define which salts are ILs and which are not. When the IL is liquid at room temperature it is referred to as a room temperature ionic liquid (RTIL).

1.1.1 Discovery and Development

The first ILs were discovered a considerable length of time ago, indeed examples have been reported for more than one hundred years. S. Gabriel and J. Weiner reported the discovery of ethanolammonium nitrate in 1888; this is a salt with a melting point of 52 to 55 ˚C which likely makes it the earliest known IL.[4] The earliest salt to be recorded with a melting point low enough to be liquid at room temperature and the widely acknowledged origin of the field of ILs was discovered in 1914. P. Walden synthesised ethylammonium nitrate which was found to have a melting point of 12 ˚C.[5] Interest in ILs was not a significant area of development until the synthesis of novel salts in the 1970s and 1980s. Mixtures of aluminium(III) chloride and *N*-alkylpyridinium were discovered to be binary ILs in 1975 followed by the discovery of 1,3-dialkylimidazolium chloride in 1982.[6,7] ILs are most commonly found to have a large and bulky cation which is not symmetric such as 1-butyl-3-methylimidazolium ($C4mim^+$). This cation will be extensively studied in this

thesis where it will normally be found with a chlorine counter ion. The structure of this important cation is shown in Figure 1-1. Performing small changes to the structure of the ions will often result in new ILs. A common example of this is changing the length of the alkyl chain in the 1-butyl-3-methylimidazolium cation. For example the 1-hexyl-3-methylimidazolium ($C6mim^+$) and 1-octyl-3-methylimidazolium ($C8mim^+$) cations have shown to form ILs.[8] The anion is also often large, however it can be smaller, such as a halogen anion. Examples of modern ILs where these structural features are present are shown in Figure 1-1. The lattice energy within ILs will be lower than for conventional salts and low melting points are a consequence of this.[3]

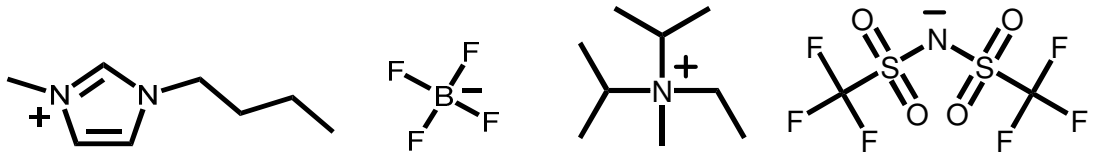

1-butyl-3-methylimidazolium Tetrafluoroborate ($C4mimBF_4$)

Ethyl-methyl-2-isopropyl ammonium bis[(trifluoromethyl)sulfonyl] imide

Figure 1-1 Structures of two common ILs.

RTILs which are stable in air and water were first reported by Wilkes and Zaworotko in 1992. These contained the 1-ethyl-3-methylimidazolium ($C2mim^+$) cation combined with the $CH_3CO_2^-$, NO_3^- or BF_4^- anions.[9] These ILs were found to absorb large amounts of water from the atmosphere, but did still offer a breakthrough for handling and preparation conditions. The range of anions which can be incorporated into these ILs has been greatly expanded over the preceding years, which included the notable work of Grätzel *et al.* who reduced the reactivity with water by using hydrophobic anions such as trifluoromethanesulfonate ($CF_3SO_3^-$) and bis(trifluoromethane)sulfonimide ($N(SO_2\ CF_3)_2^-$) also known as triflate (OTf^-) and bistriflimide (NTf_2^-) respectively.[10,11] As interest has accelerated into the development and application of ILs, phosphonium and pyrrolidinium based classes of cation have been discovered.[12] Due to the increasing number of cations and anions which can be used to produce ILs the total number of possible combinations is very

large and continues to grow.[12] The applications of ILs are likewise numerous and the IL can be selected or designed to meet a particular need or desire for the particular use. This characteristic has lead to them often being referred to as designer solvents.[3,12]

1.1.2 Applications of ILs

ILs have been used in a wide variety of systems including synthesis reactions. The first publicised commercial process was run in 2002 by BASF in Ludwigshafen, Germany.[12] The process is known as the **B**iphasic **A**cid **S**cavenging utilising **I**onic **L**iquids (BASIL^{TM}). During the production of alkoxyphenylphosphines, which are used as generic photoinitiator precursors, HCl acid is produced as a by-product. Previously triethylamine was used to scavenge the acid, however, BASF replaced this with 1-methylimidazole. As a result the IL 1-methylimidazolium chloride is produced, which exists as a separate phase allowing easy separation and recycling. This change resulted in space-time yields increasing from 8 to 690 000 $kgm^{-3}h^{-1}$ and the yield increasing from 50 % to 98 %.[12] This showed that ILs can not only be applied to commercial processes but can bring about massive commercial benefits.[13] The largest commercial usage of IL is a process from the Chinese petrochemicals company PetroChina.[14] The process has been named Ionikylation and has been retrofitted to an existing plant.[14] This involves the alkylation of isobutene and takes place in an IL based on aluminium(III) chloride which is highly Lewis acidic. Like the previous example the implementation of this process resulted in a large increase in yield and a 40 % increase in the capacity of the process unit.[12]

The use of ILs in other areas of scientific research is widespread, for example the development of Lewis-neutral ILs has become increasingly important in materials science. Indeed a 2009 review of IL applications for future energy challenges documented their growing progress and implementation.[15] The use of IL in electrodeposition systems has provided a number of positive results, in particular the direct deposition of metals which are water sensitive. The key properties for these experiments are the low vapour pressures allowing deposition to be performed at higher temperatures and the wide electrochemical window associated with ILs. The

possibility to provide corrosion protection by electrodeposition of self-passivating aluminium from ILs has been demonstrated.[16] Meanwhile the use of ILs has been shown to be a solution to the deposition of metal nanowires where the use of aqueous solutions results in hydrogen evolution and poor quality products. With the use of an IL solvent, the formation of compact silver, cobalt, germanium and silicon nanowires has been demonstrated.[15,17-19] It has been desirable to develop techniques to electrochemically deposit semiconductors, the deposition of Si_xGe_{1-x} was shown using an IL.[20] This was achieved using silicon and germanium halides in a pure IL with the resulting semiconductor showing a bandgap of 1.5 – 3.2 eV.[20] Such experiments have been touted as a cost effective method for the fabrication of solar cells as the IL use resulted in the production of sufficiently pure deposit to allow photoluminescence effects.[15]

The use of batteries has been highlighted as potentially being a key part of future energy management. This is certainly true for the use of intermittent renewable energy sources or electric vehicles. Large scale lithium batteries can be susceptible to problems such as short circuits and local overheating, potentially resulting in fire or explosion due to reactions between the organic electrolyte and components. The use of lithium ion conducting electrolytes based on ILs removes the dangerous organic solvents and as a result such devices are the subject of numerous investigations for use as highly safe batteries of the future.[21,22] Additionally, potential developments towards hydrogen powered vehicles have been made using IL based polymer membranes.[15]

Bioscience has been an area where the use of ILs has expanded rapidly. Cellulose was previously only known to be soluble in an explosive organic compound which was problematic as it is useful to the textile industry and also as a biofuel source. Indeed it is produced at a rate of 10^{11} t yr^{-1} in nature making it a potentially very valuable energy source. Cellulose was found to be very soluble in ILs producing solutions with up to 25 wt% cellulose.[15] Further to the area of bioscience it has been shown that proteins can be dissolved in certain ILs and their highly ordered structures retained along with their associated effective reactivity. This was particularly true for chlorine based ILs where strong hydrogen bonding networks are

present[23] but this characteristic could also be obtained with the addition of 20 % water. Using the IL choline dihydrogen phosphate with 20 % water the electron transfer properties of cytochrome c were retained after storage at room temperature for 18 months.[24] Meanwhile it has also been shown that biomechanical actuators can be produced with IL electrolytes.[15] These examples are a small sample of the range of practical uses for ILs which have been developed in recent years. The practical application of ILs is subject to continued development with other applications including use in matrix-assisted laser desorption/ionisation (MALDI)[25], gas chromatography, liquid chromatography[26], use in liquid-mirror telescopes[27] and food analysis.[28]

1.2 Mass Spectrometry

Recent decades have seen mass spectrometry (MS) become a key analytical technique. Over the past one hundred years MS has gone from its earliest origin to a widely used technique which has outgrown the lab and can now be found in a broad variety of conditions and areas. Mass spectrometers can now be found in hospitals,[29] rainforests,[30] volcanoes,[31] deep-sea,[32] and outer space[33] to name but a few of the numerous possible applications. The development of miniature mass spectrometers which has been driven by Cooks and co-workers has lead to the technology becoming portable and having *in situ* applications in a broad variety of situations.[34]

1.2.1 History

The field of MS is widely acknowledged to have begun in 1912 with the work of Sir Joseph John Thomson. Thomson was awarded the 1906 Nobel Prize in Physics *"in recognition of the great merits of his theoretical and experimental investigations on the conduction of electricity by gases"*.[35] Working at Trinity College, Cambridge Thomson was investigating the composition of canal rays when he distinguished the ^{20}Ne and ^{22}Ne isotopes.[36] This was the first time isotopes had been shown for a stable element. This work was continued at Trinity College by one of Thomson's students, Francis William Aston. In 1919 Aston built a mass spectrometer which he used to discover the existence of isotopes for many more elements.[37] Publications of the

isotopes of elements such as chlorine, argon and krypton demonstrated the effectiveness of his technique. Meanwhile in 1918 Arthur Jeffery Dempster described the first modern mass spectrometer which, in 1920, he used to show the discovery of his first new isotopes; ^{24}Mg, ^{25}Mg and ^{26}Mg. Along with Aston he went on to describe the isotopic compositions of 83 elements by 1948.[37]

Modern mass spectrometers are made from a wide variety of different component parts which gives a wide choice of cost, quality and range. However, they all share the same general plan beginning with an inlet where a sample is introduced into the instrument. This inlet is then connected to an ionisation source where gas-phase ions are generated from the original sample. These gas-phase ions are passed to a mass analyser which will separate the ions based on their mass-to-charge ratio and perform a variety of instrument specific operations on the ions. Many modern mass spectrometers are fitted with more than one mass analyser. The ions are then transferred to a detector where they are counted and registered. The instrument is controlled by a computer system which is responsible for the correct operation of the instrument and it will also store and present the acquired data. The computer system is also responsible for control of the internal instrument electronics which can be varied to manage the product ions. In order to minimise the scattering of the ions and ion-molecule reactions, low pressures are required. While the precise extent of the reduced pressure is instrument dependant, the modern mass spectrometer requires high vacuum.

The use of MS was radically changed by the development of ionisation sources which are capable of transferring large molecules such as proteins into the gas-phase while keeping them intact. The similar techniques of MALDI and soft laser desorption (SLD), both of which use a laser to desorb the ions, were developed in the late 1980s by Karas, Hillenkamp and Tanaka.[38,39] Meanwhile, in 1984, Fenn developed electrospray ionisation (ESI) from a technique described in 1968 by Dole.[40,41] These techniques allowed the expansion of MS to study molecules without the presence of fragmentation and saw John B. Fenn and Koichi Tanaka awarded the 2002 Nobel Prize in Chemistry, along with Kurt Wüthrich who performed similar work with Nuclear magnetic resonance spectroscopy (NMR) *"for the development of*

methods for identification and structure analyses of biological macromolecules".[42-44] The work in this thesis uses the stabilising ability of the ESI technique for the formation of large salt aggregates.

1.2.2 Applications of MS to the Study of Salts and ILs

In this work MS will be applied to the study of ILs and as such previous applications of MS to similar systems is of interest. MS has been previously applied to investigate the aggregation of different compounds including salts. Using an ESI source fitted to a triple stage quadrupole mass spectrometer Zhou and Hamburger formed different salt aggregates and sodiated aggregates of solvents.[45] They showed that it was possible to form aggregates of acetonitrile with a single sodium ion. Meanwhile it was also shown that aggregates of sodium chloride, sodium formate and sodium acetate could be formed. These salt aggregates were singly charged and had the general formula $Na_{n+1}A_n^+$ where A represents the respective anion. In addition to this, the formation of mixed aggregates was also shown for these salt systems. Aggregates incorporating both the acetate and formate anions were created with the general formula $Na(CH_3CO_2Na)_x(HCO_2Na)_y^+$.[45] This investigation clearly showed that ESI-MS could be used to induce the formation of salt aggregates including metal chlorides and also showed the ability of the technique to produce mixed species which will be later attempted in this work with ILs. Hao *et al.* extended this work by completion of a detailed study on salt cluster ions using tandem MS.[46] This study used ten different salts including the alkali metal chlorides (LiCl, NaCl, KCl, RbCl and CsCl) and an assortment of sodium salts (NaI, HCO_2Na, $CH3CO_2Na$, $NaNO_2$ and $NaNO_3$). Micromass Quattro LC TSQ and QTOF2 mass spectrometers with ESI were employed to produce and study the aggregates. The effect on the ion current was investigated as the solvent, concentration and a range of instrumental tuning parameters were varied. With high cone voltages the presence of magic number aggregates were revealed as larger aggregates were broken down, while at low cone voltages the formation of numerous multiply-charged aggregates was shown. Additionally in the case of NaCl, as the pH was varied from 3 to 11 it was possible to observe mixed aggregates incorporating HCl and NaOH as appropriate with the

NaCl.[46] Aggregation including several of these salts will be attempted in the thesis and attempts will be made to reveal magic number aggregates.

Published in 2011, Ruttick *et al.* used a combination of MS and *ab initio* computational calculations to investigate the structure and stability of anionic metal chloride aggregates containing redox active metals.[47] Bruker Ultraflex III MALDI/TOF and Bruker Esquire ESI ion trap mass spectrometers were used to produce anionic metal chloride aggregates. The formation of copper chloride and iron chloride aggregates were shown with the metal ions adopting a mixture of oxidation states. However when losses were taking place it was observed that $CuCl_2$ and $FeCl_2$ fragments were preferred over other possibilities. Using these experiments and with the formation of mixed metal aggregates, the chlorine affinity was determined to follow the order: $FeCl_3 > CuCl > CaCl_2 > FeCl_2 > AgCl \approx CuCl_2 \approx ZnCl_2 > LiCl$. The Gaussian 03 suite of programs was used to confirm the order of this series and determine the structures of the aggregates. This approach was also used to find and investigate particularly stable mixed species. A series of aggregates were discovered of the form $MFe_2Cl_8^-$ where M = Li^+, Na^+, K^+, Rb^+, Cs^+, Ag^+ and Cu^+ and were determined to have the structure $FeCl_4^-\ldots M^+\ldots{}^-Cl_4Fe$. By studying these systems with this combination of techniques they were able to show the presence of the aforementioned Cu-Cl bridging and its influence on the dissociation of these aggregates. In the aggregates where M = Cu the loss of $FeCl_3$ was observed however the other metals showed the loss of $FeCl_4^-$. The use of ESI-MS also revealed the formation of other very prominent species and the favoured loss of specific aggregates such as Cu_2Cl_4 from $(CuCl_2)_nCl^-$.[47] By combining MS and *ab initio* computational calculations it has been possible to gain a great deal of insight into the structure and dissociation characteristics of a wide variety of salt aggregates. This combination of techniques will be applied to study the aggregation of ILs throughout this thesis.

In this project, the study of ILs in the gas-phase is integral. ILs are receiving ever increasing attention and the number of articles appearing has dramatically increased in recent years. In 2007 Strasser *et al.* formed a molecular beam from IL vapour of [1-ethyl-3-methylimidazolium] [bis(trifluoromethyl-sulfonyl)imide]

([C2mim][NTf_2]).[48] Extreme ultraviolet light was used to cause single photon ionization and it was observed that primarily the IL chose to exist as isolated ion pairs. Small clusters of IL were also observed and the binding energies of ([C2mim][NTf_2])$_n$ for n = 1 to 3 were reported. Their observations were in agreement with their own gas-phase computational simulations and provided results which were similar to the available liquid phase results. However, as they admit, more experimental work is required to confirm the dominance of ion pairs and also to examine the structure of them.[48] There are numerous published studies which use ESI to gain insight into the properties of ILs. Gozzo *et al*. used a variety of imidazolium based ILs to investigate the relative strengths of hydrogen bonding.[49] They observed a series of singly charged aggregates in both positive and negative ionisation mode. For example, in positive mode, the $C_{n+1}A_n^+$ series was observed where C is the imidazolium cation and A is an anion such as BF_4^-. By using collision induced dissociation (CID) with these systems, relative hydrogen bonding strengths of different anions could be found. Using different anions with the $C4mim^+$ cation the following sequence of hydrogen bond strengths were observed: $CF_3CO_2^- > BF_4^- > PF_6^-$.[49] These experiments provide an effective way of studying discrete interactions in the gas-phase, the good agreement between experimental kinetic studies and calculated physical properties such as hydrogen bonding strengths indicate robustness in the results and the applied techniques.

Alfassi *et al.* used ESI-MS to examine solutions containing mixtures of different ILs in methanol.[50] They were successfully able to estimate the solubility of different ILs using this method. Starting with an unknown quantity of IL in methanol and then adding a known quantity of a second IL allowed quantitative estimates for the initial amount to be made. This result was related to the solubility of the first IL in methanol.[50] Thermal stability is of interest in the study of ILs[51] and ESI-MS can be used with CID to investigate decomposition routes. Lesimple *et al.* used such a technique to study decomposition pathways for a number of imidazolium based ILs.[52] Using a triple quadrupole instrument, the substituted cation was mass selected and spectra were recorded over a series of different collision energies. By monitoring the relative amounts of the parent and daughter fragments they were able to reveal a

number of interesting pathways, some of which were surprising. These losses included H and CH_3 radicals and their deuterated analogues from even electron systems, which are unusual in such CID spectra. They attempted to rationalise these observations by sighting the influence of the localised positive charge on the imidazolium ring.[52] Similar results were also found by Lesimple *et al.* in a separate study which investigated sulfur containing ILs.[53] This investigation provides an effective route for studying fragmentation pathways of species and provides evidence for homolytic decomposition mechanisms.

Chowdhury *et al.* investigated the ILs 4-amino-1,2,4-triazolium chloride (4ATCl) and 4-amino-1,2,4-triazolium nitrate (4ATN) with the aim of investigating the proton transfer mechanism which initiates their thermal decomposition.[54] To achieve this aim, combinations of Fourier transform infrared (FTIR) spectroscopy and time-of-flight (TOF) mass spectrometry were used. They were able to propose primary and secondary dissociation pathways for both of the ILs of interest along with a proposed reaction pathway for 4ATCl. The suggested pathways involved radical initiation, propagation and termination and correspond well with other experimental results.[54] This work demonstrated the ability of MS to work in partnership with other techniques and give useful information about condensed phase systems. A study of numerous ILs in the gas-phase was presented by Bini *et al.* A scale was constructed showing the relative cation-anion interaction strengths.[55] "Supramolecules" of the ILs were created by ESI and relative stabilities were compared by CID with the general formula $C_{n+1}A_n^+$ or $C_nA_{n+1}^-$. Additionally mixed complexes with different ILs were formed which gave information about the relative magnitude of these interactions. These results provide an insight into these discrete interactions however the calculations presented with this work are very limited and no conclusions have been drawn.[55] The results do show that ESI-MS combined with CID in a QIT can be effectively used to examine IL aggregates. This combination of techniques will be exploited in later chapters.

Dorbritz *et al.* used ESI-MS to investigate the aggregation of the water miscible IL C4mimBF_4 and the water immiscible IL C4mimBis-(trifluoromethylsulfonyl)imide also known as C4mimNTf_2.[56] The structure of C4mimBF_4 was previously shown in

Figure 1-1. Dilute samples of these ILs were prepared in a range of organic solvents. The aggregates formed were found to vary depending on the particular solvent and also be dependent on the anion which was present. The results presented here are a very limited study, however, they were shown to be in agreement with conductivity experiments and by increasing the concentration of the IL in aqueous solutions the solubility of acetophenone increased exponentially over a small range of IL concentrations. Leal *et al.* used Fourier transform ion cyclotron resonance (FTICR) MS to study aprotic IL vapour under conditions similar to reduced-pressure distillation.[57] They found that under these conditions the vapour consists purely of neutral ion pairs. In their experimental setup the ions are vaporized in close proximity to the ion trap and the ionic species are produced in the ion trap using an electron beam. Meanwhile in the case of protic ILs of the form $[BH]^+X^-$ it was observed that under the same conditions their vapour consists purely of neutral molecules. These molecules are isolated and of the form B and XH.[57] As both classes of IL have been applied in a variety of situations this distinction is worth bearing in mind for future applications and research. In 2009 Fernandes *et al.* used a Micromass QTOF2 instrument fitted with an ESI source to investigate the aggregation of a wide range of IL in the gas-phase.[58] In particular they looked at a range of IL singly charged cationic aggregates with 1-alkyl-3-methylimidazolium cation and the BF_4^- anion and also ILs with $C4mim^+$ cation and a range of different anions. Almost without exception they observed a preference for the formation of the $C_5A_4^+$ aggregates where C is the different cations and A represents the anion. When these aggregates were investigated with CID it was shown that the C_2A^+ and $C_5A_4^+$ aggregates were comparatively stable compared with the other aggregates and very similar trends in the dissociation energies were observed between the different series. For the $C4mim_2A^+$ series of aggregates it was observed that as ionic volumes of anion decrease, the dissociation energies of the aggregates increases.[58] This study shows that ESI-MS can be used with CID to investigate the gas-phase aggregation of ILs and gain an insight into the similarities and differences as ionic replacement takes place.

1.3 Other Complimentary Analytical Techniques

A large number of other analytical techniques have been applied to ILs in an effort to gain a more detailed understanding into their properties. Many of these studies have replaced conventional solvents with ILs in order to observe a different effect which results from the manner of interaction between IL and analyte.[59] One such study investigated the binding constants of cyclodextrins and phenols in RTILs and D_2O. In the presence of the $C4mim^+$ cation, which was previously seen in Figure 1-1, it was observed that inclusion complexes form with cyclodextrin which compete with its binding with phenol. As a result of this, the binding constants are considerably lower compared with the use of D_2O.[60] This showed the possible effects of using IL in the presence of similar species and revealed information about the manner of binding which an IL can make. A number of studies on IL have been published using fluorescence spectroscopy.[59] An example of a particularly well studied fluorescent probe is the solvation of coumarin 153 in various ILs.[59] He *et al.* used the fluorescent probe 2-(*p*-aminophenyl)-3,3-dimethyl-5-ethoxycarbonyl-3H-indole to study β-cyclodextrin and its interactions with IL.[61] As in the previous example it was shown that the IL forms a 1:1 complex with the cyclodextrin but in addition to this it was shown that the formation is enthalpy driven while being entropically unfavourable. Wang *et al.* investigated the behaviour of several 1-alkyl-3-methylimidazolium based ILs in aqueous solution.[62] They determined different densities, conductivities and polarity indexes and additionally the aggregation in aqueous solution was investigated by fluorescence spectroscopy. The results revealed that the imidazolium based cations behave similar to short or moderate chain cationic surfactants. They were seen to form micelle-like structures, where the alkyl chains acted as a core to the micelles and the imidazolium rings on the surface. This technique allowed the determination of critical aggregation concentrations (CAC) and it was seen that the formation of these structures increases as the length of the alkyl chain increases. Conductivity measurements supported this observation by showing that the anions were significantly more solvated than the cations. They were also able to achieve a reasonable agreement between their simple calculations and the experimental observations.[62]

NMR has been used in several different studies to gain a greater understanding of ILs. One such study was carried out by Singh et al. to further investigate the aggregation behaviour of different ILs in the aqueous phase.[63] Aggregation was shown to be similar to the previous example where the cations behaved similar to short chain cationic surfactants. The ^{1}H NMR technique was capable of providing information about the structural changes upon aggregation. Conformational changes were observed in the IL on aggregation and this was found to be dependant on many different factors including the counter ions, alkyl chain length, aromatic ring and also the way they interact with water molecules.[63] Zhao et al. performed a similar investigation for five further ILs, these were C*n*mimBr, where n = 4, 6, 8, 10 and 12.[8] These experiments were performed in D_2O and similar to the previous publications, it was shown that the CAC reduces as the alkyl chain length increases. Their investigation of the aggregate species showed that the imidazolium rings of the cations were exposed to water, thus indicating their position on the outside of the aggregate, however their motion was seen to be more restricted than in ion pairs, suggesting a close association. In addition to this, the possible formation of microscopic aggregates was revealed. A possible structure for this was proposed which takes into account the observed interactions between the anions and both the D_2O and the cations along with an indicated π-π stacking interaction between the imidazolium rings.[8] Many further NMR investigations have been performed on ILs, such as analysing neat samples or quantitative analysis of acidic impurities.[59]

Characteristic Raman bands have been identified for multiple different imidazolium based cations.[64,65] These studies were combined with computational calculations to confirm the presence of general structural features in the long-chain cations. In addition to this, mixtures of different ILs were prepared and these were used to further the understanding of hydrogen bonding between the imidazolium "headgroups" and the IL anions.[65] Meanwhile Saha *et al.* prepared an X-ray crystallographic structure of the IL C4mimCl.[66] The elucidation of this structure revealed the presence of an extensive hydrogen bonding network between the cations and anions and hydrophobic regions with multiple alkyl chains. The cations are observed to make between two and three interactions with different anions and tend

to adopt similar configurations to each other. While there appears to be no evidence for π-π stacking taking place, the imidazolium rings do form what the authors term corrugated sheets. They conjecture that the crystal structure is a result of three main factors. These are the alkyl hydrophobic interactions, electrostatic interactions between the ions and the presence of the hydrogen bonding network. In previous work they determined the presence of similar factors in the liquid phase by Raman spectroscopy of this IL, and as such infer the presence of similar structural features in the liquid phase as was determined in the single crystal.[66] The publications discussed here have deepened the understanding of the structure of ILs. In particular, results from fluorescence spectroscopy, NMR spectroscopy and X-ray crystallography reveal structural features of these ILs which will be utilised in computational calculations in later chapters.

1.4 Computational Chemistry of ILs

There has been an increased interest over recent years in using computational chemistry to gain a greater understanding of the interactions and behaviour of ILs and this will be continued within this thesis. One of the pioneering pieces of work using *ab initio* techniques was performed by Turner *et al.* in 2003.[67] The primary focus of this research was to investigate the ion pairs of different ILs and then use these results in an attempt to find a correlation between structure and melting point. Using the Gaussian 98 suite of programs and employing the HF and MP2 methods along with the 6-31G* and 6-31+G* basis sets the ion pairs of 1-alkyl-3-methylimidazolium halide ILs were studied. They discovered that trends were hard to come by, however they did find linear relationships in the series of $C4mim^+$ halides and 1-alkyl-3-methylimidazolium iodides.[67] For the studied $C4mim^+$ halides, the melting temperatures were seen to increase linearly with the calculated interaction energies as the anion increased in size. Also, as the chain length increased for the 1-alkyl-3-methylimidazolium iodides, the melting temperatures were found to decrease linearly as the interaction energies decreased. This showed that Gaussian calculations can be successfully applied to the study of ILs and this will be continued in the later chapters.

Later, in 2006, Hunt *et al.* performed *ab-initio* calculations for the C4mimCl ion pair. This IL will be studied throughout this thesis with both MS and computational chemistry. The structures which have been determined for the ion pair will serve as a starting point for the calculation of the larger aggregates and are thus of key interest to this thesis. These investigations used the Gaussian 03 suite of programs to investigate the electronic properties of the ion pair.[68-70] They examined these systems with a number of different computational methods, such as B3LYP, MP2 and CCSD(T). Low energy conformations for the pair were identified and these geometries were characterised. Seven such conformations were observed and are represented in Figure 1-2.

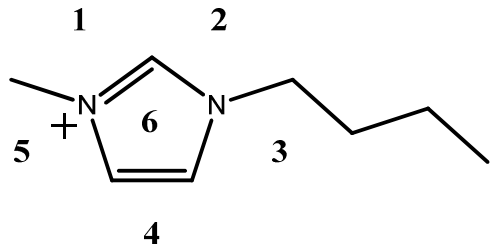

Figure 1-2 Structure of the C4mim$^+$ cation showing the six calculated positions for the Cl$^-$ anion.

Five of the conformations have the chlorine in plane with the imidazolium ring (1-5) while the final two have it directly above or below the ring (6). Gaussian calculations have shown positions 1 and 2 to be the most energetically favourable with position 4 the least favoured. Positions 3 and 5 were shown to be approximately 30 kJmol^{-1} higher in energy than positions 1 and 2. Meanwhile position 4 was approximately 30 kJmol^{-1} higher than positions 3 and 5. These structural features correspond well to those which were previously observed by X-ray crystallography. Additionally, many other fundamental properties were calculated, such as the effect of chlorine on the rotation of the butyl chain.[68] It is this IL which will be studied with computational chemistry within this thesis and the results summarised here will be used as a basis for that work.

In 2004 Voth *et al*. successfully calculated the effect of polarizability on the $C2mimNO_3$ IL using molecular dynamics (MD) simulations.[71] They showed that by considering a polarizable model for these calculations more accurate results can be found. The results provide an interesting insight with respect to physical properties such as viscosity but are limited in scope due to their preliminary status. Voth has also investigated the structure and dynamics of this IL.[72] Connections were found between the local ordering and a longer range ordering. They found that this order was caused by electrostatic interactions of the asymmetric cations and the associated charge ordering. Also it was found, as hypothesised, that there are a limited number of molecular displacements possible in the liquid. The ions are seen to vibrate within closed regions, which they call cages. It was shown that these cages could exist for in excess of 200 ps. This shows that MD calculations can be applied to study ILs and used to reveal information which has not been accessed through experimental chemistry. Meanwhile Wang *et al*. have used density functional theory (DFT) calculations to investigate the interaction between water molecules and various ILs containing $C4mim^+$ and $C2mim^+$ cations.[73] They were able to find relative strengths of interactions between water and the different species in the IL.

Koßmann *et al.* investigated cooperativity or many-body effects in ILs using static quantum chemical calculations.[74] When *m* monomer units form an oligomer and any property of the resulting oligomer is found not to be *m* times the value of the monomer the behaviour is called cooperativity. Linear and ring structures of dimethylimidazolium chlorine (C1mimCl) ion pairs were investigated with the linear chain like structures yielding the most interesting results. It was shown that as the linear chain length increases, the dipole moment increases approximately linearly with a value of about 16.3 D per monomer. Significant reductions were observed when the ring structures were considered.[74] These results clearly demonstrate cooperativity between ion pairs when they are in close proximity; this is clearly relevant and important when considering simulation of large aggregates.

In 2009 Kowsari *et al.* performed a systematic study on a range of 1-alkyl-3-methylimidazolium based ILs using MD simulations.[75] The aim of this work was to investigate the transport coefficients for these ILs. The calculations enabled the

electrical conductivity and viscosities to be determined for each of the liquids. The calculated results were seen to be in fairly good agreement with the experimental observations of other publications. It was seen that increasing the length of the alkyl side chain progressively from ethyl to butyl decreased the electrical conductivity and increased the viscosity of the IL. The likely cause of this was an increased van der Waals interaction and a decrease in the rotational freedom due to the larger and more asymmetric structures. The $C1mim^+$ cation showed viscosities higher than this series would predict, the symmetric nature of the cation along with observed good packing was the explanation for this. From their results it was summarised that the major factors to influence the transport coefficients for these ILs are the ion size, geometric shape and ionic charge on the anion.[75] Similar MD simulations were performed for 1-alkyl-3-methylimidazolium tetrachloroaluminate ILs by de Andrade *et al.* also in 2009.[76] In particular they utilised these calculations to learn more about the liquid densities, hydrogen bonding and internal energies. They found that as the chain length was increased from methyl to butyl the internal energies and electrostatic contributions decrease however the van der Waals interactions increase. The hydrogen bonding structure of the ILs was of interest in this study and it was found that hydrogen bonds form between the imidazolium ring bound hydrogen atoms and the chlorine atoms on the anions.[76] These hydrogen bonding results are similar to those previously seen for 1-alkyl-3-methylimidazolium based ILs using different techniques and similar structural features will be used to create initial structures for the computational chemistry results presented later in the thesis.[49,65,66]

Aparicio *et al.* used a combination of computational and experimental chemistry to investigate the IL C2mim L-(+)-lactate.[77] They performed calculations using the Gaussian 03 suite of programs employing the B3LYP method and the 6-311++G** basis set. By combining these calculations with different spectroscopic and thermophysical experimental techniques they were able to study both pure and hydrated samples. The presence of the hydroxyl group on the L-(+)-lactate anion helped build a strong hydrogen bonding network causing a high degree of structure in the IL. As the water content of the solution was increased the IL was able to maintain a remarkably high degree of its structuring. The IL was found to be

particularly hydrophilic and the presence of the water molecules was seen to reinforce the pre-existing network of hydrogen bonds. The authors suggest that water can be used to tune the physical properties of the mixed fluid allowing for its efficient use in a broader range of technical applications.[77] The partition coefficients or partition constants were determined for a range of specifically chosen probe molecules between several RTILs and water. Padró *et al.* performed this research with the aim of gaining greater insight into the interactions involved in RTIL/water partitioning and to predict the partition constants for other molecules of biological interest.[78] They showed that their training set of probe molecules could be used successfully to predict the partitioning of both unknown polar and hydrophobic molecules. They also noted that taking the mutual solubility of each solvent into account significantly improved the accuracy of the predictions. These examples show that computational chemistry can be successfully used to gain a greater insight into the properties of ILs including the construction of hydrogen bonding networks and the interaction with water, both of which will be of interest in later chapters.

Gao *et al.* employed a combination of Gaussian computational calculations and FTIR spectroscopy to study the interactions between ILs and volatile organic compounds (VOC).[79] The interactions were studied between C4mim$^+$ based ILs and alcohols, aldehydes, ketones, alkanes, alkynes and aromatic compounds. Calculation of the interactions suggested that the alcohols will be strongest and methanol will most strongly interact where the Cl$^-$ anion is present. When a single ion pair was used in the calculations a strong interaction was observed between C4mimCl and aldehydes and ketones however this effect was less pronounced when a second ion pair was added to the calculation. The strength of the calculations was shown by the FTIR spectroscopy where exposing the C4mimCl to either mixtures of VOCs or an individual VOC only resulted in the observation of characteristic alcohol signals. The ability of C4mimCl to selectively interact with alcohols could lead to their application in future gas-phase alcohol sensors.[79] These results show the strength of the Gaussian calculations for studying the interaction between ILs and other molecules and similar calculations will be performed in later chapters to exploit this observation. Fernandes et al. studied the interaction strengths in small gas-phase

aggregates of a variety of ILs using a combination of Gaussian calculations and MS.[80] The aggregates $[(cation)_2anion]^+$ and $[cation(anion)_2]^-$ were studied along with their dissociation where a cation and anion were lost respectively. The data collected from the calculations and MS were in good agreement showing that combining these techniques can help increase the information available about the interactions between individual ions in ILs. Higher interaction energies were observed for $[(cation)_2anion]^+$ compared with $[cation(anion)_2]^-$ and the general observed trends were shown to correspond to common thermophysical properties of the ILs which had previously been observed.[80] This combination of MS and computational chemistry is key to this thesis and the agreement achieved between these techniques is very promising.

1.5 Aims of This Work

A range of MS and computational chemistry results are reported in this thesis. The main aim of this work is to study the interactions present within gas-phase aggregates of ILs. The primary IL of interest will be 1-butyl-3-methylimidazolium chloride (C4mimCl). This combined approach of MS and computational chemistry will be used to study pure aggregates of IL and also to investigate the influence of contaminant species such as metal ions and water.

The thesis will be structured as follows. In Chapter 2, a summary of the methodology employed for IL synthesis and MS investigation is presented. Chapter 3 provides an outline of the computational methodology used throughout the thesis. Chapter 4 begins by demonstrating and comparing the formation of IL aggregates by MS using ESI, sonic spray ionisation (SSI) and plasma-assisted desorption ionisation (PADI). The $C4mim_{n+1}Cl_n^+$ aggregates for n = 1 to 7 produced by ESI are then subjected to CID to investigate their fragmentation and relative stability. Computational chemistry calculations for the possible structures adopted by these aggregates are also presented in this chapter. Finally, the binding energies are calculated and compared with the previously determined CID relative stabilities.

Chapter 5 studies the formation and structure of aggregates containing both C4mimCl and different metal ions. Lithium, sodium, potassium, caesium, magnesium and zinc were all used. ESI-MS was employed to examine the formation of these aggregates with varying solution composition and, as previously, CID was used to investigate the fragmentation and stability of several of the aggregates. Calculations for a number of aggregates containing a single metal ion are also presented within this chapter. In Chapter 6, unsuccessful methods for protonating and discretely solvating IL aggregates are shown. These methods are accompanied by calculations which attempt to investigate these experimentally challenging processes. Chapter 7 features a summary and discussion of conclusions of this work and considers possible future work.

1.6 References

(1) Horikoshi, S.; Lida, S.; Kajitani, M.; Sato, S.; Serpone, N. *Organic Process Research & Development* **2008**, *12*, 257-263.

(2) Welton, T. *Chemical Reviews* **1999**, *99*, 2071-2083.

(3) Earle, M. J.; Seddon, K. R. *Pure and Applied Chemistry* **2000**, *72*, 1391-1398.

(4) Barrer, R. M. *Transactions of the Faraday Society* **1943**, *39*, 59-66.

(5) Koel, M. *Ionic Liquids in Chemical Analysis*; CRC Press, 2008.

(6) Chum, H. L.; Koch, V. R.; Miller, L. L.; Osteryoung, R. A. *Journal of the American Chemical Society* **1975**, *97*, 3264-3265.

(7) Wilkes, J. S.; Levisky, J. A.; Wilson, R. A.; Hussey, C. L. *Inorganic Chemistry* **1982**, *21*, 1263-1264.

(8) Zhao, Y.; Gao, S. J.; Wang, J. J.; Tang, J. M. *Journal of Physical Chemistry B* **2008**, *112*, 2031-2039.

(9) Wilkes, J. S.; Zaworotko, M. J. *Journal of the Chemical Society-Chemical Communications* **1992**, 965-967.

(10) Gratzel, M. *Journal of Photochemistry and Photobiology C-Photochemistry Reviews* **2003**, *4*, 145-153.

(11) Bonhote, P.; Dias, A. P.; Papageorgiou, N.; Kalyanasundaram, K.; Gratzel, M. *Inorganic Chemistry* **1996**, *35*, 1168-1178.

(12) Plechkova, N. V.; Seddon, K. R. *Chemical Society Reviews* **2008**, *37*, 123-150.

(13) Maase, M.; Massonne, K.; Halbritter, K.; Noe, R.; Bartsch, M.; Siegel, W.; Stegmann, V.; Flores, M.; Huttenloch, O.; Becker, M.; USPTO, Ed.; BASF Aktiengesellschaft: Germany, 2003.

(14) Liu, Z. C.; Zhang, R.; Xu, C. M.; Xia, R. G. *Oil and Gas Journal* **2006**, *104*, 52–56.

(15) Armand, M.; Endres, F.; MacFarlane, D. R.; Ohno, H.; Scrosati, B. *Nature Materials* **2009**, *8*, 621-629.

(16) Caporali, S.; Fossati, A.; Lavacchi, A.; Perissi, I.; Tolstogouzov, A.; Bardi, U. *Corrosion Science* **2008**, *50*, 534-539.

(17) Kazeminezhad, I.; Barnes, A. C.; Holbrey, J. D.; Seddon, K. R.; Schwarzacher, W. *Applied Physics a-Materials Science & Processing* **2007**, *86*, 373-375.

(18) Yang, P. X.; An, M. Z.; Su, C. N.; Wang, F. P. *Chinese Journal of Inorganic Chemistry* **2007**, *23*, 1501-1504.

(19) Al-Salman, R.; Mallet, J.; Molinari, M.; Fricoteaux, P.; Martineau, F.; Troyon, M.; El Abedin, S. Z.; Endres, F. *Physical Chemistry Chemical Physics* **2008**, *10*, 6233-6237.

(20) Al-Salman, R.; Abedin, S. Z.; Endres, F. *Physical Chemistry Chemical Physics* **2008**, *10*, 4650-4657.

(21) Matsumoto, H.; Sakaebe, H.; Tatsumi, K.; Kikuta, M.; Ishiko, E.; Kono, M. *Journal of Power Sources* **2006**, *160*, 1308-1313.

(22) Shin, J. H.; Henderson, W. A.; Passerini, S. *Journal of the Electrochemical Society* **2005**, *152*, A978-A983.

(23) DiCarlo, C. M.; Compton, D. L.; Evans, K. O.; Laszlo, J. A. *Bioelectrochemistry* **2006**, *68*, 134-143.

(24) Fujita, K.; MacFarlane, D. R.; Forsyth, M.; Yoshizawa-Fujita, M.; Murata, K.; Nakamura, N.; Ohno, H. *Biomacromolecules* **2007**, *8*, 2080-2086.

(25) Mank, M.; Stahl, B.; Boehm, G. *Analytical Chemistry* **2004**, *76*, 2938-2950.

(26) Berthod, A.; Ruiz-Angel, M.; Carda-Broch, S. *Journal of Chromatography A* **2008**, *1184*, 6-18.

(27) Angel, R.; Worden, S. P.; Borra, E. F.; Eisenstein, D. J.; Foing, B.; Hickson, P.; Josset, J. L.; Ma, K. B.; Seddiki, O.; Sivanandam, S.; Thibault, S.; van Susante, P. *Astrophysical Journal* **2008**, *680*, 1582-1594.

(28) Fort, D. A.; Swatloski, R. P.; Moyna, P.; Rogers, R. D.; Moyna, G. *Chemical Communications* **2006**, 714-716.

(29) Gravet, A.; Camdessoucens-Miehe, G.; Gessier, M.; Peluso, A. R.; Vogelsperger-Fuchs, B.; Lohmann, C.; Schmitt, F.; Delarbre, J. M. *Pathologie Biologie* **2011**, *59*, 19-25.

(30) Misztal, P. K.; Owen, S. M.; Guenther, A. B.; Rasmussen, R.; Geron, C.; Harley, P.; Phillips, G. J.; Ryan, A.; Edwards, D. P.; Hewitt, C. N.; Nemitz, E.; Siong, J.; Heal, M. R.; Cape, J. N. *Atmospheric Chemistry and Physics* **2010**, *10*, 4343-4358.

(31) Diaz, J. A.; Pieri, D.; Arkin, C. R.; Gore, E.; Griffin, T. P.; Fladeland, M.; Bland, G.; Soto, C.; Madrigal, Y.; Castillo, D.; Rojas, E.; Achi, S. *International Journal of Mass Spectrometry* **2010**, *295*, 105-112.

(32) Wankel, S. D.; Joye, S. B.; Samarkin, V. A.; Shah, S. R.; Friederich, G.; Melas-Kyriazi, J.; Girguis, P. R. *Deep-Sea Research Part Ii-Topical Studies in Oceanography* **2010**, *57*, 2022-2029.

(33) Magee, B. A.; Waite, J. H.; Mandt, K. E.; Westlake, J.; Bell, J.; Gell, D. A. *Planetary and Space Science* **2009**, *57*, 1895-1916.

(34) Ouyang, Z.; Cooks, R. G. *Annual Review of Analytical Chemistry* **2009**, *2*, 187-214.

(35) Thomson, J. J.; Nobel Lecture ed.; Nobelprize.org: URL: http://nobelprize.org/nobel_prizes/physics/laureates/1906/thomson-lecture.pdf, Retrieved: 1 Jun 2011.

(36) Thomson, J. J. *Proceedings of the Royal Society of London Series a-Containing Papers of a Mathematical and Physical Character* **1913**, *89*, 1-+.

(37) Budzikiewicz, H.; Grigsby, R. D. *Mass Spectrometry Reviews* **2006**, *25*, 146-157.

(38) Tanaka, K.; Waki, H.; Ido, Y.; Akita, S.; Yoshida, Y.; Yoshida, T.; Matsuo, T. *Rapid Communications in Mass Spectrometry* **1988**, *2*, 151-153.

(39) Karas, M.; Hillenkamp, F. *Analytical Chemistry* **1988**, *60*, 2299-2301.

(40) Yamashita, M.; Fenn, J. B. *Journal of Physical Chemistry* **1984**, *88*, 4451-4459.

(41) Fenn, J. B.; Mann, M.; Meng, C. K.; Wong, S. F.; Whitehouse, C. M. *Science* **1989**, *246*, 64-71.

(42) Fenn, J. B.; Nobel Lecture ed.; Nobelprize.org: URL: http://nobelprize.org/nobel_prizes/chemistry/laureates/2002/fenn-lecture.html, Retrieved: 1 Jun 2011.

(43) Tanaka, K.; Nobel Lecture ed.; Nobelprize.org: URL: http://nobelprize.org/nobel_prizes/chemistry/laureates/2002/tanaka-lecture.html, Retrieved: 1 Jun 2011.

(44) Wüthrich, K.; Nobel Lecture ed.; Nobelprize.org: URL: http://nobelprize.org/nobel_prizes/chemistry/laureates/2002/wuthrich-lecture.html, Retrieved: 1 Jun 2011.

(45) Zhou, S. L.; Hamburger, M. *Rapid Communications in Mass Spectrometry* **1996**, *10*, 797-800.

(46) Hao, C. Y.; March, R. E.; Croley, T. R.; Smith, J. C.; Rafferty, S. P. *Journal of Mass Spectrometry* **2001**, *36*, 79-96.

(47) Ruttink, P. J. A.; Terlouw, J. K.; Luider, T. M.; Burgers, P. C. *Journal of Mass Spectrometry* **2010**, *46*, 223-229.

(48) Strasser, D.; Goulay, F.; Kelkar, M. S.; Maginn, E. J.; Leone, S. R. *Journal of Physical Chemistry A* **2007**, *111*, 3191-3195.

(49) Gozzo, F. C.; Santos, L. S.; Augusti, R.; Consorti, C. S.; Dupont, J.; Eberlin, M. N. *Chemistry-a European Journal* **2004**, *10*, 6187-6193.

(50) Alfassi, Z. B.; Huie, R. E.; Milman, B. L.; Neta, P. *Analytical and Bioanalytical Chemistry* **2003**, *377*, 159-164.

(51) Earle, M. J.; Esperanca, J.; Gilea, M. A.; Lopes, J. N. C.; Rebelo, L. P. N.; Magee, J. W.; Seddon, K. R.; Widegren, J. A. *Nature* **2006**, *439*, 831-834.

(52) Lesimple, A.; Mamer, O.; Miao, W. S.; Chan, T. H. *Journal of the American Society for Mass Spectrometry* **2006**, *17*, 85-95.

(53) Lesimple, A.; He, X.; Chan, T. H.; Mamer, O. *Journal of Mass Spectrometry* **2008**, *43*, 35-41.

(54) Chowdhury, A.; Thynell, S. T. *Thermochimica Acta* **2007**, *466*, 1-12.

(55) Bini, R.; Bortolini, O.; Chiappe, C.; Pieraccini, D.; Siciliano, T. *Journal of Physical Chemistry B* **2007**, *111*, 598-604.

(56) Dorbritz, S.; Ruth, W.; Kragl, U. *Advanced Synthesis & Catalysis* **2005**, *347*, 1273-1279.

(57) Leal, J. P.; Esperanca, J.; da Piedade, M. E. M.; Lopes, J. N. C.; Rebelo, L. P. N.; Seddon, K. R. *Journal of Physical Chemistry A* **2007**, *111*, 6176-6182.

(58) Fernandes, A. M.; Coutinho, J. A. P.; Marrucho, I. M. *Journal of Mass Spectrometry* **2009**, *44*, 144-150.

(59) Sun, P.; Armstrong, D. W. *Anal Chim Acta* **2010**, *661*, 1-16.

(60) Tran, C. D.; Lacerda, S. H. D. *Analytical Chemistry* **2002**, *74*, 5337-5341.

(61) He, Y.; Shen, X. *Journal of Photochemistry and Photobiology A: Chemistry* **2008**, *197*, 253-259.

(62) Wang, J. J.; Wang, H. Y.; Zhang, S. L.; Zhang, H. H.; Zhao, Y. *Journal of Physical Chemistry B* **2007**, *111*, 6181-6188.

(63) Singh, T.; Kumar, A. *Journal of Physical Chemistry B* **2007**, *111*, 7843-7851.

(64) Ozawa, R.; Hayashi, S.; Saha, S.; Kobayashi, A.; Hamaguchi, H. *Chemistry Letters* **2003**, *32*, 948-949.

(65) Berg, R. W.; Deetlefs, M.; Seddon, K. R.; Shim, I.; Thompson, J. M. *Journal of Physical Chemistry B* **2005**, *109*, 19018-19025.

(66) Saha, S.; Hayashi, S.; Kobayashi, A.; Hamaguchi, H. *Chemistry Letters* **2003**, *32*, 740-741.

(67) Turner, E. A.; Pye, C. C.; Singer, R. D. *Journal of Physical Chemistry A* **2003**, *107*, 2277-2288.

(68) Hunt, P. A. *Molecular Simulation* **2006**, *32*, 1-10.

(69) Hunt, P. A.; Gould, I. R. *Journal of Physical Chemistry A* **2006**, *110*, 2269-2282.

(70) Hunt, P. A.; Kirchner, B.; Welton, T. *Chemistry-a European Journal* **2006**, *12*, 6762-6775.

(71) Yan, T. Y.; Burnham, C. J.; Del Popolo, M. G.; Voth, G. A. *Journal of Physical Chemistry B* **2004**, *108*, 11877-11881.

(72) Del Popolo, M. G.; Voth, G. A. *Journal of Physical Chemistry B* **2004**, *108*, 1744-1752.

(73) Wang, Y.; Li, H. R.; Han, S. J. *Journal of Physical Chemistry B* **2006**, *110*, 24646-24651.

(74) Kossmann, S.; Thar, J.; Kirchner, B.; Hunt, P. A.; Welton, T. *Journal of Chemical Physics* **2006**, *124*.

(75) Kowsari, M. H.; Alavi, S.; Ashrafizaadeh, M.; Najafi, B. *Journal of Chemical Physics* **2009**, *130*.

(76) de Andrade, J.; Boes, E. S.; Stassen, H. *Journal of Physical Chemistry B* **2009**, *113*, 7541-7547.

(77) Aparicio, S.; Alcalde, R.; Atilhan, M. *Journal of Physical Chemistry B* **2010**, *114*, 5795-5809.

(78) Padro, J. M.; Ponzinibbio, A.; Agudelo Mesa, L. B.; Reta, M. *Analytical and Bioanalytical Chemistry* **2011**, *399*.

(79) Gao, T. T.; Andino, J. M.; Alvarez-Idaboy, J. R. *Physical Chemistry Chemical Physics* **2010**, *12*, 9830-9838.

(80) Fernandes, A. M.; Rocha, M. A. A.; Freire, M. G.; Marrucho, I. M.; Coutinho, J. A. P.; Santos, L. *Journal of Physical Chemistry B* **2011**, *115*, 4033-4041.

Chapter 2: Methodology – Ionic Liquid Synthesis and Mass Spectrometry

2.1 Ionic Liquid Synthesis

The synthesis of ILs has been an active area of research with many different methods published in the literature.[1,2] Traditionally they come in two types: metathesis of a halide salt and acid-base neutralization reactions. The method used for the synthesis of C4mimCl in this thesis used a metathesis reaction. The synthesis of C4mimCl was performed in anaerobic conditions under nitrogen using a Schlenk line apparatus. This synthesis was performed as previously detailed in the literature.[3] Briefly, 1-chlorobutane (Fisher Scientific, Leicestershire, UK, Cat# C/4750/05) was slowly added to a mixture of 1-methylimidazole (Acros Organics, Netherlands, Cat# 12699-1000) and toluene which had been cooled to 0 ˚C. The solution was then heated under reflux at 110 ˚C for 48 hours before being cooled at -20 ˚C for 3 days. A C4mimCl seed crystal was used in order to induce crystallisation. The toluene was decanted off and the resulting product first recrystallized from acetonitrile and then repeatedly from ethyl acetate. The resulting crystals were characterised by ^{1}H NMR and stored under dry ethyl acetate until required. For synthesis acetonitrile (41.05 $gmol^{-1}$), toluene (92.14 $gmol^{-1}$) and ethyl acetate (88.11 $gmol^{-1}$) were used. They were purchased from Fisher Scientific (Leicestershire, UK Cat# A/0626/17, T/2306/17 and E/0850/17 respectively).

The ILs C4mimOTf and C4mimPF_6 were prepared by the group of Prof. Tom Welton at the Department of Chemistry, Imperial College, London, UK following published procedures.[3] Anion exchange was performed on a C4mimCl precursor followed by recrystallization and characterisation by ^{1}H NMR.

2.2 Mass Spectrometry Methodology

2.2.1 Thermo Finnigan LCQ Classic mass spectrometer

The majority of the MS measurements were performed on a Thermo Finnigan LCQ Classic (LCQ) instrument. With the exception of a small number of clearly detailed experiments this was the sole instrument used; this included the MS experiments of the ILs in different solvents and the IL with metal chlorides. MS/MS experiments and the use of ESI, Sonic Spray Ionisation (SSI) and Plasma Assisted Desorption Ionisation (PADI) sources were also performed using this instrument. This instrument is fitted with an atmospheric pressure ionisation source from where ions are transferred through ion optics, a mass analyser and detector which are held under vacuum. ESI was the principle ionisation source, however other ion sources were employed and are clearly detailed where appropriate. The ions are passed through a heated capillary and ion optics before being stored in a QIT. A helium buffer gas (99.999%, BOC Gases, Surrey, UK) is used to thermalise the ions and the electrode voltages are varied in order to retain and emit ions of desired mass-to-charge ratios. The instrument can be used to detect either positive or negative ions dependant on the voltages which are applied throughout.

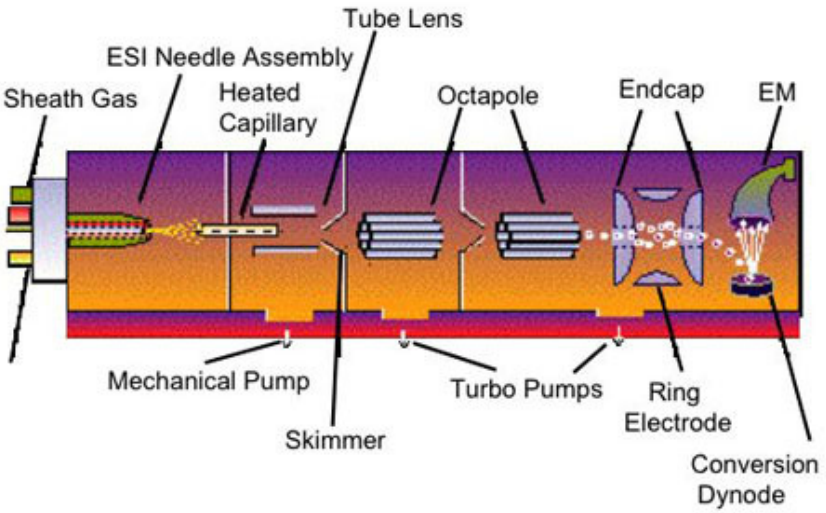

Figure 2-1 Schematic of a Thermo Finnigan LCQ Classic mass spectrometer.[4]

A schematic of the Thermo Finnigan LCQ Classic mass spectrometer is shown in Figure 2-1. The instrument consists of an interchangeable ion source [commonly ESI and atmospheric-pressure chemical ionisation (APCI)] which can be readily interfaced with liquid chromatography (LC) systems. The produced ions and charged droplets pass through a heated metal capillary to aid desolvation before being directed through a series of ion optics and skimmer which results in the formation of a focussed stream of ions. Two linear octupole mass analysers are placed consecutively after the ion optics which are used to further focus the ion beam. A quadrupole ion trap, which will be discussed in Section 2.2.5, is used to perform mass selection and collisional activation with a buffer gas before finally the ions are detected by an electron multiplier. The instrument was controlled using the standard Xcalibur® software version 1.1 from the Thermo Electron Corporation. The mass range studied using the LCQ ranged from 100 or 200 to 2000 *m/z* for MS studies where *m/z* is the mass-to-charge ratio. Instrumental limitations when performing collisional activation defined the available *m/z* range for MS/MS analysis.

There is only a very limited amount of literature available concerning the analysis of ILs by MS. So, it was therefore necessary to perform a significant amount of experimental optimisation. This was especially true concerning sample preparation and the determination of optimal instrumental parameters.

2.2.2 Electrospray Ionisation

The standard Finnigan LCQ Classic ESI head unit was used for the ESI experiments and a schematic of it is shown in Figure 2-2. Silica lines were used for infusion with an initial internal diameter of 200 μm which was reduced to 90 μm before reaching the ESI probe unit. Capillary voltages of approximately 4.5 kV were commonly used and the samples were introduced by direct infusion at a flow rate of 3 to 5 $\mu L min^{-1}$ using the attached syringe pump. A standard setup was determined and is detailed in Section 2.2.7 and deviations from this are detailed in the appropriate results section.

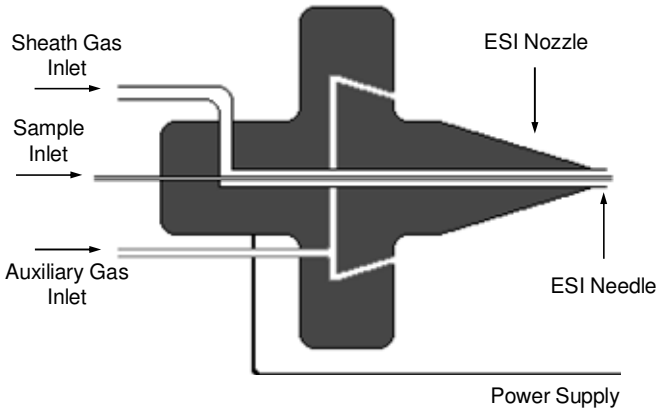

Figure 2-2 Schematic of the ESI assembly for use with the LCQ Classic instrument.[5]

2.2.3 Sonic Spray Ionisation

Sonic spray ionisation (SSI) has been shown to be useful for aggregation of species in the gas-phase and was used to aid formation of gas-phase IL aggregates.[6,7] SSI creates a supersonic spray of small droplets from solutions with an analyte in a volatile organic solvent. Methanol, water and acetonitrile are examples of typical solvents which can be used with this technique. SSI creates the supersonic spray using a pneumatic nebulizer with the spray source grounded without the need for any additional voltage to be applied, unlike ESI. A home built sonic spray source was used for the experiments and a schematic illustration of the source is shown in Figure 2-3. This apparatus consists of a silica line attached to a syringe pump. The silica line passes though a piece of stainless steel tubing and a Swagelok t-piece where a gas line is attached. Nitrogen gas was used for the SSI experiments and a stream of gas was produced through the stainless steel tubing. This acted as a sheath gas to the solvent spray in a coaxial direction and the sheath gas pressure was controlled by regulating the nitrogen gas pressure at the cylinder. The only modifications which were necessary to the LCQ instrument were the removal of the ESI source and the activation of the source interlock achieved with the design of the source.

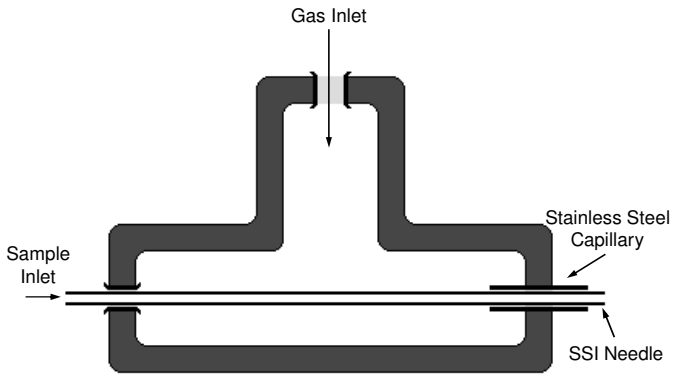

Figure 2-3 Schematic illustration of the SSI source.

To facilitate strong and consistent ion formation a significant amount of source optimisation was required. It was found that using silica tubing with an external diameter of 200 μm and an internal diameter of 120 μm resulted in a reliable spray. Setting the flow rate to 10 μL min^{-1} also gave desirable results. The SSI source unit was mounted on an XYZ stage to allow the spray position relative to the mass spectrometer inlet to be optimised. It was found that the strongest and most stable signal was produced when the SSI nozzle was directly in front of the mass spectrometer, and about 8 mm back from the inlet.

2.2.4 Plasma Assisted Desorption Ionisation

PADI is another novel ionisation technique which is still in its infancy. A low temperature, non-thermal plasma is used for direct analysis from surfaces at ambient pressure. As the plasma interacts with the surface it results in desorption and ionisation with the resulting ions sampled by the mass spectrometer. This requires the mass spectrometer inlet to be in close proximity to the sample and the plasma. An RF plasma source was used in collaboration with Prof. M.R.S. McCoustra, Heriot Watt University, Edinburgh and Hiden Analytical Ltd., Cheshire. The apparatus shown in Figure 2-4 was as detailed in previous publications and basically consists of a small RF plasma generator.[8] The PADI source is shown in operation in Figure 2-5(a) and the plasma can be brought into direct contact with an analyte while in close proximity to the inlet of the LCQ. The only modification required to use the PADI source with the LCQ was the removal of the ESI source.

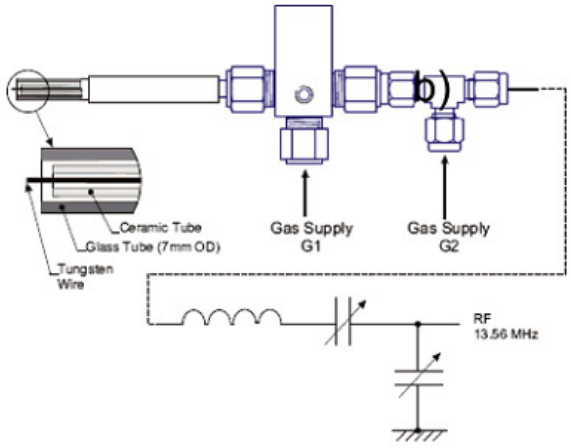

Figure 2-4 Schematic representation of the PADI probe unit.[8]

Sample preparation for use with PADI was very limited as direct analysis from the sample has been performed[8] and was further attempted in this work. A cartoon representation of this is shown in Figure 2-5(b). This method was used for the analysis of many different samples during optimization of the source. Direct analysis was attempted from paracetamol, caffeine, Doxepine and samples of the ionic liquids C4mimCl and C4mimOTf dried onto glass rods. Successful use of this easy preparation could allow the technique to be used for high throughput analysis and rapid screening of compounds.

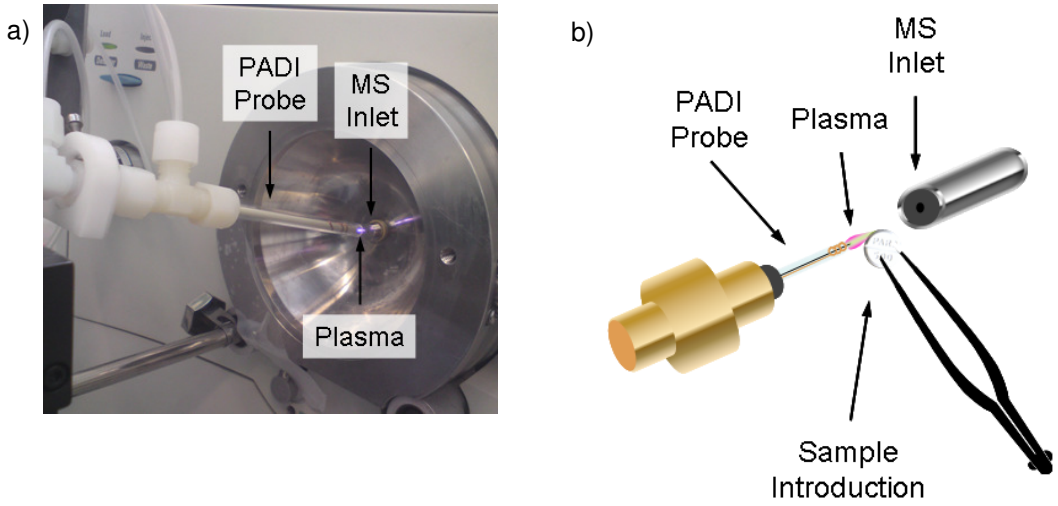

Figure 2-5 a) Photograph showing the PADI source in operation with the LCQ mass spectrometer b) Cartoon representation of direct PADI analysis of a paracetamol tablet.

It was found that introducing the samples in solution resulted in an increased signal-to-noise ratio. Therefore the apparatus shown in Figure 2-6 was used to introduce the IL samples. The IL was dissolved in a range of organic solvents and these were delivered from a syringe pump. Methanol was found to produce a relatively high signal-to-noise ratio, compared with water, and greater aggregation was observed compared to acetonitrile. The rate of introduction was varied to find the optimal value of 30 $\mu Lmin^{-1}$ and samples were introduced through a nano pipette. The use of this capillary setup caused the formation of droplets on the nano pipette which subsequently fell into the plasma resulting in the formation of charged samples.

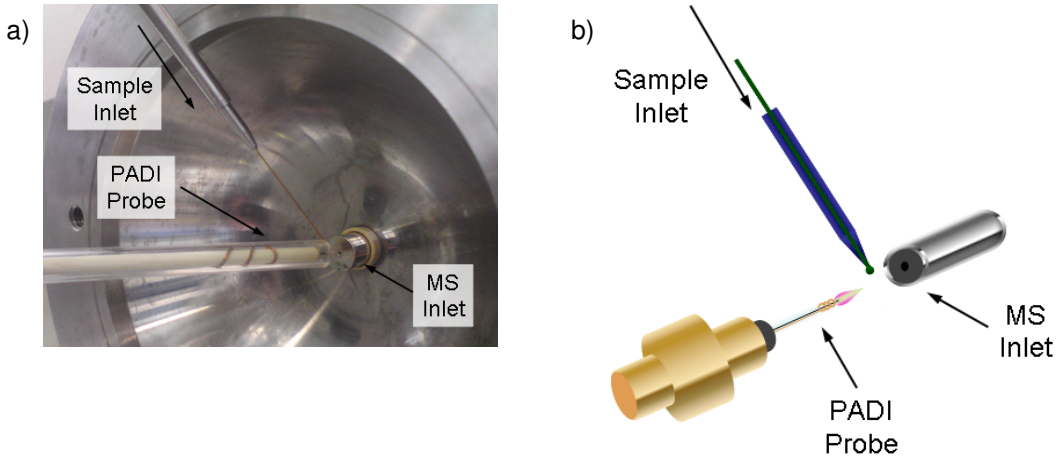

Figure 2-6 PADI setup for analysis of liquid samples. a) Photograph of PADI probe setup with LCQ MS b) Cartoon representation of PADI probe for liquid sample analysis.

2.2.5 Quadrupole Ion Trap and Collision Induced Dissociation

The quadrupole ion trap (QIT) is a device for trapping ions in the gas-phase. It was developed by Wolfgang Paul in 1957 and uses electric fields to hold the ions.[9] In 1989 Wolfgang Paul was awarded a share of the Nobel Prize in Physics *"for the development of the ion trap technique"*.[10] The QIT consists of three electrodes; one is ring-shaped and two are hyperbolic end cap electrodes with the ions held in the space between them; a schematic representation of this is shown in Figure 2-7. In order to trap ions in this space, specific voltages need to be applied to each of the electrodes. A DC voltage will be applied to the end cap electrodes while a fundamental radio frequency AC voltage is applied to the ring electrode.[11] When it is desirable to perturb the trapped ions an AC voltage is applied to the end cap electrodes for a short period. To eject the ions, the AC voltage applied to the ring electrode is increased. The electric field is constructed and controlled in such a way as to focus trapped ions by imparting a stronger restoring force as the ions distance from the centre of the trap is increased.

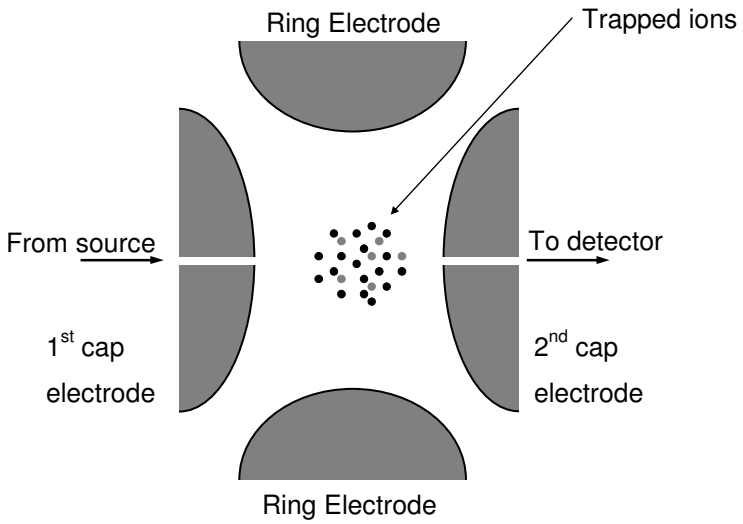

Figure 2-7 Quadrupole ion trap schematic showing trapped ions and approximate positions of entry and exit. Schematic produced by author using W. Henderson and J. S. McIndoe diagram[9] as a guide.

To reduce ion-molecule collisions a high vacuum is applied to the QIT, however, an inert buffer gas will normally be present. Through numerous low energy collisions this gas will remove excess energy from the trapped ions. In addition, as will be discussed later, the energetic collisions can be used to induce fragmentation of the trapped ions.[9] Typical buffer gases include nitrogen and the noble gases; in particular helium and argon are widely used. A constant gas pressure of approximately 0.1 Pa is maintained within the ion trap to do this. These ion traps operate at comparatively modest a pressure (for the Thermo Finnigan LCQ Classic mass spectrometer this is around 1 x 10^{-5} Torr) which has a favourable impact on the instrument cost. Additionally the control software can be used to trap an optimum number of ions as too many can impair the instrument performance by distorting the electric fields, this is known as the space-charge effect.

The early ion traps were designed to trap ions which were created *in situ* and since this time it has been desirable to couple it with other ionisation sources and transfer the ions to the trap to expand the applicability of the technique.[9] This aim was the driving force behind much of the instrument development and its success has

resulted in the wide acceptance of trapping techniques. Many different approaches have been attempted to achieve such transfer, these were through holes in the ring or end cap electrodes and also between the electrodes.[12] In order to control the directionality, *m/z* range and frequency of the injected ions, careful control of the applied potentials is essential. Successful examples of where this has been achieved include interfaces with MALDI, Secondary Ion Mass Spectrometry (SIMS) and spray techniques such as ESI.[13]

With the use of such ion traps it is possible to perform a process known as low energy collision induced dissociation (CID). This process occurs when a collision between the trapped ions and the buffer results in the transfer of translational energy into internal energy.[9] This energy is rapidly distributed between the vibrational modes of the ion which number 3*N*-5 and 3*N*-6 for linear and non-linear molecules respectively, where *N* is the number of atoms. It is possible for multiple collision events to occur and when the internal energy is sufficient, unimolecular decomposition or fragmentation of the analyte ion can take place. In practice a particular *m/z* range is selected and all of the remaining ions are discarded. The trapped ions are activated by collisions with the buffer gas and all of the resulting ions are recorded. This process is known as MS/MS. The use of an atomic gas such as helium or argon is suitable for such collisions as polyatomic gases would become vibrationally excited there by reducing the efficiency of the process. Where an atmospheric pressure source region is used, in-source CID can be performed. This occurs when energetic collisions are induced between the analyte ions and atmospheric gases prior to the ions reaching the low pressure regions of the instrument. It is possible to combine in-source CID with CID performed in an ion trap to gain additional structural information about the analyte of interest.[9]

In a QIT, variation of the applied AC voltage to the end cap electrodes will affect the trapped ions resulting in collisions being induced; this is known as a “tickle voltage”. Trapped molecular or non-covalently bound species will have a critical internal energy where they will dissociate; as the end cap potentials are altered the dissociation can be monitored.[14] Using a QIT it is possible to perform repeated cycles of MS/MS in order to gain an increasingly large amount of information about

the ionised species. These experiments are referred to as MS^n where n is the number of cycles. It has been possible to perform experiments where n was as large as ten, however high ion losses generally limit such experiments to $n = 3$ or 4. As in the previous example with MS/MS, the selection of a particular *m/z* range takes place followed by collisional activation. From the resulting daughter ion spectrum a new *m/z* range is selected to trap one of the daughter ions and the others are discarded. The cycle is then repeated as desired and as the signal strength allows.[9] In summary the QIT has been found to be a versatile, relatively inexpensive and robust mass analyser. It can provide good sensitivity and has been shown to be suitable for miniaturisation, however the collision energy in CID experiments can be poorly defined and the trap remains susceptible to the space-charge effect.[9] As a result of the development of the QIT, it has become a useful analytical tool which can be used to select ions within a particular mass-to-charge range. By activating the trapped ions to different degrees and monitoring the amount of dissociation that takes place the relative stabilities for different ionic species can be inferred. This means that we can get direct, relative information about molecular stability or weak non-covalent interactions.[15]

There is a mass dependence on the tickle voltage which is required for dissociation of different species; heavier ions require more energy than smaller ions which have a similar stability. By sampling a large number of compounds it has been shown that the applied tickle voltage for optimal fragmentation follows a linear correlation with mass. Thermo Fisher Scientific determined this relationship and developed a correction for this using "normalized collision energy" (NCE). Previous to the use of NCE, the tickle voltage had a maximum value of 5 V and was applied as a percentage of this. NCE corrects for the mass dependence by applying a lower voltage for lower mass ions and a higher voltage for higher mass ions, with the magnitude based on the previously determined relationship. For example, applying a specific NCE will no longer carry a mass dependence which allows for comparisons to be made between ions of different masses.

All of the LCQ experiments were performed using a helium buffer gas in the QIT. Throughout the presented work the pressure of helium within the cell was maintained at 0.1 Pa. The collisional activation energy and length of the activation time were controlled through the Xcalibur® 1.1 software. The collisional activation energy is related to the previously discussed "tickle" voltage applied to the end cap electrodes which causes the energetic collisions with the buffer gas. This instrument utilises NCE developed by Thermo Fisher Scientific to correct for the previously mentioned mass dependence on the tickle voltage required for fragmentation. This was previously described and gives applied collision energies as a percentage value due to historical reasons; while this limits the precise determination of energy it does give values which are comparable to each other. CID experiments were performed with NCE applied between 0% and 100% for the different experimental runs and the activation time was set to 30 ms for all samples. The accumulation time of ions within the trap was set to a maximum value of 200 μs with accumulation times limited by the charge density. Fragmentation of the parent ions was generally seen to take place with applied NCE values between 15 and 30 %.

2.2.6 Data Analysis

Data produced from the LCQ experiments were analysed with the aid of the Xcalibur® software version 2.0 (Thermo Electron Corporation), Microsoft Excel (Microsoft Office 2003) and Origin (OriginLab, Northampton, MA, USA) version 8.0725. Analysis of the raw mass spectra for species identification was done in a number of ways. These included comparing the mass with predicted aggregates, using the Xcalibur® 2.0 software to simulate the isotopic distributions and using the tandem mass spectrometry facility of the LCQ. MS/MS was used to induce fragmentation, identification of the mass losses with increasing activation energy can aid in the determination of the parent ion structure. An example will be used to demonstrate this technique using the C4mimCl IL and as a reminder, the cation structure is shown in Figure 2-8. This IL will be seen throughout this thesis.

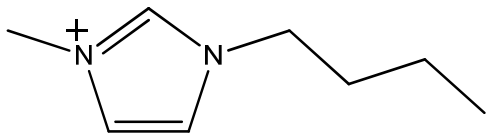

Figure 2-8 Structure of the C4mim$^+$ cation.

Fragmentation and identification of mass losses are shown in Figure 2-9. In this example the parent ion is $C4mim_5Cl_4^+$ and three sequential losses of the ion pair C4mimCl are shown to produce the daughter ions $C4mim_4Cl_3^+$, $C4mim_3Cl_2^+$ and $C4mim_2Cl^+$. The instrument was set to apply an activation energy of 17 % NCE. This energy was sufficient to cause the partial fragmentation of the parent ion causing the parent ion to no longer be the base peak for the spectrum.

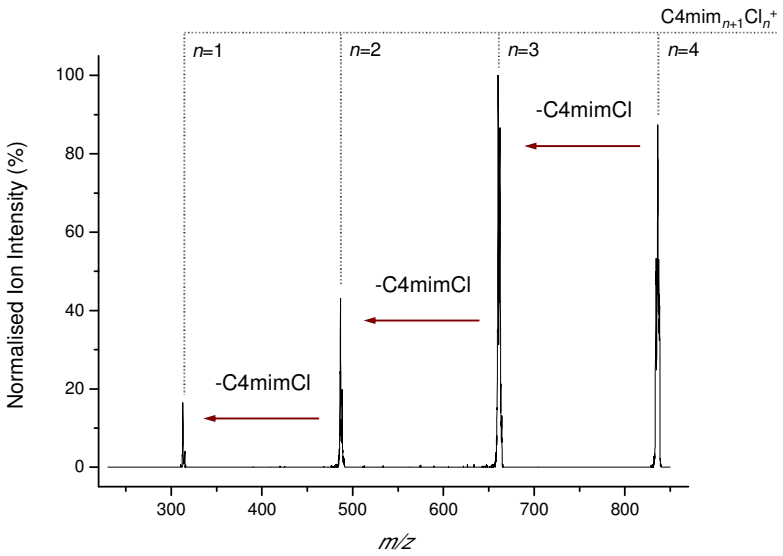

Figure 2-9 MS/MS of $C4mim_5Cl_4^+$ where an activation energy of 17% was applied.

MS/MS analysis (previously described in Section 2.2.5) was a time consuming process made up of a large number of short data collection experiments, followed by repetitive extraction of peak intensities from Xcalibur® 2.0 and amalgamation of the resulting information into Microsoft Excel and Origin. Either 20 or 30 individual scans were taken for every NCE value for each of the studied species. The ion count associated with each peak can then be calculated as a percentage of the total ion chromatogram (TIC) for the entire mass range. The TIC is the total intensity associated with the ions detected for every mass at each point during an analysis.

Graphs of the relative abundance of each species against the NCE were then created such as can be seen in Figure 2-10. These graphs show the change in the intensity of the species which are present with varying collisional activation. The entire process was repeated three separate times for each ion in order to determine average values.

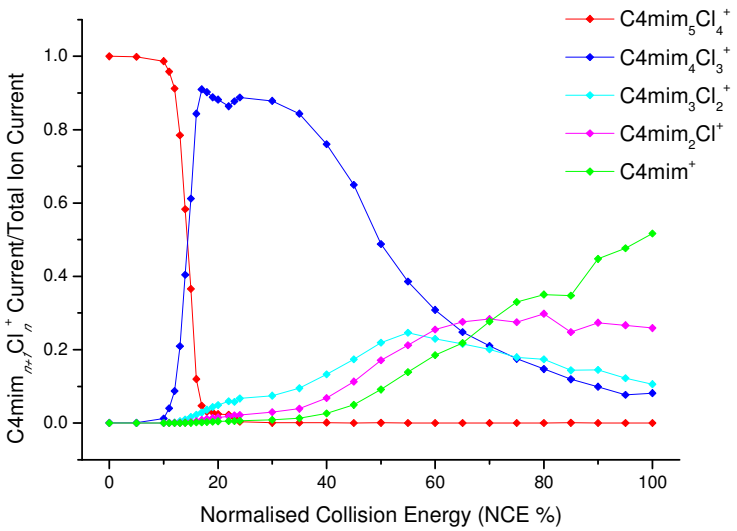

Figure 2-10 Sample graph of $C4mim_{n+1}Cl_n^+$ Ion Current/Total Ion Current for the parent and daughter ions with NCE between 0 and 100 %. The parent ion case was $C4mim_5Cl_4^+$.

The concept of a survival yield has been in published in the literature.[16] This allows for the characterisation and comparison of the stability for different species in MS/MS. The survival yield is the relative abundance of the parent ion as a function of the TIC and this can be calculated using Equation 2-1[16]:

$$SY = \frac{I_M}{I_M + \sum I_F} \qquad \textbf{Equation 2-1}$$

Where SY is the survival yield, I_M is the intensity of the parent ion and the intensity of the fragment ions is I_F. The graphs of survival yield showed that the decreasing precursor ion signal follows a sigmoidal curve and the Origin 8.0 software was subsequently used to fit sigmoidal curves to these data sets. The value at which the survival yield had reached its midpoint was determined for each curve as shown in Figure 2-11. This energy is sometimes referred to as the characteristic collision

energy (CCE) and is characteristic of the gas-phase stability allowing for comparison to be made between different species. The repeated measurements for the same species were averaged and standard deviation errors could be readily determined.

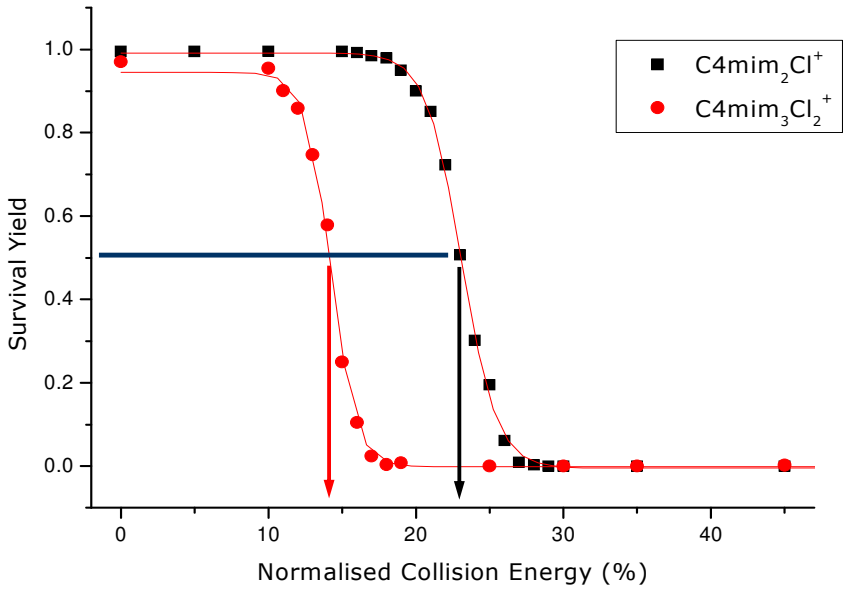

Figure 2-11 Breakdown curves (SY vs. NCE) of $C4mim_3Cl_2^+$ and $C4mim_2Cl^+$ with fitted sigmoidal curves shown in red. The determination of the 50% SY and CCE are demonstrated with heavy lines.

2.2.7 Instrument Optimisation

It was necessary to determine the voltages and temperatures which need to be applied to the instrument in order to obtain an optimal signal. This was additionally accompanied by optimisation of the solvent choice and the analyte concentration used in the experiments.

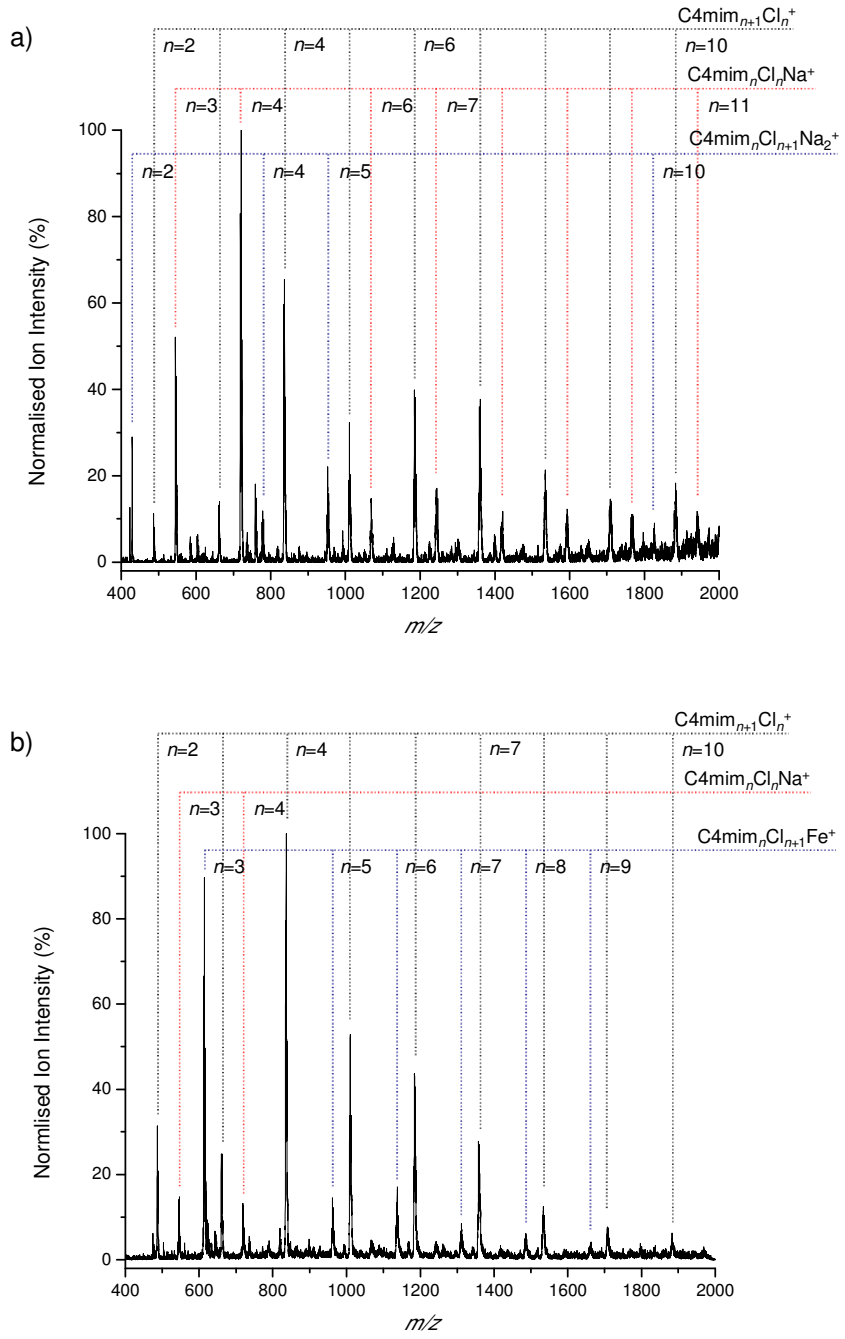

Figure 2-12 Mass spectra of C4mimCl in MeOH with a concentration of a) 1.1 mM and b) 5.0 mM. The C4mim$_{n+1}$Cl$_n^+$ (n = 2 to 11) series is highlighted in grey and adduct peaks are labelled as indicated.

Figure 2-12 shows the mass spectra produced from solutions with two different concentrations of C4mimCl in methanol. Figure 2-12(a) was produced with a concentration of 1.1 mM and shows the formation of the C4mim$_{n+1}$Cl$_n^+$ series for n =

2 to 10 along with several sodium containing aggregates. Figure 2-12(b) shows the result of increasing the concentration to 5.0 mM, in this case the $C4mim_{n+1}Cl_n^+$ series for n = 2 to 10 is again seen along with other mixed aggregates. The signal-to-noise ratio has increased significantly with increasing concentration and the number of mixed species appears to have decreased. The $C4mim_{10}Cl_9^+$ and $C4mim_{11}Cl_{10}^+$ appear to have decreased in intensity however this is just the relative intensity and the signal associated with these species has actually increased. The precise mixed species which are observed is dependant on the sample preparation and instrument condition so does vary between spectra, however trends of having sodium, potassium and iron present are often observed. These are two sample spectra of a study to investigate the effect of varying analyte concentration. It was found that in order to produce optimal signal intensity along with a wide range of singly charged cationic aggregates, concentrations of IL between 3 and 5 mM were favourable. Similar concentrations were additionally found to produce good signal intensity with a wide range of aggregates for the study of the ILs C4mimOTf and $C4mimPF_6$.

The effect of varying the solvent was taken into account and it was found that using methanol as a primary solvent gave a good return in terms of signal strength, aggregation, solubility and cost. However when additional chloride salts were added to the solution it proved necessary to have a small percentage of water to aid dissolution. 90:10 mixtures of methanol and water were found to be suitable and were commonly used. Further studies were undertaken to find the optimal instrumental parameters for these IL. Extensive tuning was required for the capillary temperatures used and voltages which were applied to the ion optics. This allowed for the optimal ion production and transmission giving consistent, reliable and reproducible results. These values were used throughout the thesis unless otherwise stated. The optimised instrument settings for ESI-MS and ESI-MS/MS were as follows:

Solution Flow Rate:	5 $\mu Lmin^{-1}$
Sheath Gas Pressure:	50 psi

Auxiliary Gas Pressure:	0 psi
Spray Needle Voltage:	4.5 kV
Capillary Temperature:	200 ˚C
Capillary Voltage:	46 V
Tube Lens Offset:	15 V
Octupole 1 Offset:	-2.00 V
Lens Voltage:	-16 V
Octupole 2 Offset:	-4.5 V
Octupole RF Amplitude (peak to peak):	400 V
Electron Multiplier Voltage:	-970 V.

2.2.8 Solvents and Salts

The solvents which were used were acetonitrile (41.05 $gmol^{-1}$), water (18.02 $gmol^{-1}$), methanol (32.05 $gmol^{-1}$), hydrochloric acid (36.46 $gmol^{-1}$), acetic acid (60.05 $gmol^{-1}$) and formic acid (46.03 $gmol^{-1}$). These solvents were all obtained from Fisher Scientific (Leicestershire, UK Cat# A/0626/17, W/0112/15, M/4026/17, A/0360/PB08, H/1150/PB15 and A117-50 respectively) and used as provided.

Mixed metal chloride and IL aggregate experiments used various metal chloride salts which were purchased from Fisher Scientific (Leicestershire, UK). The salts purchased were lithium chloride, sodium chloride, potassium chloride, caesium chloride, magnesium chloride and zinc chloride (cat# L/2200/48, BPE358-1, BPE366-500, C/0640/46, BPE214-500 and Z/0850/60 respectively)

2.2.9 QTOF1 and nano-ESI

Analysis of C4mimCl gas-phase aggregate formation was also studied on a Waters Micromass QTOF1 mass spectrometer (QTOF). As shown in Figure 2-13, the instrument contains an ionisation source, ion optics, a quadrupole to act as an ion guide and to perform *m/z* selection, a collision cell with hexapole for CID if required and a reflection time-of-flight mass analyser and microchannel plate (MCP) detector. This instrument provided a significantly higher mass resolution than the LCQ and an improved signal-to-noise ratio.

This instrument uses a time-of-flight (TOF) mass analyser which determines the *m/z* ratio of ions by measurement of time. Briefly, ions are accelerated by an electric field which results in ions of like charge having the same kinetic energy. The velocity of the ions and subsequently the time taken to reach the detector depends on their *m/z* ratio. To correct for any small distribution of kinetic energies within ions of the same *m/z* ratio, a reflectron TOF uses an electrostatic field to reflect all of the ions towards a detector. More energetic ions penetrate further into the field and consequently take a longer path to reach the detector than less energetic ions. The detector is placed so that ions with different energies will impact the detector at the same time. A MCP is a device used to detect ions. It is a plate consisting of an array of small cylindrical tubes leading from one face to the other. These tubes are microchannels and act as electron multipliers. Ions impacting the side of a tube cause a cascade of electrons by secondary emission which results in a much larger signal exiting the MCP allowing for detection.

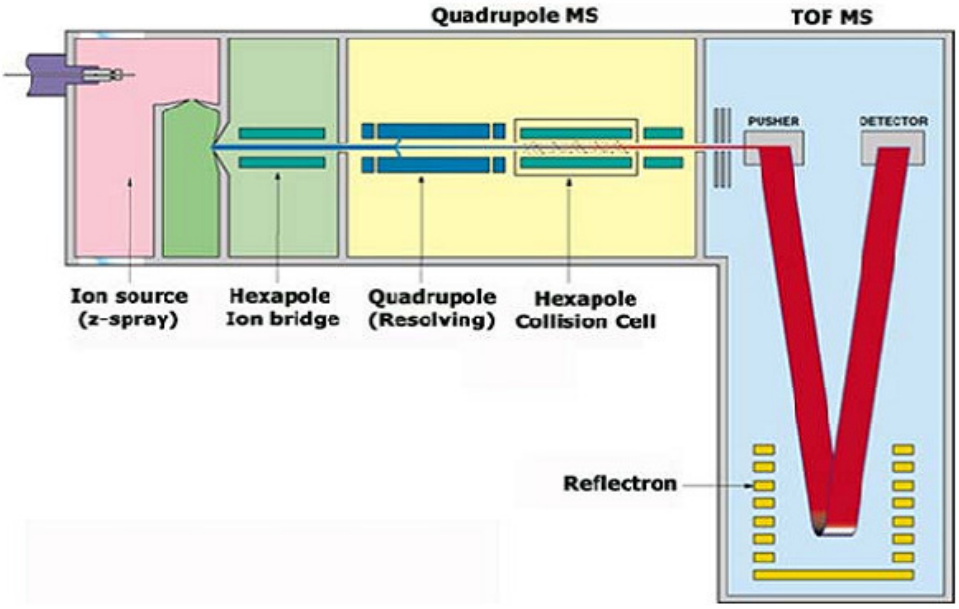

Figure 2-13 Schematic representation of a Waters Micromass QTOF1 instrument showing quadrupole and ToF regions.

A Micromass Z-spray ion source was used with ESI and nano-ESI for these experiments. This source applies a series of voltages within the source region in order to bend the ion beam through two 90 ˚ turns. The quantity of neutral species is significantly reduced both due to their non-deflection with voltage application and the skimmers positioned on the beam path. This produces a focused ion beam which is directed towards the low pressure regions beginning with the hexapole. The nano-ESI source uses lower capillary voltages (1.5 kV compared with 4 kV for ESI) and used reduced sample volumes. The tips required for nano-ESI analysis were produced in house using a Flaming/Brown Micropipette Puller (P-97, Sutter Instrument Company, Novato, CA, USA). Tips were pulled from borosilicate glass capillary tubes with an internal diameter of 1.2 mm (Kwik-Fil, World Precision Instruments, Sarasota, FL, USA). Optimal settings for the tip puller were determined by the Dr Perdita Barran Research Group and the resulting tips were 4-5 cm in length with tip diameters of 10-30 μm.

2.3 References

(1) Hallett, J. P.; Welton, T. *Chemical Reviews* **2011**, *111*, 3508-3576.

(2) Welton, T. *Chemical Reviews* **1999**, *99*, 2071-2083.

(3) Cammarata, L.; Kazarian, S. G.; Salter, P. A.; Welton, T. *Physical Chemistry Chemical Physics* **2001**, *3*, 5192-5200.

(4) Beauchamp Research Group; http://www.jlb.caltech.edu/research/lcq/ Retrieved: 20 Oct 2010: Caltech, Pasadena, CA.

(5) Finnigan *LCQ Manual, Getting Started*; B ed.; Thermo Electron Corporation: San Jose, 2005.

(6) Hirabayashi, A.; Sakairi, M.; Koizumi, H. *Analytical Chemistry* **1995**, *67*, 2878-2882.

(7) Myung, S.; Julian, R. R.; Nanita, S. C.; Cooks, R. G.; Clemmer, D. E. *Journal of Physical Chemistry B* **2004**, *108*, 6105-6111.

(8) Ratcliffe, L. V.; Rutten, F. J. M.; Barrett, D. A.; Whitmore, T.; Seymour, D.; Greenwood, C.; Aranda-Gonzalvo, Y.; Robinson, S.; McCoustra, M. *Analytical Chemistry* **2007**, *79*, 6094-6101.

(9) Henderson, W.; McIndoe, J. S. *Mass Spectrometry of Inorganic, Coordination and Organometallic Compounds*; John Wiley & Sons, Ltd, 2005.

(10) Paul, W.; Nobel Lecture ed.; Nobelprize.org: URL: http://nobelprize.org/nobel_prizes/physics/laureates/1989/paul-lecture.html, Retrieved: 1 Jun 2011.

(11) Stafford Jr, G. C.; Kelley, P. E.; Syka, J. E. P.; Reynolds, W. E.; Todd, J. F. J. *International Journal of Mass Spectrometry and Ion Processes* **1984**, *60*, 85-98.

(12) Todd, J. F. J. *Mass Spectrometry Reviews* **1991**, *10*, 3-52.

(13) March, R. E. *Rapid Communications in Mass Spectrometry* **1998**, *12*, 1543-1554.

(14) Shukla, A. K.; Futrell, J. H. *Journal of Mass Spectrometry* **2000**, *35*, 1069-1090.

(15) de Hoffmann, E.; Stroobant, V. *Mass Spectrometry: Principles and Applications*; 2nd ed.; John Wiley & Sons, Ltd, 2002.

(16) Memboeuf, A.; Nasioudis, A.; Indelicato, S.; Pollreisz, F.; Kuki, A.; Keki, S.; van den Brink, O. F.; Vekey, K.; Drahos, L. *Analytical Chemistry* **2010**, *82*, 2294-2302.

Chapter 3: Methodology – Computational Chemistry

3.1 A Background to Ab Initio Calculations

Computing technology has rapidly developed in recent decades with the available computational power ever growing. This technology has seen its application grow to include almost every area of society and this is as true in scientific research as anywhere else. The field of computational chemistry has its earliest origins in the 1950s and can now be found in use across chemistry. Despite the rapid growth in available computing power, it remains finite and as such, calculations of chemical systems remain restricted. However, the *in silico* investigation of chemical systems can provide a vast amount of information. *Ab initio* methods, density functional theory (DFT) calculations and simulation methods such as molecular dynamics (MD) simulations are the main types of calculations which currently feature prominently in the literature. *Ab initio* and DFT methods in particular can reveal information about the properties and structure of isolated molecules and small aggregates. This information can allow chemists to gain a greater degree of understanding into the properties of physical systems and better understand experimental results. In addition it can be used to investigate situations which are experimentally inaccessible or difficult to create and also screen a range of potential experimental directions in order to help determine the course of action with the highest probability of success. A large amount of information has been previously published about these computational methods and will be used to construct a brief introduction to their background.[1-6]

While these techniques can be very powerful, misuse of them can provide misleading results. Great care should be taken when employing such techniques, but as their range of uses in chemistry increases further, the end users are often not experts in computational chemistry. In order to prevent the production of deceptive results it is important that these techniques should not be used as a black box and an understanding of some of the reasoning behind them be understood. *Ab initio* techniques were used to study IL aggregates for this thesis as they have been shown

to be applicable to a wide range of chemical systems with a high degree of accuracy and reliability. As a result of this, the following sections will focus on giving an overview and some theoretical details of the types of calculation which were used and similar ones for context and understanding. This type of calculation is used to calculate the electronic properties and structure of a chosen molecule or molecules from first principles, however, other computational techniques adopt a more classical approach. Every calculation which a chemist makes involves a trade-off between the computational cost of the calculation and the accuracy which is achieved because, as in many areas of science and the wider world, you generally get what you pay for.

The difference between the exact non-relativistic energy of the studied system and the relatively basic Hartree-Fock limit calculated energy is known as the correlation energy. The correlation energy arises from the interaction between electrons in the studied system or more precisely their limited representation in Hartree-Fock calculations and, as the Hartree-Fock energy is an upper bound to the exact energy, the correlation energy will always be negative. This arises as a result of the variation principle which uses the variational integral shown as the integral in Equation 3-1.

$$\int \phi^* \hat{H} \phi d\tau \geq E_1 \qquad \textbf{Equation 3-1}$$

Where $\hat{H}$ is the time independent Hamiltonian operator, E is the lowest energy eigenvalue and ϕ is a normalised function known as the trial variation function. In order to produce a good approximation to E_1, different trial variation functions are used to find the one which minimises the variational integral. Equation 3-1 shows that the minimum value of the variational integral gives the best approximation of E_1. These calculations use a set of functions to find a mathematical representation of the molecular orbitals. The set of functions used to do this are known as a basis set and are expanded as a linear combination of functions. Thus the molecular orbitals are represented by a basis set with the coefficients or weights to be established. Computational chemists have produced many different methods of performing *ab initio* calculations and the level of theory which is achieved is generally determined by two factors. These are the degree to which the calculation will approximate or include the correlation energy and the basis set completeness which is used. The

former factor places a fundamental limit on these calculations which can not be overcome by increasing the latter. These considerations are discussed in the following sections.

3.1.1 Foundations of *ab initio* calculations

Solving the time-independent Schrödinger equation to determine the structure and properties of one or several molecules is the aim of all quantum chemical calculations. The problem is that the Schrödinger equation can only be solved precisely for a single electron system because of the quantum nature of electrons and the many body problem. This clearly places an undesirable limit for the study of real world or model systems. In order to use these techniques for larger systems which are more widely applicable it was necessary to impose a number of approximations on the calculations. The great inequality between the masses of nuclei and electrons leads to the first approximation that will be applied. This approximation allows for all modern quantum chemical calculations and is known as the Born-Oppenheimer approximation. The wavefunction is divided into electronic and nuclear components; this is possible as the electrons can be considered to react instantaneously to changes in the nuclei positions due to their lower mass meaning that the electron distribution becomes dependant only on the nuclei position and not their movement. As a result of this, the Schrödinger equation may be solved for a particular nuclear configuration, however by performing a series of iterative calculations it is possible to chart the energy of the molecule for a series of configuration changes.

Application of the Born-Oppenheimer approximation results in the form of the Schrödinger equation seen in Equation 3-2. In this equation the electronic wavefunction [$\Psi(r : R)$] and electronic energy [$E(R)$] can be seen along with parameters relating to the nuclear (R) and electronic (r) positions.

$$\hat{H}\Psi(r:R) = E(R)\Psi(r:R) \qquad \textbf{Equation 3-2}$$

Following on from this, the molecular Hamiltonian can be expressed as shown in Equation 3-3. The first term describes the kinetic energy of the electrons and the

second term describes the nuclei-electron Coulombic attraction. The electron-electron repulsion is described by the third term and the final term is a classical component based on nuclear-nuclear repulsion.

$$\hat{H} = \hat{T}_e + \hat{V}_{en} + \hat{V}_{ee} + \hat{V}_{nn} \qquad \textbf{Equation 3-3}$$

The electron coupling described by the third term of Equation 3-3 is the one which provides the greatest number of problems. This means that a many body wavefunction can not be expressed as a combination of one-electron functions leading to the necessity of further approximations in the calculation.

Electron coupling comes from two main effects which are known as exchange and correlation. In 1925 the work of Wolfgang Pauli proposed the Pauli Exclusion Principle. From this it is not possible for two identical fermions to simultaneously occupy the same quantum state. As electrons are fermions, the exchange effect arises and on the interchange of two electrons, the electronic wavefunctions must be anti-symmetric. As a consequence of the Pauli Exclusion Principle and the anti-symmetric wavefunctions to reduce exchange energy, electrons which posses the same principle, azimuthal and magnetic quantum numbers must have different spin projection quantum numbers and where electrons have the same spin projection quantum number they must stay away from each other and occupy different orbitals. The electronic correlation arises from two sources. The first of these is the electrostatic effect that all of the other electrons in a system have on the electron of interest. The electrons in a system are kept apart as the Coulombic repulsion between electrons means that the motion of one affects the motion of all of the remaining electrons. Also the previously mentioned electrons with the same spin need to be separated due to the Pauli Exclusion Principle. When the electrons stay out of each others way an exchange or Fermi hole is formed. By guaranteeing the presence of properly anti-symmetrical wavefunctions the aforementioned exchange effects can be taken into account. The presence of these correlation effects can be troublesome to include in calculations however different methods to approximate these have been developed in order to allow them to be taken into account. The following sections describe relevant methods to do this.

3.1.2 Hartree-Fock

Douglas Hartree introduced a method to calculate approximations of wavefunctions and also estimate the energies of different atoms and ions. This procedure was later refined by Vladimir Fock to produce the Hartree-Fock (HF) method. The electronic correlation effects for electrons of opposite spin are completely neglected in this procedure. The original Hartree method applies mean field theory to take account of the exchange energy; this means that an electron of interest now interacts with a single field created from averaging all of the other electrons and nuclei present in the calculation. Doing this has the result of the removal of coupling due to correlation however the generated wavefunctions are not anti-symmetric and the method violates the Pauli Exclusion Principle. Fock imposed corrections upon Hartrees theory which prevented it from violating this theory and takes account of the exchange term explicitly. This term takes electron exchange into account between electrons with the same spin however it remains otherwise ignored.

Using this method it is possible to divide the wavefunction into spin orbitals, which are a series of one-electron wavefunctions. The spatial component of these is called the atomic orbital, however spin orbitals also contain a second part which is a spin component that indicates if the electrons posses alpha- or beta-spin. A common feature of many *ab initio* techniques which is shared by the HF method is the necessity to know all of the wavefunctions in order to solve the calculation, in this case to find solutions to the Hartree-Fock equation. This problem may be solved using the Self-Consistent Field (SCF) method. This is an iterative technique which is allowed to progress until the result is within a defined tolerance. The HF ground-state wavefunction is then constructed from the optimised set of spin orbitals. These spin orbitals are the ones which were found to conform to the defined tolerance of the SCF method. As stated previously the HF method is able to calculate energy and the calculated orbitals are arranged according to this energy. The electrons then occupy the lowest energy orbitals and it is these occupied orbitals which form the ground-state wavefunction.

For such an extreme simplification of the correlation effects, the HF method has been shown to be remarkably successful. It is aided by its comparatively low computational cost when compared with other *ab initio* techniques. HF methods scale as N^4 where N is the number of basis functions, but with techniques such as pre-screening this can be reduced to N^3 or N^2.

3.1.3 Post-Hartree-Fock

In order to break through the Hartree-Fock limit, several different variations have been made to the HF method in order to better model the electron correlation. The main methods are known as Configuration Interaction (CI), Møller-Plesset (MP) perturbation theory, Coupled Cluster, Quadratic Configuration Interaction and quantum chemistry composite methods.[7] These methods fall into the category known as post-Hartree-Fock methods, a group of procedures which add electron correlation effects to HF. Two of the most common methods, CI and MP, will be described in more detail to illustrate the different approaches which can be adopted.

The fundamental theory behind CI is implied by its name; firstly *configuration* describes a process where the wavefunction is formed from a linear combination of Slater determinants. Slater determinants represent the wavefunction of multi-fermionic systems while also satisfying the requirements for anti-symmetry. On the exchange of fermions the Slater determinant will change the sign satisfying the Pauli Exclusion Principle. CI allows for the presence of different electronic configurations which can be used to produce multiple many-electron wavefunctions. The second part of the name, *interaction*, arises as these wavefunctions are then permitted to mix with each other in order to achieve a better result. CI has proved to be a computationally expensive technique (CI scales around N^6) for performing calculations and as a result its use has been limited to systems with small numbers of atoms.

MP theory however represents the electron correlation by applying a perturbation to the HF method using Rayleigh–Schrödinger perturbation theory. Due to the nature of the perturbation theory, unlike with CI the previously mentioned variational principle

does not apply here and therefore the calculated energy may be lower than the real energy. The Hamiltonian is divided into an unperturbed Hamiltonian operator and a relatively small perturbation. This method is represented as MP*n* where *n* is the order to which this correction is truncated. It can be changed in integer values commonly between 2 and 5 thus if the technique is truncated at the third-order the label MP3 is used. While these calculations are found to be more computationally expensive than HF, they are cheaper than CI (MP2 scales around N^5).

3.1.4 Density Functional Theory

Physicists developed a novel method of calculation called DFT to study systems in the solid state. These calculations use a different approach and are described in the following section. During the mid-1960s, Hohenberg, Kohn and Sham developed the DFT method. The original work of Hohenberg and Kohn[8] observed that for a many particle system the ground state wavefunction and the corresponding electron density can be mapped 1:1. It was therefore possible for them to create a method where a system of electrons in space can have its total electronic energy expressed in terms of the electron probability density (ρ) at the same configuration. This allows the total energy of the system (E[ρ]) to be expressed as a functional of the electron probability density rather than the more abstract concept of the wavefunction. Thus the main difference between DFT and the HF based methods is that DFT calculates the ground state energy and other electronic properties based on the electron density. In principle it is possible to perform orbital-free DFT calculations however the modern success of DFT is based on the use of an auxiliary set of orbitals suggested by Kohn and Sham.

Kohn and Sham[9] produced a method for finding the ground state electron density by assuming that a system of electrons was non-interactive in a static potential field. This took the form of a series of one electron equations which allow for the determination of the electron density. The ground state electronic energy of the system can be expressed in terms of the electron probability density shown in Equation 3-4.

$$E[\rho(r)] = T_{nl}[\rho(r)] + V_{ne}[\rho(r)] + V_{ee}[\rho(r)] + \Delta T[\rho(r)] + \Delta V_{ee}[\rho(r)] \quad \textbf{Equation 3-4}$$

In Equation 3-4 the first term describes the kinetic energy associated with the non-interacting electrons and the second term describes the nuclear-electron interactions. Meanwhile the remaining terms are respectively the electron-electron repulsive Coulomb interaction, kinetic energy corrections due to electron interactions and non-classical corrections arising from electron-electron repulsion. The final two terms are commonly combined and described as the exchange-correlation energy (E_{xc}).

Equation 3-5 gives the expression for the exact ground state electron density at a position labelled r where the Kohn-Sham orbitals are represented as Ψ_i for the system of interest. To form molecular orbitals a linear combination of atomic-like orbitals (LCAO) is often used. As was mentioned above, pure DFT does not require the use of any orbitals however as can be seen the Kohn-Sham approach does require their use. In order for this method to be successfully used the summation needs to be made over all of the occupied orbitals.

$$\rho(r) = \sum_{i=1}^{n} |\Psi_i(r)|^2 \qquad \textbf{Equation 3-5}$$

These equations are solved in a similar manner to that which was employed for the Hartree-Fock method. This means that the SCF method is again employed. In this case the starting point for the calculations comes from an initial guess of the electron probability density. For molecular systems this will often be based on a superposition of the atomic densities. A rough form of the dependence of exchange-correlation energy on the electron density is set and this allows for the calculation of a new set of Kohn-Sham orbitals by solving the Kohn-Sham equations. In turn this allows for the calculation of a new electron probability density allowing for the whole process to be repeated. This cycle is allowed to continue until the electron probability density and the exchange-correlation energy both come within a defined tolerance. Once this happens the electronic energy of the system can be calculated by Equation 3-4.

For DFT calculations (which scale as N^4 however this can be reduced to N^2 or N^3 using special techniques) the most challenging area of the calculation is modelling the exchange-correlation energy. As a result of this the choice of the functional used

to describe this term is the largest source of error for the calculations. There have been a large number of attempts at creating suitable functionals to overcome this problem and the most basic of these is known as the Local Density Approximation (LDA). The LDA is a method which has proved suitable for dealing with periodic systems such as solids however is not very suitable for use with molecular systems. This approximation is based on the widely investigated homogeneous electron gas model for which the exchange-correlation energy is known. This model is also known as Jellium and relies on a uniform distribution of charge. From this it is clear why this method is largely unsuitable for the study of molecules where the distribution of charges is generally more varied. In order to account for this non-uniformity, corrections have been made to the functional in order to take the gradient of the density into account. These corrections are known as Generalised Gradient Approximations (GGAs) and can result in DFT achieving results close to MP2 based calculations. A further advance on these functionals is known as meta-GGA. Meta-GGA functionals include an additional term which depends on density along with the gradient and Laplacian of the density. Methods which include part of the exchange energy calculated from Hartree-Fock theory along with exchange and correlation from DFT are known as hybrid functionals. The most well known is B3LYP which is a hybrid of the Becke three-parameter (exchange) and Lee-Yang-Parr (correlation) functions.[10-13] This has proved to be very useful for a wide variety of molecular systems and is extensively used in this thesis. B3LYP is far from the only hybrid functional and indeed several different ones have been created and many can provide improved results over B3LYP for different systems, however this sometimes comes at a large computational cost. One such functional is known as M05 which is classified as a hybrid meta-GGA functional combining both the characteristics of a hybrid and a meta-GGA functional and has been modified to work more accurately at longer range.[14]

3.1.5 Basis Sets

An orbital is the wavefunction for a single particle (an electron). As we are interested in the electronic structure of molecules, molecular orbitals will be used for the

wavefunctions of electrons in a molecule. The molecular orbitals (Ψ_i) describe the positions of the nuclei and electrons in a molecule. However, as was seen previously from the Born-Oppenheimer approximation the nuclei can be considered to be stationary and the electron motion is considered separately. This means that the type of function and also the number of functions used to describe the electrons in the system of interest will have a large influence on the accuracy of the calculation. While the precise form of the orbitals is unknown it is possible to describe them as a linear combination of one-electron functions which are known. Equation 3-6 describes how each orbital can be expanded as such a linear combination.

$$\Psi_i = \sum_{\mu=1}^{N} c_{\mu i}\phi_\mu \qquad \textbf{Equation 3-6}$$

In this equation ϕ_μ are the basis functions and $c_{\mu i}$ are the expansion coefficients. These basic functions come together to compose the basis set for a calculation. At this point it is theoretically possible to model any orbital through the use of an infinite or complete basis set. As with all areas of computational chemistry the technical limitations need to be carefully considered once more. As an infinite number of basis functions are required by such a basis set however this is computationally not possible and a limit must be set to the number of functions which are used in practice. While using a greater number of basis functions can better model the orbital, using a lower number is computationally attractive and this means that a balance has to be struck between the two considerations. A sufficiently large number of basis functions must be used to accurately describe the wavefunction however this must be small enough in order for it not to be computationally too expensive. As there are different types of basis function, choosing ones which are more similar to the system of interest can greatly aid in reducing the cost. Slater type orbitals (STO) and Gaussian type orbitals (GTO) are the major functions currently used in molecular quantum chemistry.

STOs were introduced in 1930[15] and their use in computational chemistry largely predates the use of GTOs. In these orbitals the nuclear charge is scaled in order to

account for electron-electron repulsion and they can be described as shown in Equation 3-7.

$$\phi_{STO} = Nr^{n-1}\exp(-\zeta r)Y_l^m(\theta,\psi) \qquad \textbf{Equation 3-7}$$

Where N is the normalization constant, r is the electron-nucleus distance, *n* is the principle quantum number of the orbital and ζ is the orbital exponent which is related to the effective nuclear charge. Meanwhile Y_l^m is the spherical harmonic with order *m* and degree *l*. These orbitals give rise to a large number of multi-site integrals which are difficult to solve efficiently which limits their use with larger systems.

GTOs were introduced in 1950[16] as an alternative to STOs and their use was shown to be advantageous. These functions include a radial decay based on $\exp(-\alpha r^2)$ compared with $\exp(-\zeta r)$ as seen before. These orbitals have become the most widely used to study isolated molecules however a single one is not sufficient to model an atomic orbital and several are still required for accurate calculation. The main advantage to the use of GTOs is when multi-centre integrals are considered, they can be reduced to two-centre integrals which have considerably lower computational cost. The use of GTOs requires the presence of large basis sets in order to accurately model atomic orbitals near the nucleus. This is because unlike STOs and the hydrogen-like 1s orbital, GTOs are not discontinuous at the nucleus. The solution to this is the use of a contracted Gaussian type function (CGTF) which is a linear combination of Gaussian functions to better represent this case.

There are now literally hundreds of different possible basis sets available for computational calculations. The simplest such examples are known as minimal basis sets and use the lowest possible number of basis functions to estimate the behaviour of all the electrons. This means that each occupied atomic orbital with different principal and angular momentum quantum numbers is represented by a single basis function. An example of such a basis set is STO-3G where three GTOs are used to fit a STO. Due to their simplicity, these basis sets are computationally cheap however they are not normally sufficiently large to provide reliable results with their use generally restricted to larger systems.

Double, triple and quadruple- ζ basis sets are common improvements to the minimal example above. In these examples the number of basis functions is increased to various degrees relative to the minimal basis set. In the double-ζ example it is doubled, for triple-ζ it is tripled and so on. Performing this change results in a significant improvement of the calculation accuracy however as might be expected it does result in a corresponding increase in cost. At this point it is worth noting the difference in terms of chemistry between the core and valence electrons. The core electrons are much less important to chemical bonding than the valence electrons are and as a result the computational cost can be reduced by limiting the number of functions used for the core electrons. Such basis sets are known as split-valence basis sets and use more functions to model the valence electrons. The 6-311G basis set is an example of a spilt-valence basis set. In this case the core electrons are described by the summation of six Gaussian functions and the valence electrons are described by a triple-ζ basis set. A triple-ζ basis set uses three different sizes of contracted function for each type of orbital allowing the orbitals to change size, in this case the most highly contracted is comprised of 3 GTOs and the remaining two are each comprised of a single GTO.

Two further noteworthy refinements can be made to many of the common basis sets and they are known as adding polarisation and diffuse functions. Polarized basis sets include unoccupied orbitals which have a higher angular momentum. This change allows the orbitals to change shape as well as alter their size. This is represented in one of two ways, either 6-311G(d) or 6-311G* and in this case d functions have been added to the non-hydrogen atoms. In order to also add these functions to the hydrogen atoms either 6-311G(d,p) or 6-311G** would be used and it is worth noting that it is available up to 6-311G(3df,3pd). As for diffuse functions, this adds larger sized s- and p-type functions to the basis set. This has the effect of allowing orbitals to occupy larger regions than would otherwise be possible and is especially useful for systems where the electrons are a large distance from the nucleus. Adding these functions to the 6-311G(d) basis set would be represented as 6-311+G(d) where they are added to the non-hydrogen atoms only or 6-311++G(d) where they are also added to the hydrogen atoms.[3]

3.1.6 Effective Core Potentials

The inclusion of large atoms can provide problems when performing *ab initio* calculations. These atoms come with a large number of electrons which in turn means that a large number of basis functions are required to model the atom. As most of the electrons are in the core it would be possible to use minimal basis sets to investigate such systems however the cost can grow rapidly especially if there are multiple heavy atoms present. Relativistic effects are also present in many heavy atoms as the velocity of the inner core electrons accelerates towards the speed of light. In very heavy atoms these relativistic effects can not be ignored as they can have a significant effect on the chemical properties which are of interest. This means that it will not be possible to use the non-relativistic Hamiltonian operator to accurately study these systems.

The solution to these problems was found by Hellmann in 1935 who proposed replacing the core electrons with a set of functions which would interact with outer electrons to mimic the presence of a complete core. This core would produce an accurate estimate of the interactions between the nuclear-electronic core and the remaining electrons in a significantly more efficient manner than an all electron calculation. These functions are known as effective core potentials (ECP) and when used with *ab initio* calculations need to account for a number of effects.[2] In addition to representing the Coulomb repulsion effects the ECP must also ensure the Pauli Exclusion Principle holds. An ECP will replace all the electrons that fill a complete shell however there is a choice about precisely how many electrons are replaced. A large core ECP will replace everything but the valence electrons whereas a small core ECP will also leave the next lowest complete shell. Due to the interactions present between the valence electrons and the next lowest shell it is preferential to use the small core where possible. There have been many different ECPs, also known as pseudopotentials, developed for use in *ab initio* calculations. Common examples include the Stuttgart/Dresden potentials developed by Dolg *et al.*, the Los Alamos National Laboratory (LanL) potentials from Hay and Wadt and those developed by Stevens *et al.* such as the CEP-31G* potential.[2]

3.2 Calculation Details

The calculations which are reported in the following chapters were performed on a SUSe 9.x Linux HPC cluster consisting of 68 AMD Opteron processing cores. The cluster is known as Hare and is a resource of the Research Computing Facility at EaStChem. The Gaussian 03 suite of programs[4] was used for all of the following calculations. The default convergence criteria were used unless otherwise stated at which point tighter parameters (maximum force = 1.4 x 10^{-5}, RMS force = 1.0 x 10^{-5}, maximum displacement = 6.0 x 10^{-5} and RMS displacement = 4.0 x 10^{-5}) were used. The initial starting geometries were based on the structure from X-ray diffraction[17] and the previous ion pair calculations from Hunt *et al.*[18-20] From the ion pair, further ions were progressively added to increase the size of the aggregate which was being investigated. The most stable structures were used to build initial structures for the larger aggregates thus incorporating the acquired knowledge. The vast majority of the calculations were performed using the B3LYP hybrid DFT method which was previously detailed in this chapter. This method was employed due to its applicability to a wide variety of systems and its previous successful application to similar calculations. Several of the small calculations, in particular the different conformations of $C4mim_3Cl_2^+$ and $C4mim_2Cl_2K^+$, were investigated using the M05 method which is an example of a hybrid meta-GGA method. This method was mentioned previously in this chapter and it is meant to be a better model of weak interactions however it is considerably computationally more expensive.[14,21] These calculations were used as a test to show the reproducibility of conformation and energy trends between the different methods.

The initial calculations used the same basis set as used by Hunt *et al.* during their investigation of the gas-phase C4mimCl ion pair.[19] These calculations used the split-valence 6-311+G(d,p) basis set which was used for the majority of the small aggregates along with an ultrafine integration grid however it proved computationally too expensive to continue using it for larger aggregates. In order to expand the aggregates which could be studied the basis set was reduced to CEP-31G*.[22-24] As the diffuse functions were removed the fine optimisation was likewise removed from the basis set. The CEP-31G* basis set is an example of a highly

compact pseudopotential and test calculations were performed to ensure that it gave consistent results with those obtained with the 6-311+G(d,p) basis set.

The results proved consistent however it was not possible to use this basis set for all of the desired aggregates as it only exists for elements up to argon. The alternative which was selected was the LanL2DZ basis set[25-27] for the heavy atoms (Na, Mg, Cl, K, Zn and Cs) using an ECP and the D95V(d,p) basis set on the light atoms (H, Li, C, N and O). These basis sets have been shown to be suitable for use with a large number of gas-phase aggregates including potassium and caesium which lead to their selection for this use.[28-32] In order to ensure consistency with previous basis sets and to directly compare results between different metal containing aggregates, many of the previously studied aggregates were also calculated using this basis set. Examples of where this was done include the $C4mim_2Cl_2Li^+$ and $C4mim_2Cl_2Na^+$ aggregates which allowed comparison between the range of alkali metals. When changing the basis sets there are some characteristics which are of particular interest to ensure their suitability, these are the weakly bound Cl to H distances and the energy differences between the conformations. For calculations where convergence proved difficult the quadratic convergence SCF procedure was used. This is called with the SCF=QC keyword and was particularly useful for dealing with the aggregates containing zinc. This method is more reliable than the default however is significantly more costly.

3.3 References

(1) Atkins, P. W.; Friedman, R. S. *Molecular Quantum Mechanics*; Oxford University Press: New York, 1997.

(2) Cramer, C. J. *Essentials of Computational Chemistry: Theories and Models*; Second ed.; John Wiley & Sons Ltd.: Chichester, 2004.

(3) Foresman, J. B.; Frisch, A. *Exploring Chemistry with Electronic Structure Methods*; Second ed.; Gaussian, Inc.: Pittsburgh, PA, 1996.

(4) Frisch, M. J. T., G. W.; Schlegel, H. B.; Scuseria, G. E.; Robb, M. A.; Cheeseman, J. R.; Montgomery, Jr., J. A.; Vreven, T.; Kudin, K. N.; Burant, J. C.; Millam, J. M.; Iyengar, S. S.; Tomasi, J.; Barone, V.; Mennucci, B.; Cossi, M.; Scalmani, G.; Rega, N.; Petersson, G. A.; Nakatsuji, H.; Hada, M.; Ehara, M.; Toyota, K.; Fukuda, R.; Hasegawa, J.; Ishida, M.; Nakajima, T.; Honda, Y.; Kitao, O.; Nakai, H.; Klene, M.; Li, X.; Knox, J. E.; Hratchian, H. P.; Cross, J. B.; Bakken,

V.; Adamo, C.; Jaramillo, J.; Gomperts, R.; Stratmann, R. E.; Yazyev, O.; Austin, A. J.; Cammi, R.; Pomelli, C.; Ochterski, J. W.; Ayala, P. Y.; Morokuma, K.; Voth, G. A.; Salvador, P.; Dannenberg, J. J.; Zakrzewski, V. G.; Dapprich, S.; Daniels, A. D.; Strain, M. C.; Farkas, O.; Malick, D. K.; Rabuck, A. D.; Raghavachari, K.; Foresman, J. B.; Ortiz, J. V.; Cui, Q.; Baboul, A. G.; Clifford, S.; Cioslowski, J.; Stefanov, B. B.; Liu, G.; Liashenko, A.; Piskorz, P.; Komaromi, I.; Martin, R. L.; Fox, D. J.; Keith, T.; Al-Laham, M. A.; Peng, C. Y.; Nanayakkara, A.; Challacombe, M.; Gill, P. M. W.; Johnson, B.; Chen, W.; Wong, M. W.; Gonzalez, C.; and Pople, J. A. In *Gaussian 03, Revision E.01*; Gaussian, Inc., Wallingford CT: 2004.

(5) Jensen, F. *Introduction to Computational Chemistry*; Second ed.; John Wiley & Sons Ltd: Chichester, 2007.

(6) Parr, R. G.; Yang, W. *Density-functional theory of atoms and molecules*; First ed.; Oxford University Press: New York, 1989.

(7) Moller, C.; Plesset, M. S. *Physical Review* **1934**, *46*, 0618-0622.

(8) Hohenberg, P.; Kohn, W. *Physical Review B* **1964**, *136*, B864-&.

(9) Kohn, W.; Sham, L. J. *Physical Review* **1965**, *140*, 1133-&.

(10) Becke, A. D. *Journal of Chemical Physics* **1993**, *98*, 5648-5652.

(11) Lee, C. T.; Yang, W. T.; Parr, R. G. *Physical Review B* **1988**, *37*, 785-789.

(12) Vosko, S. H.; Wilk, L.; Nusair, M. *Canadian Journal of Physics* **1980**, *58*, 1200-1211.

(13) Stephens, P. J.; Devlin, F. J.; Chabalowski, C. F.; Frisch, M. J. *Journal of Physical Chemistry* **1994**, *98*, 11623-11627.

(14) Zhao, Y.; Schultz, N. E.; Truhlar, D. G. *Journal of Chemical Physics* **2005**, *123*.

(15) Slater, J. C. *Physical Review* **1930**, *36*, 0057-0064.

(16) Boys, S. F. *Proceedings of the Royal Society of London Series a-Mathematical and Physical Sciences* **1950**, *200*, 542-554.

(17) Saha, S.; Hayashi, S.; Kobayashi, A.; Hamaguchi, H. *Chemistry Letters* **2003**, *32*, 740-741.

(18) Hunt, P. A.; Gould, I. R. *Journal of Physical Chemistry A* **2006**, *110*, 2269-2282.

(19) Hunt, P. A.; Kirchner, B.; Welton, T. *Chemistry-a European Journal* **2006**, *12*, 6762-6775.

(20) Kossmann, S.; Thar, J.; Kirchner, B.; Hunt, P. A.; Welton, T. *Journal of Chemical Physics* **2006**, *124*.

(21) Zhao, Y.; Schultz, N. E.; Truhlar, D. G. *Journal of Chemical Theory and Computation* **2006**, *2*, 364-382.

(22) Stevens, W. J.; Basch, H.; Krauss, M. *Journal of Chemical Physics* **1984**, *81*, 6026-6033.

(23) Stevens, W. J.; Krauss, M.; Basch, H.; Jasien, P. G. *Canadian Journal of Chemistry-Revue Canadienne De Chimie* **1992**, *70*, 612-630.

(24) Cundari, T. R.; Stevens, W. J. *Journal of Chemical Physics* **1993**, *98*, 5555-5565.

(25) Hay, P. J.; Wadt, W. R. *Journal of Chemical Physics* **1985**, *82*, 270-283.

(26) Hay, P. J.; Wadt, W. R. *Journal of Chemical Physics* **1985**, *82*, 299-310.

(27) Wadt, W. R.; Hay, P. J. *Journal of Chemical Physics* **1985**, *82*, 284-298.

(28) Gupta, A. K.; Krishnamurthy, M. *Physical Review A* **2003**, *67*, 023201.

(29) Toman, P.; Makrlík, E.; Vaňura, P. *Monatshefte für Chemie / Chemical Monthly* **2011**, *142*, 569-571.

(30) Burke, R. M.; Boxford, W. E.; Dessent, C. E. H. *Journal of Chemical Physics* **2007**, *126*, 9.

(31) Fu, Y.; Shen, K.; Liu, L.; Guo, Q.-X. *Journal of the American Chemical Society* **2007**, *129*, 13510-13519.

(32) Miller, D. J.; Lisy, J. M. *Journal of Chemical Physics* **2006**, *124*, 7.

Chapter 4: Pure Ionic Liquid Aggregate Results

This section of the thesis will focus on MS and computational data obtained for aggregates of ILs. MS produces data for charged species; in the case of pure IL aggregates these have an imbalance in the number of cations to anions. The most commonly formed aggregates have the general formula $C_{n+1}A_n^+$ or $C_nA_{n+1}^-$ where C and A are the singly positively charged cation and anion respectively.

4.1 Mass Spectrometry

The primary IL used was C4mimCl, the synthesis of which was previously described in Section 2.1. The structure of the 1-butyl-3-methylimidazolium ($C4mim^+$) cation is shown in Figure 4-1(a) for reference accompanied by an electrostatic potential mapped onto an electron density isosurface in Figure 4-1(b).

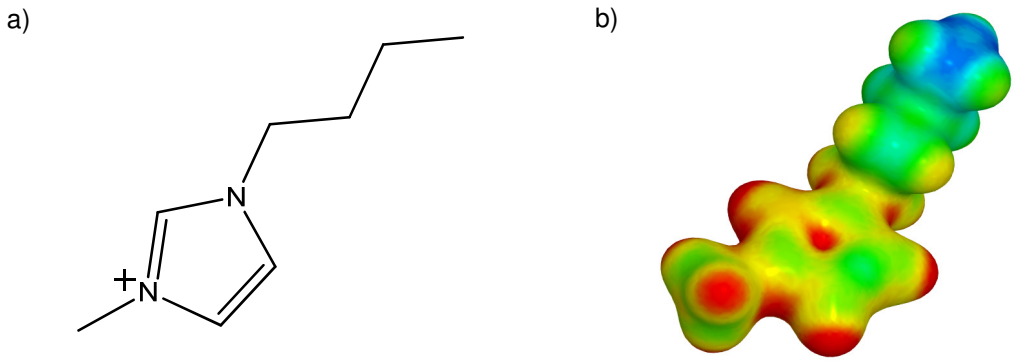

Figure 4-1 a) Structural formula and b) electrostatic potential mapped onto an electron density isosurface for the $C4mim^+$ cation.

The use of MS to study ILs has been limited in the past and as a result it was important to find a consistent way of performing the experiments. The instrument which was employed was very robust and allowed for a wide range of different samples to be used along with great flexibility in the ionisation source which could be utilised. This gave the potential to compare the effectiveness of these sources independent of other instrument parameters. Additionally, as with any MS experiment, the solvent choice and instrument parameters were critical to the

formation of spectra. The instrument parameters used are given in Section 2.2.7 and any deviations from this are listed with the appropriate data.

The spectra which were observed showed similar characteristics to other mass spectra from ILs and also from higher melting point salts.[1,2] It was commonly observed that the series of ions ($C_{n+1}A_n^+$ or $C_nA_{n+1}^-$ depending on the polarity of the mass spectrometer) were complete and could often be produced over the entire mass range (*m/z* range 100-2000).

Mass spectra of many different species have found that clusters with particular numbers of atoms are observed more frequently than others. These numbers are special and are commonly referred to as magic numbers.[3,4] It has been shown that these clusters often exhibit high symmetry and also high packing efficiency, in many cases corresponding to triangular, tetrahedral, octahedral and cubic arrangements. Nucleation and growth processes are governed by factors relating to packing and bonding which have been shown to be closely related to the formation of magic number clusters.[3]

In this thesis there are numerous cases where the formation of a particular species seemed to be consistently diminished or enhanced relative to the adjacent ions in the general series leading to the observation of magic number species. The observed species were further investigated with CID and computational chemistry. In doing so, the stabilities of the different species were investigated. This allowed for the investigation of the properties of the observed magic number aggregates. These species have been suggested as a link or a step in the nucleation process for the formation of bulk liquids.[5] A greater understanding of these species could allow for a more detailed analysis of the formation processes in many ILs.

The CID investigations performed on the aggregates show the consistent loss of one or more ion pairs. This is in line with previous gas phase studies of ILs that have shown the preference for forming neutral ion pairs.[5] This would be expected due to the strong electrostatic attraction between the ions. The presence of such losses is analogous to ion pair evaporation from clusters using other techniques such as

infrared spectroscopy, ultra high vacuum evaporation combined with line of sight MS or differential mobility analysers allowing a comparison and broader understanding of the characteristics of ILs at a molecular level.[2,5,6]

4.1.1 Electrospray Ionisation

4.1.1.1 LCQ

The standard ionisation technique used was ESI. Figure 4-2 shows the mass spectrum from C4mimCl sprayed using the Thermo Finnigan LCQ Classic mass spectrometer (LCQ) at a concentration of 1.36 mM in 100% MeOH. The tube lens voltage was set to 10 V. The concentrations required to obtain mass spectra of salts are typically on the order of mM which is significantly greater than what is required for most biological MS.[2,7] To observe salts, an imbalance is required in the number of cations and anions, thus to produce MS, an ion pair must be separated. Meanwhile most biological and organic MS requires the addition or loss of one or more protons; this is commonly a less energetic process. Varying the concentration below 1.2 mM has a large effect on the spectra which are produced with an especially large number of contaminant adduct peaks distorting the spectra. However varying the concentration between 1.2 and 5 mM has little effect on the overall shape of the spectra which are produced and largely influences the signal-to-noise ratio observed. C4mimCl is soluble in pure methanol however the alkali metal chlorides used in Chapter 5 are less soluble in methanol and it was useful to have a small percentage of water in order to aid this. 10 % water was used in many of the experiments to reduce the variations between these experiments and allow for closer comparison between them.

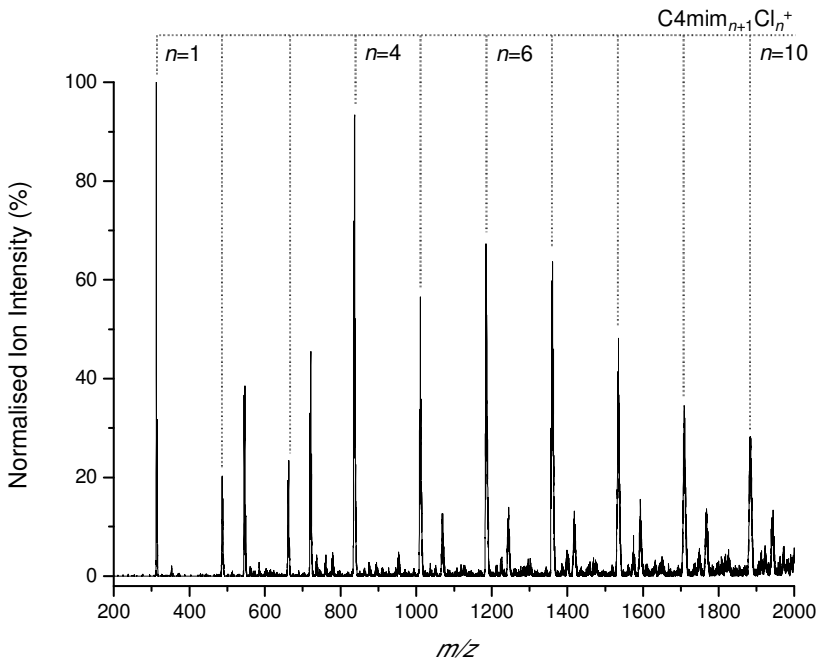

Figure 4-2 Mass spectrum of 1.36 mM C4mimCl sprayed in 100% MeOH on the LCQ using ESI with the C4mim$_{n+1}$Cl$_n^+$ series highlighted for n = 1 to 10 and the tube lens was set to 10 V.

The series of singly changed cationic aggregates with general formula C4mim$_{n+1}$Cl$_n^+$ can clearly be observed for n = 1 to 10 in Figure 4-2. For reference, the structure of the C4mim$^+$ cation can be found in Figure 4-1(a). In order to verify the identification of the species a theoretical prediction of the *m/z* for each species is compared with the observed positions for the maximum intensity in Table 4-1. The standard deviations given for the observed *m/z* values in Table 4-1 are the calculated uncertainties within the three repeated measurements.

Table 4-1 Predicted and observed position of the maximum intensities for $C4mim_{n+1}Cl_n^+$ where *n* = 1 – 10. The observed values are an average of three spectra taken on the LCQ.

Value of *n* in $C4mim_{n+1}Cl_n^+$	Averaged observed *m/z* for maximum intensity	Predicted *m/z* for maximum intensity
1	312.91 ± 0.03	313.22
2	486.67 ± 0.07	487.31
3	662.84 ± 0.16	663.40
4	836.67 ± 0.17	837.49
5	1010.64 ± 0.28	1011.58
6	1184.58 ± 0.39	1185.67
7	1359.32 ± 1.27	1361.76
8	1534.53 ± 0.58	1535.85
9	1708.45 ± 0.50	1709.94
10	1883.96 ± 0.67	1886.05

The predicted values were calculated using the Qual Browser feature of the Xcalibur® software version 2.0 from the Thermo Electron Corporation using a Gaussian profile with a resolution of 0.6 Daltons. The values which were observed are commonly about 1-2 mass units lower than those which were predicted by the software. This was a persistent calibration error constant throughout which could not be readily corrected. The LCQ instrument is a low resolution mass spectrometer and as such when isotopic profiling was considered for identification of the unknown peaks in the spectra it was useful that the vast majority of the species were found to be singly charged. Chlorine has two stable isotopes, ^{35}Cl and ^{37}Cl which have a naturally abundant ratio of approximately 3 to 1. As a result, species with multiple

chlorine ions present produce very distinctive isotopic distributions with dominant peaks separated by two mass units. Thus the relatively low instrumental resolution allowed for isotopic profiling of most species to be made in order to ensure accurate identification.

Figure 4-2 shows a typical mass spectrum for C4mimCl where the series of aggregates $C4mim_{n+1}Cl_n^+$ for n = 1 to 10 is marked allowing for comparison between their relative abundances. This shows that the aggregates with n = 1 and 4 have an anomalously high ion intensity. In contrast the aggregates with n = 2 and 3 appear comparatively weaker whereas n = 5 to 10 shows a smooth dependence with a maximum value at n = 6. The remaining unassigned peaks are the result of contamination with primarily Na^+ and K^+ ions which will be further illustrated in section 4.1.1.3.

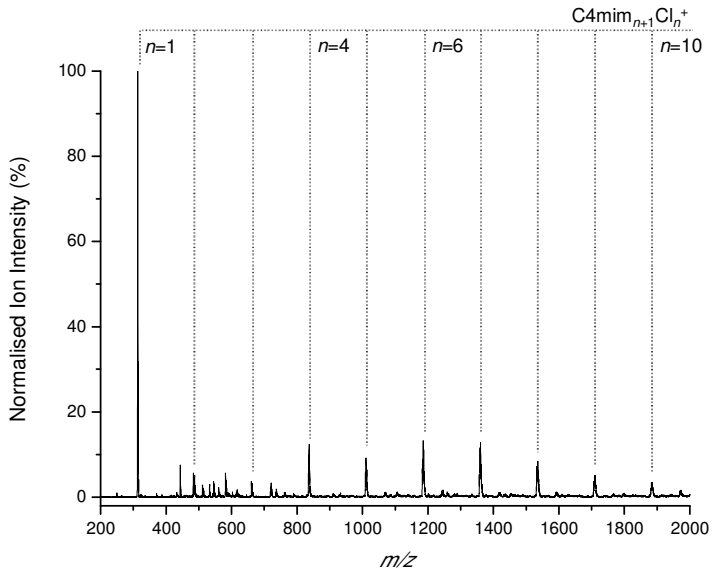

Figure 4-3 Mass spectrum of C4mimCl sprayed at 3 mM in a 9:1 solution of MeOH:H_2O with a tube lens offset of -35 V.

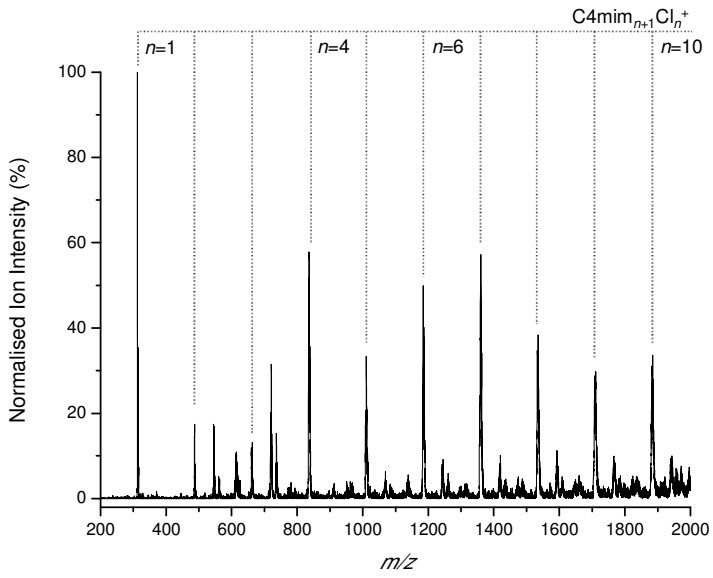

Figure 4-4 Mass spectrum of C4mimCl sprayed at 1 mM in 100% MeOH with a tube lens offset of 15 V.

As the sample preparation and instrument parameters were varied the patterns observed were consistently observed and reproducible, examples of this behaviour can be observed in Figure 4-3 and Figure 4-4. The tube lens sits between the heated capillary and skimmer arrangements and before the ion optics. As a result, varying this value can have a large effect on the spectra observed. While large changes are observed, the most obvious of which is the relative reduction in intensity of the prominent $C4mim_2Cl^+$ aggregate, the characteristics mentioned above remain constant. Setting the tube lens to + 10 or 15 V was seen to give a higher relative intensity for $n = 2$ to 10, however setting the tube lens to -30 V gave a greater signal intensity overall.

These trends will be discussed in greater detail concerning further investigation of the ions by CID and computational chemistry in later sections. However the increased presence of the $n = 4$ aggregate is in line with published work using MS which observed the preferred formation of corresponding aggregates for similar ILs.[2] Additionally in Figure 4-4 the species $n = 10$ is larger than $n = 9$ which is the opposite to the previous case indicating the possibility of further magic number aggregates.

4.1.1.2 QTOF

Higher resolution spectra were obtained by working on a Waters Micromass QTOF1 mass spectrometer as previously described in Section 2.2.9. Both ESI and nano-ESI data were collected on this instrument. Figure 4-5 shows a spectrum obtained using this spectrometer.

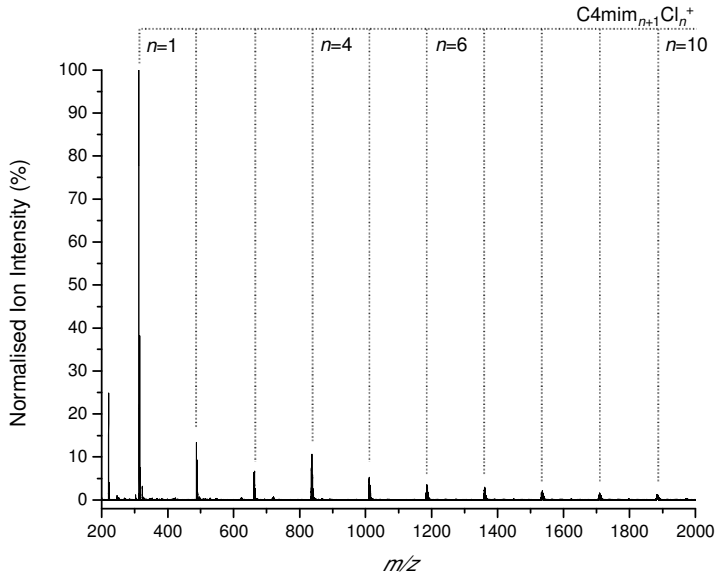

Figure 4-5 C4mimCl sprayed at 3 mM in 9:1 methanol:water using ESI on the QTOF instrument.

As was previously seen using the LCQ, a similar pattern of intensities is observed where aggregates with n = 1 and 4 appear more intense than aggregates with n = 2 and 3. The remaining aggregates with n = 5 to 10 show steadily decreasing maximum intensity values.

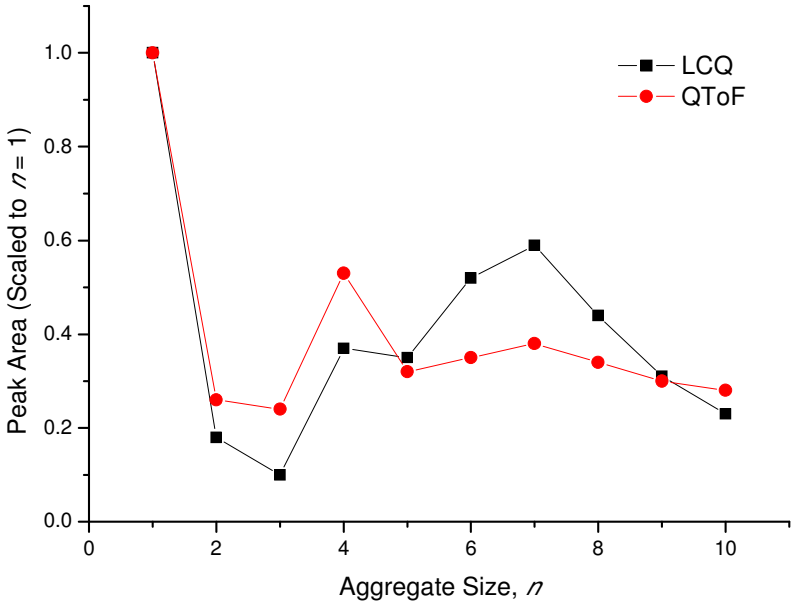

Figure 4-6 Scaled peak areas for C4mim$_{n+1}$Cl$_n^+$ for n = 1 to 10 in spectra produced on an LCQ and QTOF instrumentation.

The presence of multiple chlorine ions produces complex isotopic distributions and as a result the maximum peak intensity measure is not the most reliable judge of signal intensity. Any similar trends observed between the different instrumentation will be more clearly observed by integrating over relevant areas of the spectra to get peak areas. These peak areas are scaled to be a fraction of the most intense peak to allow for clearer comparison between the series. Figure 4-6 displays the peak areas for aggregates C4mim$_{n+1}$Cl$_n^+$ where each series has been scaled against the n = 1 aggregate.

The LCQ spectrum shows a modest increase in the scaled peak area at n = 4 where it was observed with a value of 0.37, while n = 3 and 5 are 0.10 and 0.35 respectively. However in the case of the QTOF spectrum a significantly more pronounced change was observed. In this case n = 4 had the second largest peak area with a value of 0.53. The adjacent peaks at n = 3 and 5 have values of 0.24 and 0.32 respectively. A smooth dependence is also observed between n = 5 and 10 with a maximum observed at n = 7. It has been shown that the QTOF can be successfully used to

produce the same series of singly charged cationic aggregates and similarities persist between the spectra.

4.1.1.3 Contaminant Metals

Contamination of ILs is a great problem when they are used for practical processes. The presence of contaminants can have a great effect on the overall physical properties of the IL. Common contaminants which are found to be harmful to the IL include halides, water and metal ions. Using ESI it is common to observe aggregation of many different species with charged contaminants, especially the group 1 alkali metals such as sodium and potassium.[8] It is particularly likely when an analyte is difficult to analyse and the charged contaminant brings an overall charge to the aggregate. The source of these trace contaminants is commonly ascribed to the glassware and solvents used in sample storage and preparation.

ILs, like other salts, have a poor ionisation efficiency. As a consequence of this, multiple series of IL aggregates have been observed containing contaminant ions. Figure 4-7 shows an example of this where the IL aggregates ($C4mim_{n+1}Cl_n^+$ for n = 1 to 10) are highlighted, along with a series with sodium adducts ($C4mim_nCl_nNa^+$ for n = 2 to 11).

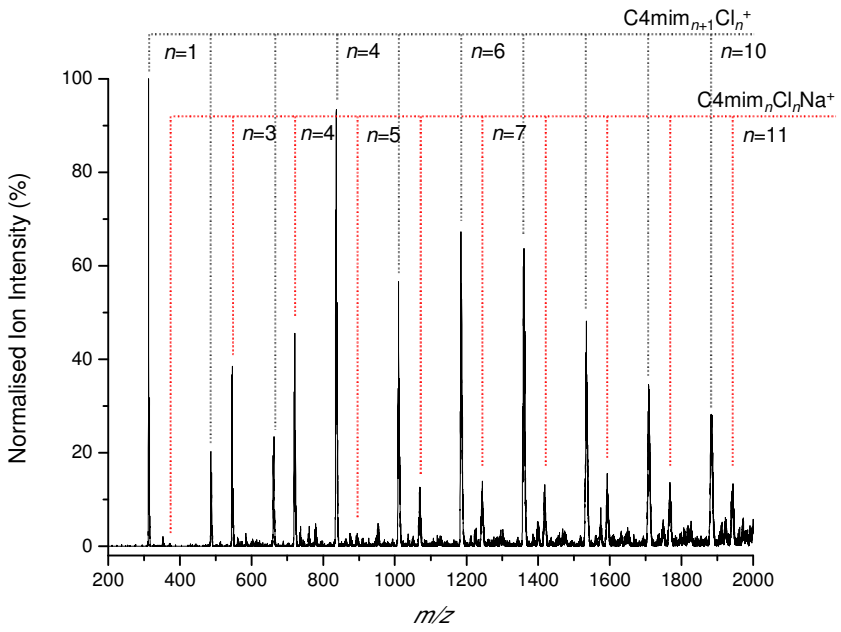

Figure 4-7 Mass spectrum of 1.36 mM C4mimCl sprayed in 100% MeOH on the LCQ using ESI with the C4mim$_{n+1}$Cl$_n^+$ (*n* = 1 to 10) and C4mim$_n$Cl$_n$Na$^+$ (*n* = 2 to 11) series highlighted in grey and red respectively.

From Figure 4-7 it can be seen that the C4mim$_n$Cl$_n$Na$^+$ series forms a very different pattern to its pure IL equivalent (C4mim$_{n+1}$Cl$_n^+$). C4mim$_n$Cl$_n$Na$^+$ with n = 3 and 4 are found with a very large ion intensity compared to the rest of the series. In contrast to this a very low ion intensity was found for n = 2 and 5. Indeed from n = 3 up to n = 11 strong signals are observed only with the very notable absence of n = 5 to break up this trend. Similar to the C4mim$_{n+1}$Cl$_n^+$ series, the C4mim$_n$Cl$_n$Na$^+$ series contains aggregates which appear more prominent than others.

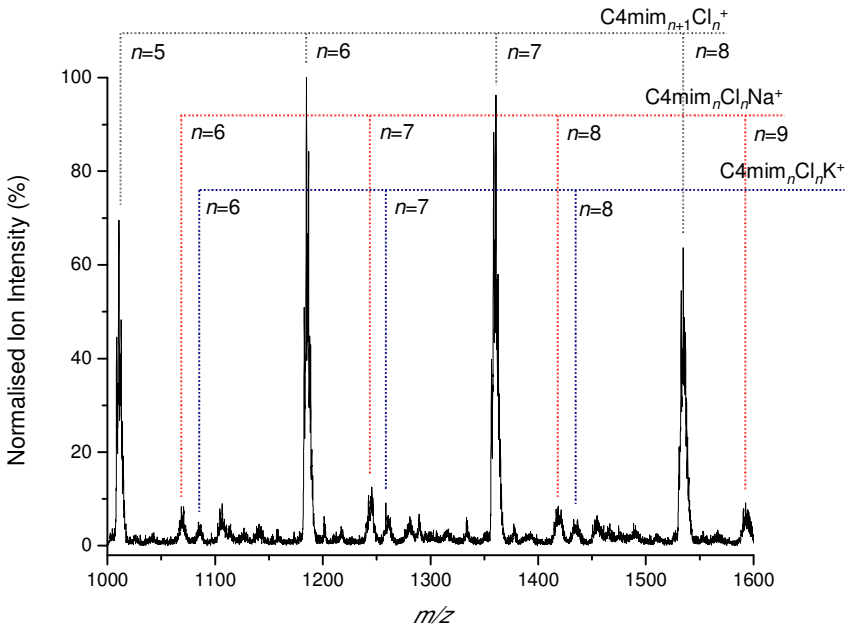

Figure 4-8 Mass spectrum of C4mimCl sprayed at 3 mM in a 9:1 solution of MeOH and H_2O using the LCQ. Highlighted are C4mim$_{n+1}$Cl$_n^+$ (grey), C4mim$_n$Cl$_n$Na$^+$ (red) and C4mim$_n$Cl$_n$K$^+$ (blue).

In addition to the series of C4mim$_n$Cl$_n$Na$^+$ aggregates, one of the most prominent series was C4mim$_n$Cl$_n$K$^+$. Figure 4-8 shows the presence of these aggregates in a mass spectrum of C4mimCl in a 9:1 MeOH and H_20 mixture. The spectrum was selected due to the good signal-to-noise ratio in this region, however the K$^+$ adducts were also observed without water present. The scaled peak area for the series C4mim$_n$Cl$_n$Na$^+$ and C4mim$_n$Cl$_n$K$^+$ that were observed are displayed in Figure 4-9.

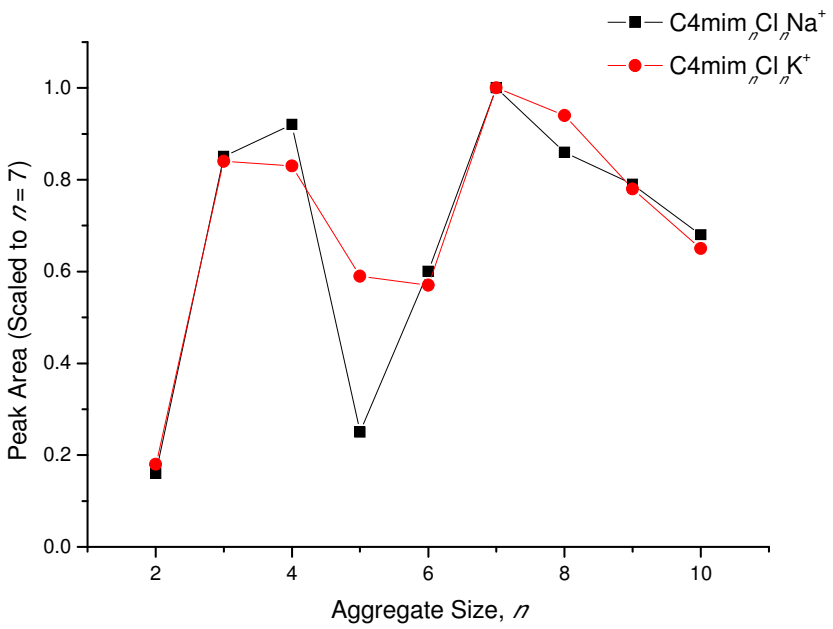

Figure 4-9 Scaled peak areas for C4mim$_n$Cl$_n$Na$^+$ and C4mim$_n$Cl$_n$K$^+$ for n = 2 to 10 in a MS of C4mimCl sprayed at 3 mM in a 9:1 solution of MeOH and H_2O using the LCQ.

The C4mim$_n$Cl$_n$Na$^+$ series shows a low intensity at n = 2, 5 and 6 with n = 3 and 4 having a much larger integrated peak area. From a peak at n = 7 the intensity drops steadily towards n = 10. The C4mim$_n$Cl$_n$K$^+$ series shows a very similar pattern to C4mim$_n$Cl$_n$Na$^+$ however, the intensity of the n = 5 peak is significantly smaller. The possible magic number at n = 4 which is inferred for these aggregates is not as pronounced in C4mim$_n$Cl$_n$K$^+$ as in C4mim$_n$Cl$_n$Na$^+$ potentially implying a steric effect. The significance of this change will be investigated in later with CID and computational chemistry. Due to the harmful nature of contamination, the propensity for formation of these mixed aggregates will be exploited to study the nature of the specific interactions taking place in Chapter 5.

4.1.1.4 C4mimOTf and C4mimPF$_6$

Mass spectra were recorded for the ILs 1-butyl-3-methylimidazolium trifluoromethanesulfonate (C4mimOTf) and 1-butyl-3-methylimidazolium hexafluorophosphate (C4mimPF$_6$) using the LCQ instrument. These ILs have melting points of 16 ºC and 6.5 ºC respectively.

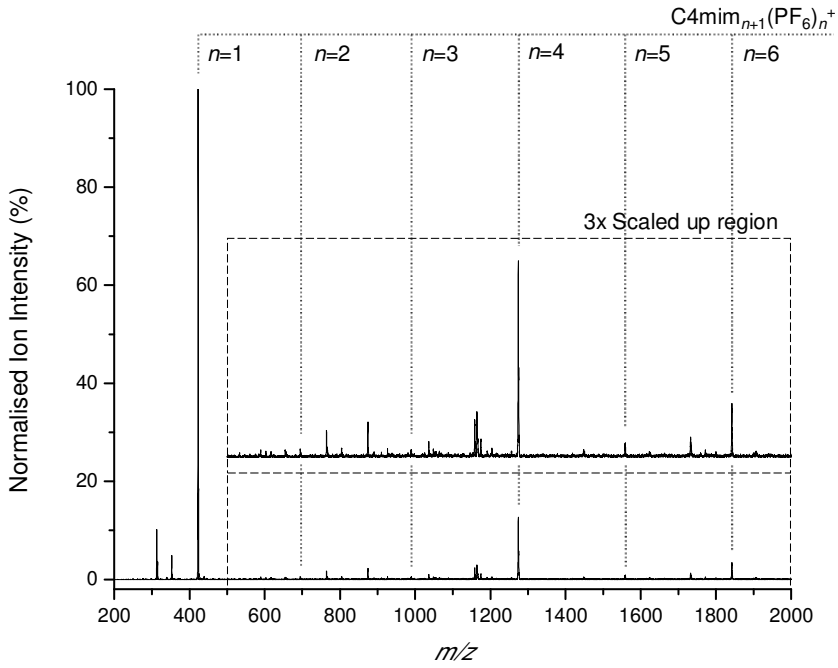

Figure 4-10 Mass spectrum of C4mimPF$_6$ in MeOH sprayed by ESI at a concentration of 2 mM on the LCQ instrument. The series C4mim$_{n+1}$(PF$_6$)$_n^+$ is highlighted in grey. The region between 500 and 2000 *m/z* is scaled up by a factor of 3.

The mass spectrum of C4mimPF$_6$ in MeOH is shown in Figure 4-10 and shows the formation of ions with the general formula C4mim$_{n+1}$(PF$_6$)$_n^+$ for n = 1 to 6. The individual ion intensity of the different aggregates varies greatly. The spectrum is dominated by the presence of the n = 1 aggregate with aggregates n = 4 and 6 much lower but these appear much larger than n = 2, 3 and 5.

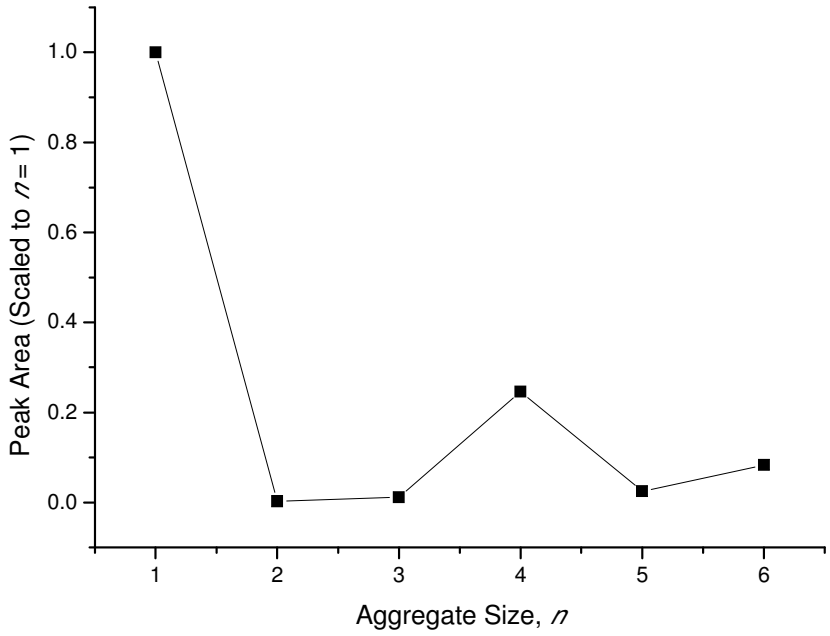

Figure 4-11 Scaled peak areas for C4mim$_{n+1}$(PF$_6$)$_n^+$ with n = 1 to 6 present in the MS of 2 mM C4mimPF$_6$ in 100% MeOH.

Figure 4-11 illustrates that the species with n = 2 doesn't form. Meanwhile the peaks at n = 3 and 5 are small but can be clearly identified at 1.2 % and 2.5 % of the total area for n = 1. As suggested from Figure 4-10 the overall signal intensity rises going from n = 6 to n = 4 with n = 1 as the maximum observed signal. The peak areas for n = 4 and 6 are 8.3 % and 24.6 % of the area for n = 1.

Similar to what was observed for the IL C4mimCl, a clear preference for the formation of certain aggregates exists. These results are in line with published results for this IL which have suggested the possibility of a magic number at n = 4.[2] The observation of corresponding results using the given instrumentation and method gives confidence about the trends which are observed. The case of C4mimPF$_6$ is even more extreme than C4mimCl with the increased dominance of the n = 1 species and the very low intensity of n = 2 and to a lesser extent n = 3 and 5.

Figure 4-12 shows the mass spectrum obtained on the LCQ for a 4 mM sample of C4mimOTf in 100% MeOH. The series of aggregates with the general formula C4mim$_{n+1}$OTf$_n^+$ is highlighted in this spectrum for n = 1 to 6.

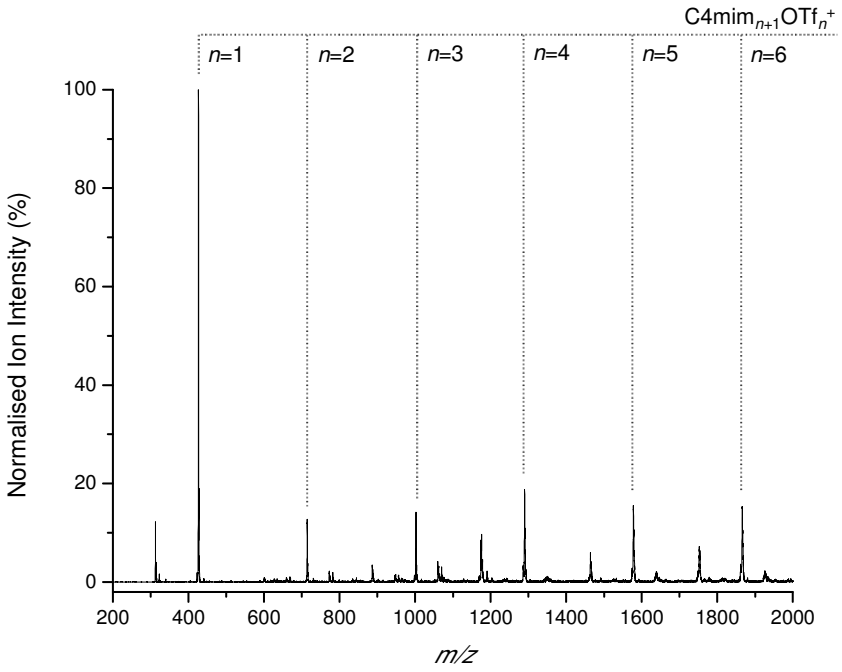

Figure 4-12 Mass spectrum of C4mimOTf in MeOH sprayed by ESI at a concentration of 4 mM on the LCQ instrument. The series C4mim$_{n+1}$OTf$_n^+$ is highlighted in grey.

The spectrum is dominated by the $n = 1$ species, however, unlike the spectra for C4mimCl and C4mimPF_6 the remaining observed species have relatively strong ion intensities. The $n = 2$ and 3 peaks again appear weaker than the remainder of the series however they are easily distinguishable in the spectrum. The peak at $n = 4$ again seems to be important in the spectrum with a possible dominance over the surrounding peaks.

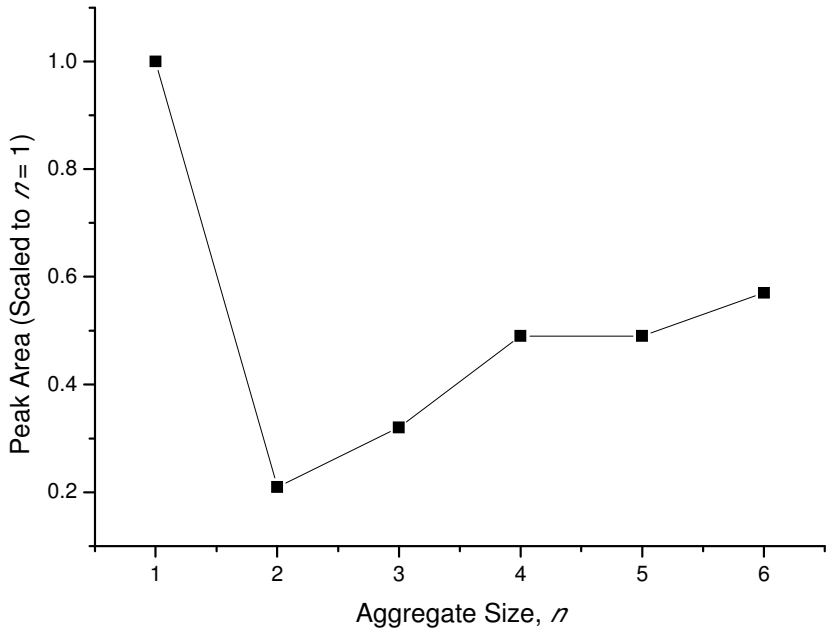

Figure 4-13 Scaled peak areas for C4mim$_{n+1}$OTf$_n^+$ with n = 1 to 6 present in the MS of 4 mM C4mimOTf in 100% MeOH.

Analysis of the peak areas for the observed series can be found in Figure 4-13. The peak areas increase as n increases from 2 to 6. The scaled peak area increases by approximately 0.1 between each aggregate, however n = 4 lies out of sequence with the series and higher than expected, indeed it is equal to n = 5. The preference for formation of certain aggregates is not as clear as with C4mimCl and C4mimPF$_6$ however again the spectrum was dominated by n = 1. The trends observed for n = 2, 3 and 4 are repeated with C4mimOTf however they are significantly less obvious for this case.

4.1.2 Sonic-Spray Ionisation

Sonic-spray ionisation (SSI) is a relatively new ionisation technique which can act as a softer ionisation source than ESI, for example it has been shown to increase aggregation of species and increase the ionisation of low charge state proteins.[9,10] From the earliest results using amino acids SSI was shown to have the possibility for increased aggregation.[9]

SSI is a technique which has been applied to a large number of different areas of MS and has proved versatile. Many of the earliest applications were to biological systems such as amino acids and the identification of oligosaccharides from human serum.[9,11] However the use of the technique spread and was combined with LC apparatus for the detection of endocrine-disrupting chemicals in environmental water samples.[12] It became clear that SSI was able to provide especially soft ionisation conditions; this fact was highlighted by the ionisation of weakly bound metal cage assemblies and the ionisation of large numbers of serine clusters which were cationized by alkali metals.[13,14] More recently this technique has been used to develop a novel atmospheric ionisation source. The source known as easy ambient sonic-spray ionisation (EASI) directs a sonic-spray source directly at a sample surface with resulting gas-phase ions collected directly into a mass spectrometer.[15]

As SSI is a novel ion source the apparatus requires a great deal of optimization. The key factors which influence its effectiveness include the nebulising gas pressure, desolvation temperature and nozzle position. In addition to this, the sample infusion rate and nature of the sample are important. In order to test the applicability of the source, NaCl solutions were used.

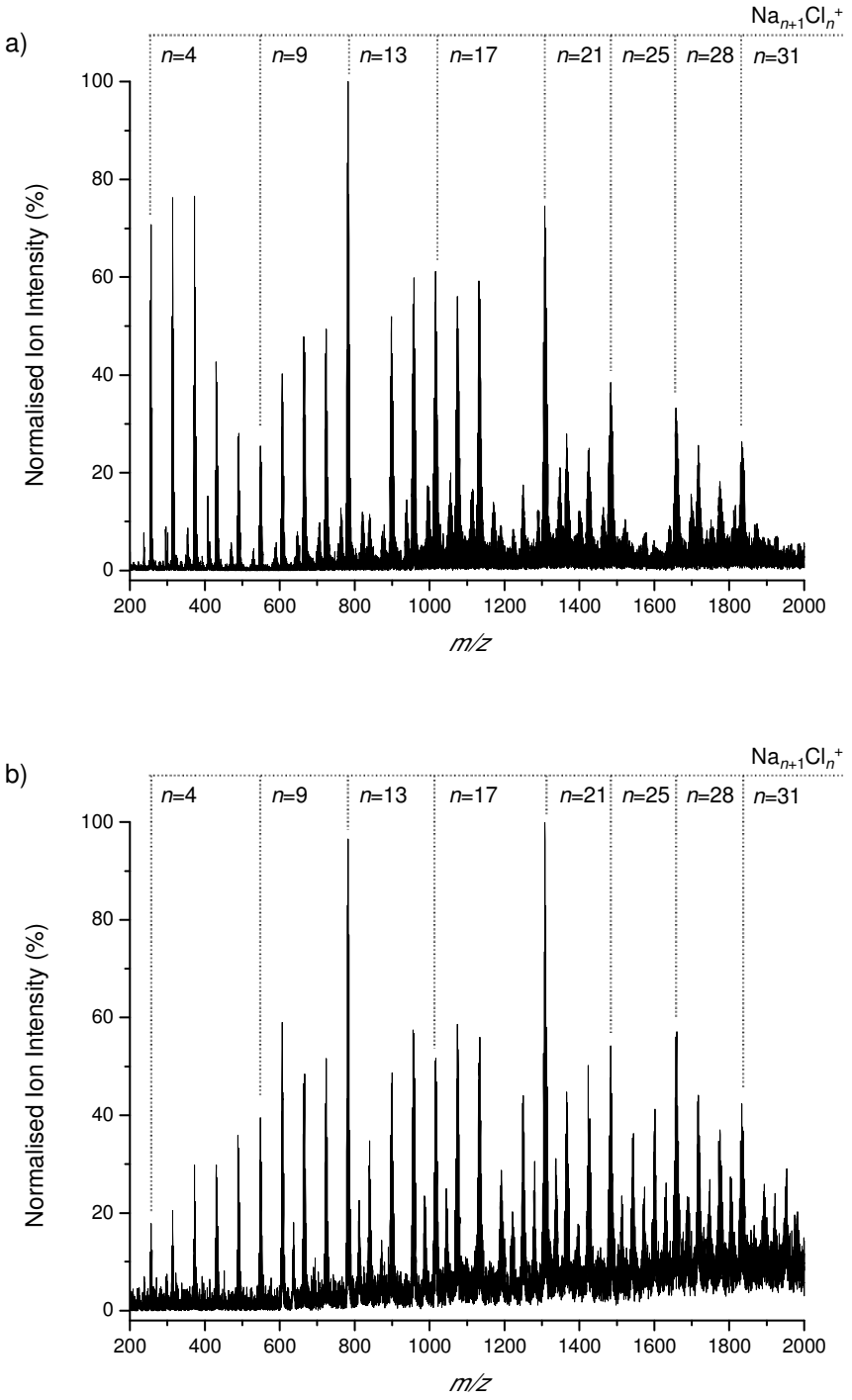

Figure 4-14 LCQ mass spectra of 10 mM NaCl in a 50:50 mixture of H_2O and MeOH with a) an ESI source and b) a SSI source. Selected aggregates from the $Na_{n+1}Cl_n^+$ series are highlighted in grey.

SSI was found to preferentially favour the formation of larger salt aggregates relative to an ESI source. The mass spectra for 10 mM NaCl in a 50:50 mixtures of water and methanol can be seen in Figure 4-14, in these spectra the series of $Na_{n+1}Cl_n^+$ from n = 4 to 33 can be observed. Figure 4-14(a) shows two strong peaks corresponding to n = 13 and 21. In addition to this there are several peaks which are observed with a strong intensity and within this a general trend can be summarised. From n = 4 up to n = 21 the peaks are generally strong and observed with a large intensity however from n = 22 to n = 33 the peaks are much weaker.

When Figure 4-14(a) is compared to Figure 4-14(b) some similarities and differences can be observed. Figure 4-14(b) again shows two peaks with a large ion intensity which correspond to n = 13 and 21 however the general trends change for the remainder of the peaks. The peaks from n = 4 to 12 are seen to generally decrease while the peaks from n = 13 to 21 remain about the same. Meanwhile the peaks from n = 22 to n = 33 are seen to gain ion intensity. This is in line with what may be predicted from the previous literature work where there is a general move to favour the larger aggregates.[9,10] This successful test of SSI was followed by its use with the IL C4mimCl. Spectra generated from a 3 mM solution of C4mimCl in methanol utilising both ESI and SSI are shown in Figure 4-15. The structure of the $C4mim^+$ cation can be found in Figure 4-1(a).

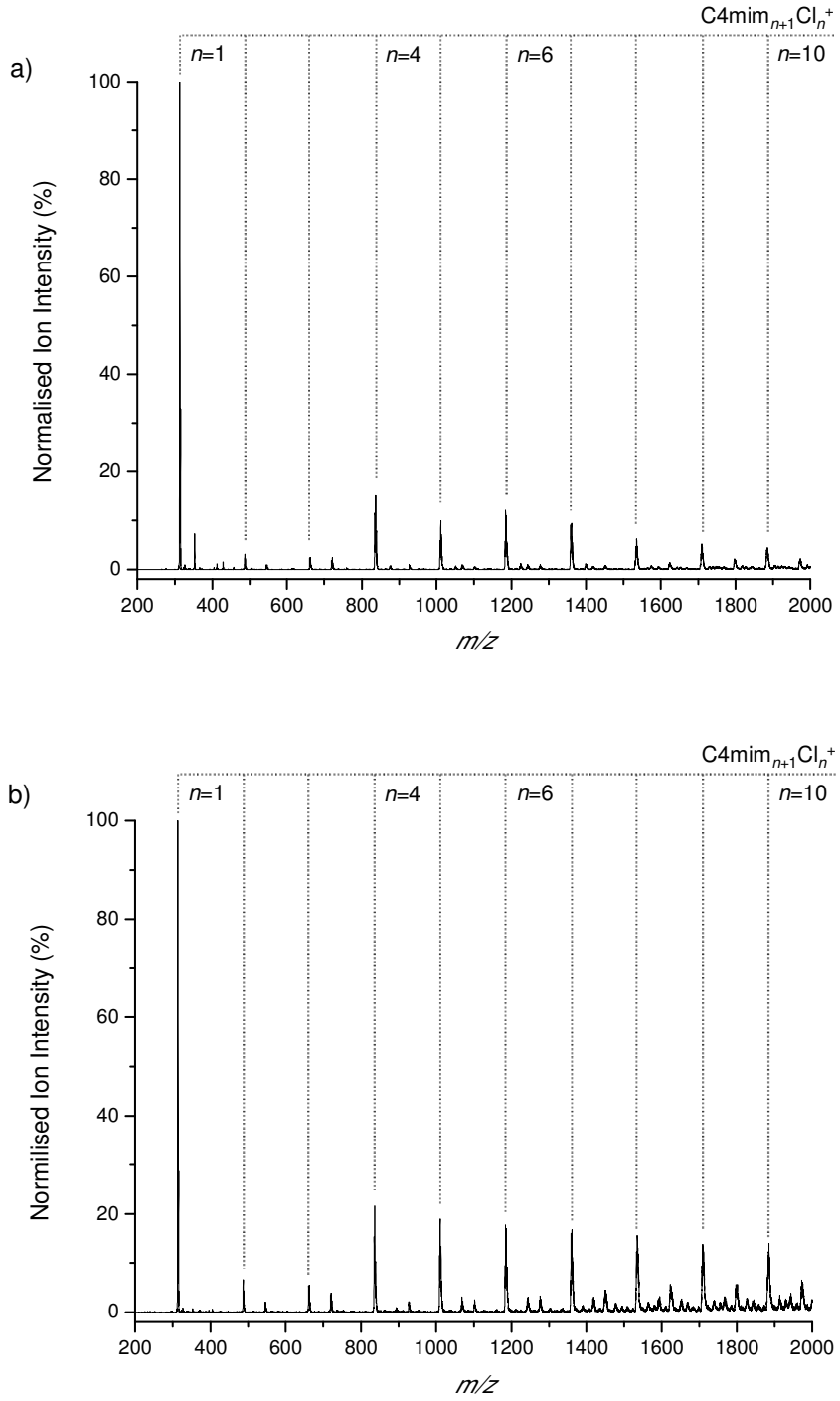

Figure 4-15 LCQ mass spectra of 3 mM C4mimCl in a 100% MeOH with a) an ESI source and b) a SSI source. Selected aggregates from the C4mim$_{n+1}$Cl$_n^+$ series are highlighted in grey.

The instrumental parameters used for both sources were as given in Chapter 2. The ESI and SSI spectra shown in Figure 4-15 show the successful formation of the

series of IL aggregates with the general formula $C4mim_{n+1}Cl_n^+$ with size from $n = 1$ to $n = 10$. Both spectra are dominated by the $n = 1$ aggregate however an apparent increase in ion intensity is observed between $n = 2$ and $n = 10$ for SSI over ESI.

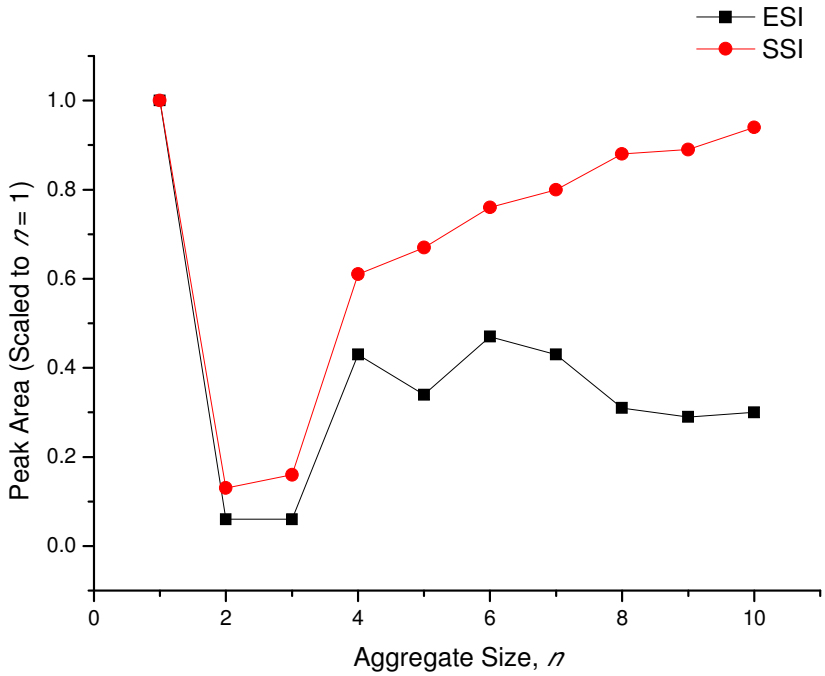

Figure 4-16 Scaled peak areas for $C4mim_{n+1}Cl_n^+$ peaks present in the MS of 3 mM C4mimCl in a 100% solution of MeOH using an ESI and SSI source.

An analysis of the spectra presented in Figure 4-15 is shown in Figure 4-16. From this data we can see that both spectra are dominated by the aggregate at $n = 1$. In addition to this, the previously observed lack of prominence of aggregates $n = 2$ and 3 can be seen relative to $n = 4$ to 10. However there is an increase in signal for the $n = 2$ to 10 aggregates. From the previous results obtained from the SSI source this would be hoped for, an increase in the ionisation of larger aggregates was displayed. These results show that SSI can be successfully applied to the formation of IL aggregates and can be used to favour the formation of larger aggregates compared with ESI. In addition it is worth noting the unexpected trend in the peak areas observed with the SSI source for $n = 4$ to $n = 10$. Unlike in the previously presented examples with C4mimCl using an ESI source, the scaled peak areas here increase with increasing aggregate size from 0.61 at $n = 4$ up to 0.94 at $n = 10$. It is observed

that the increased aggregation from the SSI source is even great enough to obscure the previously predicted magic number properties of $n = 4$. SSI has been previously shown to increase the number of larger aggregates which are formed by reducing the in-source fragmentation.[9] Magic numbers are typically observed where there is a fragmentation of larger species which the SSI source may not be giving.

4.1.3 Plasma Assisted Desorption Ionisation

PADI is a relatively new ionisation technique which has been used for direct sampling from surfaces without the need for extensive sample preparation.[16] The PADI source was discussed in Section 2.2.4 and also previously in the literature.[16] In this thesis the analysis of the ILs C4mimCl and C4mimNTf_2 with PADI is reported. Using the PADI source it had proved difficult to consistently ionise directly from surfaces. Initially direct surface analysis was attempted, however the capillary setup described in Chapter 2 was developed to allow analysis from solutions of the analyte in a volatile organic solvent. All of the experiments were performed on the LCQ instrument with the PADI source employed in place of the standard ESI source.

In order to test and optimise the PADI source it was used to analyse directly from paracetamol tablets, caffeine, doxepin, overhead projector pen and from the ILs C4mimCl and C4mimNTf_2. Direct analysis of a paracetamol table showed the presence of the protonated parent ion and a protonated fragment of the paracetamol molecule. These examples were rare and difficult to reproduce. In order to obtain such results it was necessary to increase the applied power beyond the source capabilities which resulted in damage to the instrumentation and also to the sample being analysed. In the case of analysing tablets, the successful use of the PADI source caused the tablet to burn, thus could not be used where the sample must remain undamaged. The PADI source was not able to directly ionise the ILs C4mimCl and C4mimNTf_2. In order to obtain a stronger and more consistent signal a technique was developed to introduce the samples via a solution. This capillary technique was described in Section 2.2.4.

When samples of paracetamol and caffeine were introduced in solution protonated parent ions could be observed in each case. In addition a protonated dimer of paracetamol was also observed. These test cases have shown that the PADI source can be combined with the capillary technique to ionise a sample and produce improved results compared with direct surface analysis. It had not proved possible to ionise the ILs using PADI by direct surface analysis when they were dried onto glass rods, however when introducing them via the capillary setup, ionisation was observed.

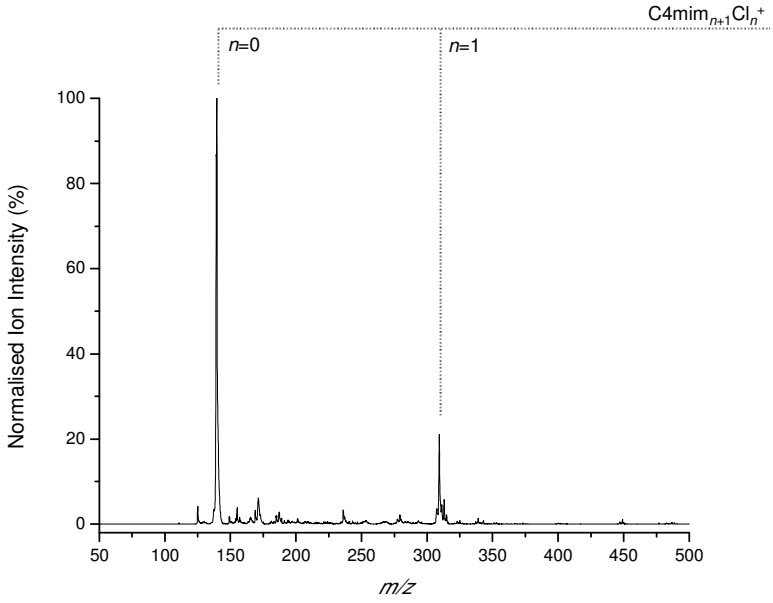

Figure 4-17 Mass spectrum of 10 mM C4mimCl in MeOH introduced to PADI via capillary.

Figure 4-17 shows a mass spectrum produced from a 10 mM solution of C4mimCl in 100 % methanol. This spectrum shows the presence of the $C4mim^+$ cation and the $C4mim_2Cl^+$ aggregate. This shows that the PADI source can be used to ionise samples of an IL and even a limited amount of aggregation can be observed using it. When this spectrum is compared with similar examples produced using ESI or SSI the range of aggregation is very modest. Indeed the concentration of IL required was double the maximum previously used (10 mM compared with 5 mM) and the sample flow rate was also much larger (30 $\mu Lmin^{-1}$ compared to 5 $\mu Lmin^{-1}$). Thus while the

PADI source has been shown capable of performing this ionisation it was nowhere near as efficient as the previously discussed sources.

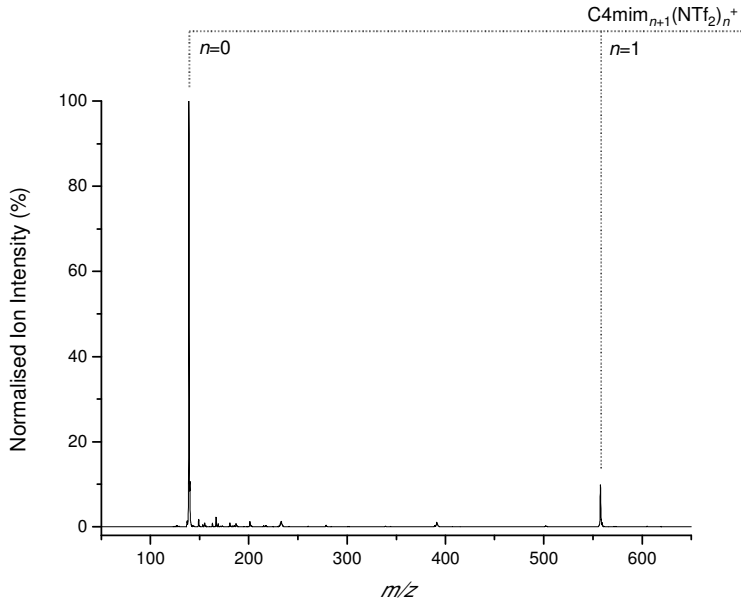

Figure 4-18 Mass spectrum of 10 mM $C4mimNTf_2$ in MeOH introduced to PADI via capillary.

The final example showing the use of the PADI source was using the $C4mimNTf_2$ IL. The mass spectrum resulting from this IL is shown in Figure 4-18 where a similar mass spectrum to the C4mimCl example in Figure 4-17 can be seen. The lone $C4mim^+$ cation can be observed along with the $C4mim_2NTf_2^+$ aggregate which shows that the PADI source can successfully be used to ionise different ILs. Once again the range of aggregates which were produced and the intensity of these are very disappointing. Varying the solvent used with the IL had a particularly large effect on the resulting spectra. The use of water produced very noisy spectra where only the $C4mim^+$ cation could be observed. When acetonitrile was used as the solvent, the signal-to-noise ratio was greatly improved however only the $C4mim^+$ cation could be observed. While the range of aggregates produced with methanol was very limited it was the only case where this was observed to occur. PADI was used to ionise a range of different samples however its use has been shown to be

troublesome. The production of high quality mass spectra to rival ESI and SSI proved elusive particularly when used for direct surface analysis.

4.1.4 Collision Induced Dissociation

Collision induced dissociation was performed using helium gas in the ion trap of the LCQ instrument. CID is a widely used technique which gives information about the fragmentation pathways of ions and the relative stability of different species. It is a fairly standard technique which has been applied to an incredibly varied number of different species. Some of these include large biological molecules and assemblies, small drug molecules, inorganic metal complexes and salts.[17-21] Available literature using CID to study IL aggregates is very limited.[2,22] However the previous work does suggest there are some trends which can be investigated and used for comparison. These include the presence of a magic number at $n = 4$ for many ILs with the general formula $C_{n+1}A_n^+$ where C is a singly charged cation and A is the singly charged counter anion.

CID experiments were performed at optimised conditions using 5 mM C4mimCl in a 90:10 mixture of methanol and water. The structure of the $C4mim^+$ IL cation can be observed in Figure 4-1(a). The concentration was at the upper end of what was previously used to ensure a good signal-to-noise ratio. This is especially important because as was previously observed some species, for example with $n = 2$ and 3, were observed with a lower intensity than others. As was discussed previously C4mimCl is soluble in pure methanol however the alkali metal chlorides used in Chapter 5 are less soluble in methanol and thus it was useful to have a small percentage of water in order to aid their solubility. 10 % water was used in as many of the CID experiments as possible to reduce the variations between the experiments and therefore allow for closer comparison between them.

CID experiments were performed for $n = 1$ to $n = 7$ for the series of aggregates $C4mim_{n+1}Cl_n^+$. The instrument software required a parent mass (m/z) to be specified along with an isolation width (m/z) for each species; these were estimated from a new raw mass spectrum with no isolation. This spectrum was kept as a reference to

ensure consistency. This spectrum allowed the position and intensity to be verified before the CID was performed. Once the individual species were isolated a visual check was performed to ensure that the correct species had been isolated and the isotopic distribution was complete and had not been deformed. Only once these checks had been performed was the CID experiment started.

The energetic collisions between the isolated ion and the helium buffer gas were controlled by the software parameter called NCE (%). This is controlled by variations in the voltages applied to the end cap electrodes. As described in Section 2.2.5 the effect of altering this voltage is related to the mass of the isolated ion and the NCE includes a manufacturer correction for this dependence thereby allowing direct comparisons between different masses. The activation time was set and remained constant at 30 ms. Once a species had been isolated, a spectrum was recorded with the NCE set to 0 %; this created a baseline intensity allowing the reduction of the parent ion intensity to be monitored. The NCE was subsequently slowly increased with spectra being recorded at different NCE values between 0 % and 100 %. The NCE was varied at different rates with smaller changes used where the parent ion intensity was reducing.

The ion count associated with the individual ions was calculated as a function of the total ion count. This process was performed for the parent ion and each of the daughter ions. This ratio was plotted against the NCE in the Origin 8.0 software for each of the ions in order to show the make up of the spectra with varying collision energy. The sigmoidal fit feature of the Origin 8.0 software which uses Equation 4-1 was used to fit the parent ion dissociation curves.

$$Y = A2 + \frac{A1 - A2}{1 + \exp\left(\frac{X - X_c}{dX}\right)} \qquad \textbf{Equation 4-1}$$

A1 and A2 are the determined maximum and minimum y-axis limits for each curve, while the Xc value is the x-axis value corresponding to the point of inflection of the fit. This value is characteristic of the dissociation curve and is referred to as the characteristic collision energy (CCE). The value of the CCE is used to compare the

NCE which is required to dissociate the various parent ions. By comparing them, information about the relative stability of the different ions can be obtained.

Table 4-2 Experimental trapping parameters used for the series of $C4mim_{n+1}Cl_n^+$.

Aggregate size, *n*	Selected Parent Mass (*m/z*)	Isolation Width (*m/z*)
1	313	10
2	485	10
3	661	10
4	836	12
5	1010	15
6	1183	15
7	1360	15

The positions of the selected masses can be seen in Table 4-2; these were selected in a way as to ensure all of the isotopes were trapped. The isolation widths increase with the aggregate size due to the increasing number of isotopes and the spreading of the ion intensity over a greater range.

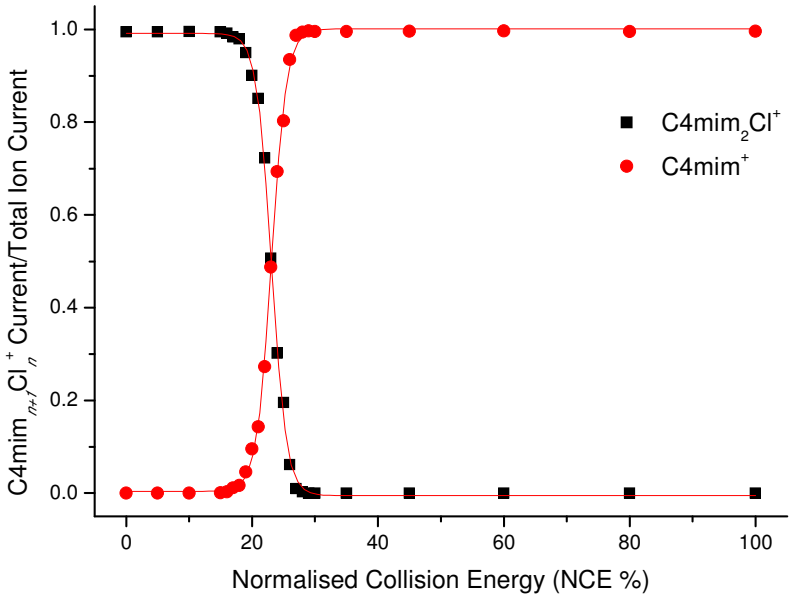

Figure 4-19 $C4mim_{n+1}Cl_n^+$ Ion Current/Total Ion Current for the collisional activation of $C4mim_2Cl^+$ with varying NCE.

Figure 4-19 shows the result for collisional activation of $C4mim_2Cl^+$. The y-axis displays the ion current associated with the parent and daughter ions divided by the total ion current for the mass spectrum at that NCE value. When there is little or no activation, NCE % below 15, it was found that the spectrum consists almost entirely of the parent $C4mim_2Cl^+$ cation. However, as the NCE % is increased between 15 and 30 % a rapid change occurred. The signal associated with the $C4mim_2Cl^+$ ion decreased from approximately 1 to 0 indicating a complete loss of the parent ion by 30 % NCE. Above 30 % NCE the $C4mim_2Cl^+$ signal remained at zero. Simultaneously the ion current for the $C4mim^+$ cation increases from 0 below 15 % NCE to 1 above 30 % NCE. This indicates that the parent $C4mim_2Cl^+$ has been fragmented into $C4mim^+$ and other non-observable fragments which would be likely to include the neutral ion pair C4mimCl.

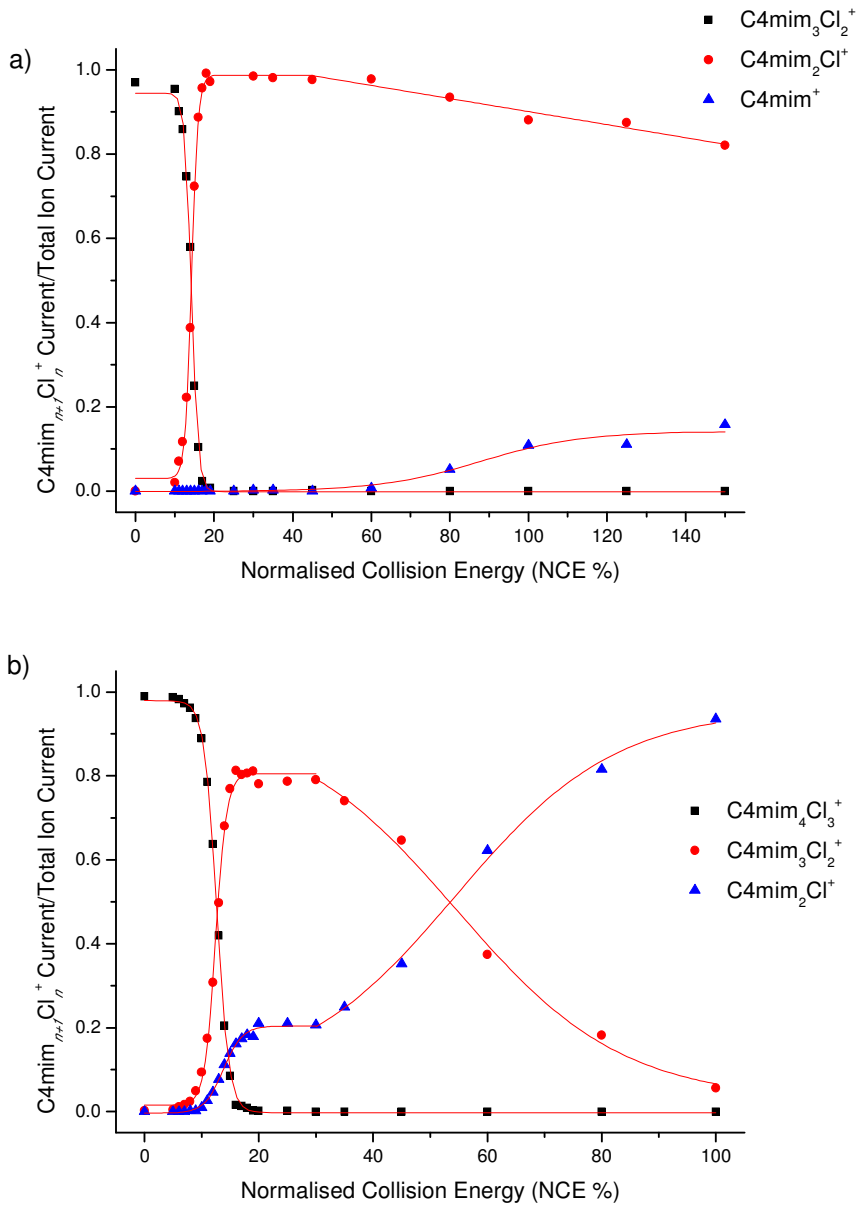

Figure 4-20 $C4mim_{n+1}Cl_n^+$ Ion Current/Total Ion Current for the collisional activation for a) $C4mim_3Cl_2^+$ and b) $C4mim_4Cl_3^+$ with varying NCE.

The breakdown curves of $C4mim_3Cl_2^+$ and $C4mim_4Cl_3^+$ can be seen in Figure 4-20. Figure 4-20(a) shows that the activation of the aggregate $C4mim_3Cl_2^+$. In this case, for NCE values of between 0 and 50 %, the breakdown of the parent ion is observed and the fragmentation process results in the observation of the $C4mim_2Cl^+$ aggregate almost exclusively. The dominant formation of $C4mim_2Cl^+$ closely mimics the observations for the breakdown of $C4mim_2Cl^+$ which was shown in Figure 4-19.

However as the NCE is increased above 50 % the $C4mim^+$ ion is observed. The intensity of this signal remains small in comparison with that of the $C4mim_2Cl^+$ however it is seen to increase with increasing NCE.

These results suggest that the parent $C4mim_3Cl_2^+$ aggregate is losing a stable ion pair with the result that $C4mim_2Cl^+$ is observed. This aggregate is then stable enough to withstand activation up to 50 % NCE however above this it can fragment as observed in the case of $C4mim_2Cl^+$ activation. It is also possible that the increased NCE is activating a second fragmentation pathway which will result in the direct formation of the $C4mim^+$ cation.

Figure 4-20(b) shows the breakdown curve associated with the collisional activation of $C4mim_4Cl_3^+$. The fragmentation of $C4mim_4Cl_3^+$ exhibits some different characteristics compared with the breakdown of $C4mim_3Cl_2^+$ and $C4mim_2Cl^+$ before it. NCE values greater than 5 % resulted in the formation of two observable fragments. This was in comparison with one lone fragment which was observed in the previous examples for similar NCE %.

Complete loss of the parent ion occurs between 5 and 20 % NCE and as the parent ion is completely diminished, $C4mim_3Cl_2^+$ and $C4mim_2Cl^+$ form in a 4:1 ratio. For NCE values between 20 and 30 % each species holds approximately constant. Above 30 % a breakdown is seen in the $C4mim_3Cl_2^+$ intensity with the resulting formation of $C4mim_2Cl^+$.

These results indicate a second process is occurring above 30 % NCE which results in the breakdown of the $C4mim_3Cl_2^+$ into the $C4mim_2Cl^+$ aggregate with the loss of a C4mimCl ion pair. These results seem to indicate two different pathways for the formation of $C4mim_2Cl^+$ from $C4mim_4Cl_3^+$, one direct and another pathway where $C4mim_3Cl_2^+$ acts as an intermediate.

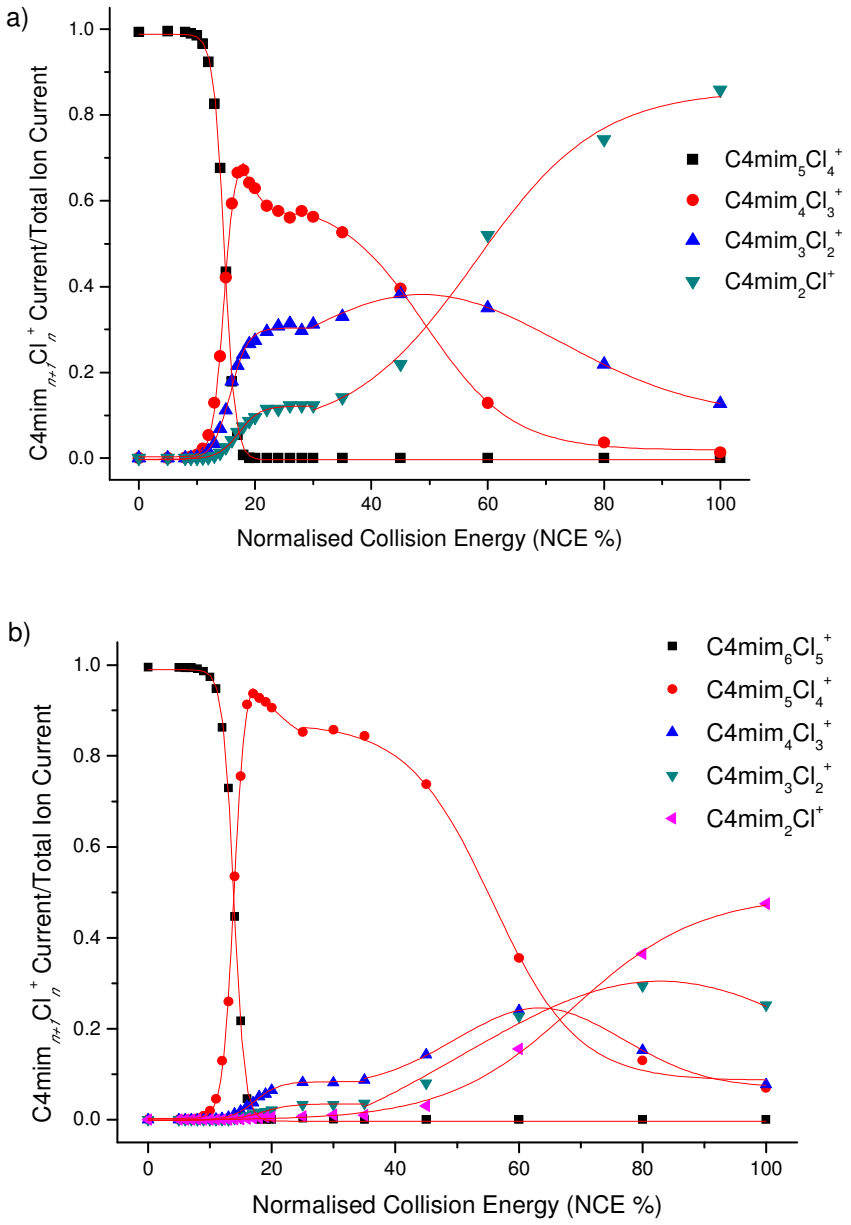

Figure 4-21 $C4mim_{n+1}Cl_n^+$ Ion Current/Total Ion Current for the collisional activation for a) $C4mim_5Cl_4^+$ and b) $C4mim_6Cl_5^+$ with varying NCE.

The breakdown of the $C4mim_5Cl_4^+$ aggregate is shown in Figure 4-21(a), the parent ion signal is observed to decrease from approximately 1 to 0 over a small range with multiple fragments forming as in the previous examples. The fragmentation of the parent ion results in the immediate formation of three different observable fragments. These are the $C4mim_4Cl_3^+$, $C4mim_3Cl_2^+$ and $C4mim_2Cl^+$ aggregates.

The fragment $C4mim_4Cl_3^+$ rapidly forms with a high intensity however there is a rapid decrease in the associated ion current as the NCE is increased above 18 %. This has the effect that the $C4mim_4Cl_3^+$ trace exhibits an abrupt peak before decreasing. When the NCE is between 20 and 30 % the parent and fragment ions retain an approximately equal intensity and the different traces are seen to plateau. At this point the $C4mim_4Cl_3^+$, $C4mim_3Cl_2^+$ and $C4mim_2Cl^+$ aggregates show a ratio of their intensities of approximately 6:3:1. Above 30 % NCE the intensity of the $C4mim_4Cl_3^+$ aggregate begins to decrease with the $C4mim_3Cl_2^+$ and $C4mim_2Cl^+$ aggregates increasing as a result for NCE between 30 and 50 %. However the increase in the $C4mim_3Cl_2^+$ intensity is slight and decreases significantly above 50 %.

The immediate formation of the three different aggregates upon activation suggests that there is no clear energetic pathway driving the formation of any particular aggregate and as a result different numbers of ion pairs are seen to dissociate form the aggregate. This might imply that there is a relative weakness or instability associated with the aggregates with $n = 2$ and 3. This implication would be in line with observations made previously concerning the low propensity of formation for these aggregates relative to those which are closely related.

Breakdown curves associated with the fragmentation of the aggregate $C4mim_6Cl_5^+$ can be seen in Figure 4-21(b). As with all of the previous examples the parent ion is seen to decrease in intensity from 1 to 0 over a small range of NCE and the fragments increase in intensity at larger NCE %. Similar to the $C4mim_4Cl_3^+$ aggregate in Figure 4-21(a), the $C4mim_4Cl_3^+$ rapidly increases in intensity before once again decreasing forming a narrow peak prior to the presence of a plateau or broad shoulder with increasing NCE. However, unlike the example in Figure 4-21(a) where three different aggregates were present only this ion is formed at a significant intensity. The slight decrease in the intensity of the $C4mim_5Cl_4^+$ aggregate corresponds to the formation of the $C4mim_4Cl_3^+$ and $C4mim_3Cl_2^+$ aggregates. A plateau is then observed between and NCE of 25 and 35 %. This NCE value is larger than was observed for the previous aggregates which were around 5 % lower than observed here. Above an NCE of 35 % the aggregates $C4mim_4Cl_3^+$, $C4mim_3Cl_2^+$ and $C4mim_2Cl^+$ all increase in intensity. However the $C4mim_4Cl_3^+$ aggregate peaks at

around 60 % and the $C4mim_4Cl_3^+$ aggregate peaks at around 80 % before each of them decrease in intensity leaving $C4mim_2Cl^+$ alone.

The initial formation of a single fragment suggests that this fragment species is relatively stable compared to the smaller aggregates and that there is a low energy pathway to reach it through the loss of a single stable ion pair. This is further backed up by the plateau position being at a higher NCE than the previous examples indicating that a larger amount of energy is required to further fragment this stable aggregate. Additionally the low stability of the $n = 2$ and 3 is further indicated by the absence of a dominant fragment at high NCE.

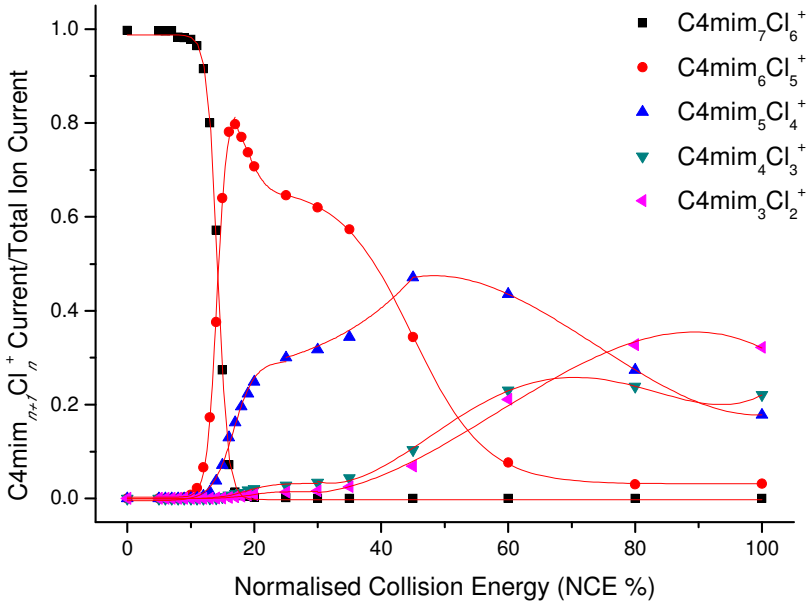

Figure 4-22 $C4mim_{n+1}Cl_n^+$ Ion Current/Total Ion Current for the collisional activation of $C4mim_7Cl_6^+$ with varying NCE.

The mass range which can be observed during MS^n using the LCQ instrument is limited due to technical restrictions. When isolation is made the low mass limit of the mass range is determined by the software based upon the selected parent ion mass. Thus as the parent ion *m/z* increases with increasing aggregate size (*n*) the low mass limit increases too. As a result of this, as the aggregate size increases certain fragments can no longer be observed but may still be formed during the activation.

Figure 4-22 shows the intensities of the parent $C4mim_7Cl_6^+$ and the observable fragment ions on collisional activation in the LCQ. In this case the *m/z* of the observed parent ion is large enough so that the instrument is unable to observe the $C4mim_2Cl^+$ possible fragment. As with all of the previous examples the parent ion is seen to rapidly decrease from approximately 1 to 0. In this case, the decrease is accompanied by an increase in the intensities of two different aggregates, $C4mim_6Cl_5^+$ and $C4mim_5Cl_4^+$. Initially the $C4mim_6Cl_5^+$ aggregate increases more rapidly and similar to what was observed in Figure 4-21, a bump is observed which exists over a small NCE range. At the high NCE side of the bump the $C4mim_6Cl_5^+$ and $C4mim_5Cl_4^+$ aggregates roughly have a 3:1 intensity ratio. This high intensity associated with the smaller $C4mim_5Cl_4^+$ fragments further suggests a relatively high stability and propensity to formation when compared with its neighbouring $C4mim_{n+1}Cl_n^+$ aggregates.

Between 20 and 35 NCE % the general trend sees the $C4mim_6Cl_5^+$ intensity diminish and the $C4mim_5Cl_4^+$ intensity increase with the other fragments remaining dormant. Above 35 % NCE the $C4mim_4Cl_3^+$ and $C4mim_3Cl_2^+$ fragments slowly increase and at 45 % NCE the $C4mim_5Cl_4^+$ aggregate begins to reduce in intensity. As would be readily predicted the higher NCE spectra are dominated by the smaller fragments. $C4mim_5Cl_4^+$ continually reduces in intensity however $C4mim_4Cl_3^+$ plateaus above 60 % and $C4mim_3Cl_2^+$ plateaus above 80 % NCE. It is notable that between 45 and 60 % NCE the spectra are dominated by the $C4mim_5Cl_4^+$ aggregate to an extent that the previous examples were not by a secondary fragment.

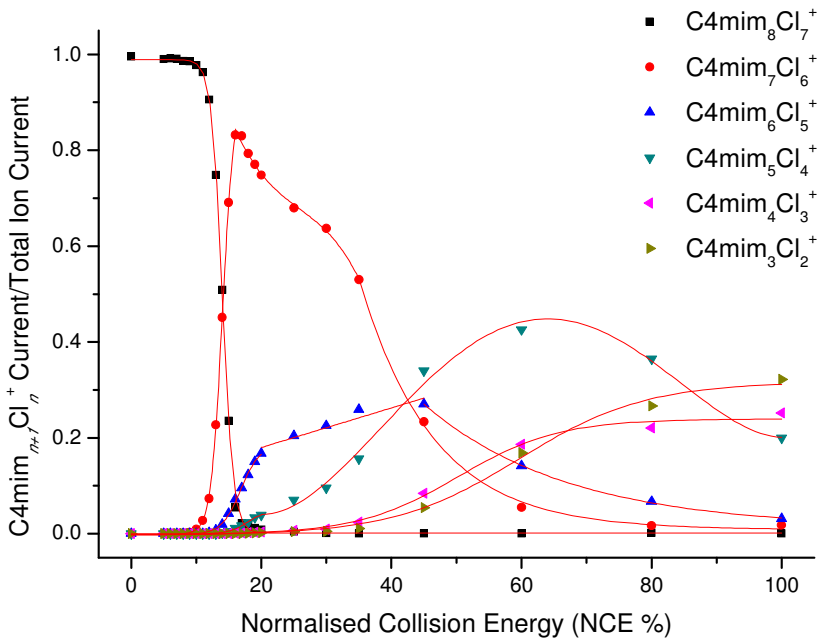

Figure 4-23 $C4mim_{n+1}Cl_n^+$ Ion Current/Total Ion Current for the collisional activation of $C4mim_8Cl_7^+$ with varying NCE.

Figure 4-23 displays the final example of a $C4mim_{n+1}Cl_n^+$ breakdown curve, showing the collisional activation of $C4mim_8Cl_7^+$. As with all of these cases the parent ion rapidly decreases from 1 to 0 and fragment ions are then observable. Initially, from about 10 % NCE, two fragments begin to form; these are $C4mim_7Cl_6^+$ and $C4mim_6Cl_5^+$. A bump, similar to those seen in previous examples, is observed in the intensity of the $C4mim_7Cl_6^+$ fragment. The early fragmentation is dominated by the $C4mim_7Cl_6^+$ aggregate, at the high energy side of the bump the ratio of intensities with the next aggregate, $C4mim_6Cl_5^+$, is roughly 4:1. From 15 % NCE the $C4mim_7Cl_6^+$ aggregate decreases in intensity and the $C4mim_6Cl_5^+$ aggregate continues to increase in intensity. At this point the smaller $C4mim_5Cl_4^+$ begins to form too, which may suggest a fragmentation pathway from $C4mim_7Cl_6^+$ to $C4mim_5Cl_4^+$ which bypasses the intermediate $C4mim_6Cl_5^+$.

When the NCE is at 25 % the smaller $C4mim_4Cl_3^+$ and $C4mim_3Cl_2^+$ aggregates can start to be observed. The fragment ion intensities increase and then decrease with increasing NCE, this happens in sequence with the $C4mim_6Cl_5^+$ aggregate reaching a

maximum value at 45 % and the $C4mim_5Cl_4^+$ aggregate having its maximum value at 60%. Meanwhile $C4mim_4Cl_3^+$ plateaus above 80 % NCE and $C4mim_3Cl_2^+$ reaches its maximum ion intensity at 100 % NCE. The $C4mim_5Cl_4^+$ aggregate continues to exhibit magic number like characteristics by displaying an obvious prominence over a wide range of NCE especially between 45 % and 85 %.

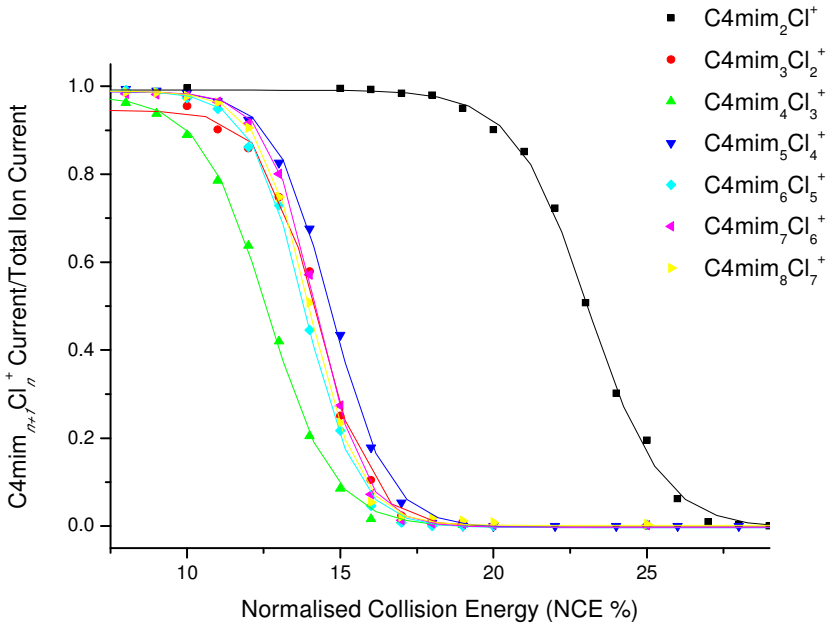

Figure 4-24 $C4mim_{n+1}Cl_n^+$ Ion Current/Total Ion Current for the collisional activation of $C4mim_{n+1}Cl_n^+$ for *n* = 1 to 7 with varying NCE. Breakdown of the parent ions only are displayed.

Expanded sections of the individual breakdown curves for the seven parent ions are plotted together in Figure 4-24. These series are fitted with the Boltzmann function and the resulting curves are a comparison of the parent ions shown between Figure 4-19 and Figure 4-23. By comparison of the NCE required for fragmentation (using the CCE of each one) information can be gathered about the relative stabilities of the different species.

From the examples in Figure 4-24 it can be clearly seen that the $C4mim_2Cl^+$ aggregate (black) is significantly more stable than the other aggregates. However, the comparative instability of the $C4mim_4Cl_3^+$ aggregate (green) can also be

distinguished. The remaining aggregates are similar in level of NCE to induce fragmentation and are difficult to distinguish by eye.

As discussed previously, the CCE will be used for comparison of the different ions. This is given by the X_c component in Equation 4-1 for sigmoidal fits to the NCE breakdown curves. Three repeats of the above analysis were performed for the aggregates $C4mim_{n+1}Cl_n^+$ for n = 1 to 7 allowing for average CCE values to be calculated along with associated standard deviations for the datasets. These calculated CCE values are displayed in Figure 4-25.

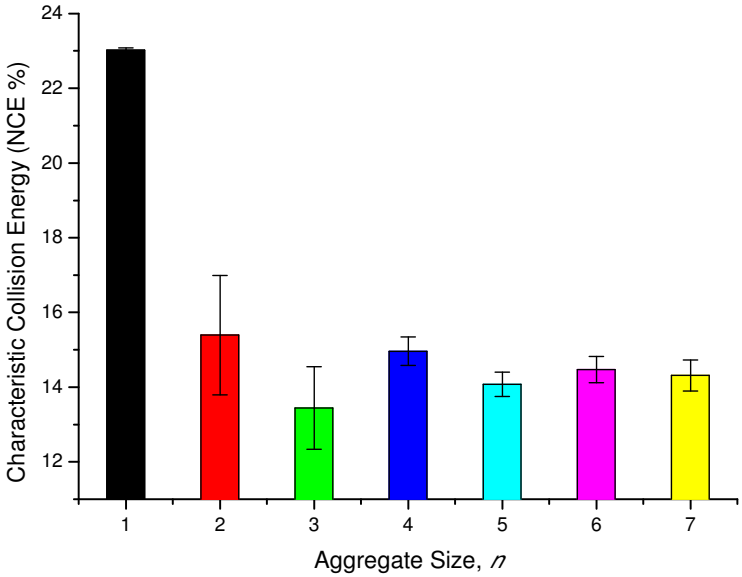

Figure 4-25 The CCE values of the parent ion breakdown curves plotted against the aggregate size of $C4mim_{n+1}Cl_n^+$ for n = 1 to 7.

Figure 4-25 shows that, as inferred from Figure 4-24, the $C4mim_2Cl^+$ aggregate is significantly more stable than the remainder of the series. This observation corresponds well with the apparent propensities for formation previously observed. A consequence of these apparent propensities for formation can be observed in the standard deviations plotted in Figure 4-25. The n = 1 aggregate consistently exhibited a favourable formation which resulted in a very high signal-to-noise ratio and low error in the calculated CCE values. Large errors are present for n = 2 and 3, these aggregates were formed very poorly and had a comparatively low signal-to-noise ratio.

Further to the numerous previous observations, the $n = 4$ aggregate exhibits a resistance to fragmentation in comparison to its neighbouring species. This aggregate has consistently displayed a special stability and many magic number characteristics. The CID results displayed in Figure 4-25 show that the instability of the $n = 3$ aggregate compared with the $n = 4$ aggregate may well indicate that a sequential growth process is difficult and the comparatively stable $n = 4$ aggregate plays an important role in the formation of larger structures.

4.2 Computational Chemistry

The different conformations which can be adopted by a C4mimCl ion pair was investigated in the gas phase by Hunt *et al.* as discussed in Section 1.4.[23] Briefly they found that the ion pair could adopt seven different stable structures; for simplicity the computational chemistry results presented here will use a similar labelling system. The imidazolium ring of the $C4mim^+$ cation is used as a reference and the different conformations are named based on the chlorine position relative to this ring. Figure 4-26 shows representations of the stable structures which were previously published.

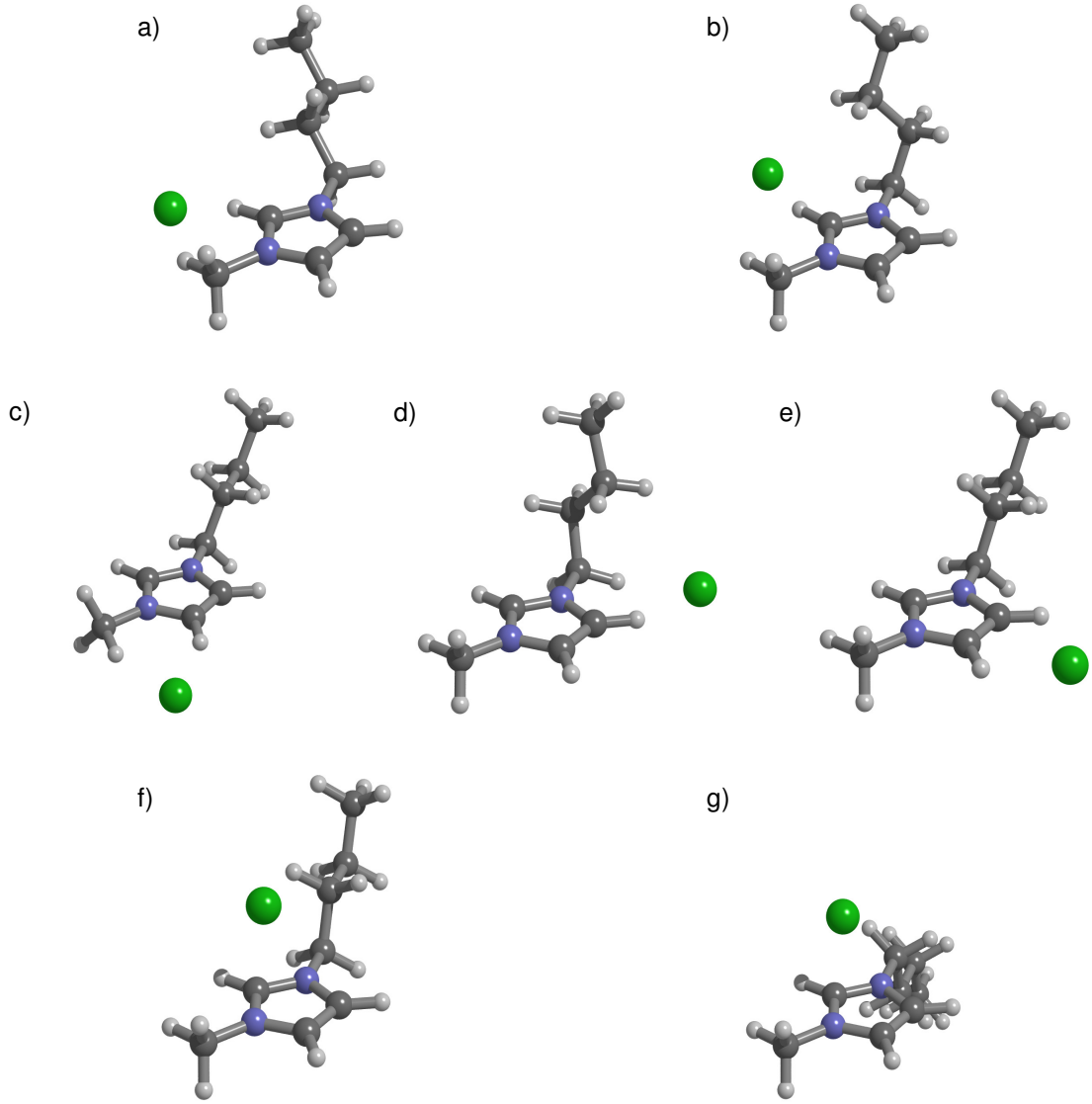

Figure 4-26 Reproduced stable conformations of the C4mimCl ion pair in the gas phase.

The naming of these structures labels the unsaturated C-N-C region of the imidazolium ring as the front of the ring and the C=C region as the back. Figure 4-26(a) to (e) have the chlorine anion lying in the same plane as the imidazolium ring. Conformation (a) has the chlorine anion close to the front of the imidazolium ring and towards the methyl group rather that the butyl chain. As a result of this,

conformation (a) is referred to as the “front methyl” position or simply “FrM”. In a similar fashion, conformation (b) becomes “front butyl” or “FrB”.

The regions of the imidazolium ring which connect the front to the back are labelled as sides. This sees conformation (c) become the “methyl side” or “MeS” conformation and conformation (d) become the “butyl side” or “BuS” conformation. The final conformation with the chlorine anion in the plane sees it close to the back region and conformation (e) is the “back” conformation.

The remaining two conformations have the chlorine anion out of plane and placed above or below the ring. The top and bottom of the ring is defined by the position of the butyl chain which is commonly out of the ring plane. Conformation (f) shows the “top” conformation with the chlorine anion above the ring and on the same side as the butyl chain. The “bottom” conformation is shown in Figure 4-26(g) and is similar to conformation (f) however the chlorine anion is on the opposite side of the imidazolium ring. The two front positions were found to be the lowest energy conformations. The next lowest were the side positions which were found to be about 30 $kJmol^{-1}$ higher in energy followed by the back position which was a further 30 $kJmol^{-1}$ higher than the side positions.

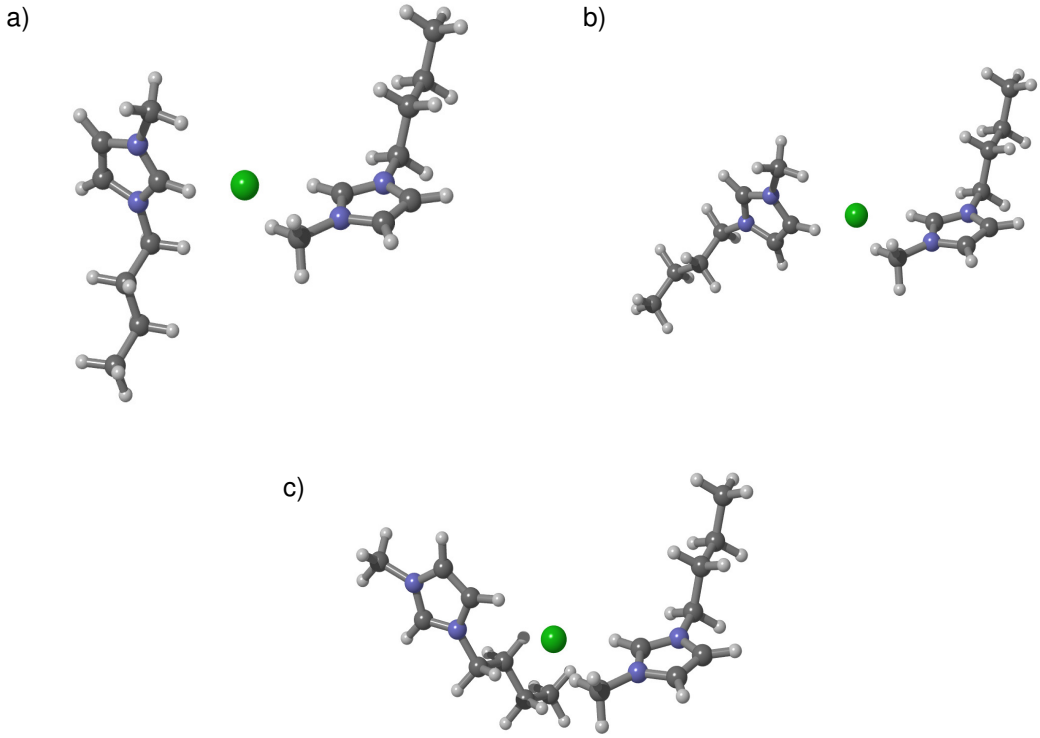

Figure 4-27 Three of the stable calculated conformations of $C4mim_2Cl^+$ a) FrM-FrM b) FrM-MeS and c) FrM-BuS.

Figure 4-27 shows three of the stable conformations for $C4mim_2Cl^+$ which were determined using the Gaussian 03 suite of programs.[24] These calculations were performed using the B3LYP hybrid DFT method and the 6-311+G(d,p) basis set. The density-based SCF convergence criterion was set to 10^{-9} Hartrees and an "ultrafine" integration grid was employed to increase the density of Gaussian calculation points. All of the results displayed have been fully optimised and confirmation of their minimum energy status was confirmed by frequency analysis.

These aggregates have been labelled according to the conformation each of the cations adopts with the chlorine anion which is positioned between them. For simplicity during comparison, the cation which adopts the lowest energy conformation will be given a higher priority compared with the higher energy

conformations. The priority order which was used was as follows: FrM > FrB > MeS > BuS > Back.

The addition of a second C4mim$^+$ cation to the stable ion results in conformations which have the two cations positioned either side of the anion as would be readily predicted. Figure 4-27(a) shows the most stable conformation where two of the favoured FrM conformations are formed to make the aggregate. The two imidazolium rings are twisted to have a torsional angle between them of roughly 90 ° and the butyl chains are separated as much as possible which results in limited steric strain on the aggregate. For the conformation shown in Figure 4-27(b) the first cation remains in the FrM conformation however the second cation has now adopted a MeS conformation as was seen previously in Figure 4-26(c). In a similar fashion the conformation shown in Figure 4-27(c) has one FrM and one BuS conformation present. The latter pair of structures are less stable than the FrM-FrM aggregate due to the relative instability of the side positions.

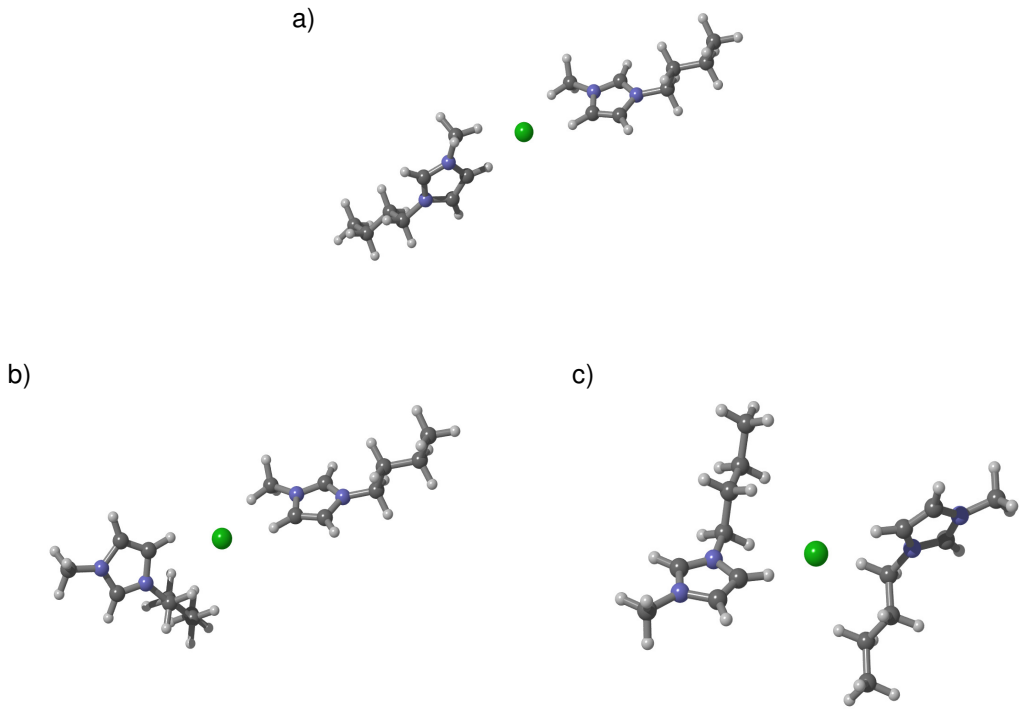

Figure 4-28 A further three of the stable calculated conformations of C4mim$_2$Cl$^+$ a) MeS-MeS b) MeS-BuS and c) BuS-BuS.

There were a total of six different conformations which were found using this level of computational theory and the remaining three are displayed in Figure 4-28. These three conformations show cations which are exclusively interacting with the chlorine anion in one of the two available side conformations. These structures are very similar in energy, however they are observed to be less stable than the examples previously shown. The minimisation of the overall energy of these structures was ensured by reduction of the steric hindrance and certified by the computation of numerous different possible conformations.

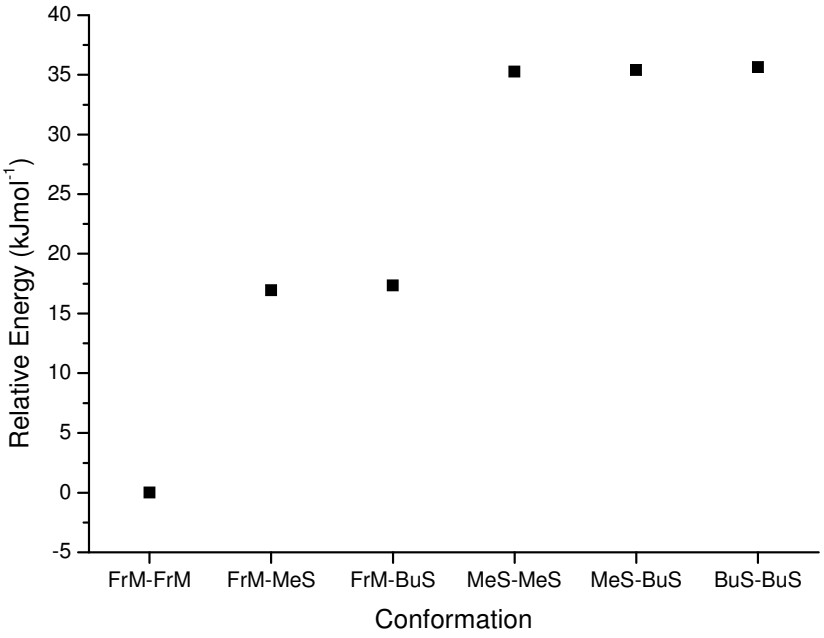

Figure 4-29 The calculated relative energy of the $C4mim_2Cl^+$ conformations which are displayed in Figure 4-27 and Figure 4-28.

The overall energy of the structures is computed automatically during the Gaussian calculation which allows for direct comparison between the different isometric forms of the aggregates. The relative energy is the calculated difference relative to the most stable conformation and the results for the six calculated conformations can be seen in Figure 4-29.

Figure 4-29 shows that the presence of the stable FrM conformation reduces the overall energy indicating a greater stability of the aggregate. The change from two

FrM cations to only one FrM and one side cation has an energy penalty of approximately 16 to 18 $kJmol^{-1}$. A similar change in the ion pair resulted in a 30 $kJmol^{-1}$ jump which is almost twice as large. This indicates that the binding of a second cation to a single ion results in a significantly weaker interaction than was observed in the case of the ion pair.

The energy penalty associated with having both cations in side positions is about 35 $kJmol^{-1}$. This figure is twice as large as the penalty for only having one cation in such a position. This suggests that the penalties for making such a change may be additive allowing estimates to be made for similar structures without the need for exhaustive calculation.

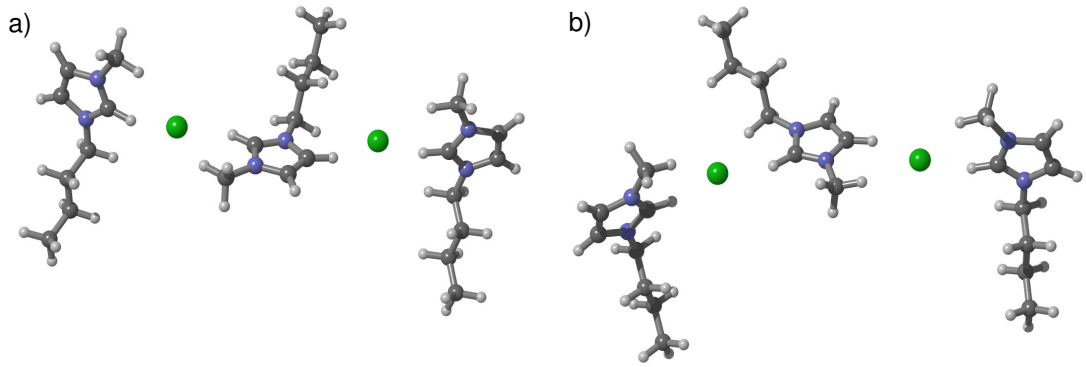

Figure 4-30 The two stable calculated conformations of $C4mim_3Cl_2^+$ a) FrM-BuS and b) FrB-MeS.

Addition of a further C4mimCl ion pair to the above $C4mim_2Cl^+$ aggregate is displayed in Figure 4-30. In this case chain like structures have been assembled with the outer $C4mim^+$ cations taking the FrM conformation which has been shown to be lowest in energy. As a result, the only two conformations which were found to be stable are remarkably similar, indeed only a rotation of the central $C4mim^+$ cation has been made.

Figure 4-30(a) shows a conformation with the central cation adopting a FrM and a BuS conformation while Figure 4-30(b) shows a structure with where FrB and MeS conformations are taken by the central cation. Stable structures were not found for

the cases where the chlorine anions were either both on the methyl or butyl side or where one was in the back position.

Table 4-3 Calculated relative energy of the $C4mim_3Cl_2^+$ conformations displayed in Figure 4-30.

First conformation at central $C4mim^+$	Second conformation at central $C4mim^+$	Relative Energy ($kJmol^{-1}$)
FrM	BuS	0.00
FrB	MeS	1.76

The relative energies of the two different conformations are shown in Table 4-3. The different structures were found to be only 1.76 $kJmol^{-1}$ apart in energy. This is unsurprising due to the similar nature of the conformations however the slight difference does favour the structure with the consistently observed FrM conformations rather than the FrB.

These calculations were becoming increasingly computationally expensive to perform, for example the frequency analysis alone had cpu job times of approximately eleven days. In order to make comparisons with the MS results it was favourable to increase the size of the aggregates by at least one or two further ion pairs. The computational cost of performing such a change would have made calculation prohibitively expensive and as such a reduction in the basis set was performed.

The CEP-31G* pseudopotentials (PP) were selected for use. These PPs are highly compact and allowed for calculations involving much larger numbers of atoms to be performed without such a prohibitive computational cost. As the diffusion functions were removed the ultrafine integration was relaxed, however, the density-based SCF convergence criterion remained set to 10^{-9} Hartrees. In order to ensure a continued accuracy of the calculations it was necessary to repeat the previous calculations and check the consistency between the different basis sets before further calculation was

performed on the larger aggregates. The distances between the H atoms on the cations and the Cl^- anion with which they were interacting was monitored along with the differences in relative energy.

Table 4-4 Comparison of the H to Cl distances in the $C4mim_2Cl^+$ aggregates calculated using both the 6-311+G(d,p) and the CEP-31G* basis set.

Cation 1 Conf.	Cation 2 Conf.	H Position	Cation 1 Distances (Å)		Cation 2 Distances (Å)	
			6-311+	CEP-31	6-311+	CEP-31
FrM	FrM	Ring	2.23	2.21	2.23	2.21
		Chain	2.70	2.70	2.70	2.70
FrM	MeS	Ring	2.20	2.19	2.37	2.36
		Chain	2.69	2.69	2.51	2.52
FrM	BuS	Ring	2.20	2.19	2.37	2.35
		Chain	2.69	2.69	2.66	2.67
MeS	MeS	Ring	2.34	2.33	2.34	2.33
		Chain	2.49	2.49	2.49	2.49
MeS	BuS	Ring	2.35	2.33	2.35	2.34
		Chain	2.49	2.49	2.64	2.66
BuS	BuS	Ring	2.35	2.34	2.35	2.34
		Chain	2.64	2.65	2.64	2.65

Table 4-4 shows the H to Cl distances for the $C4mim_2Cl^+$ aggregates with both the original basis set (6-311+G(d,p)) and the PP basis set (CEP-31G*). The calculated distances are remarkably similar using both basis sets with the largest difference observed for the Cl to butyl chain bound H in cation 2 of the MeS-BuS

conformation. This difference was 0.021 Å aggregates with the average difference less than 0.1 Å at 0.09(5) Å.

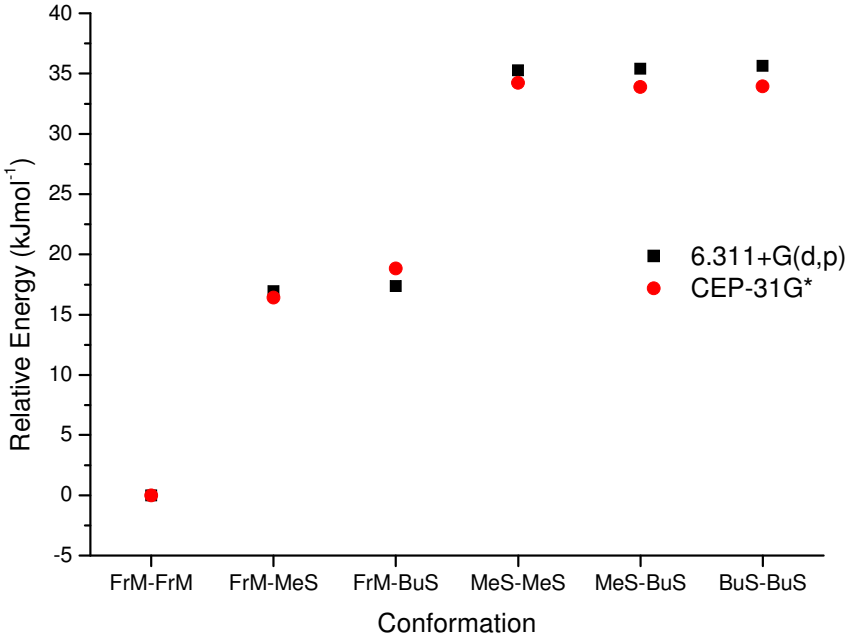

Figure 4-31 Comparison of the relative energy differences in the $C4mim_2Cl^+$ aggregates calculated using both the 6-311+G(d,p) (black) and the CEP-31G* (red) basis set.

The calculated relative energies for the series of $C4mim_2Cl^+$ aggregates with both the original basis set (6-311+G(d,p)) and the PP (CEP-31G*) are shown in Figure 4-31. From this table very similar trends can be observed with each basis set. Energy penalties of 16 to 19 $kJmol^{-1}$ are present for moving cation 2 from a front to a side position. Additionally, very similar penalties are present to change both cations to side positions; both basis sets give relative energies 34 to 35 $kJmol^{-1}$ higher.

Table 4-5 Comparison of the H to Cl distances in the $C4mim_3Cl_2^+$ aggregates calculated using both the 6-311+G(d,p) and the CEP-31G* basis set.

$C4mim^+$	H Position	H to Cl Distances (Å)			
		FrM-BuS		FrB-MeS	
		6.311+G(d,p)	CEP-31G*	6.311+G(d,p)	CEP-31G*
Central	Fr Ring	2.33	2.33	2.33	2.33
Central	Fr Chain	2.66	2.66	2.71	2.72
Central	Side Ring	2.45	2.44	2.45	2.44
Central	Side Chain	2.76	2.76	2.59	2.59
Outer 1	Ring	2.18	2.16	2.18	2.16
Outer 1	Chain	2.67	2.67	2.67	2.67
Outer 2	Ring	2.16	2.14	2.16	2.14
Outer 2	Chain	2.67	2.67	2.66	2.66

Comparison of the $C4mim_3Cl_2^+$ aggregates was also performed in order to further verify the suitability of the CEP-31G* PP for these aggregates. Table 4-5 compares the various Cl to H distances present in the aggregates. A strong similarity is revealed between the different basis sets. Indeed the largest observed difference was a modest 0.018 Å which was between the Cl to Ring bound H on the second outer $C4mim^+$ of the FrM-BuS conformation. The average difference was 0.007(6) Å in total over all of the different distances, the relatively large error shows that there is a high degree of randomness in the changes thus it is unlikely that there are any systematic errors.

Table 4-6 Comparison of the relative energy differences in the $C4mim_3Cl_2^+$ aggregates calculated using both the 6-311+G(d,p) and the CEP-31G* basis set.

First conformation at central $C4mim^+$	Second conformation at central $C4mim^+$	Relative Energy ($kJmol^{-1}$)	
		6.311+G(d,p)	CEP-31G*
FrM	BuS	0.00	0.00
FrB	MeS	1.76	2.01

Table 4-6 shows a comparison of the calculated relative energies of the $C4mim_3Cl_2^+$ aggregates using both of the basis sets. While the range of values is small, when compared with the magnitude of differences for the $C4mim_2Cl^+$ aggregates the differences between these relative energies is very small. Taking all of these comparisons into consideration the differences between the various calculations were small and the series of aggregates were extended with the CEP-31G* pseudo potentials.

Using the CEP-31G* basis set allowed for the series of $C4mim_2Cl^+$ and $C4mim_3Cl_2^+$ aggregates to be expanded and studied more exhaustively. Stable, low energy conformations corresponding to all of the different possible combinations of FrM, FrB, MeS, BuS and Back positions were successfully calculated.

Table 4-7 The relative energy differences of the expanded series of $C4mim_2Cl^+$ aggregates calculated using the CEP-31G* basis set.

Cation 1 Conformation	Cation 2 Conformation	Relative Energy ($kJmol^{-1}$)
FrM	FrM	0.0
FrM	FrB	1.3
FrB	FrB	2.6
FrM	MeS	16.4
FrB	MeS	17.6
FrB	BuS	17.8
FrM	BuS	18.8
FrM	Back	33.2
FrB	Back	34.3
BuS	BuS	34.0
BuS	MeS	33.9
MeS	MeS	34.2
MeS	Back	52.3
BuS	Back	52.0
Back	Back	72.4

The different conformations are detailed in Table 4-7 along with the calculated relative energies compared with the FrM-FrM combination. In a similar fashion to what was previously observed in Figure 4-31, the different combinations fall into groups with similar relative energy values. Combinations of a front with a side have similar energy values, a side and a back are similar to each other and these trends run

through the whole series. The possibility of predicting unknown energy penalties would remain as each time a cation is changed front to side or side to back the energy is increased by about 16 to 18 $kJmol^{-1}$ and these values can be added together to get an estimate of the other members of the series. This is born out by the approximate degeneracy between the aggregates with a front and a back cation and aggregates with two side conformations.

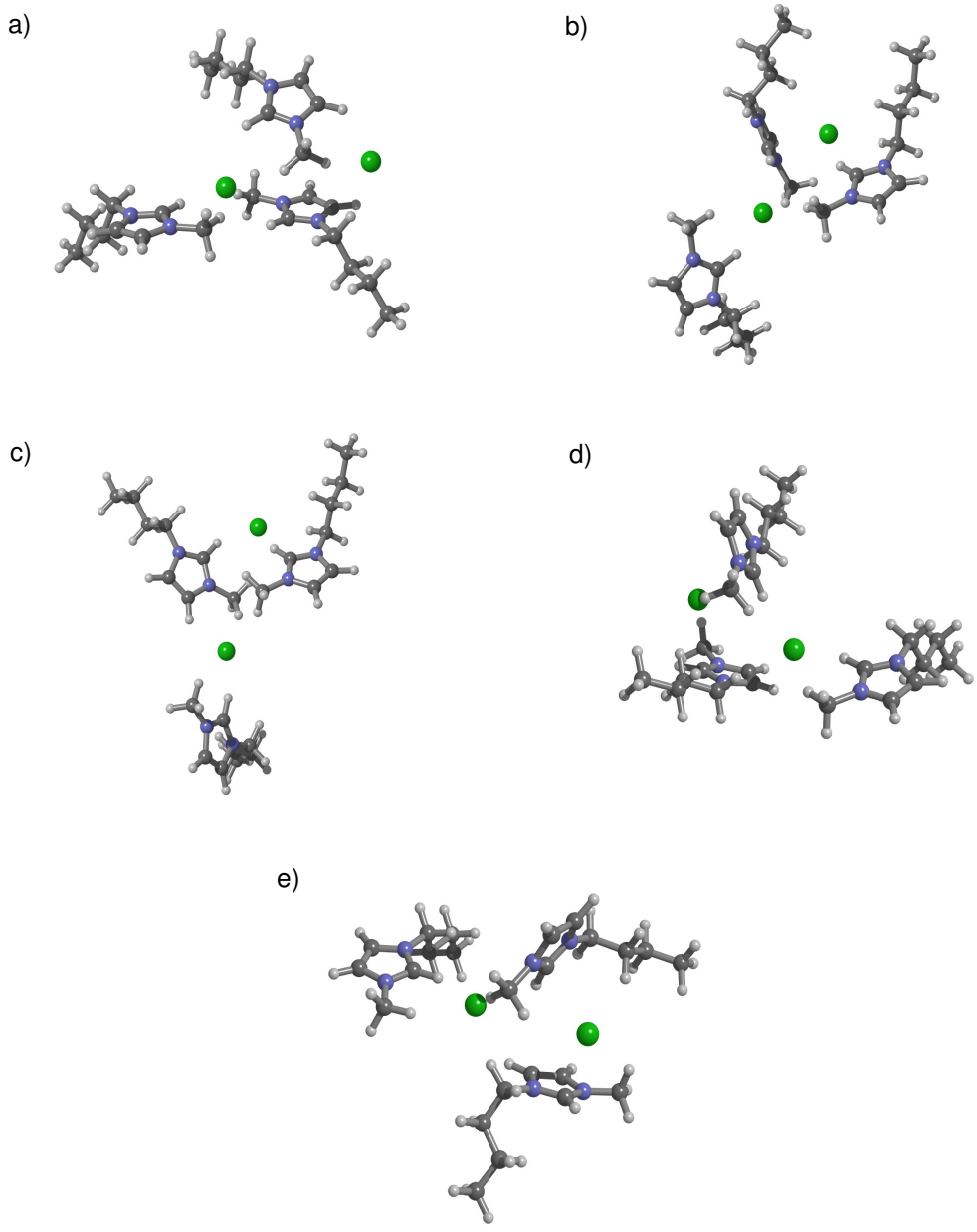

Figure 4-32 Five additional stable calculated conformations of $C4mim_3Cl_2^+$ which were calculated using the B3LYP DFT method and the CEP-31G* basis set.

The series of $C4mim_3Cl_2^+$ aggregates was also expanded using the CEP-31G* basis set. In addition to the two conformations which were previously shown, five further structures were found. Unlike the previous examples these were all non-linear and can be seen in Figure 4-32. These conformations include structural features such as the top conformation (b, d and e) and the binding of the front region of a $C4mim^+$ to multiple chlorine anions (b and c). While all of these structures were stabilised in the gas-phase calculations, it was observed that there was an energy penalty associated with them compared to the structure shown in Figure 4-30(a). All of these structures display cases where a single anion is surrounded by three different cations. Supramolecular aggregates of ILs have shown these motifs, where extended networks of hydrogen bonds form with one cation surrounded by three anions or vice versa, it is very promising that such features have been observed in such small aggregates.[2,25]

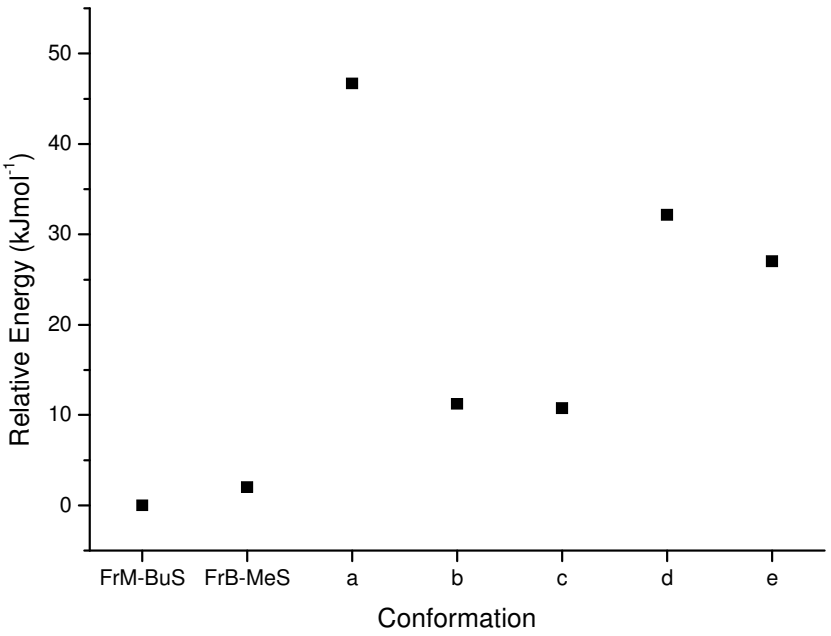

Figure 4-33 The relative energy differences of the expanded series of $C4mim_3Cl_2^+$ aggregates calculated using the CEP-31G* basis set.

The relative energies of the different $C4mim_3Cl_2^+$ aggregates are shown in Figure 4-33. The two linear examples (FrM-BuS and FrB-MeS) are the most stable examples with the remaining ones higher in energy. The structures (b) and (c) were

found to be lowest in energy amongst the non-linear conformations. These structures are the best examples of spatial separation while sharing the anions between as many of the cations as possible.

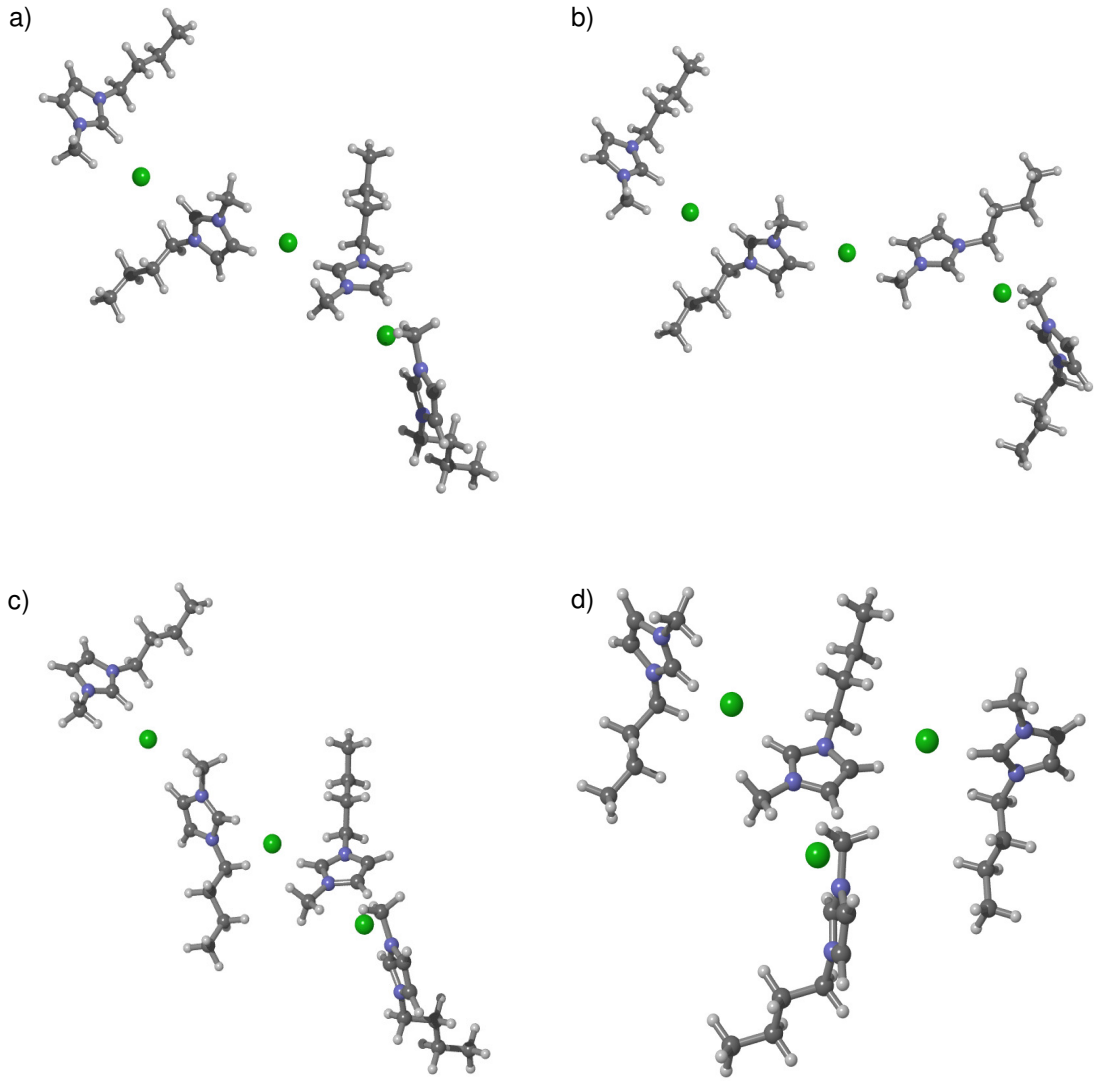

Figure 4-34 Calculated stable structures of the $C4mim_4Cl_3^+$ aggregate.

An additional ion pair was added to the previous $C4mim_3Cl_2^+$ aggregate to find minimum energy structures for $C4mim_4Cl_3^+$ in the gas phase. Four stable structures were determined for this aggregate and they are displayed in Figure 4-34. The structures all display the most favoured FrM conformation for the outermost cations while the inner cations are all set to the FrB-MeS conformation to allow for more direct comparison. Structures (a), (b) and (c) are linear extensions based on the

previously determined linear structures of $C4mim_3Cl_2^+$. Taking the central anion as a reference point, structure (a) has one $C4mim^+$ associated in a front conformation and one in a side conformation. Structure (b) has two side conformations and structure (c) has two front conformations. Structure (d) appears very different to the other ones because there are now three anions bound to the central cation with the remaining cations bound on the outside of the anions. As mentioned above this structural motif where cations are surrounded by three anions is also observed in the published literature structures where it has been observed with X-ray diffraction, solution 1H NMR spectroscopy, conductivity, microcalorimetry and MS so it is encouraging that it can be stabilised in the gas phase calculations of the smallest suitable $C4mim_{n+1}Cl_n^+$ aggregate.[2,25]

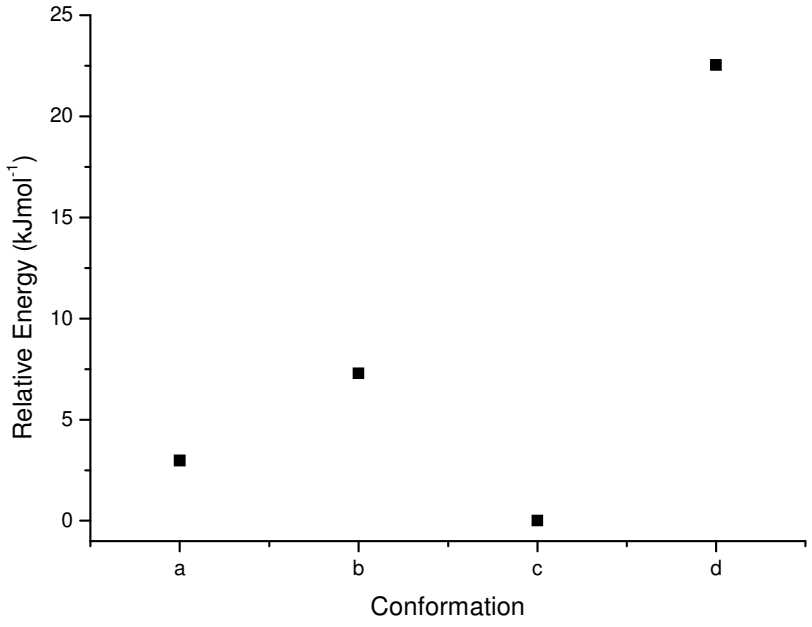

Figure 4-35 Relative energies for the calculated conformations of the $C4mim_4Cl_3^+$ aggregate.

Figure 4-35 shows the calculated relative energies for the different conformations of the $C4mim_4Cl_3^+$ aggregate which were shown in Figure 4-34. It reveals that the most stable conformation is structure (c) which had the central chlorine anion associated with two front facing cations. An energy increase of 3.0 $kJmol^{-1}$ was observed to structure (a) where one of the cations is in the side conformation and a further

increase of 4.3 kJmol^{-1} for structure (b) where both cations now adopt side conformations. Structure (d) where a central cation is surrounded by three cations is 22.5 kJmol^{-1} higher in energy.

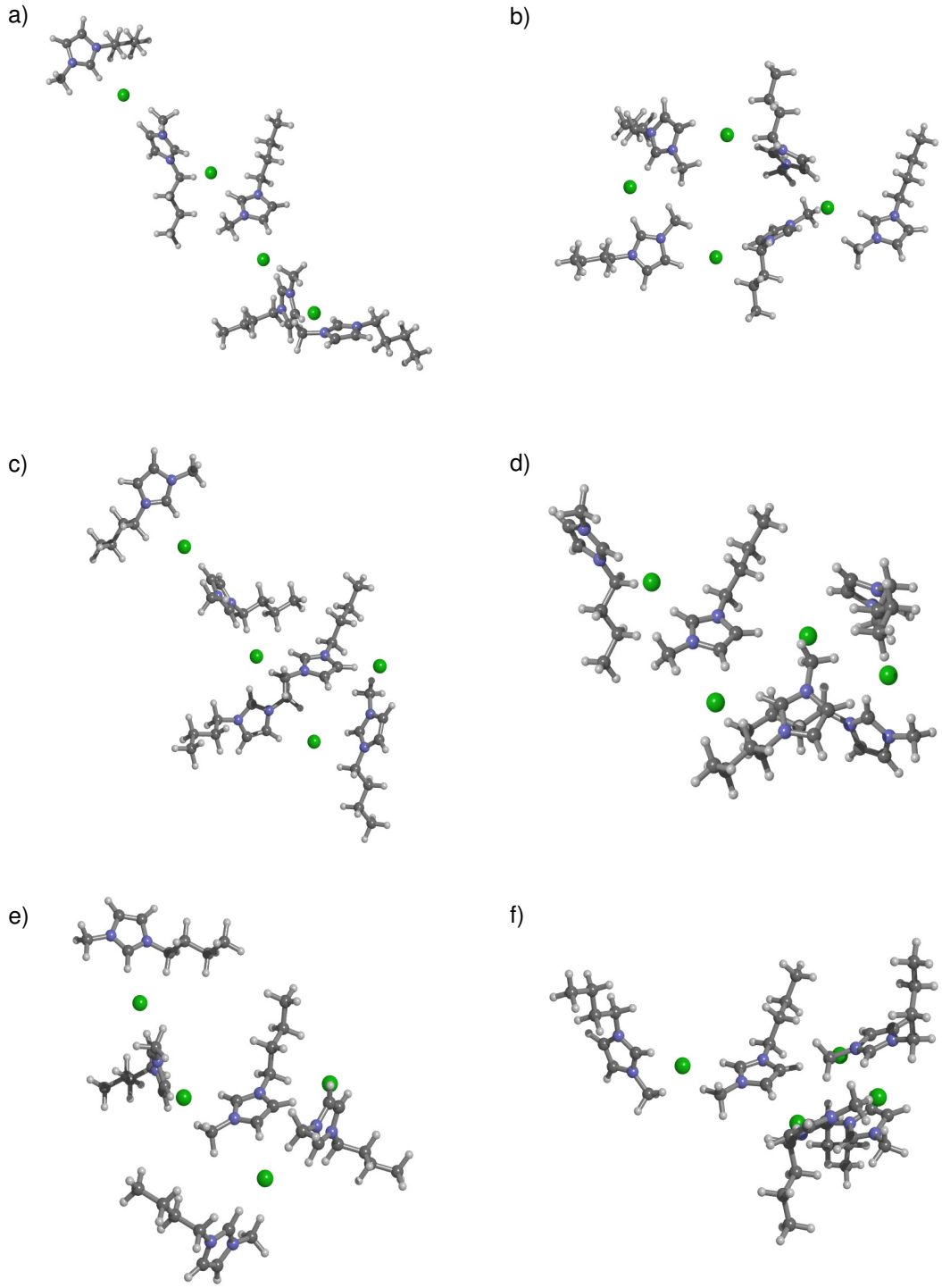

Figure 4-36 Calculated stable structures of the C4mim$_5$Cl$_4^+$ aggregate.

Minimum energy structures for the aggregate $C4mim_5Cl_4^+$ were calculated as above. The calculated minimum energy structures for this aggregate are displayed in Figure 4-36. Conformation (a) is an example of a linear structure where the ions are bound to a maximum of two counter ions. The remaining structures are more complicated in nature and show multiple different binding patterns.

In structure (b) the chlorine anions have formed a ring joined together by four of the cations with the final cation perched on the outside of the anions. Structures (c) and (d) have regions where three of the anions form a triangle with three of the cations making multiple interactions with them. These interactions vary in number and orientation but the most complex of the structures is (d) where two of the cations interact with all three of the anions. Structures (e) and (f) are similar however structure (f) appears to show the presence of pi-stacking between two of the imidazolium rings with three chlorine anions arranged around the stacked configuration.

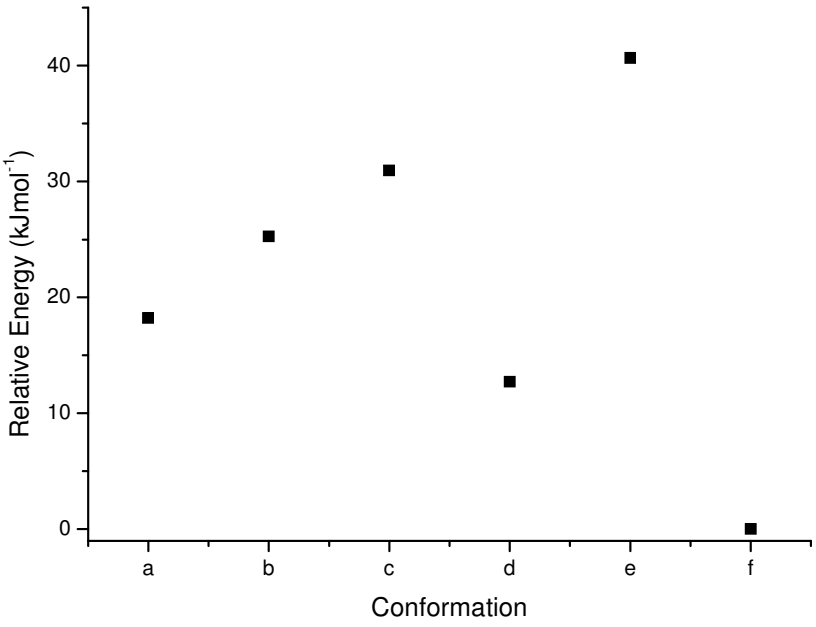

Figure 4-37 Relative energies for the calculated conformations of the $C4mim_5Cl_4^+$ aggregate.

The relative energies of the $C4mim_5Cl_4^+$ aggregates are shown in Figure 4-37 relative to the most stable structure, structure (f). Structure (f) is a non-linear

conformation and as such this is a significant change from the smaller aggregates where the linear structures were the most stable. This difference may indicate that the aggregates are large enough at this stage for a change in the driving forces for aggregate formation in the gas phase.

The second most stable structure was (d) with an energy increase of 12.7 $kJmol^{-1}$. Similar to structure (f), the interactions present are significantly more numerous and complex than the linear examples. This further suggests that as the size of aggregate increases there is a rise in the importance of these second and third interactions with oppositely charged ions. Indeed the linear structure (a) was found to be 18.2 $kJmol^{-1}$ less stable than structure (f).

By considering the most stable conformation for each $C4mim_{n+1}Cl_n^+$ aggregate for n = 0 to 4 and the most stable calculated ion pair conformation (FrM) the binding energies between each step were calculated. Binding energies are calculated by considering the energies of the reactant and product species and deducing the difference for the reaction. The magnitude of the energy gain is not constant and as such the incremental binding energies for each step were found. The binding energies include an estimate of the basis set superposition error (BSSE). The counterpoise method was used to correct for the BSSE using the counterpoise keyword within the Gaussian 03 suite of programs.[24] The BSSE was calculated for geometries which were previously optimised using uncorrected potential energy surfaces.

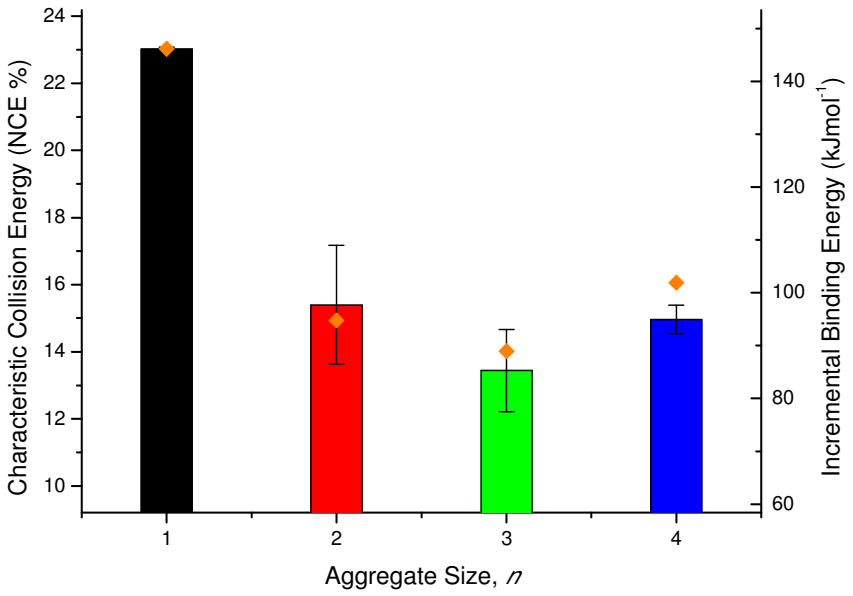

Figure 4-38 CCE (bars) plotted with the calculated incremental binding energies (orange diamonds) corresponding to the transition studied using the CID experiments. These are both plotted against the aggregate size of $C4mim_{n+1}Cl_n^+$ for n = 1 to 4.

The incremental binding energies are plotted in orange on Figure 4-38 along with some of the experimental stabilities which were previously shown in Figure 4-25. The axis limits are set to 105 % and 40 % of the value corresponding to $n = 1$ to allow for direct comparison of the series. A similarity is observed between the experimental and computational results for this series of aggregates. Both the experimental and computational results describe an increased stability of the $n = 1$ species and a minimum at $n = 3$. Additionally the magic number aggregate at $n = 4$ is shown to have a significantly increased stability using both methods.

This consistency indicates that the computational method of study produces an accurate picture of what is observed during the practical experiments. In doing so, the two branches of research should be an effective complement for each other. This will help to build a more complete picture of the gas-phase aggregation of these species. This is an encouraging link between experiment and theory and allows the project to continue with confidence using the methods as described.

4.3 References

(1) Charles, L.; Pepin, D.; Gonnet, F.; Tabet, F. C. *Journal of the American Society for Mass Spectrometry* **2001**, *12*, 1077-1084.

(2) Fernandes, A. M.; Coutinho, J. A. P.; Marrucho, I. M. *Journal of Mass Spectrometry* **2009**, *44*, 144-150.

(3) Feldheim, D. L.; Foss, C. A. *Metal nanoparticles: synthesis, characterization, and applications*; Marcel Dekker, 2002.

(4) Harbola, M. K. *Proceedings of the National Academy of Sciences of the United States of America* **1992**, *89*, 1036-1039.

(5) Hogan, C. J.; de la Mora, J. F. *Journal of the American Society for Mass Spectrometry* **2010**, *21*, 1382-1386.

(6) Deyko, A.; Lovelock, K. R. J.; Licence, P.; Jones, R. G. *Physical Chemistry Chemical Physics* **2011**, *13*, 16841-16850.

(7) Zhang, H. R.; Ding, L.; Qu, C. L.; Li, D.; Zhang, H. Q. *Spectrochimica Acta Part a-Molecular and Biomolecular Spectroscopy* **2007**, *68*, 312-316.

(8) Ho, Y. P.; Huang, P. C.; Deng, K. H. *Rapid Communications in Mass Spectrometry* **2003**, *17*, 114-121.

(9) Takats, Z.; Nanita, S. C.; Cooks, R. G.; Schlosser, G.; Vekey, K. *Analytical Chemistry* **2003**, *75*, 1514-1523.

(10) Yang, S. P.; Zhou, Y. F.; Hit, X. L.; Liang, H. Z.; Li, J. Q.; Hu, B.; Chen, H. W. *Chinese Journal of Analytical Chemistry* **2008**, *36*, 266-272.

(11) Takegawa, Y.; Deguchi, K.; Ito, S.; Yoshioka, S.; Nakagawa, H.; Nishimura, S. *Analytical Chemistry* **2005**, *77*, 2097-2106.

(12) Benijts, T.; Gunther, W.; Lambert, W.; De Leenheer, A. *Rapid Communications in Mass Spectrometry* **2003**, *17*, 1866-1872.

(13) Gardner, J. S.; Harrison, R. G.; Lamb, J. D.; Dearden, D. V. *New Journal of Chemistry* **2006**, *30*, 1276-1281.

(14) Nanita, S. C.; Sokol, E.; Cooks, R. G. *Journal of the American Society for Mass Spectrometry* **2007**, *18*, 856-868.

(15) Haddad, R.; Sparrapan, R.; Eberlin, M. N. *Rapid Communications in Mass Spectrometry* **2006**, *20*, 2901-2905.

(16) Ratcliffe, L. V.; Rutten, F. J. M.; Barrett, D. A.; Whitmore, T.; Seymour, D.; Greenwood, C.; Aranda-Gonzalvo, Y.; Robinson, S.; McCoustra, M. *Analytical Chemistry* **2007**, *79*, 6094-6101.

(17) Sobott, F.; Watt, S. J.; Smith, J.; Edelmann, M. J.; Kramer, H. B.; Kessler, B. M. *J Am Soc Mass Spectrom* **2009**, *20*, 1652-9.

(18) Canon, F.; Pate, F.; Meudec, E.; Marlin, T.; Cheynier, V.; Giuliani, A.; Sarni-Manchado, P. *Analytical and Bioanalytical Chemistry* **2009**, *395*, 2535-2545.

(19) Helenkar, A.; Sebok, A.; Zaray, G.; Molnar-Perl, I.; Vasanits-Zsigrai, A. *Talanta* **2010**, *82*, 600-607.

(20) Ohashi, K.; Inoue, K.; Iino, T.; Sasaki, J.; Judai, K.; Nishi, N.; Sekiya, H. *Journal of Molecular Liquids* **2009**, *147*, 71-76.

(21) Hao, C. Y.; March, R. E. *Journal of Mass Spectrometry* **2001**, *36*, 509-521.

(22) Fernandes, A. M.; Rocha, M. A. A.; Freire, M. G.; Marrucho, I. M.; Coutinho, J. A. P.; Santos, L. *Journal of Physical Chemistry B* **2011**, *115*, 4033-4041.

(23) Hunt, P. A.; Kirchner, B.; Welton, T. *Chemistry-a European Journal* **2006**, *12*, 6762-6775.

(24) M. J. Frisch, G. W. T., H. B. Schlegel, G. E. Scuseria, M. A. Robb, J. R. Cheeseman, J. A. Montgomery, Jr., T. Vreven, K. N. Kudin, J. C. Burant, J. M. Millam, S. S. Iyengar, J. Tomasi, V. Barone, B. Mennucci, M. Cossi, G. Scalmani, N. Rega, G. A. Petersson, H. Nakatsuji, M. Hada, M. Ehara, K. Toyota, R. Fukuda, J. Hasegawa, M. Ishida, T. Nakajima, Y. Honda, O. Kitao, H. Nakai, M. Klene, X. Li, J. E. Knox, H. P. Hratchian, J. B. Cross, V. Bakken, C. Adamo, J. Jaramillo, R. Gomperts, R. E. Stratmann, O. Yazyev, A. J. Austin, R. Cammi, C. Pomelli, J. W. Ochterski, P. Y. Ayala, K. Morokuma, G. A. Voth, P. Salvador, J. J. Dannenberg, V. G. Zakrzewski, S. Dapprich, A. D. Daniels, M. C. Strain, O. Farkas, D. K. Malick, A. D. Rabuck, K. Raghavachari, J. B. Foresman, J. V. Ortiz, Q. Cui, A. G. Baboul, S. Clifford, J. Cioslowski, B. B. Stefanov, G. Liu, A. Liashenko, P. Piskorz, I. Komaromi, R. L. Martin, D. J. Fox, T. Keith, M. A. Al-Laham, C. Y. Peng, A. Nanayakkara, M. Challacombe, P. M. W. Gill, B. Johnson, W. Chen, M. W. Wong, C. Gonzalez, and J. A. Pople, *Gaussian 03, Revision E.01, Gaussian, Inc., Wallingford CT, 2004.*

(25) Consorti, C. S.; Suarez, P. A. Z.; de Souza, R. F.; Burrow, R. A.; Farrar, D. H.; Lough, A. J.; Loh, W.; da Silva, L. H. M.; Dupont, J. *Journal of Physical Chemistry B* **2005**, *109*, 4341-4349.

Chapter 5: Mixed Metal Chloride and Ionic Liquid Aggregate Results

In Chapter 4 it was observed that the IL C4mimCl readily forms aggregates incorporating sodium or potassium ions. In order to further study the effect of such contamination, metal chloride salts were added at various concentrations and corresponding geometry optimisation calculations were performed for a number of these. The aims for this investigation included a desire to learn more about the effect of varying the concentrations of contaminant. In addition to this it was hoped that the way the contaminant will interact with the IL on a molecular level and the strength of the binding compared with both clean ILs and other contaminant species could be understood better. There are numerous literature cases where ILs have been doped in order to achieve different properties especially with the aim of catalysing different processes occurring in the liquid. These investigations should increase the understanding of how a range of secondary species interact with ILs.

Throughout this chapter the mole fraction will be used to describe the solution composition. For a mixture containing more than one constituent part, the mole fraction describes the amount of a particular component in the mixture. It is calculated as shown in Equation 5-1 where x_i is the mole fraction, n_i is the amount of the constituent under consideration and n_{total} is the total amount of all constituents in the mixture.

$$x_i = \frac{n_i}{n_{Total}} \qquad \textbf{Equation 5-1}$$

5.1 Mass Spectrometry

5.1.1 NaCl and C4mimCl

Following on from the observations in Chapter 4, varying concentrations of NaCl were doped into the solution of C4mimCl. The solvent was kept constant at a 90:10 mixture of methanol and water thereby preventing problems with solubility and

allowing closer comparison. The effect of the addition of NaCl was monitored by observing changes in relative intensity of the $C4mim_{n+1}Cl_n^+$ aggregates for n = 1 to 10 and also the relative intensities of $C4mim_nNa_mCl_{n+m-1}^+$ where n and m were greater than one. In order to control the total ion current the samples were prepared with the mole fraction varying between them, keeping the same overall ion concentration within the solutions. The solutions were all prepared with a consistent 3 mM total ion concentration which gave a stable and observable signal over a wide range of salt samples. The mole fractions are presented for C4mimCl ($x_{C4mimCl}$) which meant that the compositions of the solutions were 3x mM C4mimCl + 3(1-x) mM NaCl in the 9:1 methanol and water mixture. Each individual composition was scanned for a total of 250 scans which were summed to produce the resulting spectra. This allowed for a reasonable signal-to-noise ratio to be gained while keeping the instrumental tuning parameters constant.

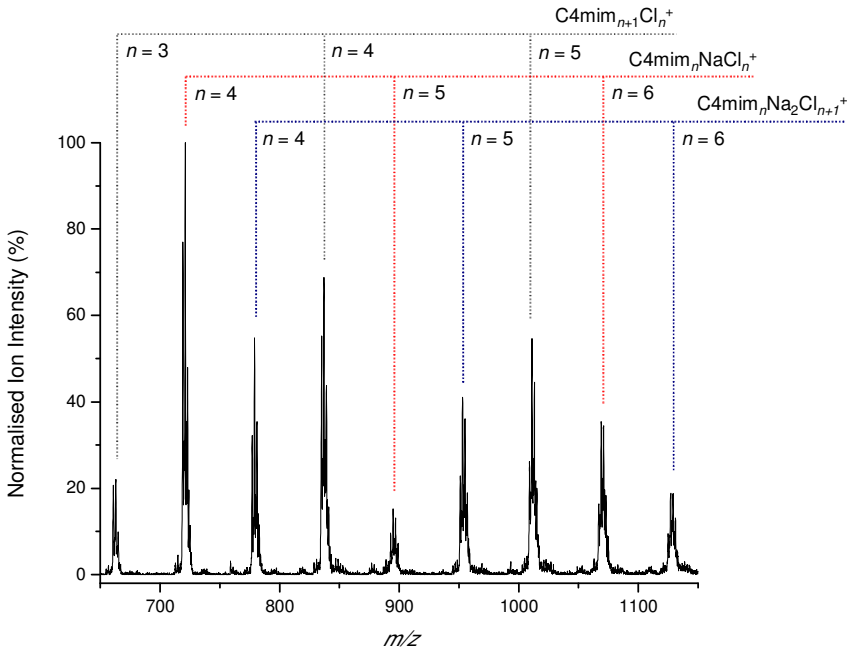

Figure 5-1 Mass spectrum of 2.70 mM C4mimCl and 0.30 mM NaCl in a 9:1 MeOH:H_2O solution. The aggregates $C4mim_{n+1}Cl_n^+$ (grey), $C4mim_nNaCl_n^+$ (red) and $C4mim_nNa_2Cl_{n+1}^+$ (blue) are highlighted.

A solution where 10 % of the total ion concentration was NaCl with the remaining 90 % C4mimCl was prepared; a section of the resulting mass spectrum is given in

Figure 5-1. This spectrum shows the presence of a number of different aggregates. The series $C4mim_{n+1}Cl_n^+$ is displayed for n = 3 to 5 while the series $C4mim_nNaCl_n^+$ and $C4mim_nCl_{n+1}Na_2^+$ are highlighted for n = 4 to 6. The relative intensities of the peaks are remarkably different to what was observed for the IL samples without the addition of NaCl. The aggregates which contain one and two sodium ions are significantly larger showing that the addition of NaCl to the solution has resulted in the increased formation of the mixed aggregates. It was previously seen that the IL peaks were many times the intensity of the sodium adduct peaks with the doubly sodiated aggregates barely observable. However, with only 10 % of the total ion composition altered the sodium-containing species are at least as intense as the IL species and often more so.

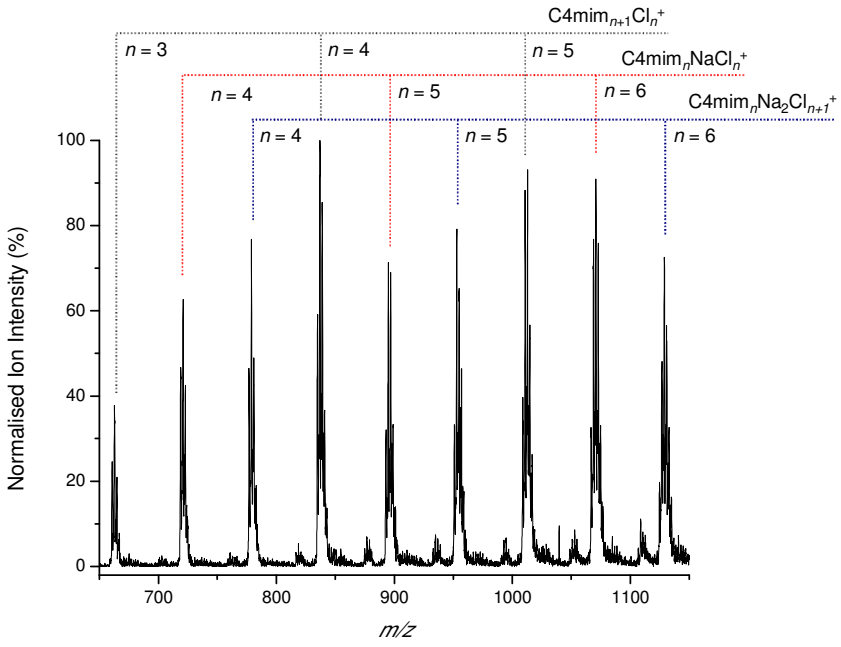

Figure 5-2 Mass spectrum of 1.95 mM C4mimCl and 1.05 mM NaCl in a 9:1 MeOH:H_2O solution. The aggregates $C4mim_{n+1}Cl_n^+$ (grey), $C4mim_nNaCl_n^+$ (red) and $C4mim_nNa_2Cl_{n+1}^+$ (blue) are highlighted.

An increase from 10 % of the total ion concentration to 35 % of NaCl resulted in the production of Figure 5-2. This spectrum shows the surprising increase in the intensity of the $C4mim_{n+1}Cl_n^+$ aggregate series. This occurrence is due to the overlap of different aggregates. The molecular weight of NaCl is 58.44 which results in a

molecular weight of 175.32 for Na_3Cl_3. Meanwhile C4mimCl has a molecular weight of 174.67. While they are not exactly the same, given the low resolution obtained with the LCQ instrument it is not possible to uniquely distinguish between such similar species. This results in the loss of distinct peaks for each species with the recorded signals coming from multiple different ions. For Figure 5-2 this means that in particular the peaks which are labelled $C4mim_{n+1}Cl_n^+$ and $C4mim_nNaCl_n^+$ will likely have significant contributions from aggregates containing three and four sodium ions respectively. However, a clear progression from the IL dominated aggregates to ones with an increasingly large amount of Na incorporated is observed as the mole fraction of the IL is reduced.

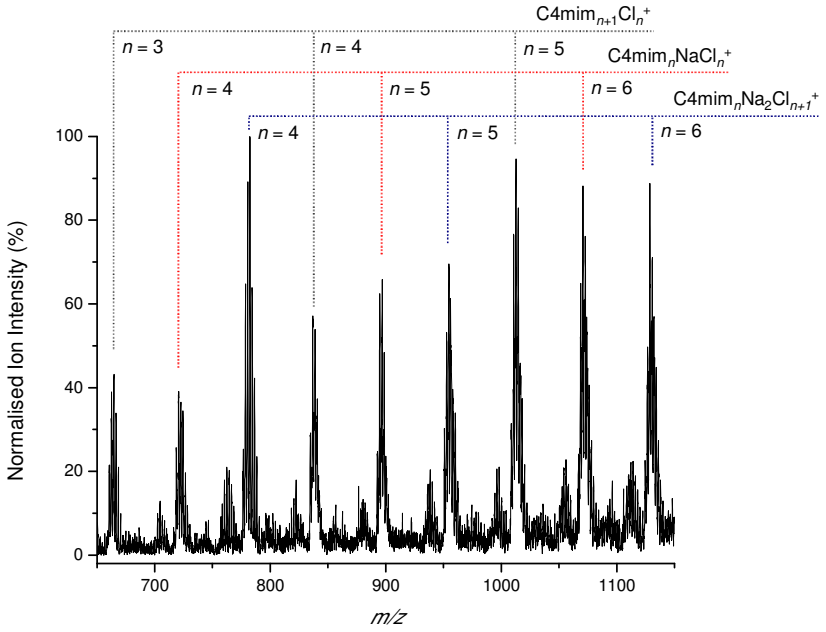

Figure 5-3 Mass spectrum of 1.05 mM C4mimCl and 1.95 mM NaCl in a 9:1 MeOH:H_2O solution. The aggregates $C4mim_{n+1}Cl_n^+$ (grey), $C4mim_nNaCl_n^+$ (red) and $C4mim_nNa_2Cl_{n+1}^+$ (blue) are highlighted.

The concentration of NaCl was increased further at the expense of the IL. When the NaCl made up 65 % of the total ion composition the mass spectrum shown in Figure 5-3 was produced. At this point the many different species are producing overlapping peaks; the highlighted series will have their intensity highly distorted. The peak width at each of these markers has increased from what can be seen in the earlier spectra. The width of the overall isotopic distribution is driven by the ^{35}Cl and ^{37}Cl

isotopes which exist in a 3:1 ratio. As the aggregates become increasingly sodium rich there is a corresponding increase in the quantity of chlorine incorporated. A significant increase in sodium incorporation would increase the number of chlorine anions which in turn would be expected to spread the intensity producing wider signals in the mass spectrum.

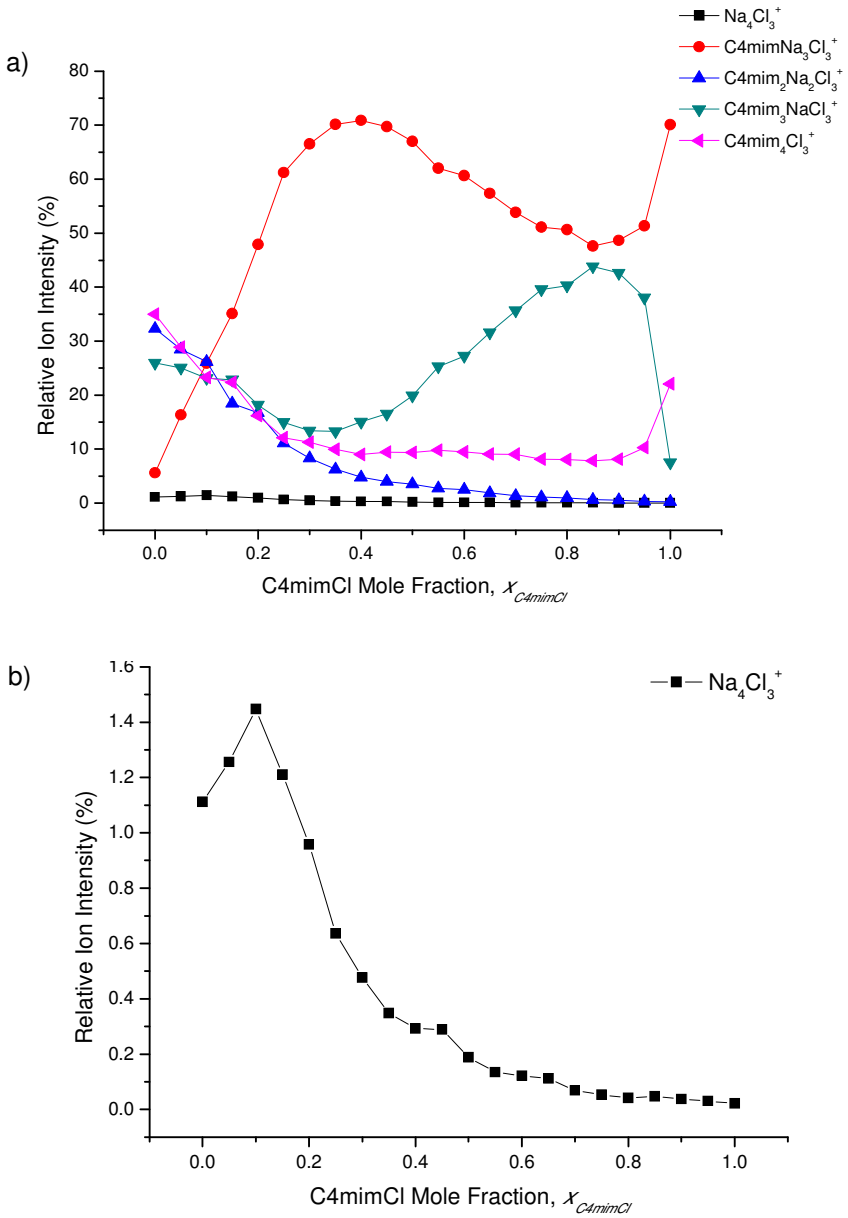

Figure 5-4 Relative ion intensity as the C4mimCl mole fraction is varied from zero to one in mixtures with NaCl. Intensities are shown for a) all of the aggregates $C_4Cl_3^+$ where C is $C4mim^+$ or Na^+ b) $Na_4Cl_3^+$ only.

The experiments were repeated at 5 % NaCl intervals to produce a series of C4mimCl mole fraction results from zero to one. Due to the overlapping peaks it was difficult to track the changes as the mole fractions were varied. This was attempted for a series of the smaller aggregates where it was hoped that there would be less interference. The series of aggregates $C_4Cl_3^+$ was used, where C represented the cation which would be either $C4mim^+$ or Na^+. The individual peaks in each of the spectra were integrated to give the peak areas of each of the five possible aggregates. For each spectrum, these values were summed and peak areas calculated relative to each other. The result of this calculation can be seen in Figure 5-4. Figure 5-4(a) shows all of the different aggregates at the same time while Figure 5-4(b) is an expansion of the lowest intensity aggregate ($Na_4Cl_3^+$).

When $x_{C4mimCl} = 1$, the $C4mim_4Cl_3^+$ aggregate was at a maximum value which initially reduces as the NaCl concentration increases. This reduction continues until the amount of NaCl had increased to 10 % at which point the relative intensity of the $C4mim_4Cl_3^+$ aggregate reached a plateau before increasing as $x_{C4mimCl}$ approached zero. This was likely due to the presence of overlapping species and the increase in Figure 5-4 is due to the increased presence of high sodium aggregates for example $Na_{12}Cl_{11}^+$. The species labelled as the single sodium aggregate ($C4mim_3NaCl_3^+$) initially increases in intensity as sodium is added to the solution with a maximum intensity at $x_{C4mimCl} = 0.9$. The relative intensity then decreases as aggregates with higher sodium concentration are favoured before increasing again as $x_{C4mimCl}$ approaches zero likely due to the increase in overlapping species.

The $C4mim_2\ Na_2Cl_3^+$ aggregate was not well observed between $x_{C4mimCl} = 1$ and 0.3 however a slight increase was observed as the mole fraction of C4mimCl was decreased below 0.7. Based on the decrease of the $C4mim_3NaCl_3^+$ aggregate, this likely coincided with the formation of the desired aggregate. As with the other examples, an increase in intensity was observed between $x_{C4mimCl} = 0.3$ and 0, likely due to the high sodium aggregates. The effect of the overlapping peaks is very clearly observed for the $C4mim\ Na_3Cl_3^+$ aggregate which overlaps with the previously dominant $C4mim_2Cl^+$ aggregate. This peak dominates the other species for almost all of the compositions. As $x_{C4mimCl}$ is reduced from 1 there is an initial

decrease in relative intensity as the single sodium containing aggregate is formed, however, by $x_{C4mimCl} = 0.4$ the intensity has again recovered due to the prominence of the $C4mim_2Cl^+$ aggregate. When $x_{C4mimCl}$ is below 0.4 the intensity of this species falls away due to the decreasing quantity of IL present and by $x_{C4mimCl} = 0$ the spectrum is dominated by the large $Na_{n+1}Cl_n^+$ aggregates. In Figure 5-4(a) the relative intensity of $Na_4Cl_3^+$ is very low, appearing that it does not form at any solution composition. However, when this series is expanded in the y-axis as shown in Figure 5-4(b) detail can be observed. For high $x_{C4mimCl}$ values, this aggregate is not formed but, similar to $C4mim_2Na_2Cl_3^+$, as $x_{C4mimCl}$ decreases the intensity increases. This continues until $x_{C4mimCl} = 0.1$ at which point the intensity begins to fall once again. This is likely due to the increase in the intensity of the larger $Na_{n+1}Cl_n^+$ aggregates suppressing the relative intensity of this small aggregate.

5.1.2 LiCl and C4mimCl

Following the success of the additions of NaCl to the IL, LiCl was added to C4mimCl solutions. These experiments were performed at the same conditions as the NaCl examples shown above. The same 3 mM overall concentration was maintained and the mole fractions which were studied were also kept constant. Na and Li are both group one alkali metals, so making this alteration in the aggregates should keep many of the parameters constant. They will exhibit similar characteristics meaning that the cause of the differences which are observed can be potentially better understood. A large contributing factor may be the significantly smaller ionic radius of the Li^+ at 76 pm compared to 102 pm for the Na^+ which will likely cause an increase in the steric hindrance in the mixed aggregates.

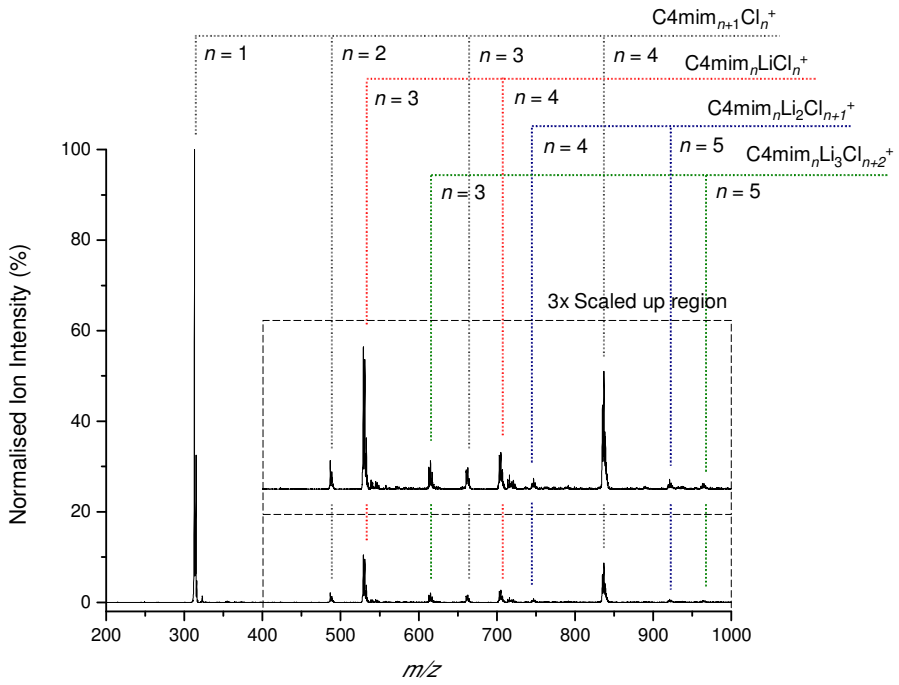

Figure 5-5 Mass spectrum of 2.85 mM C4mimCl and 0.15 mM LiCl in a 9:1 MeOH:H_2O solution. The aggregates C4mim$_{n+1}$Cl$_n^+$ (grey), C4mim$_n$LiCl$_n^+$ (red), C4mim$_n$ Li$_2$Cl$_{n+1}^+$ (blue) and C4mim$_n$ Li$_3$Cl$_{n+2}^+$ (green) are highlighted. The region between 400 and 1000 *m/z* is scaled up by a factor of 3.

10 % of the total ion concentration was changed to LiCl by producing a solution with 2.85 mM C4mimCl and 0.15 mM LiCl. The resulting mass spectrum is shown in Figure 5-5 where the series of ions C4mim$_{n+1}$Cl$_n^+$, C4mim$_n$LiCl$_n^+$, C4mim$_n$ Li$_2$Cl$_{n+1}^+$ and C4mim$_n$ Li$_3$Cl$_{n+2}^+$ are highlighted. Figure 5-5 additionally shows the region between 400 and 1000 *m/z* scaled up along the y-axis. The C4mim$_{n+1}$Cl$_n^+$ series can be seen across the mass range with particularly large intensity at n = 1 and 4 as was seen in Chapter 4. The aggregates C4mim$_n$LiCl$_n^+$ can be clearly observed for n = 3 and 4, this shows that the mixed aggregates observed with Na can also be seen when the solutions are doped with LiCl. The species with n = 5 was not observed however, this may be down to steric factors where the Li ion is acting as a core and the fifth chlorine anion can not be accommodated by the Li ion. This will be investigated in greater detail later exploiting the computational calculations. Albeit they have low ion intensity, the series of aggregates C4mim$_n$ Li$_2$Cl$_{n+1}^+$ and C4mim$_n$ Li$_3$Cl$_{n+2}^+$ are observed in Figure 5-5. This demonstrates that even with the relatively small amount

of Li present in the solution, it remains possible to form aggregates with more than one Li ion.

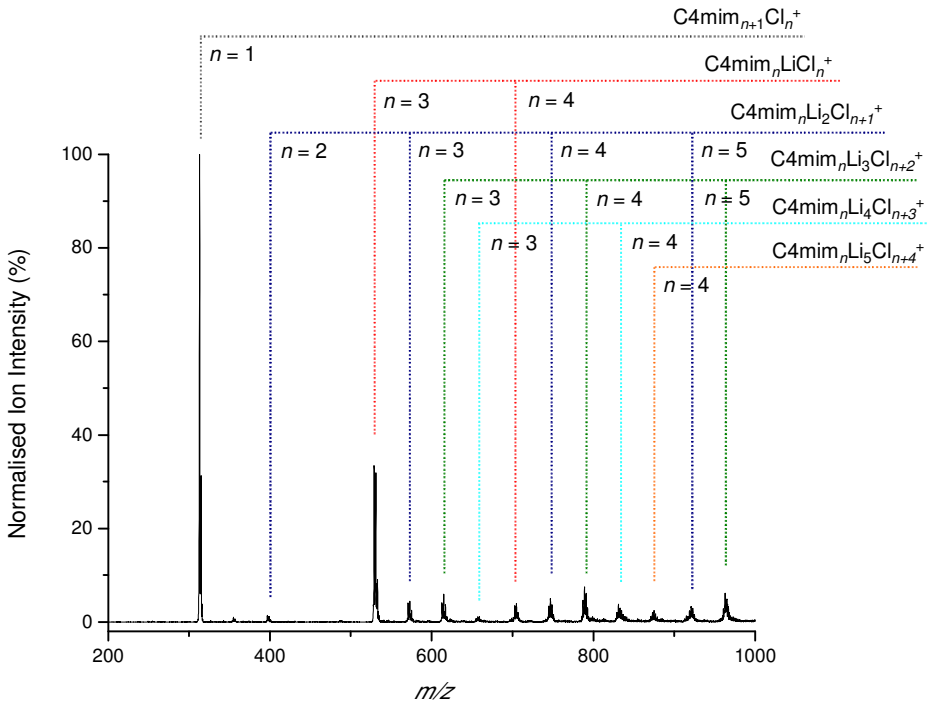

Figure 5-6 Mass spectrum of 2.10 mM C4mimCl and 0.90 mM LiCl in a 9:1 MeOH:H_2O solution. The aggregates C4mim$_{n+1}$Cl$_n^+$ (grey), C4mim$_n$LiCl$_n^+$ (red), C4mim$_n$ Li$_2$Cl$_{n+1}^+$ (blue), C4mim$_n$ Li$_3$Cl$_{n+2}^+$ (green), C4mim$_n$ Li$_4$Cl$_{n+3}^+$ (turquoise) and C4mim$_n$ Li$_5$Cl$_{n+4}^+$ (orange) are highlighted.

The LiCl concentration was increased to 0.90 mM with the C4mimCl concentration reduced to 2.10 mM. This meant that LiCl made up 30 % of the total ion concentration and the resulting mass spectrum is shown in Figure 5-6. This spectrum shows the presence of many more aggregates and with a significantly increased relative ion intensity compared with Figure 5-5. The intensity of the C4mim$_{n+1}$Cl$_n^+$ aggregates with n = 2, 3 and 4 have been diminished however the n = 2 aggregate remains dominant. These have been replaced by aggregates containing increasingly large numbers of Li^+ ions. Aggregates with up to five Li^+ ions have been observed within this region showing that increasing the amount of Li^+ in the solution successfully results in an increased incorporation of them into the mixed aggregates.

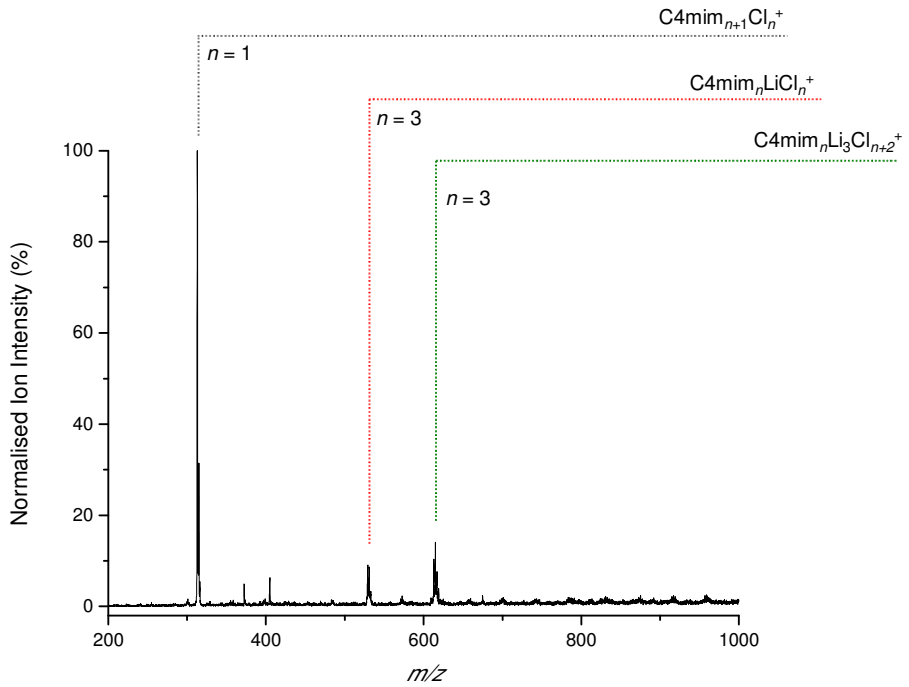

Figure 5-7 Mass spectrum of 1.50 mM C4mimCl and 1.50 mM LiCl in a 9:1 MeOH:H_2O solution. The aggregates C4mim$_{n+1}$Cl$_n^+$ (grey), C4mim$_n$LiCl$_n^+$ (red) and C4mim$_n$ Li$_3$Cl$_{n+2}^+$ (green) are highlighted.

When the amount of LiCl in the solution is increased to 50 % the resulting spectrum is remarkably different. The mass spectrum for the solution with 1.50 mM LiCl and 1.50 mM C4mimCl is shown in Figure 5-7. This spectrum shows the presence of three aggregates, $C4mim_2Cl^+$, $C4mim_3LiCl_3^+$ and $C4mim_3Li_3Cl_5^+$. There is some evidence that other aggregates are formed, however they are difficult to distinguish from the noise. There are two more signals observed at 372.40 and 404.93 *m/z* which could not be identified, however the isotopic distribution indicates that they are not chlorine-containing so they are likely to be contaminant species from the solvents or the glassware which was used.

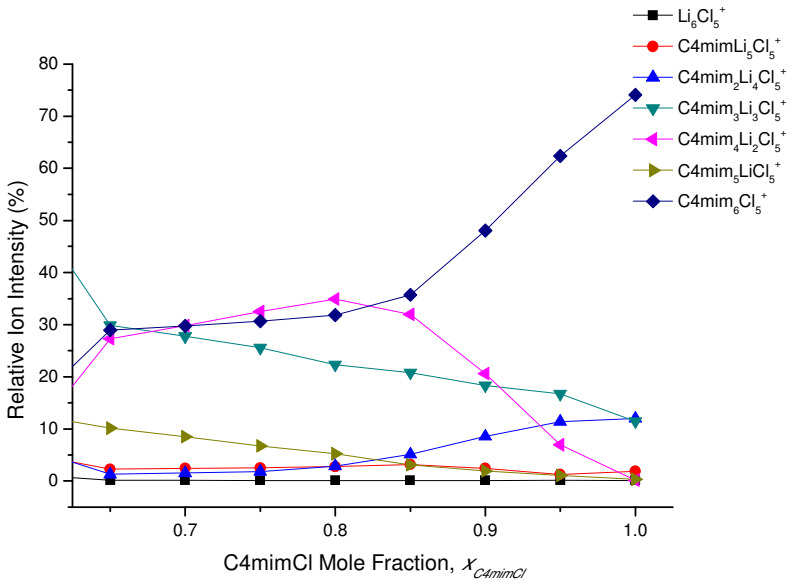

Figure 5-8 Relative ion intensity as the C4mimCl mole fraction is varied from 0.65 to 1 in mixtures with LiCl. Intensities are shown for all of the aggregates $C_6Cl_5^+$ where C is $C4mim^+$ or Li^+.

In the same way as the NaCl study, the experiments were repeated at 5 % LiCl intervals to produce a series of C4mimCl mole fraction results from zero to one. Due to the low molecular weight of Li, the series of aggregates $C_6Cl_5^+$ where C is $C4mim^+$ or Li^+ was selected for study in order to get all of the series within the observable mass range. This resulted in the formation of a very complicated graph of intensities so for clarity this has been split into three sections to allow effective comparison. Figure 5-8 shows the resulting relative ion intensity vs. C4mimCl mole fraction graph where $x_{C4mimCl}$ was varied between 0.65 and 1. The $C4mim_6Cl_5^+$ aggregate is the most intense as would be predicted when $x_{C4mimCl} = 1$ and decreases steadily as the LiCl concentration is increased throughout this region. As was observed above in the analysis of Figure 5-6 the $C4mim_5LiCl_5^+$ aggregate is very poorly formed which will be further investigated later with the computational calculations. This trend is observed in Figure 5-8 by the low but increasing intensity of this aggregate. As $C4mim_6Cl_5^+$ reduces in intensity the aggregates $C4mim_4Li_2Cl_5^+$ and $C4mim_3Li_3Cl_5^+$ are seen to increase. A progression from the pure IL aggregate towards increasingly Li containing species is observed as first the $C4mim_4Li_2Cl_5^+$ and then the $C4mim_3Li_3Cl_5^+$ aggregates sequentially increase. The remaining

aggregates ($C4mim_2Li_4Cl_5^+$, $C4mimLi_5Cl_5^+$ and $Li_3Cl_5^+$) are formed very poorly in this region as would be predicted. The trace shown for $C4mim_2Li_4Cl_5^+$ shows the presence of some $C4mim_3Cl_2^+$ due to an overlap with this peak allowing for its loss to be tracked in a similar way to $C4mim_6Cl_5^+$.

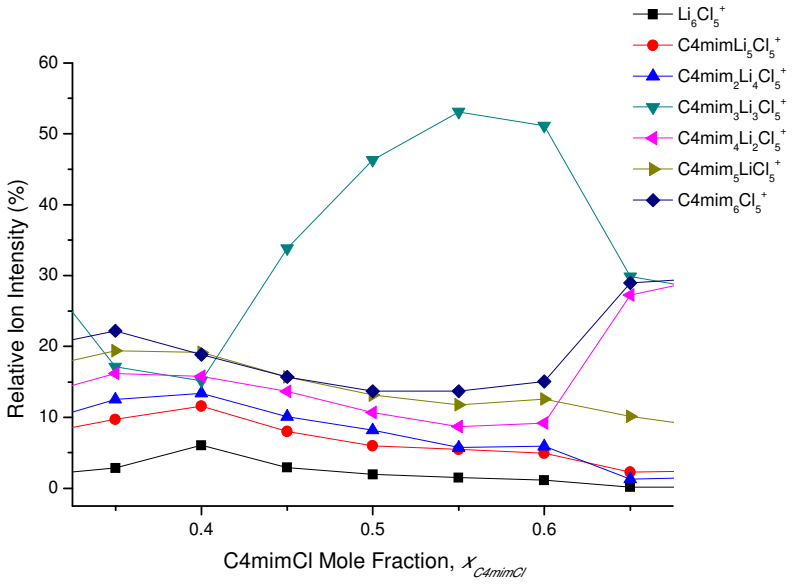

Figure 5-9 Relative ion intensity as the C4mimCl mole fraction is varied from 0.35 to 0.65 in mixtures with LiCl. Intensities are shown for all of the aggregates $C_6Cl_5^+$ where C is $C4mim^+$ or Li^+.

Figure 5-9 shows the central region for the C4mimCl mole fraction with $x_{C4mimCl}$ between 0.35 and 0.65. This region is dominated by the formation of the $C4mim_3Li_3Cl_5^+$ aggregate which increases to a maximum at $x_{C4mimCl} = 0.55$ before once again rapidly decreasing. This ion forms at the expense of the $C4mim_6Cl_5^+$ and $C4mim_4Li_2Cl_5^+$ aggregates which rapidly decrease in intensity as it begins to become more prominent. As indicted by Figure 5-7 the other aggregates have a significantly lower intensity and are at times difficult to distinguish from the noise as a select few ions dominate the spectra.

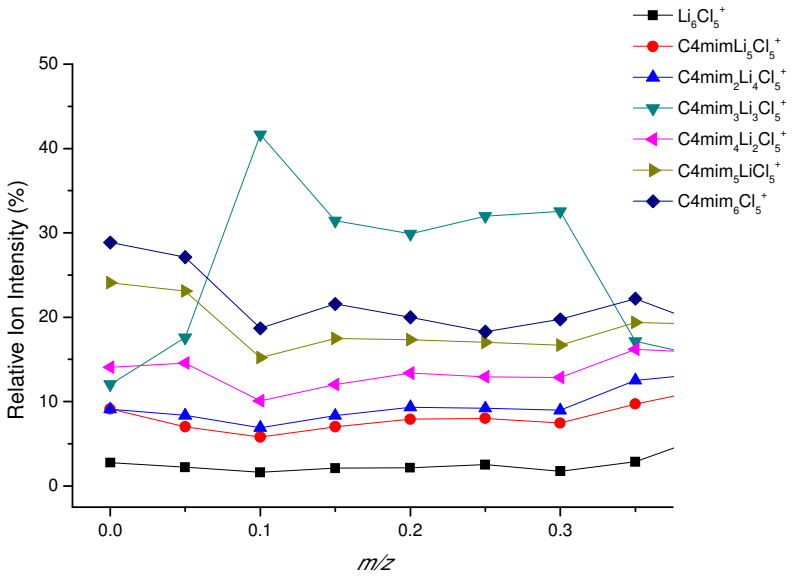

Figure 5-10 Relative ion intensity as the C4mimCl mole fraction is varied from 0 to 0.35 in mixtures with LiCl. Intensities are shown for all of the aggregates $C_6Cl_5^+$ where C is $C4mim^+$ or Li^+.

The region with a low C4mimCl mole fraction is shown in Figure 5-10 with $x_{C4mimCl}$ between 0 and 0.35. In this region the $Li_{n+1}Cl_n^+$ ions with higher values of n than are shown here were seen to be preferentially formed. As a result the signals here are weak and it is very difficult to distinguish clear trends. However it can be observed that the $C4mim_3Li_3Cl_5^+$ aggregate is seen to form but even this gives little information.

5.1.3 CsCl and C4mimCl

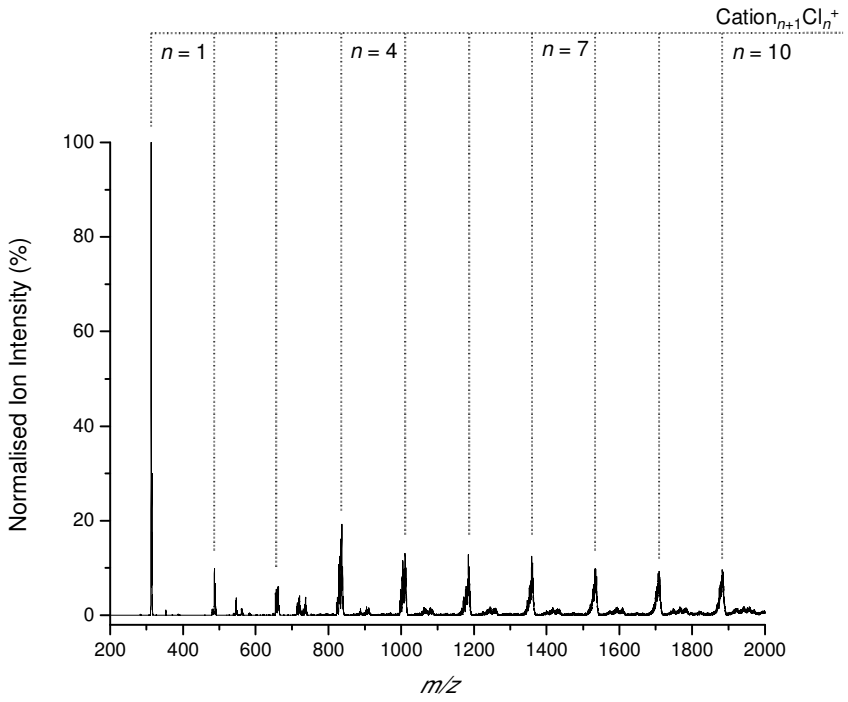

Figure 5-11 Mass spectrum of 2.90 mM C4mimCl and 0.10 mM CsCl in a 9:1 MeOH:H_2O solution. The aggregates Cation$_{n+1}$Cl$_n^+$ (grey) are highlighted where Cation = C4mim$^+$ or Cs$^+$.

In a similar fashion to the Na and Li examples previously presented, mixed solutions of C4mimCl and CsCl were prepared. This served as an extension of the group 1 alkali metal study and as such it may be anticipated that successful formation of a wide range of mixed aggregates may be possible. The total concentration of each solution was 3 mM as above, however, the solutions were prepared at 0.10 mM intervals which equated to 3.33 % between each consecutive solution. The molecular weight of a Cs^+ cation is 132.91 while as we found previously the molecular weight of a $C4mim^+$ cation is 139.22. This similarity results in the aggregates with the same number of ions appearing close to each other in the mass spectra. Each additional Cs^+ ion results in the peaks *m/z* value reducing by approximately 6. The broad isotopic distribution due to the presence of multiple chlorine anions results in the different species overlapping. However they remain separated sufficiently to gain a good estimate of the various contributions.

Figure 5-11 shows the mass spectrum of a solution with 2.90 mM C4mimCl and 0.10 mM CsCl. Due to the similar *m/z* of aggregates with the same number of ions it is not possible to distinguish separate ions on this scale. However it is possible to observe that a complete range of ions forms with *n* from 1 to 10. The highest normalised ion intensity belongs to the species with *n* = 1 however a large intensity is observed for all of the species.

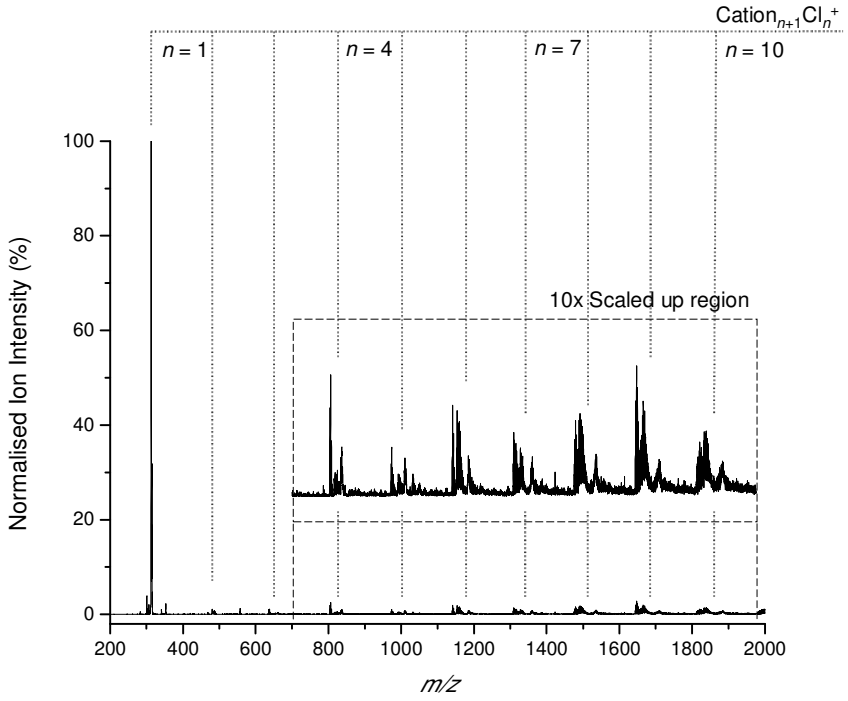

Figure 5-12 Mass spectrum of 1.50 mM C4mimCl and 1.50 mM CsCl in a 9:1 MeOH:H_2O solution. The aggregates Cation$_{n+1}$Cl$_n^+$ (grey) are highlighted where Cation = C4mim$^+$ or Cs$^+$. The region between 500 and 1975 *m/z* is scaled up by a factor of 10.

When the CsCl concentration was increased to 1.50 mM with the C4mimCl concentration also at 1.50 mM the mass spectrum in Figure 5-12 was produced. Similar to Figure 5-11, a full series of aggregates is produced with *n* ranging from 1 to 10. The peaks associated with the different aggregate sizes have broadened significantly from the previous example. This is a clear indication that a wider range of aggregates have been produced. As the concentration of CsCl has increased there has been an increased incorporation of the Cs^+ cations into the mixed aggregates. Cs^+ (167 pm) has a much larger ionic radius that Na^+ (102 pm) and Li^+ (76 pm) observed

previously which may result in a larger flexibility in the aggregates which can be produced due to a decrease in the steric hindrance. This may be a contributing factor to the observation of such a wide range of aggregates with similar relative intensities.

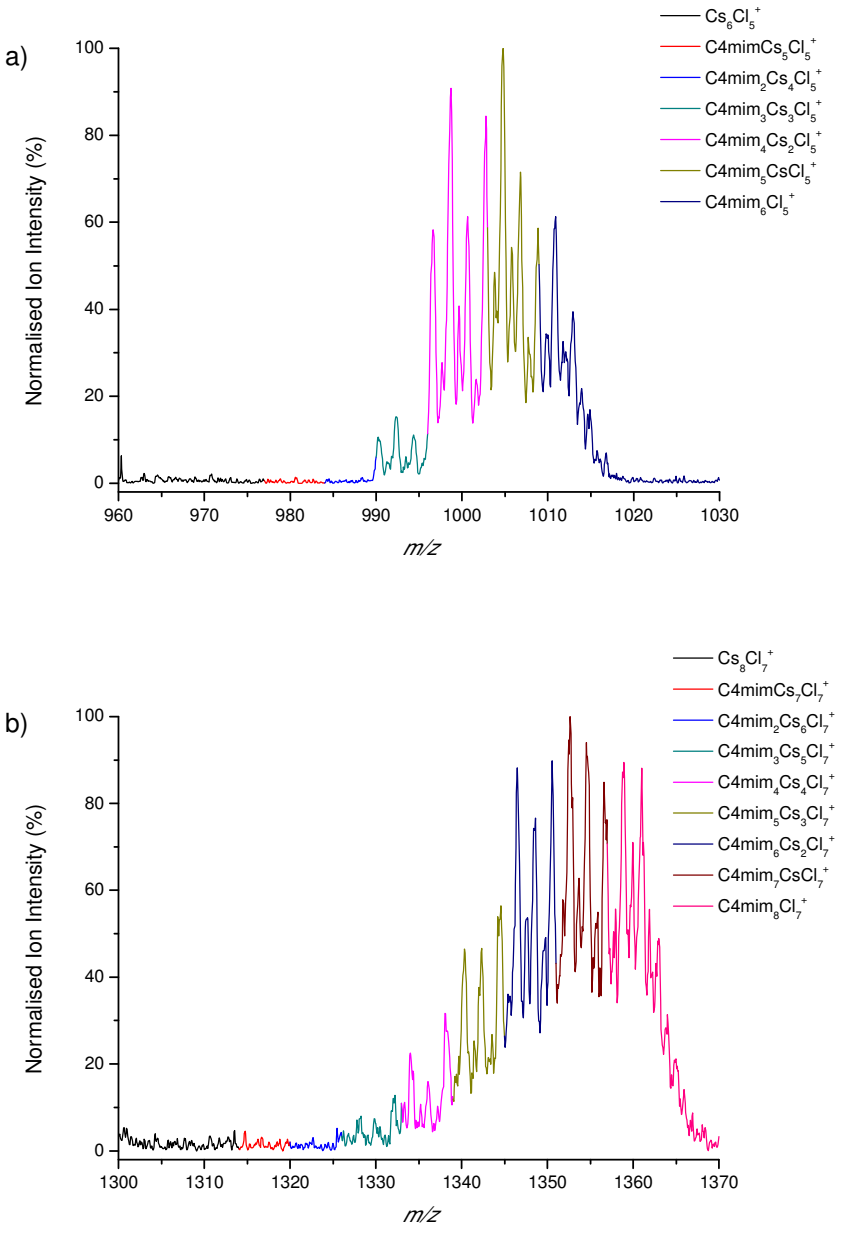

Figure 5-13 Mass spectra of 2.80 mM C4mimCl and 0.20 mM CsCl in a 9:1 MeOH:H_2O solution showing a) $Cation_6Cl_5^+$ and b) $Cation_8Cl_7^+$. Cation = $C4mim^+$ or Cs^+ and the different combinations are highlighted as indicted for the individual spectra.

Two regions from the mass spectrum of 2.80 mM C4mimCl and 0.20 mM CsCl are shown in Figure 5-13. These regions include all of the different aggregates produced with C4mimCl and CsCl with the general formulae $Cation_6Cl_5^+$ and $Cation_8Cl_7^+$. The spectra are coloured to indicate which ion is dominant in each region. The low CsCl concentration results in the primary formation of the aggregates with 0, 1 or 2 Cs^+ cations. This is similar to what was observed for Na and Li in the previous sections. While it is difficult to pick out the individual ions it is clear that contributions are present from a range of different ions.

Increasing the CsCl concentration to 0.90 mM and correspondingly reducing the C4mimCl concentration to 2.10 mM results in the formation of the mass spectra extracts shown in Figure 5-14. As was seen above for Figure 5-13, regions of the spectra have been assigned to different ions. In this case the spectra are primarily dominated by mixed aggregates in the middle of the series. In the case of $Cation_6Cl_5^+$ the dominant species are $C4mim_4Cs_2Cl_5^+$ and $C4mim_3Cs_3Cl_5^+$. While $C4mim_5Cs_3Cl_7^+$ to $C4mim_3Cs_5Cl_7^+$ are the largest species for $Cation_8Cl_7^+$. This demonstrates the progressive incorporation of Cs^+ into the mixed aggregates as postulated from Figure 5-12.

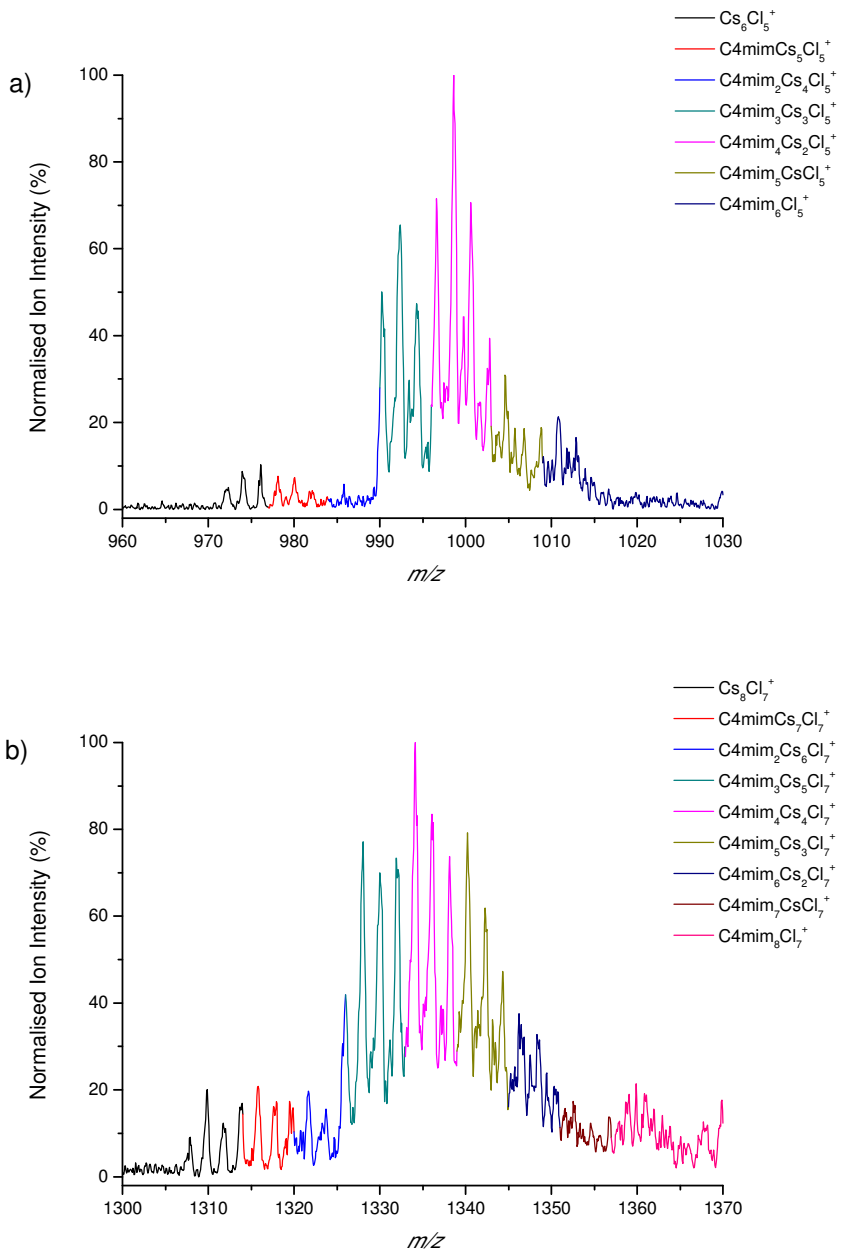

Figure 5-14 Mass spectra of 2.10 mM C4mimCl and 0.90 mM CsCl in a 9:1 MeOH:H_2O solution showing a) Cation$_6Cl_5^+$ and b) Cation$_8Cl_7^+$. Cation = $C4mim^+$ or Cs^+ and the different combinations are highlighted as indicted for the individual spectra.

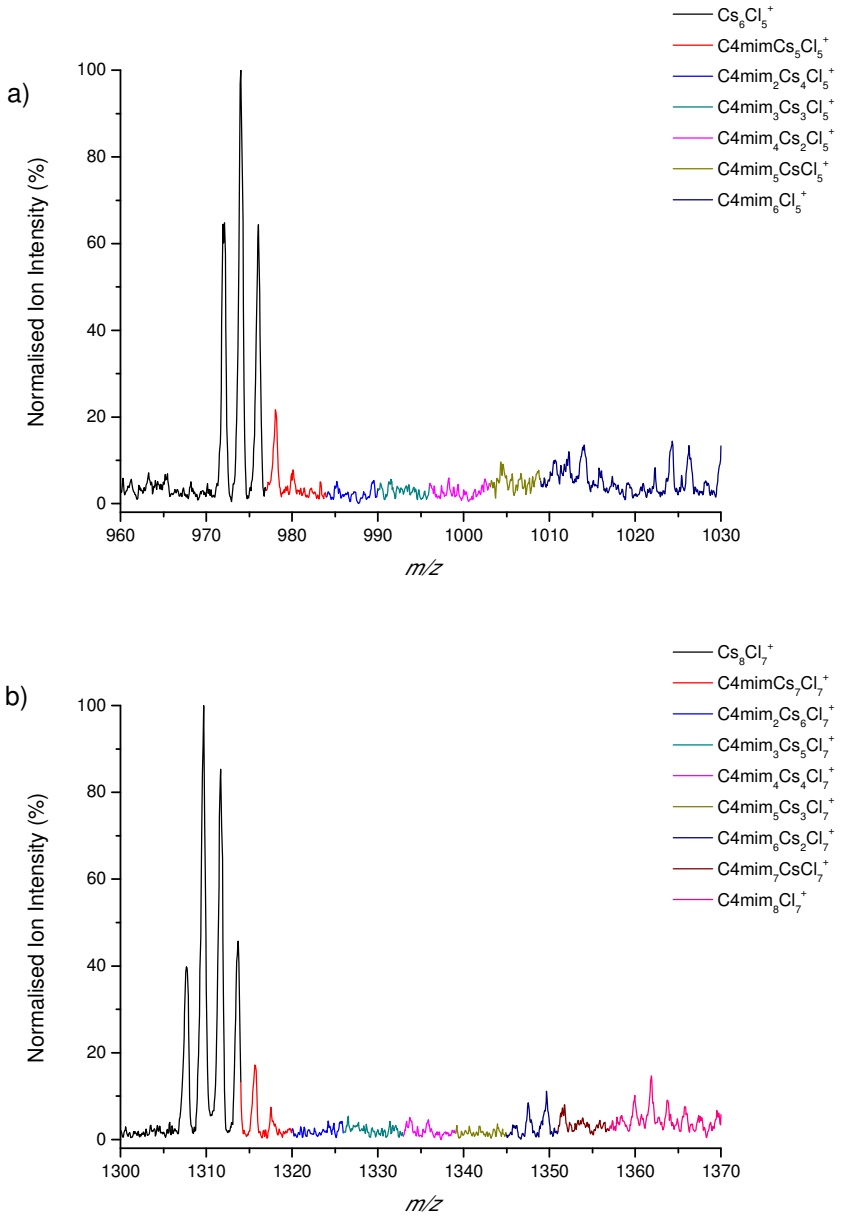

Figure 5-15 Mass spectra of 0.20 mM C4mimCl and 2.80 mM CsCl in a 9:1 MeOH:H_2O solution showing a) Cation$_6Cl_5^+$ and b) Cation$_8Cl_7^+$. Cation = C4mim$^+$ or Cs$^+$ and the different combinations are highlighted as indicted for the individual spectra.

The mass spectra in Figure 5-15 are produced by a solution of 0.20 mM C4mimCl and 2.80 mM CsCl. As the CsCl has become dominant in the solution the progressive incorporation of Cs has been clearly demonstrated in both examples. The spectra for Cation$_6Cl_5^+$ and Cation$_8Cl_7^+$ are dominated by the pure CsCl species which are $Cs_6Cl_5^+$ and $Cs_8Cl_7^+$ respectively. Small contributions can be observed for the pure C4mimCl aggregates and also $C4mim_6Cs_2Cl_7^+$. The larger *m/z* isotopes for the

$Cs_{n+1}Cl_n^+$ aggregates are observed in the regions which are assigned to the aggregates each containing one $C4mim^+$ cation. The effect of this will be seen later in Figure 5-17 however there is little evidence that mixed aggregates which are dominated by Cs^+ cations are formed in great abundance.

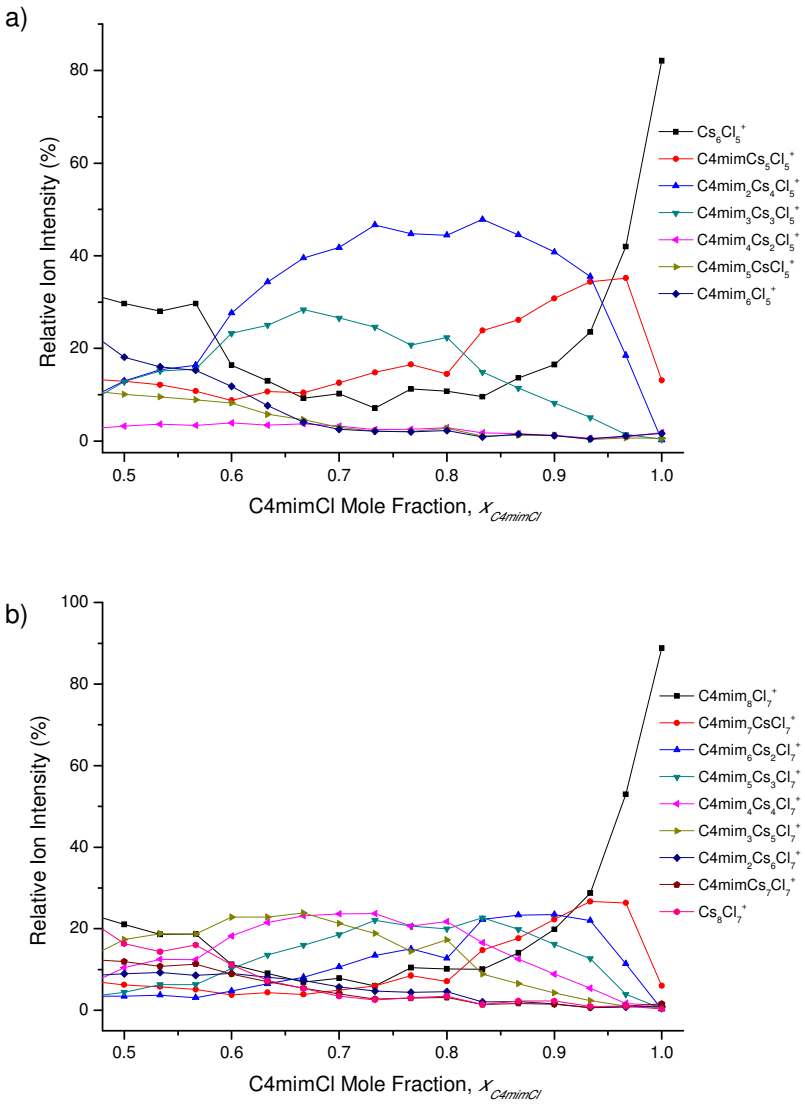

Figure 5-16 Relative ion intensity as the C4mimCl mole fraction is varied from 0.5 to 1.0 in mixtures with CsCl. Intensities are shown for all possible aggregates a) $Cation_6Cl_5^+$ b) $Cation_8Cl_7^+$ where Cation is $C4mim^+$ or Cs^+.

The C4mimCl mole fraction was varied from 0 to 1 recording mass spectra at 0.10 mM intervals. The relative intensities of $Cation_6Cl_5^+$ and $Cation_8Cl_7^+$ are shown for $x_{C4mimCl}$ between 0.5 and 1.0 in Figure 5-16. In each example when $x_{C4mimCl} = 1.0$ the

spectra are dominated by the $C4mim_6Cl_5^+$ and $C4mim_8Cl_7^+$ aggregates. Then as the concentration of CsCl is increased up to 50 % sequential replacements of the IL by caesium are observed. In Figure 5-16(a) maximum relative intensities are observed at $x_{C4mimCl}$ = 0.95, 0.80 and 0.65 for $C4mim_{6-n}Cs_nCl_5^+$ where n = 1, 2 and 3 respectively. Meanwhile in Figure 5-16(b) maximum relative intensities are observed at $x_{C4mimCl}$ = 0.95, 0.90, 0.80, 0.70 and 0.65 for $C4mim_{6-n}Cs_nCl_5^+$ where n = 1 to 5 respectively.

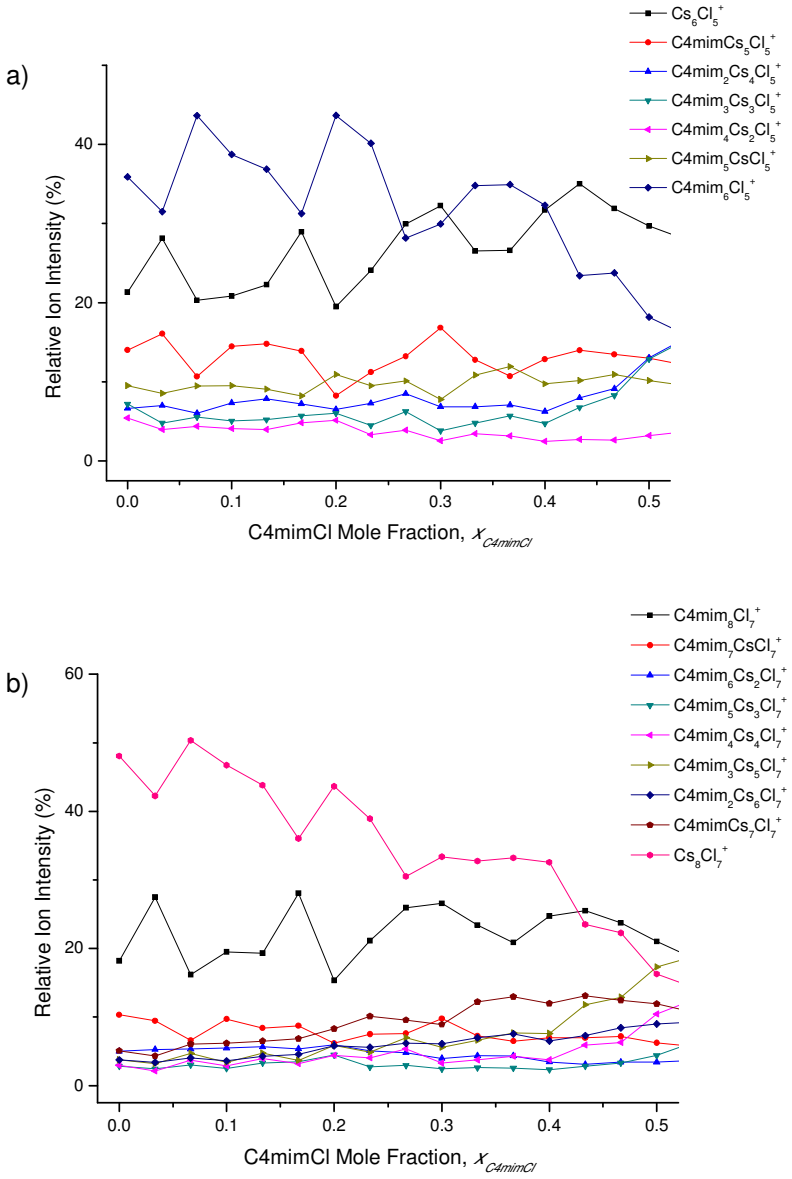

Figure 5-17 Relative ion intensity as the C4mimCl mole fraction is varied from 0.0 to 0.5 in mixtures with CsCl. Intensities are shown for all possible aggregates a) $Cation_6Cl_5^+$ b) $Cation_8Cl_7^+$ where Cation is $C4mim^+$ or Cs^+.

The remaining relative intensities where $x_{C4mimCl}$ is varied between 0.0 and 0.5 for $Cation_6Cl_5^+$ and $Cation_8Cl_7^+$ are shown in Figure 5-17. These graphs are remarkably different from those observed previously in Figure 5-16. The relative intensities of most of the aggregates show low intensities with very little trend observed. The spectra became dominated by the $Cs_6Cl_5^+$ and $Cs_8Cl_7^+$ aggregates however in these regions there is also a strong presence of $C4mim_6Cl_5^+$ and $C4mim_8Cl_7^+$. It was found that the Cs^+-rich mixed aggregates are very poorly formed and not observed at any concentration of CsCl. It is possible that the structure breaking characteristics of Cs^+ compared with the relative structure making effects of Na^+ and Li^+ are responsible for this contrast. The structure breaking ions disrupt the solvent surrounding them, thus preventing the formation of aggregates rich in these cations.[1]

5.1.4 $MgCl_2$ and C4mimCl

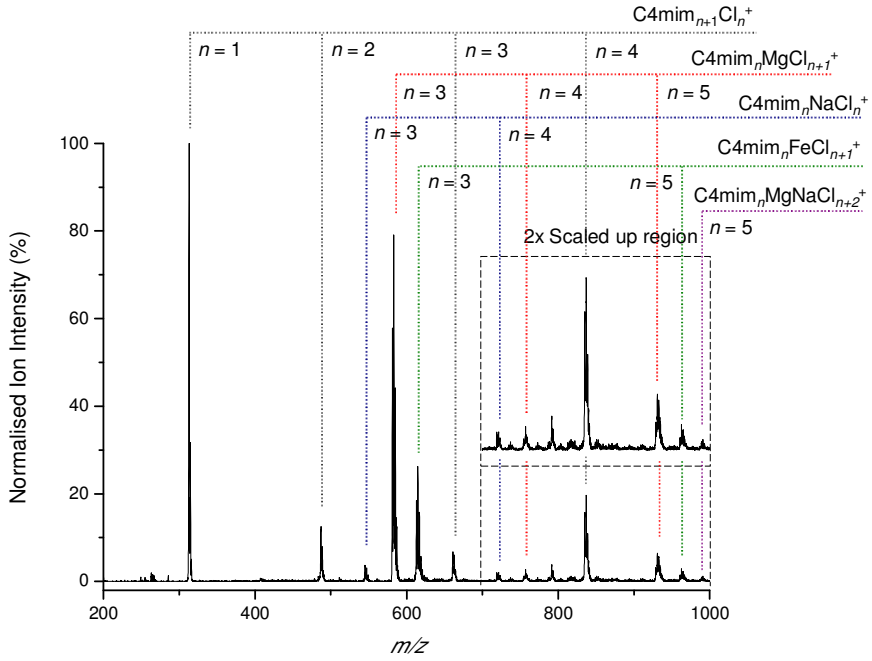

Figure 5-18 Mass spectrum of 2.85 mM C4mimCl and 0.15 mM $MgCl_2$ in a 9:1 MeOH:H_2O solution. The aggregates $C4mim_{n+1}Cl_n^+$ (grey), $C4mim_nMgCl_{n+1}^+$ (red), $C4mim_n NaCl_n^+$ (blue), $C4mim_n FeCl_{n+1}^+$ (green) and $C4mim_n MgNaCl_{n+2}^+$ (purple) are highlighted. The region between 700 and 1000 *m/z* is scaled up by a factor of 2.

Mixed solutions of $MgCl_2$ and C4mimCl were prepared with a total concentration of 3 mM. The mole fraction of C4mimCl was varied from 1 to 0 in 5 % intervals and the resulting spectra were investigated. Unlike the previous examples magnesium is divalent so will likely form very different aggregates. The mass spectrum of 2.85 mM C4mimCl and 0.15 $MgCl_2$ is shown in Figure 5-18. The aggregates $C4mim_{n+1}Cl_n^+$ are highlighted for n = 1 to 4. This is in line with the previous examples where at low C4mimCl concentrations these aggregates can still be observed. The next most intense series in this spectrum is $C4mim_nMgCl_{n+1}^+$ for n = 3 to 5. The largest peak is at n = 3 with the remaining peaks much lower in ion intensity. The n = 3 species is similar to the $C4mim_3NaCl_3^+$ species which was also observed to have a high abundance. Additionally in this spectrum there is a number of sodium and iron adducts which are likely contaminants similar to what was seen in Chapter 4. As was previously observed the presence of these adducts may indicate difficulty in ionising these samples with adducts being used as a lower energy pathway to charge.

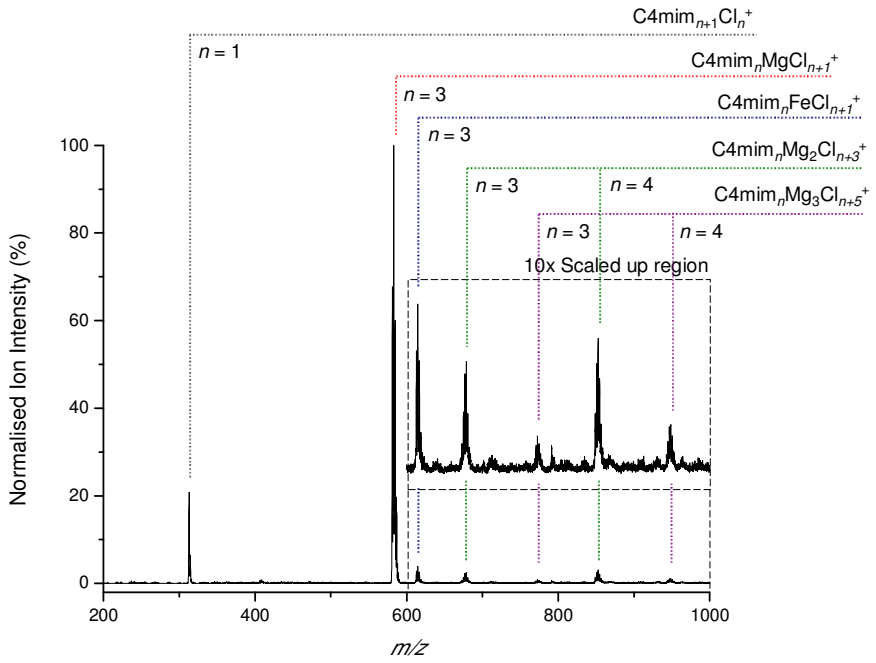

Figure 5-19 Mass spectrum of 2.25 mM C4mimCl and 0.75 mM $MgCl_2$ in a 9:1 MeOH:H_2O solution. The aggregates $C4mim_{n+1}Cl_n^+$ (grey), $C4mim_nMgCl_{n+1}^+$ (red), $C4mim_n FeCl_{n+1}^+$ (blue), $C4mim_n Mg_2Cl_{n+3}^+$ (green) and $C4mim_n Mg_3Cl_{n+5}^+$ (purple) are highlighted. The region between 600 and 1000 *m/z* is scaled up by a factor of 10.

The effect of increasing the $MgCl_2$ concentration to 0.75 mM with the C4mimCl down to 2.25 mM is shown in Figure 5-19. The series of aggregates $C4mim_{n+1}Cl_n^+$ has been reduced to a single member with $n = 1$ surviving but with a considerably lower intensity. This would be expected with the increased concentration of $MgCl_2$ resulting in the presence of more mixed aggregates. In addition to this peak there is also the $C4mim_3FeCl_4^+$ aggregate which is again from contamination. However the spectrum is increasingly dominated with the mixed aggregates containing both Mg^{2+} and $C4mim^+$ ions. The most abundant peak now belongs to $C4mim_3MgCl_4^+$ which is the only observed aggregate with one magnesium ion. The increased concentration of $MgCl_2$ produced mixed aggregates with two and three magnesium ions. These are both seen to form with both three and four $C4mim^+$ cations and naturally the two magnesium examples are more abundant.

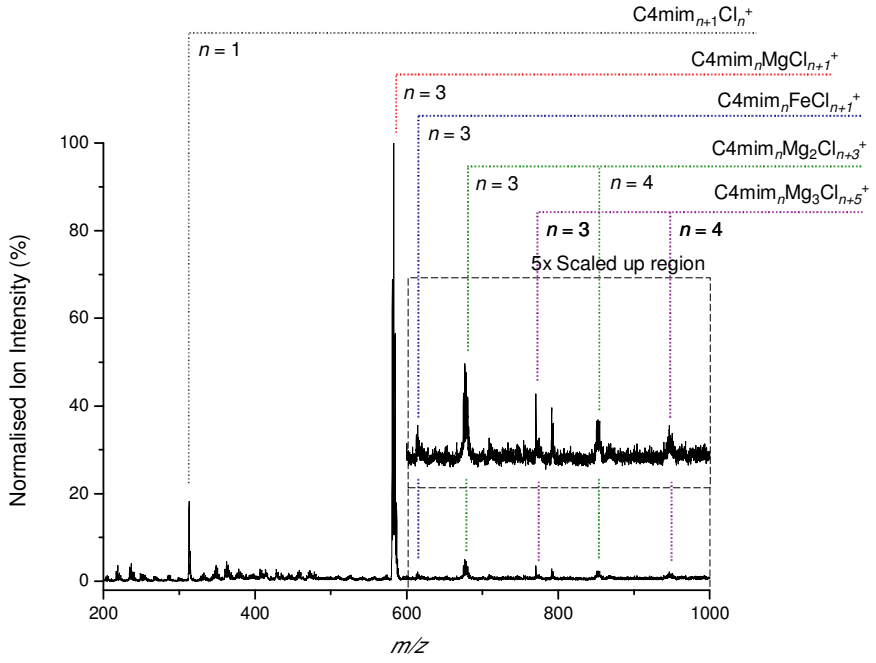

Figure 5-20 Mass spectrum of 1.50 mM C4mimCl and 1.50 mM $MgCl_2$ in a 9:1 MeOH:H_2O solution. The aggregates $C4mim_{n+1}Cl_n^+$ (grey), $C4mim_nMgCl_{n+1}^+$ (red), $C4mim_n FeCl_{n+1}^+$ (blue), $C4mim_n Mg_2Cl_{n+3}^+$ (green) and $C4mim_n Mg_3Cl_{n+5}^+$ (purple) are highlighted. The region between 600 and 1000 *m/z* is scaled up by a factor of 5.

Figure 5-20 shows the mass spectrum of 1.50 mM C4mimCl and 1.50 mM $MgCl_2$. This spectrum is very similar to that observed in Figure 5-19 for a higher C4mimCl

concentration. This clearly displays a consistency and preference for the above set of aggregates. In particular the single magnesium containing $C4mim_3MgCl_4^+$ which remains the most abundant ion despite the concentration alteration.

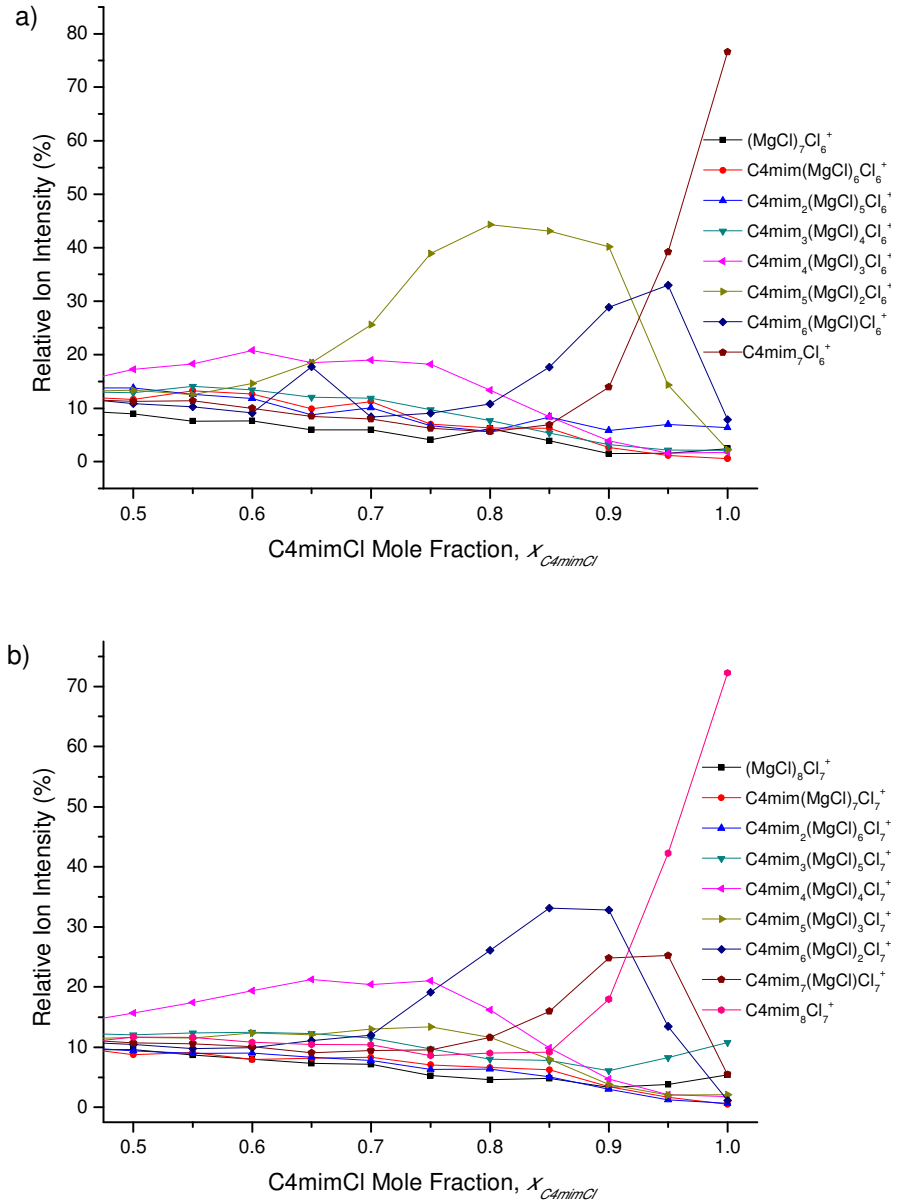

Figure 5-21 Relative ion intensity as the C4mimCl mole fraction is varied from 0.5 to 1.0 in mixtures with $MgCl_2$. Intensities are shown for all possible aggregates a) $Cation_7Cl_6^+$ b) $Cation_8Cl_7^+$ where Cation is $C4mim^+$ or $(MgCl)^+$.

The C4mimCl mole fraction was varied from 0 to 1 in solutions with $MgCl_2$ at 5 % intervals. The relative ion intensities were recorded as $x_{C4mimCl}$ varied and $Cation_7Cl_6^+$

and $Cation_8Cl_7^+$ where Cation is $C4mim^+$ or $(MgCl)^+$ were graphed. The graphs for these aggregates can be seen respectively in Figure 5-21(a) and Figure 5-21(b) for $x_{C4mimCl}$ between 0.5 and 1.0. When $x_{C4mimCl} = 1$ the spectra are predictably dominated by the pure IL aggregates. Then, as was seen for the group 1 alkali metal chlorides, sequential replacement of $C4mim^+$ by $MgCl^+$ takes place. For $C4mim_{7-n}(MgCl)_nCl_6^+$ maximum relative intensities are observed at $x_{C4mimCl} = 0.95$, 0.80 and 0.60 for $n = 1$, 2 and 3 respectively. This is very similar to what was observed in the similar cases for the mixed solutions of CsCl and C4mimCl. Meanwhile in Figure 5-21(b) maximum relative intensities are observed at $x_{C4mimCl} = 0.95$, 0.85, 0.75 and 0.65 for $C4mim_{6-n}(MgCl)_nCl_5^+$ where $n = 1$ to 4 respectively. This shows that the divalent magnesium chloride is acting in a similar fashion to what was previously observed and will be investigated further with computational calculations.

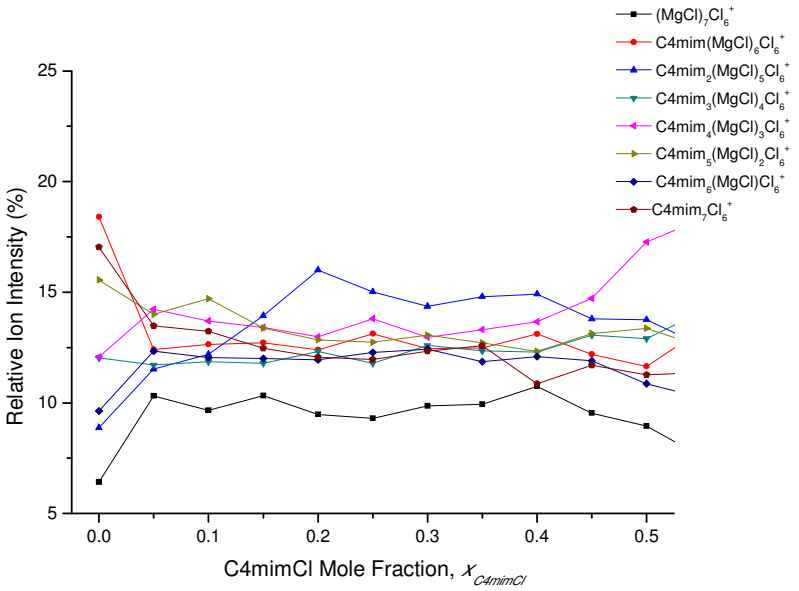

Figure 5-22 Relative ion intensity as the C4mimCl mole fraction is varied from 0.0 to 0.5 in mixtures with $MgCl_2$. Intensities are shown for all possible aggregates $Cation_7Cl_6^+$ where Cation is $C4mim^+$ or $(MgCl)^+$.

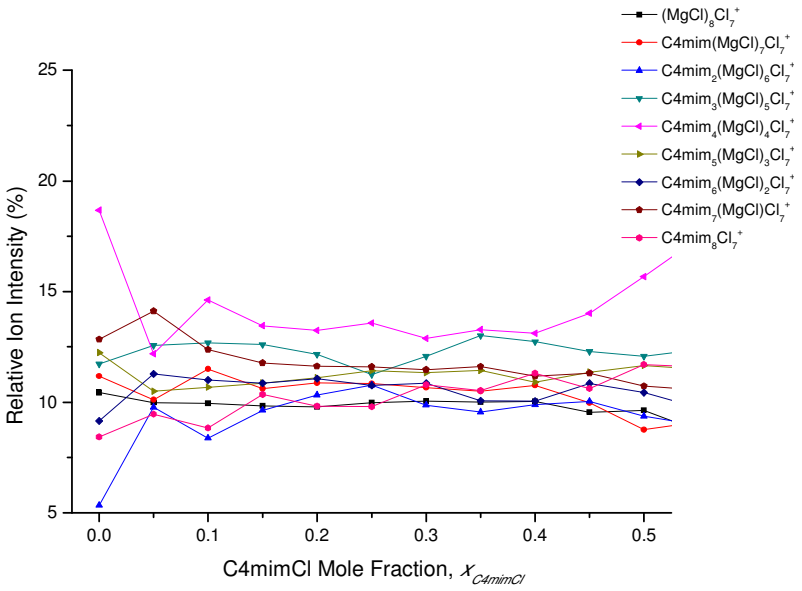

Figure 5-23 Relative ion intensity as the C4mimCl mole fraction is varied from 0.0 to 0.5 in mixtures with $MgCl_2$. Intensities are shown for all possible aggregates $Cation_8Cl_7^+$ where Cation is $C4mim^+$ or $(MgCl)^+$.

The plots of relative ion intensity against C4mimCl mole fraction between 0.0 and 0.5 are shown in Figure 5-22 and Figure 5-23. For these solutions it was challenging to obtain a strong ion signal and as a result the data which can be gathered from Figure 5-22 and Figure 5-23 is limited. These spectra were largely dominated by the $C4mim_3MgCl_4^+$ aggregate which was seen to be persistent in Figure 5-19 and Figure 5-20. As a result of this preference it is not possible to distinguish trends from these graphs.

5.1.5 $ZnCl_2$ and C4mimCl

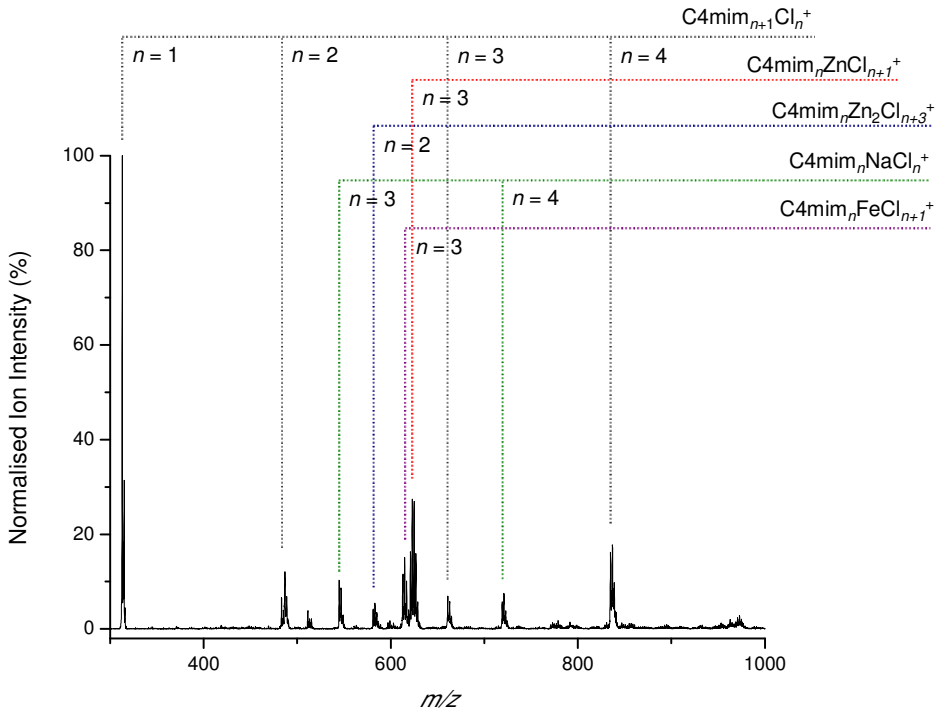

Figure 5-24 Mass spectrum of 2.85 mM C4mimCl and 0.15 mM $ZnCl_2$ in a 9:1 MeOH:H_2O solution. The aggregates C4mim$_{n+1}$Cl$_n^+$ (grey), C4mim$_n$ZnCl$_{n+1}^+$ (red), C4mim$_n$ Zn$_2$Cl$_{n+3}^+$ (blue), C4mim$_n$ NaCl$_n^+$ (green) and C4mim$_n$ FeCl$_{n+1}^+$ (purple) are highlighted.

Mixed solutions of C4mimCl and $ZnCl_2$ were prepared with an overall concentration of 3 mM. These were prepared with a mole fraction of C4mimCl varying between 0 and 1 at 5 % intervals. Zinc is dominated by the 2+ oxidation state which sees the loss of the pair of outer *s* electrons. The resulting ion has a full *d* shell with the configuration [Ar]3d^{10}. In the solid phase it forms 4-coordinate tetrahedral structures however in aqueous solutions it adopts an octahedral structure. These characteristics mean that Zn is interesting to study. Figure 5-24 shows the mass spectrum produced with 2.85 mM C4mimCl and 0.15 mM $ZnCl_2$. The series of aggregates C4mim$_{n+1}$Cl$_n^+$ can be observed for n = 1 to 4 similar to previous examples. The aggregates C4mim$_3$ZnCl$_4^+$ and C4mim$_2$Zn$_2$Cl$_5^+$ can also be observed here. This shows the incorporation of Zn^{2+} and the presence of mixed aggregates. The aggregate C4mim$_3$ZnCl$_4^+$ corresponds to an equivalent containing magnesium which was

preferentially formed showing a similarity between the two divalent series. As was also seen in the magnesium examples sodium and iron adducts are observed.

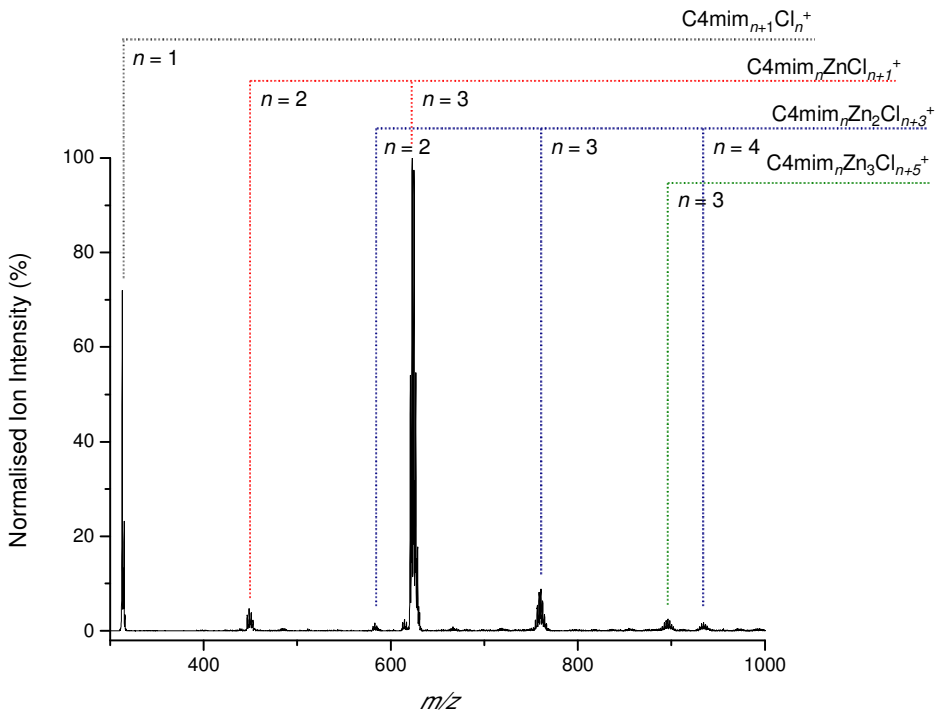

Figure 5-25 Mass spectrum of 2.25 mM C4mimCl and 0.75 mM $ZnCl_2$ in a 9:1 MeOH:H_2O solution. The aggregates C4mim$_{n+1}$Cl$_n^+$ (grey), C4mim$_n$ZnCl$_{n+1}^+$ (red), C4mim$_n$ Zn$_2$Cl$_{n+3}^+$ (blue) and C4mim$_n$ Zn$_3$Cl$_{n+5}^+$ (green) are highlighted.

The concentration of $ZnCl_2$ was increased to 0.75 mM and the resulting mass spectrum shown in Figure 5-25. Similar to what was seen for the magnesium solutions the spectrum becomes dominated by a single ion at the expense of the others. In this case it is the aggregate $C4mim_3ZnCl_4^+$ which dominates. The aggregate $C4mim_2ZnCl_3^+$ is also observed along with ions containing 2 and 3 zinc ions. However these remaining series are dominated by the presence of the very intense $C4mim_3ZnCl_4^+$ species.

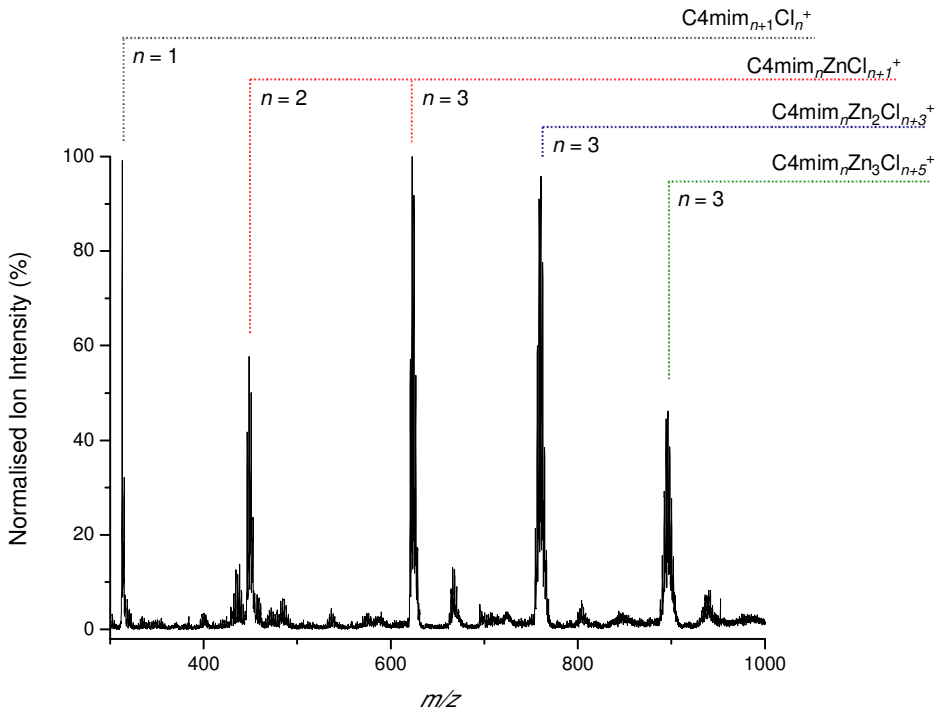

Figure 5-26 Mass spectrum of 1.50 mM C4mimCl and 1.50 mM $ZnCl_2$ in a 9:1 MeOH:H_2O solution. The aggregates $C4mim_{n+1}Cl_n^+$ (grey), $C4mim_nZnCl_{n+1}^+$ (red), $C4mim_n\ Zn_2Cl_{n+3}^+$ (blue) and $C4mim_n\ Zn_3Cl_{n+5}^+$ (green) are highlighted.

When the concentrations of $ZnCl_2$ and C4mimCl were both 1.50 mM the mass spectrum in Figure 5-26 was produced. In this case the aggregates $C4mim_2Cl^+$ and $C4mim_3ZnCl_4^+$ remain strong and are observed as before. The aggregates $C4mim_2ZnCl_3^+$ and $C4mim_3Zn_2Cl_6^+$ and $C4mim_3Zn_3Cl_8^+$ are also present and with a large normalised ion intensity. This shows that as the amount of zinc which is available increases, there is a resulting increase in its incorporation in the mixed aggregates. This is similar to what was seen with the alkali metals however this effect was largely unseen with the divalent magnesium. The number of aggregates which forms is very limited in comparison with the alkali metals. The aggregates which are observed correspond closely to the $C4mim_3ZnCl_4^+$ aggregate with the differences being the loss of a C4mimCl ion pair or the addition of one or two $ZnCl_2$ units.

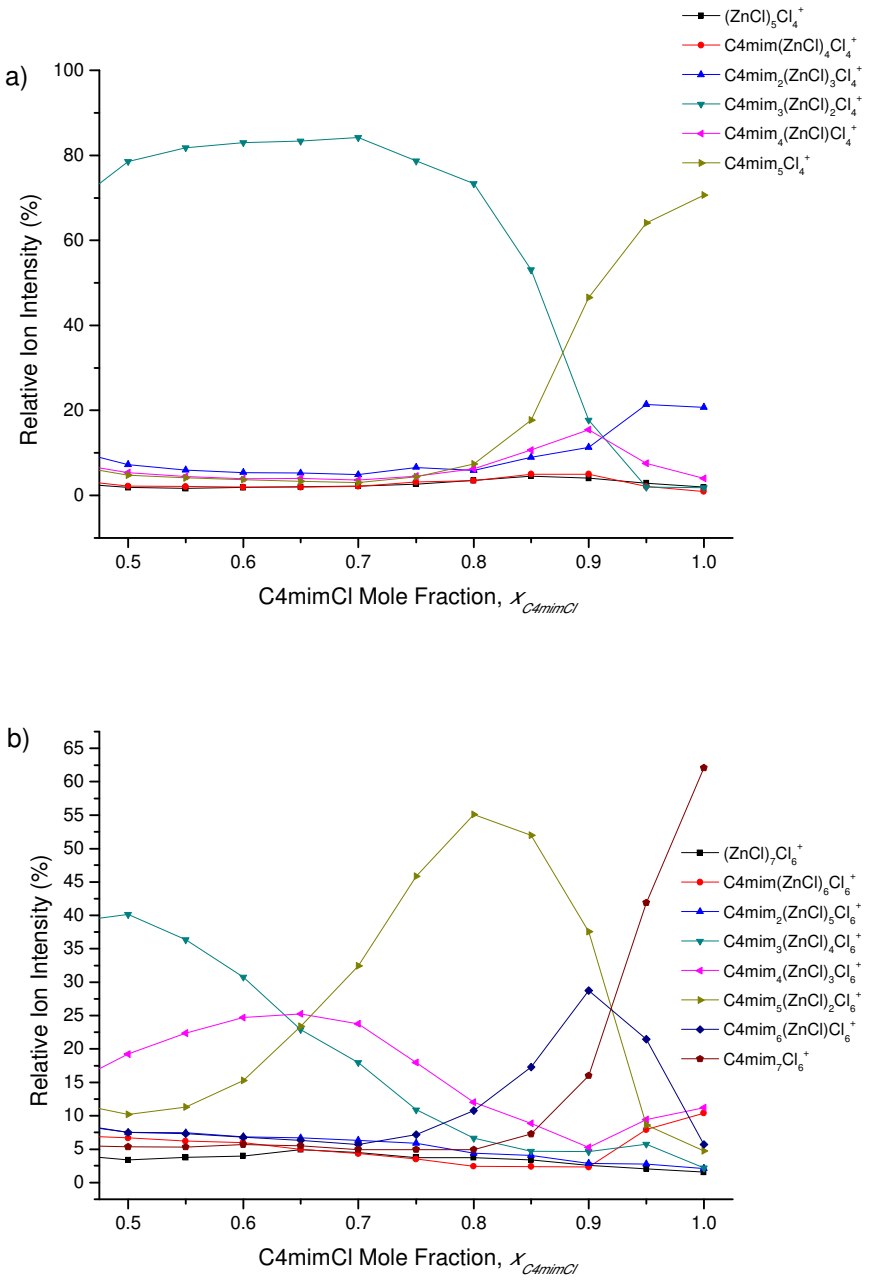

Figure 5-27 Relative ion intensity as the C4mimCl mole fraction is varied from 0.5 to 1.0 in mixtures with $ZnCl_2$. Intensities are shown for all possible aggregates a) $Cation_5Cl_4^+$ b) $Cation_7Cl_6^+$ where Cation is $C4mim^+$ or $(ZnCl)^+$.

As stated above the C4mimCl mole fraction was varied from 0 to 1 in solutions with $ZnCl_2$ at 5 % intervals. The relative ion intensities were recorded as $x_{C4mimCl}$ varied for the aggregates $Cation_5Cl_4^+$ and $Cation_7Cl_6^+$ where Cation is $C4mim^+$ or $(ZnCl)^+$. The relative ion intensities are shown as a function of C4mimCl mole fraction in the

range $0.5 \leq x_{C4mimCl} \leq 1.0$ in Figure 5-27. When $x_{C4mimCl} = 1$ the spectrum is dominated by the pure IL peaks. However with increasing $ZnCl_2$ concentration mixed aggregates rapidly form. Figure 5-27(a) is dominated by the ion $C4mim_3Zn_2Cl_6^+$ which was seen to form with a very high abundance. This is true all the way from $x_{C4mimCl} = 0.85$ to below 0.5. Figure 5-27(b) is very different; it shows the formation of many different mixed complexes as was seen with previous metals. Sequential substitution of an IL $C4mim^+$ cation by $(ZnCl)^+$ is seen throughout this graph. The maximum relative intensities are observed at $x_{C4mimCl} = 0.90$, 0.80, 0.65 and 0.50 for $C4mim_{7-n}(ZnCl)_nCl_6^+$ where $n = 1$ to 4 respectively.

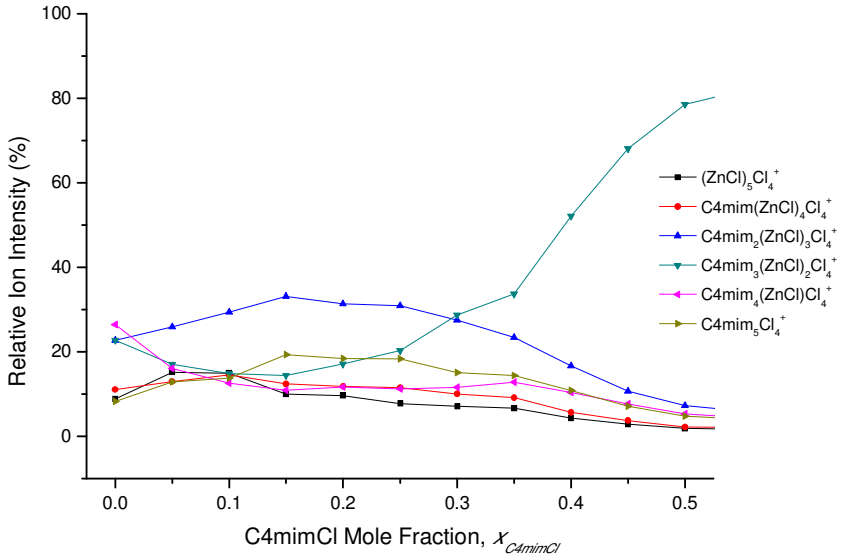

Figure 5-28 Relative ion intensity as the C4mimCl mole fraction is varied from 0.0 to 0.5 in mixtures with $ZnCl_2$. Intensities are shown for all possible aggregates $Cation_5Cl_4^+$ where Cation is $C4mim^+$ or $(ZnCl)^+$.

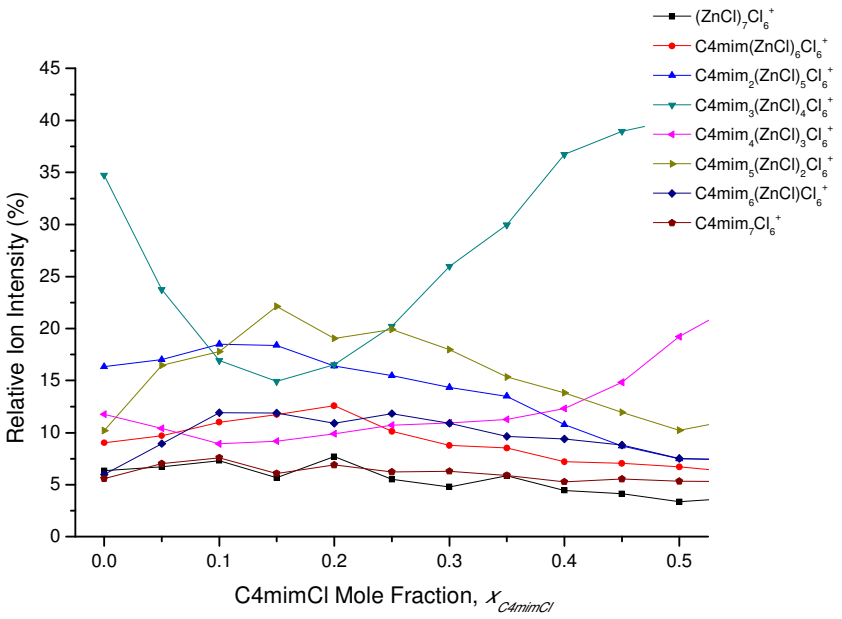

Figure 5-29 Relative ion intensity as the C4mimCl mole fraction is varied from 0.0 to 0.5 in mixtures with $ZnCl_2$. Intensities are shown for all possible aggregates $Cation_7Cl_6^+$ where Cation is $C4mim^+$ or $(ZnCl)^+$.

Figure 5-28 and Figure 5-29 show the result of the C4mimCl mole fraction varying between 0.0 and 0.5. In these graphs the aggregates which contain 0 or 1 $C4mim^+$ are not seen as they are not preferentially formed. However in Figure 5-28 the presence of $C4mim_3Zn_2Cl_6^+$ continues until $x_{C4mimCl} = 0.3$ when the aggregate $C4mim_2Zn_3Cl_7^+$ is seen to form with a maximum value at $x_{C4mimCl} = 0.15$. Figure 5-29 shows the decrease of $C4mim_3Zn_4Cl_{10}^+$ and an increase in the $C4mim_2Zn_5Cl_{11}^+$ series as might be expected. There are also unexpected rises in the series labelled $C4mim_3Zn_4Cl_{10}^+$ and $C4mim_5Zn_2Cl_8^+$; however, this is due to the overlapping of different species.

5.1.6 Collision Induced Dissociation

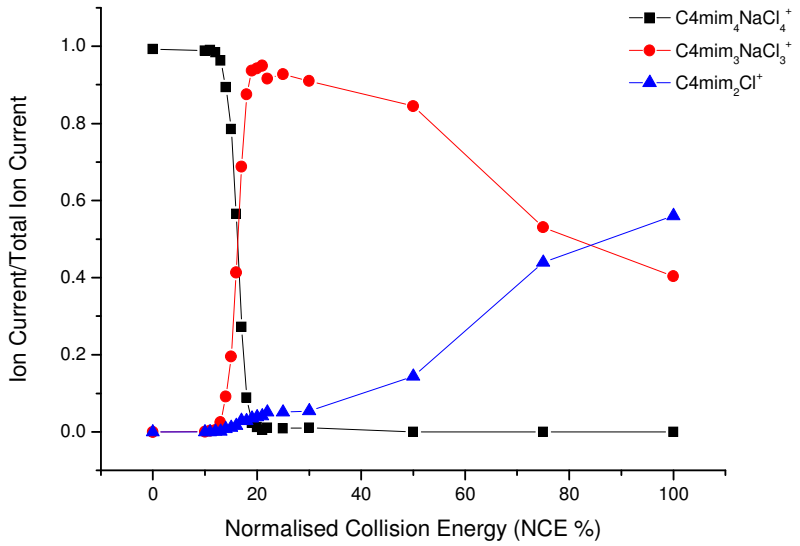

Figure 5-30 Ion Current/Total Ion Current for the collisional activation for $C4mim_4NaCl_4^+$ with varying NCE.

CID experiments were performed on a number of the mixed aggregates which were formed during the MS experiments. The mole fraction studies in the previous sections showed that solutions with 10 % of the concentration from the metal chloride and 90 % of the solution from the C4mimCl resulted in the formation of aggregates with a single metal ion. Solutions were prepared with this ratio of salts and a total concentration of 5 mM (0.5 mM metal chloride and 4.5 mM C4mimCl) in a 90:10 mixture of methanol and water. These solutions were used for the following CID investigations. Figure 5-30 shows the result of a CID experiment on $C4mim_4NaCl_4^+$. With increasing NCE the loss of the parent ion can be observed which can be seen to rapidly decrease from 1 to 0 indicating its complete loss for higher NCE values. Meanwhile the aggregate $C4mim_3NaCl_3^+$ increases as $C4mim_4NaCl_4^+$ decreases. This indicates that the initial fragmentation is by the loss of a neutral C4mimCl ion pair. However there is additionally a small amount, about 5 %, of the aggregate $C4mim_2Cl^+$ present. As the NCE value becomes larger than 30 % the $C4mim_3NaCl_3^+$ aggregate decreases. There is also a corresponding increase in $C4mim_2Cl^+$. While not shown, this pattern of breaking down to $C4mim_3MCl_3^+$ was present throughout the alkali metal series for $M = Li^+$, Na^+, K^+ and Cs^+. This was

followed by the increase in the $C4mim_2Cl^+$ aggregate which has been seen to be prominent in many different mass spectra with occasionally a very small formation of $C4mim_2MCl_2^+$ particularly where $M = Cs^+$.

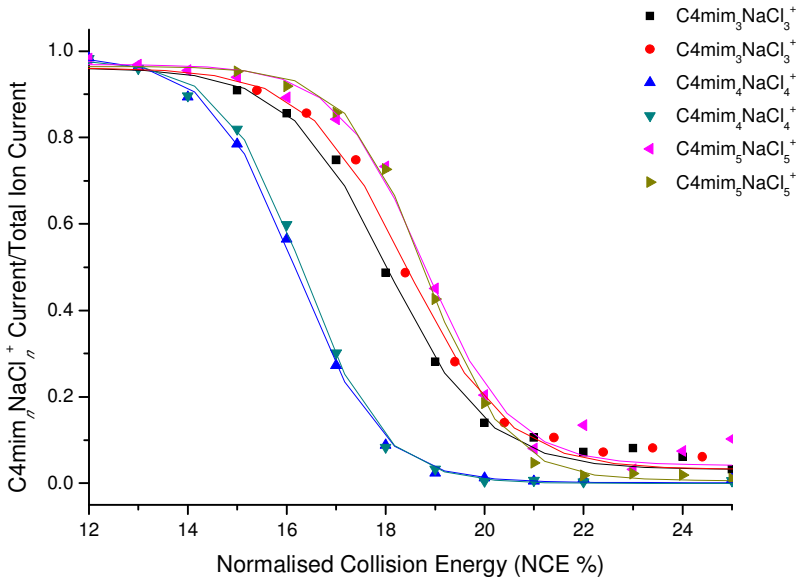

Figure 5-31 $C4mim_nNaCl_n^+$ Ion Current/Total Ion Current for the collisional activation of $C4mim_nNaCl_n^+$ for n = 3 to 5 with varying NCE. Breakdown of the parent ions only are displayed.

The breakdown curves obtained for the CID experiment with $C4mim_nNaCl_n^+$ for n = 3 to 5 are shown in Figure 5-31. Each of the different aggregates has 2 repeated runs to show the consistency between the curves. The amount of energy required to fragment the parent ion is an indication of its relative stability. Thus Figure 5-31 indicates that the $C4mim_4NaCl_4^+$ aggregate is the least stable. The $C4mim_3NaCl_3^+$ aggregate is the next least stable followed by the $C4mim_5NaCl_5^+$ aggregate. The high stability of n = 3 compared with n = 4 potentially suggests a steric factor where the additional ion pair is causing an instability with a possible structural change taking place for n = 5.

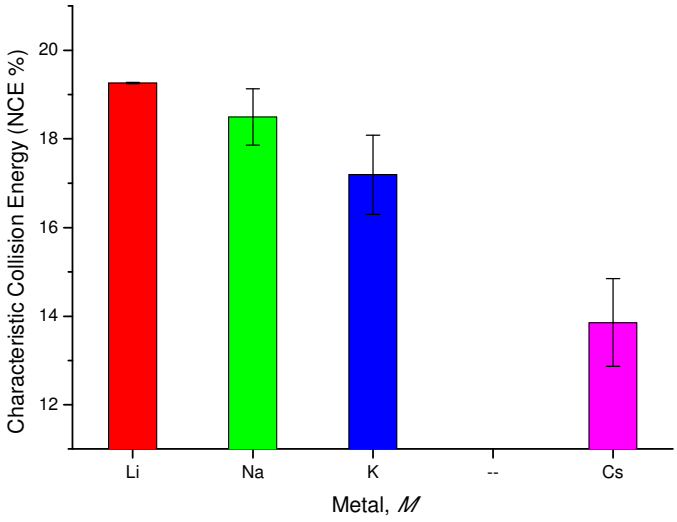

Figure 5-32 The CCE of the parent ion breakdown curves plotted against the aggregate size of $C4mim_3MCl_3^+$ for $M = Li^+$, Na^+, K^+ and Cs^+.

The CID experiments were repeated for mixed aggregates containing Li^+, K^+ and Cs^+. The NCE required to break down the aggregates $C4mim_3MCl_3^+$ is shown in Figure 5-32 for $M = Li^+$, Na^+, K^+ and Cs^+. The error bars indicate the standard deviation in the different repeats. This graph shows that as the metal ion is sequentially replaced going down group 1 of the periodic table the relative stability of the aggregates decreases. When this is compared with the lattice energies for the alkali metal chlorides it is in line with this trend. The lattice energies for LiCl (834 $kJmol^{-1}$), NaCl (769 $kJmol^{-1}$), KCl (701 $kJmol^{-1}$) and CsCl (657 $kJmol^{-1}$) were calculated using the Born-Haber cycle.[2] This close similarity suggests that the experimental stabilities are primarily due to the strength of the alkali metal to chlorine binding.

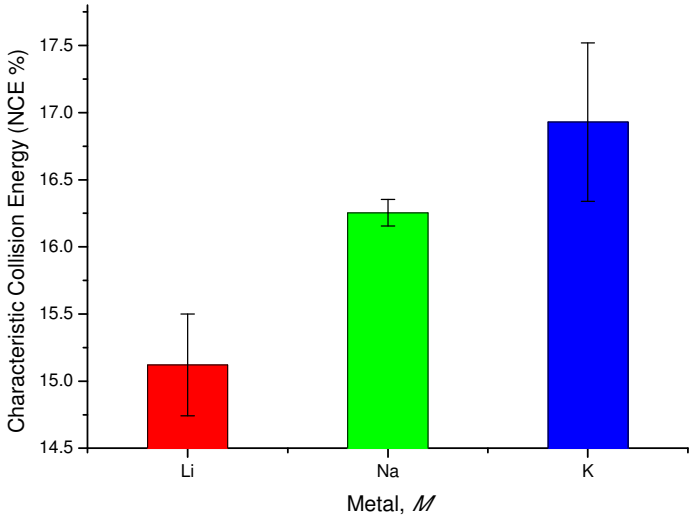

Figure 5-33 The CCE of the parent ion breakdown curves plotted against the aggregate size of C4mim$_4$*M*Cl$_4^+$ for *M* = Li$^+$, Na$^+$ and K$^+$.

The experiments were repeated for C4mim$_4$*M*Cl$_4^+$ where *M* = Li$^+$, Na$^+$ and K$^+$. The experimental stabilities are shown in Figure 5-33 with associated standard deviations obtained for the multiple repeats of the experimental series. This graph shows a trend which is opposite to what was previously observed in Figure 5-32. In this case as the size of the metal ion increases the relative stability of the aggregate also increases. As was seen previously when the C4mim$_3$*M*Cl$_3^+$ aggregates fragment, the lone observable fragment in the mass spectra is C4mim$_2$Cl$^+$. However the larger C4mim$_4$*M*Cl$_4^+$ aggregates fragment to a combination of the C4mim$_3$*M*Cl$_3^+$ and C4mim$_2$Cl$^+$ aggregates. There may be a driving force to reach the C4mim$_3$*M*Cl$_3^+$ aggregates where of course the smaller metal ions are most stable but it seems probable that there is a steric factor involved. As the size of the metal ion increases there is more space around to accommodate the larger number of ions. This steric factor may then be a larger factor than the metal-chlorine bonding strengths for determining the aggregate stability. The structure of these ions will be investigated in greater detail later in this chapter.

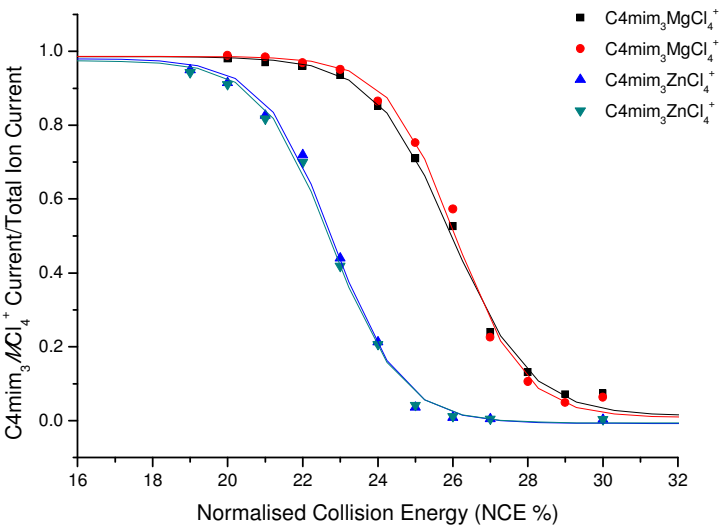

Figure 5-34 $C4mim_3MCl_4^+$ Ion Current/Total Ion Current for the collisional activation of $C4mim_3MCl_4^+$ for *M* = Mg^{2+} and Zn^{2+} with varying NCE. Breakdown of the parent ions only are displayed.

The breakdown curves for $C4mim_3MCl_4^+$ are shown in Figure 5-34 for the metals Mg^{2+} and Zn^{2+}. Two repeated measurements are shown for each metal to show consistency and reproducibility. These aggregates were formed in large abundance during the previous mole fraction studies for these mixed solutions which led to their further study. Figure 5-34 shows that the traces for $C4mim_3MgCl_4^+$ have a significantly higher CCE values indicating that they are more stable than their zinc counter parts.

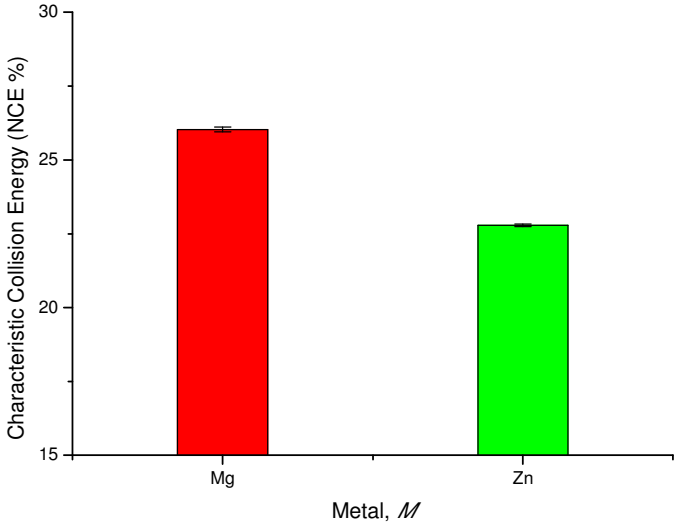

Figure 5-35 CCE of the parent ion breakdown curves plotted against the aggregate size of $C4mim_3MCl_4^+$ for $M = Mg^{2+}$ and Zn^{2+}.

The experimental stabilities are shown in Figure 5-35 for $C4mim_3MgCl_4^+$ and $C4mim_3ZnCl_4^+$. As was suggested above, the magnesium example was found to be higher in energy. The difference in NCE between the two aggregates was calculated to be 3 %. The structure of these aggregates will be investigated later in the chapter using computational calculations in order to gain more insight.

5.2 Computational Chemistry

The structures of different $C4mim_{n+1}Cl_n^+$ aggregates were determined by DFT calculations using the Gaussian 03 suite of programs in Section 4.2.[3] The structures of some of the mixed aggregates previously seen in this chapter were investigated in a similar fashion. In order to investigate these aggregates the previous structures were taken as a starting point and modified while maintaining the same structural motifs. These calculations were performed using the B3LYP hybrid DFT method and initially the CEP-31G* basis set. This basis set was used but in later sections this was replaced due to its limitations and where this is the case the replacement basis set is clearly given. All of the results displayed have been fully optimised and confirmation of their minimum energy status was confirmed by frequency analysis. Many of the $C4mim_2NaCl_2^+$ calculations were repeated with the 6-311+G(d,p) basis set to ensure

consistency with the higher level of theory similar to the $C4mim_{n+1}Cl_n^+$ aggregates previously shown.

5.2.1 NaCl and C4mimCl

The first mixed aggregate studied by computational chemistry was $C4mim_2NaCl_2^+$. This aggregate is similar to $C4mim_2Cl^+$ and $C4mim_3Cl_2^+$; the former with an additional NaCl ion pair and the latter with a $C4mim^+$ replaced by Na^+. Many different conformations were postulated and eventually stabilised based on the previously determined structures.

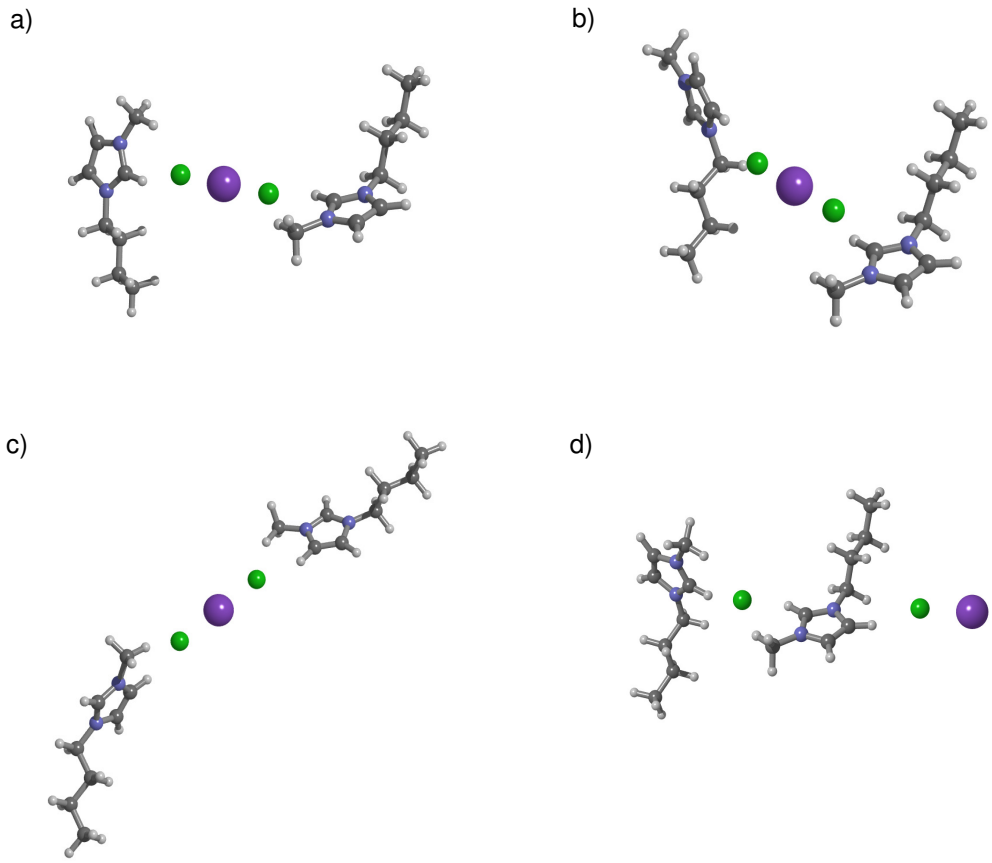

Figure 5-36 Four of the stable calculated conformations of $C4mim_2NaCl_2^+$ which were calculated using the B3LYP DFT method and the CEP-31G* basis set. Structures are labelled a) FrM-FrM b) FrB-BuS c) MeS-MeS d) BuS-FrM-out.

Four of the stabilised structures of $C4mim_2NaCl_2^+$ are shown in Figure 5-36. Considering these as $C4mim_2Cl^+$ with an additional NaCl ion pair there are clear

similarities between the structures. The structures shown in Figure 5-36(a), (b) and (c) have the additional ion pair inserted into the centre of the aggregate with the two $C4mim^+$ cations each adopting conformations as were seen before. Figure 5-36(a) shows an elongated FrM-FrM conformation which was previously observed to be the most stable in the absence of sodium. For simplicity these structures with the sodium in the centre will be named as was previously done for the $C4mim_2Cl^+$ aggregates. As a result, Figure 5-36(a) is the FrM-FrM conformation, Figure 5-36(b) is FrB-BuS and Figure 5-36(c) is the MeS-MeS conformation. Figure 5-36(d) shows an example where the sodium cation is no longer acting as a core to the aggregate and is now resident on the outside. These structures can be considered equivalent to adding the NaCl ion pair to the outside of $C4mim_2Cl^+$ or replacing an outer $C4mim^+$ cation in $C4mim_3Cl_2^+$. These conformations will be labelled according to the central cation with the conformation adopted on the metal side being given first. Additionally a clear indication will be given to show the metal lies on the outside of the aggregate. As a result the species shown in Figure 5-36(d) is labelled BuS-FrM-out. Nineteen structures of $C4mim_2NaCl_2^+$ have been stabilised; 15 have the Na^+ inside the aggregate while only 4 have it residing on the outside.

Table 5-1 Relative energy differences of the complete series of $C4mim_2NaCl_2^+$ aggregates calculated using the CEP-31G* basis set.

Cation 1 Conformation	Cation 2 Conformation	Na^+ Position	Relative Energy ($kJmol^{-1}$)
FrM	FrM	Inside	0.0
FrM	FrB	Inside	0.6
FrB	FrB	Inside	1.1
FrM	MeS	Inside	16.9
FrM	BuS	Inside	15.5
FrB	MeS	Inside	17.5
FrB	BuS	Inside	16.0
FrM	Back	Inside	34.5
FrB	Back	Inside	32.9
MeS	MeS	Inside	31.3
MeS	BuS	Inside	31.3
BuS	BuS	Inside	33.0
MeS	Back	Inside	49.0
BuS	Back	Inside	47.4
Back	Back	Inside	63.9
FrB	MeS	Outside	86.2
FrM	BuS	Outside	84.8
MeS	FrB	Outside	82.2
BuS	FrM	Outside	79.9

Table 5-1 shows all of the different stabilised structures along with relative energies compared with the lowest energy FrM-FrM conformation. Similar to what was previously seen for $C4mim_2Cl^+$, groupings of relative energy are observed. Combinations of two front conformations are seen to be the most stable and the different possibilities are seen to be effectively degenerate. Then energy penalties are seen for transforming each $C4mim^+$ cation into side and back conformations. The energy penalty for changing from a front conformation to a side conformation is around 16 to 18 $kJmol^{-1}$. Meanwhile the difference between a $C4mim^+$ cation in front position and a back position is about 31 to 33 $kJmol^{-1}$. As was previously seen for $C4mim_2Cl^+$ the energy penalties are additive so estimates for the whole series can be made with only a few values. The last four conformations are examples where the Na^+ cation is located on the outside of the aggregate rather than inside. These structures are close in energy to each other and all of them are between 79 $kJmol^{-1}$ and 87 $kJmol^{-1}$ higher in energy than the most stable conformation. While they are close in energy, it can be seen that the aggregates where the central $C4mim^+$ is oriented with the front side of the imidazolium ring away from the Na^+ cation are more stable than the ones where it faces towards it.

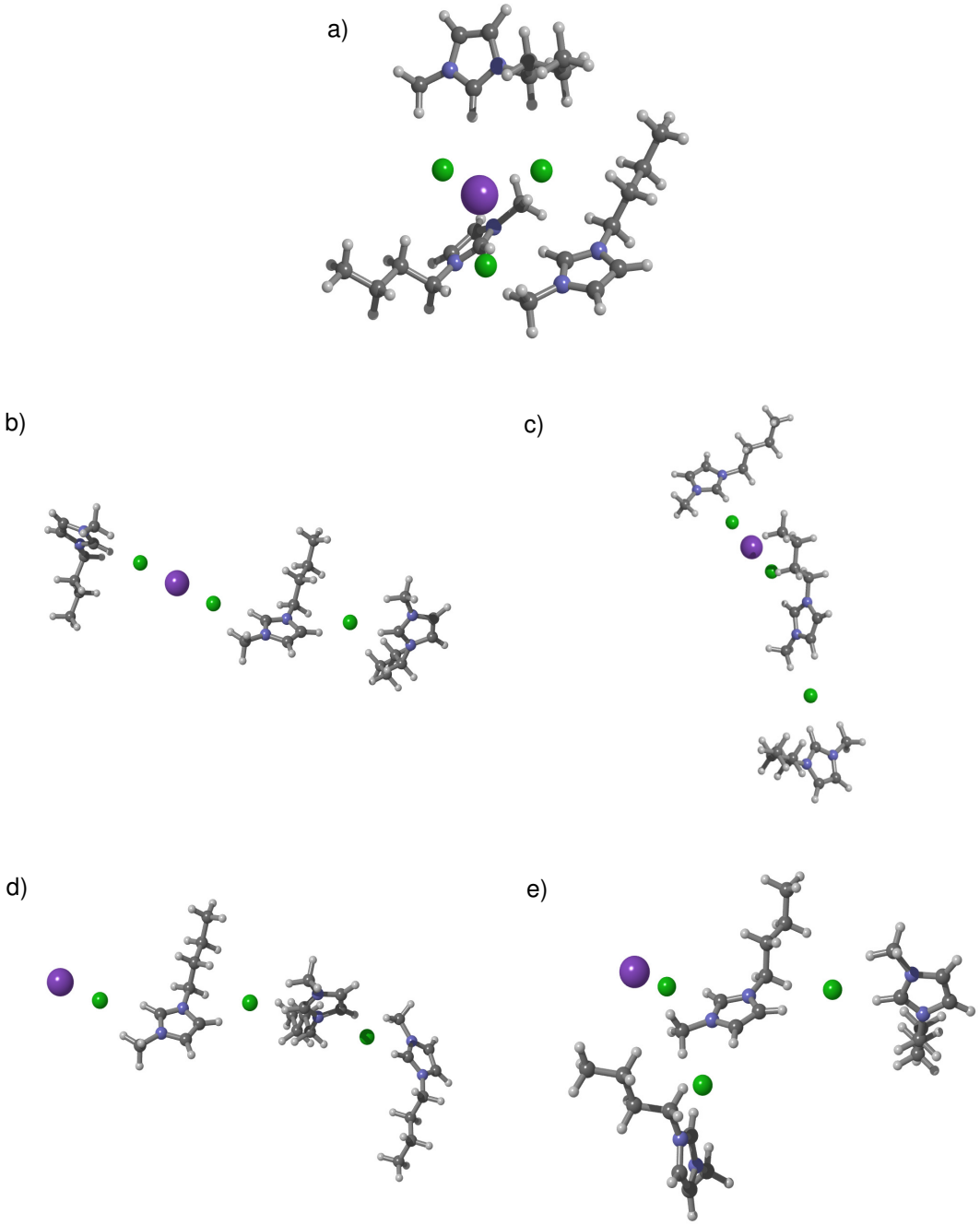

Figure 5-37 Stable calculated conformations of $C4mim_3NaCl_3^+$ which were calculated using the B3LYP DFT method and the CEP-31G* basis set.

The next aggregate to be studied was also in the $C4mim_nNaCl_n^+$ series with $n = 3$. The calculated low minimum energy structures are displayed in Figure 5-37. These

structures can be categorised into three different sets. The first set consists only of the conformation in Figure 5-37(a). The Na^+ cation is observed to interact with three different chlorine anions with the $C4mim^+$ cations forming an outer shell with all of them interacting via their front positions. The sodium ion appears to be acting as a core for the aggregate. Additionally two of the cations are seen to interact with two of the chlorine anions. The second set of structures would be in Figure 5-37(b) and (c) where the sodium cation is now only interacting with two different anions. These structures strongly resemble the stable FrM-FrM and FrM-FrM conformations of $C4mim_2NaCl_2^+$ with an additional C4mimCl ion pair binding to the outside of the aggregate either via a BuS or MeS conformation in Figure 5-37(b) and (c) respectively. The final set of structures is shown in Figure 5-37(d) and (e). In these structures the sodium cation only binds to a single chlorine anion. Figure 5-37(d) is an example where the C4mimCl ions form a chain progressing away from the sodium adopting similar patterns previously seen in Chapter 4. Meanwhile in Figure 5-37(e) the chain branches and one of the $C4mim^+$ cations forms bonds with all three of the present anions. Thus unlike the example in Figure 5-37(a) it is a $C4mim^+$ acting as a core to the aggregate. In this case it is worth noting that the outer $C4mim^+$ cations are not able to bind to multiple chlorine anions. Thus stable structures have been found with the sodium appearing anywhere from the core of the aggregate to the outer reaches of the ion.

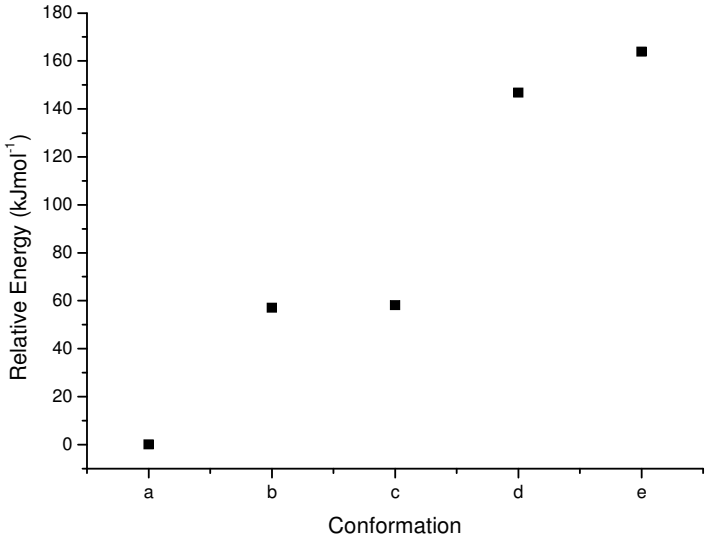

Figure 5-38 Relative energy differences of the $C4mim_3NaCl_3^+$ aggregates calculated using the CEP-31G* basis set.

The calculated relative energy differences of the structures shown in Figure 5-37 are displayed in Figure 5-38. Conformation (a) is seen to be the most stable structure. This follows on from $C4mim_2NaCl_2^+$ where the structures with the Na^+ ion at the centre of the aggregate between front positions were the most stable. The second set of structures is seen to be approximately 60 $kJmol^{-1}$ higher in energy. The Na^+ continues to act as a core in this case however one of the C4mimCl ion pairs has moved to the outside. Considering the third set of structures, it is found that they are even higher in energy showing a preference in this case for the metal to be surrounded by progressively large numbers of chlorine anions. Conformation (d) is seen to be more stable than conformation (e) which indicates a preference for the $C4mim^+$ cations to bind with two anions rather than three in this aggregate.

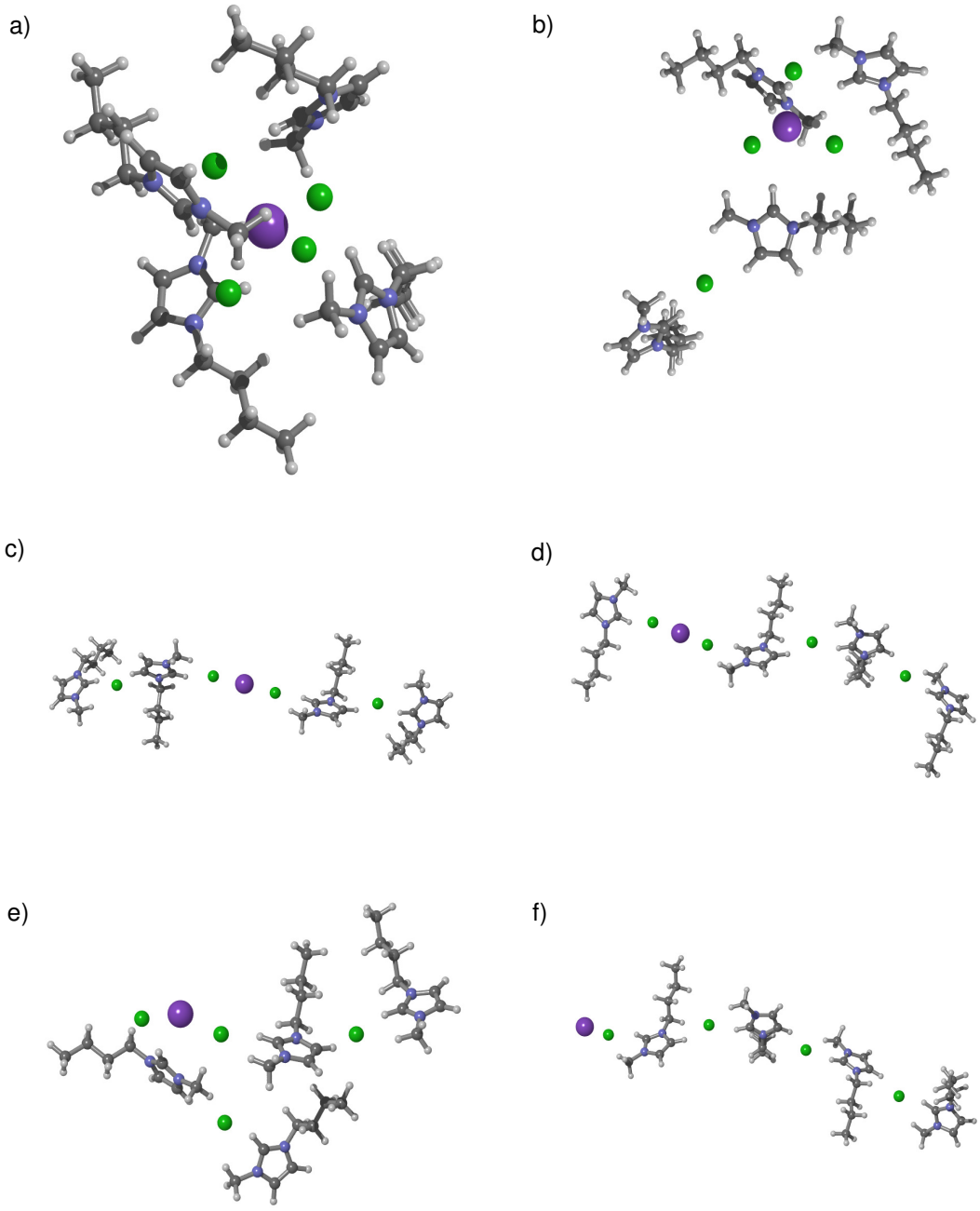

Figure 5-39 Stable calculated conformations of $C4mim_4NaCl_4^+$ which were calculated using the B3LYP DFT method and the CEP-31G* basis set.

The series of aggregates containing a single sodium cation was extended by a further C4mimCl ion pair and structures of $C4mim_4NaCl_4^+$ were stabilised. The stabilised structures of these aggregates are displayed Figure 5-39. As was previously done, the aggregates can be described in terms of the number of chlorine anions interacting with the metal cation. The conformation in Figure 5-39(a) is surrounded by all four

of the available chlorine anions. In this case the sodium is the core of the aggregate with the other ions tightly positioned around the centre. Conformation (b) is very similar to the low energy structure of $C4mim_3NaCl_3^+$ with an additional C4mimCl ion pair bound to the outside of one of the $C4mim^+$ cations. In this case the sodium ion is surrounded by three chlorine anions. The conformations (c), (d) and (e) all have two chlorine anions adjacent to the sodium cation. Structures (c) and (d) are linear with two C4mimCl ion pairs on each side of the metal in (c) and the ions pairs split three and one on each side in (d). Conformation (e) is similar to (c) however the linear structure has been wrapped back on itself allowing an additional $C4mim^+$ to Cl^- interaction. This has the effect of decreasing the Cl-Na-Cl angle to 139.6 °, in turn exposing one side of the ion. Conformation (f) is a linear structure where the sodium ion only interacts with a single chlorine anion. This structure is very similar to structure (d) for $C4mim_3NaCl_3^+$ which was seen to be one of the least stable for that ion.

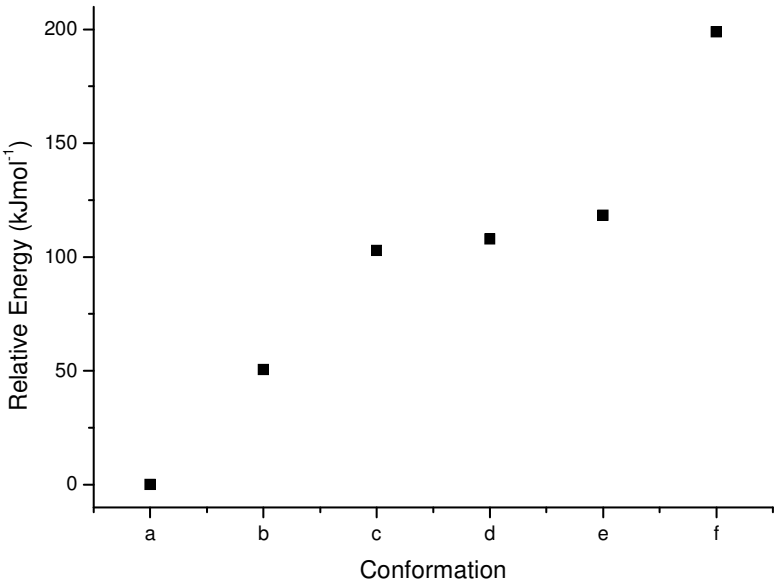

Figure 5-40 Relative energy differences of the $C4mim_4NaCl_4^+$ aggregates calculated using the CEP-31G* basis set.

Figure 5-40 shows the calculated relative energy values for the conformations of $C4mim_4NaCl_4^+$ displayed in Figure 5-39. Conformation (a) was found to be the most stable. This continues the trend of the metal ion acting as a core for the aggregates

for the lowest energy conformations. Moving one of the cations away from the metal to the outside of the $C4mim^+$ in (b) has an energy penalty of about 50 $kJmol^{-1}$. Meanwhile moving a second ion pair away from the metal core costs a further 50 $kJmol^{-1}$ as shown for structures (c), (d) and (e). These are displayed in order of increasing relative energy with small energy increases associated with going from (c) to (d). A larger penalty is observed to reach conformation (e) which may be due to an increased steric repulsion or the strain put on the Na^+ ion. Conformation (f) with its single metal to chlorine interaction was found to be significantly higher in energy further underlining the cost of exposing the metal cation.

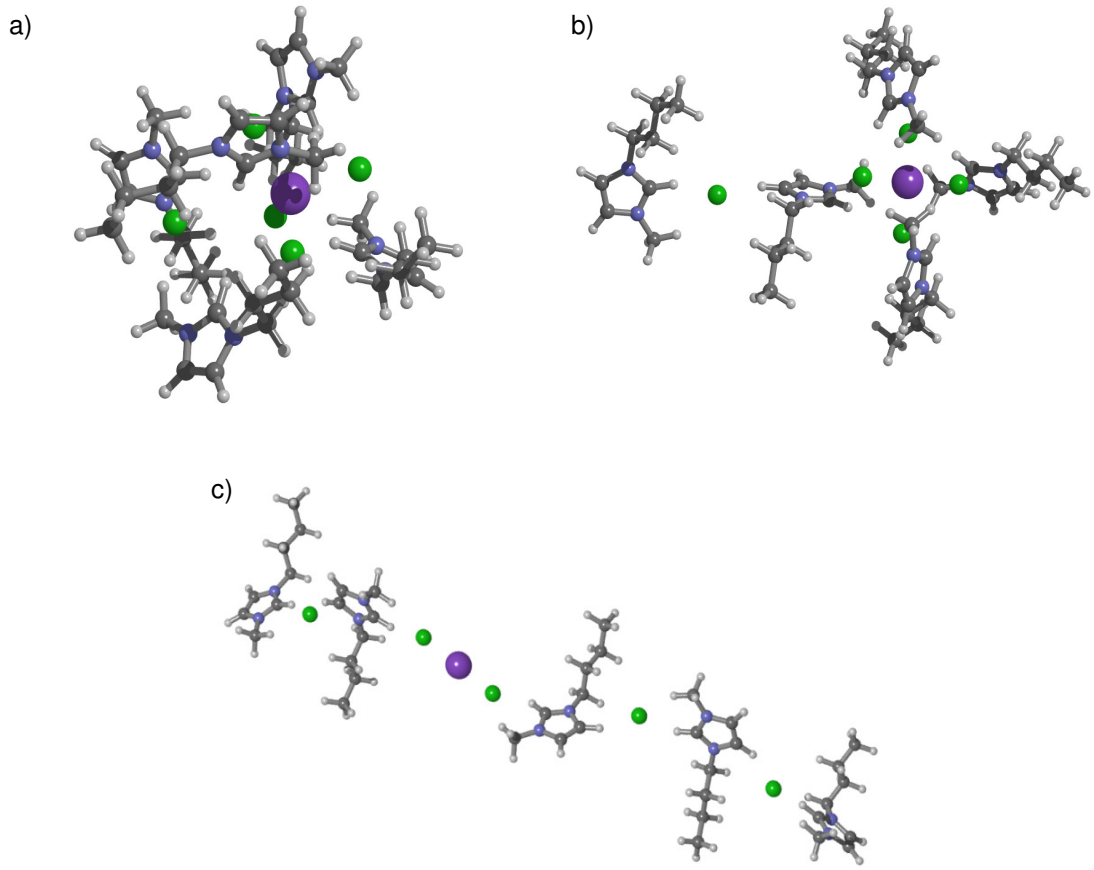

Figure 5-41 Stable calculated conformations of $C4mim_5NaCl_5^+$ which were calculated using the B3LYP DFT method and the CEP-31G* basis set.

The series of sodium containing aggregates was further extended to $C4mim_5NaCl_5^+$. Three structures were stabilised for this 131 atom aggregate and they are shown in

Figure 5-41. The conformation shown in Figure 5-41(a) is very difficult to display however it has the sodium ion acting as a core with all five of the C4mimCl ion pairs arranged around it. They are not evenly spaced with one of the chlorine ions further away as is shown on the left side of the picture. The remaining four chlorine ions form a distorted tetrahedral structure with a vacant space towards the fifth anion. Conformation (b) is similar to the low energy structure of $C4mim_4NaCl_4^+$ with an additional ion pair bound to the outside of the aggregate. This aggregate therefore has four of the chlorine anions directly interacting with it. Meanwhile the final conformation only has two ions interacting with the metal centre. Indeed conformation (c) is an extended linear structure similar to Figure 5-39(c).

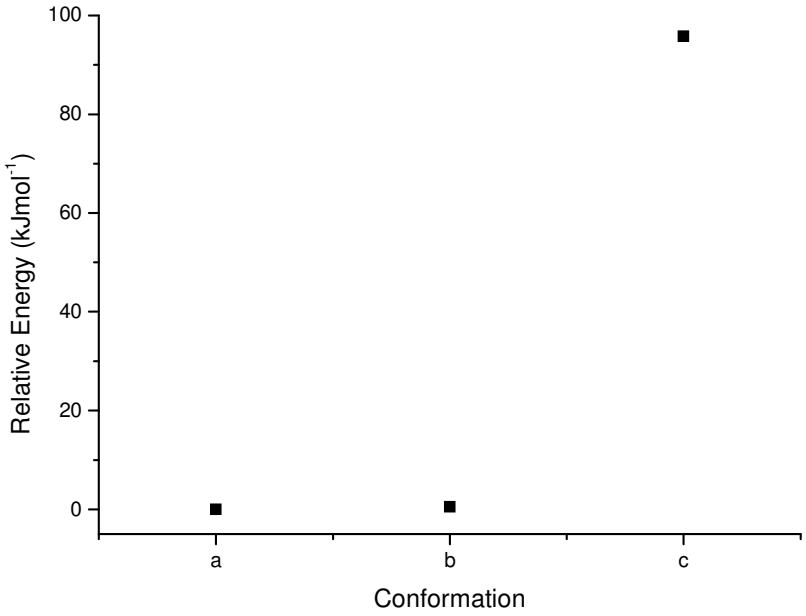

Figure 5-42 Relative energy differences of the $C4mim_5NaCl_5^+$ aggregates calculated using the CEP-31G* basis set.

The relative energies of the different structures of the $C4mim_5NaCl_5^+$ aggregates shown in Figure 5-41 are displayed in Figure 5-42. It can be observed that conformation (a) is the most stable conformation. This is the aggregate most similar to the previous low energy structures with the metal as the core. However there was clearly a large degree of steric hindrance in this structure and as a result this conformation is almost degenerate with structure (b). If this aggregate was following

the previous trends, conformation (b) would be 40 to 50 kJmol^{-1} higher in energy than a however that is clearly not the case. This similarity clearly indicates that having all the ions around the Na^+ ion is becoming prohibitively difficult for this size of aggregate. The energy difference of about 100 kJmol^{-1} between conformations (b) and (c) is very similar to the corresponding change between conformations (a) and (c) for $C4mim_4NaCl_4^+$. This indicates that the additional C4mimCl is not greatly influencing the relative stability of these particular structures.

5.2.2 LiCl and C4mimCl

Table 5-2 Relative energy differences of the complete series of $C4mim_2NaCl_2^+$ and $C4mim_2LiCl_2^+$ aggregates calculated using the CEP-31G* basis set.

Cation 1 Conformation	Cation 2 Conformation	Metal Position	Relative Energy (kJmol^{-1})	
			$C4mim_2NaCl_2^+$	$C4mim_2LiCl_2^+$
FrM	FrM	Inside	0.0	0.0
FrM	FrB	Inside	0.6	0.7
FrB	FrB	Inside	1.1	0.7
FrM	MeS	Inside	16.9	15.9
FrM	BuS	Inside	15.5	14.1
FrB	MeS	Inside	17.5	16.2
FrB	BuS	Inside	16.0	14.4
FrM	Back	Inside	34.5	32.6
FrB	Back	Inside	32.9	30.6
MeS	MeS	Inside	31.3	28.6
MeS	BuS	Inside	31.3	28.0
BuS	BuS	Inside	33.0	29.7

Cation 1 Conformation	Cation 2 Conformation	Metal Position	Relative Energy ($kJmol^{-1}$)	
			$C4mim_2NaCl_2^+$	$C4mim_2LiCl_2^+$
MeS	Back	Inside	49.0	44.9
BuS	Back	Inside	47.4	42.9
Back	Back	Inside	63.9	57.6
FrB	MeS	Outside	86.2	109.8
FrM	BuS	Outside	84.8	109.0
MeS	FrB	Outside	82.2	106.8
BuS	FrM	Outside	79.9	101.4

Following from the calculations of sodium containing mixed aggregates, the structures of lithium containing aggregates which were previously observed by MS were also calculated. As lithium and sodium are both group 1 alkali metals they would be expected to interact in a similar manner with the IL. The structures which were found for the $C4mim_2LiCl_2^+$ aggregate are very similar to those seen for the $C4mim_2NaCl_2^+$ aggregate. The different structures are listed and associated relative energy values given for $C4mim_2NaCl_2^+$ and $C4mim_2LiCl_2^+$ in Table 5-2. The same combinations of conformations are observed for both series and they are grouped accordingly in the table. It can be readily observed that while the metal ion remains in the centre of the aggregate, the relative energy trends are very similar to each other. The energy penalty for changing a front conformation to a side conformation is between 14 and 16 $kJmol^{-1}$. Meanwhile the difference between a front and a back conformation is between 30 and 32 $kJmol^{-1}$.The relative energy differences for the $C4mim_2LiCl_2^+$ are found to be 1 to 6 $kJmol^{-1}$ lower than the equivalent values for the $C4mim_2NaCl_2^+$ with this value increasing as the aggregates diverge more from the low energy conformation. There is a significant difference between the relative energy values for the aggregates where the metal ion resides on the outside. For the

sodium containing aggregates these conformations were between 80 and 90 kJmol^{-1} higher in energy. However, for $C4mim_2LiCl_2^+$ the difference has increased to be between 100 and 110 kJmol^{-1}. Both of these aggregates favour having two anions bound to the metal however the aggregate incorporating lithium favours this to a greater degree. For these aggregates there is little or no problem with the steric hindrance around the metal centres, but the metal to chlorine bond strength is increasing from sodium to lithium which may be a factor in this increased stability.

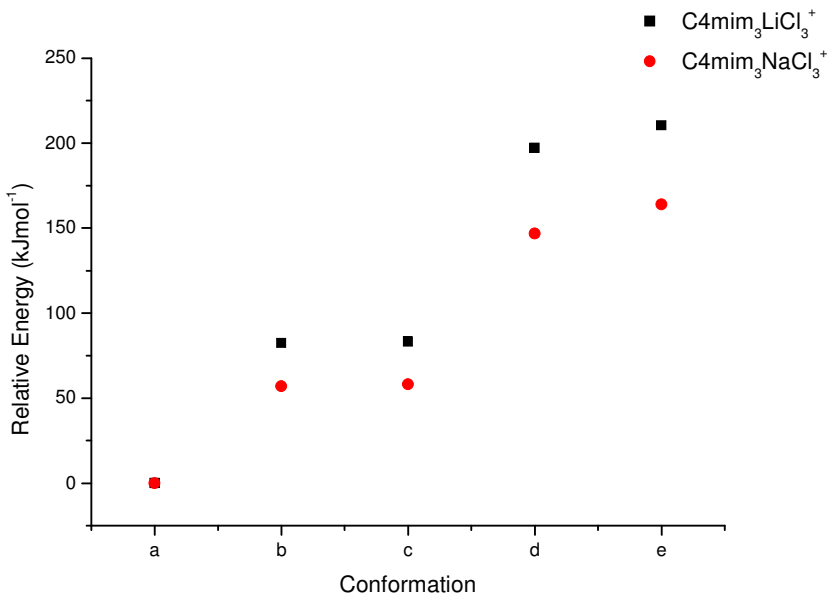

Figure 5-43 Relative energy differences of the $C4mim_3LiCl_3^+$ and $C4mim_3NaCl_3^+$ aggregates calculated using the CEP-31G* basis set.

The aggregate size was once again increased by a C4mimCl ion pair to produce $C4mim_3LiCl_3^+$. Similar conformations to those observed for the sodium equivalent in Figure 5-37 were stabilised for this aggregate. The $C4mim_3LiCl_3^+$ structures were very similar with the reduced metal to chlorine bond distance generally the only difference. However the equivalent structure to the one shown in Figure 5-37(a) was most affected by this change with twisting observed of the $C4mim^+$ cations and their butyl chains to take account of the larger steric hindrance. The relative energy was again calculated relative to the most stable aggregate and these values along with the equivalent results for $C4mim_3NaCl_3^+$ are shown in Figure 5-43. The two series follow a very similar pattern with conformation (a) as the most stable, then structures

(b) and (c) roughly degenerate. Finally the relative energy is seen to rise for conformations (d) and (e). The two series do exhibit very different magnitudes of the observed energy differences. The relative energy of conformations (b) and (c) is about 25 kJmol^{-1} higher for $C4mim_3LiCl_3^+$ while for (d) and (e) that difference is about 50 kJmol^{-1}. This follows on from the $C4mim_2LiCl_2^+$ structures where multiple metal-chlorine interactions gave a larger stability increase for lithium compared with sodium.

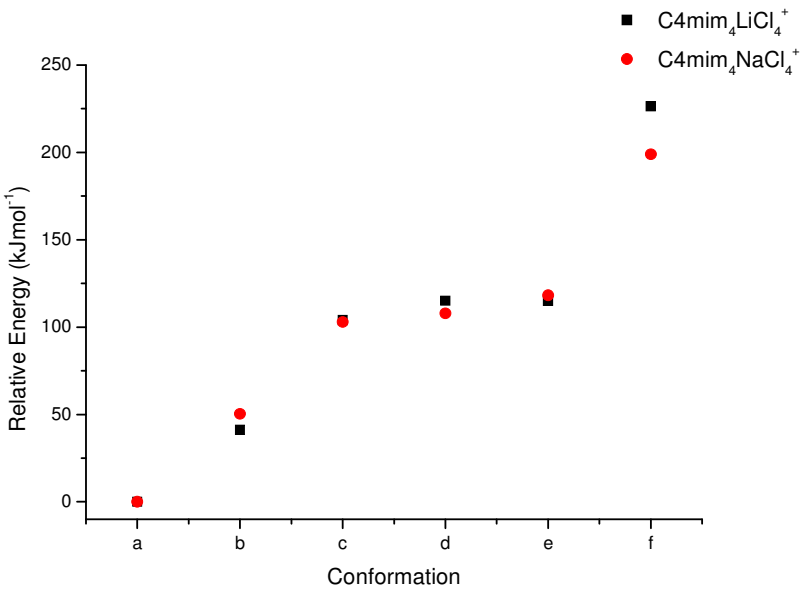

Figure 5-44 Relative energy differences of the $C4mim_4LiCl_4^+$ and $C4mim_4NaCl_4^+$ aggregates calculated using the CEP-31G* basis set.

The size of the aggregate was once again increased by incorporating a fourth C4mimCl ion pair. As was the case with the smaller aggregates, conformations which were equivalent to the sodium containing aggregates were found to be stable. Due to the smaller size of the lithium ion the metal-chlorine distance was significantly smaller. When the larger number of anions were surrounding the metal it was increasingly difficult to accommodate such a large number of $C4mim^+$ cations in such close proximity. As a result of this, the $C4mim^+$ cations are oriented as far away from each other as possible, this limits the possibility for interactions with multiple chlorine anions. None of the cations appear to interact with more than two

of the anions while an interaction with up to three anions was seen in the other examples.

The relative energy differences were calculated for $C4mim_4LiCl_4^+$ and are presented along with the equivalent differences for the $C4mim_4NaCl_4^+$ aggregates in Figure 5-44. This graph is remarkably different from Figure 5-43 where the relative energies for the lithium aggregates were much larger than the sodium examples, in this case the two series are very similar in energy. While the metal core surrounded by four chlorine anions is the most stable conformation for both aggregates the energy penalty for moving one anion away from the metal is now lower. This is likely due to the reduction in the metal-chlorine distance and the associated crowding of the ions, especially the bulky $C4mim^+$ ions. This repulsion starts to favour the less crowded structures. The relative energies structures (c), (d) and (e) where there are two metal-chlorine interactions are very similar for both aggregates. The perceived benefit of multiple interactions for the lithium has completely gone with the less sterically hindered conformations seeing no difference with sodium or lithium. Conformation (f) contrasts the previous examples and shows a higher relative energy with lithium. In this case, even the increasing steric hindrance is not sufficient to counteract the instability due to the decreasing number of metal-chlorine interactions. The difference of 25 $kJmol^{-1}$ is considerably smaller than what would be predicted from the smaller aggregates.

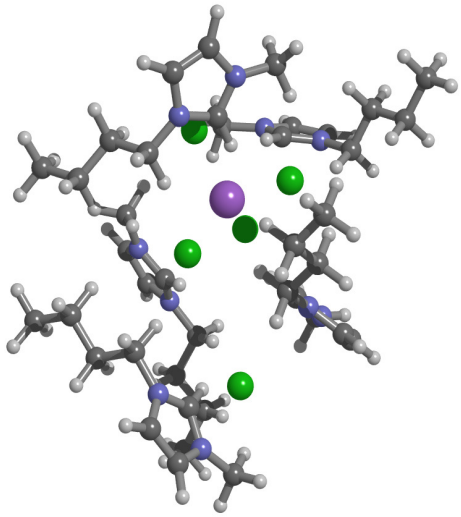

Figure 5-45 Conformation (a) of $C4mim_5LiCl_5^+$ which was calculated using the B3LYP DFT method and the CEP-31G* basis set.

The lithium containing aggregate was expanded to include five C4mimCl ion pairs, equalling the largest sodium containing aggregate which was studied. Similar conformations were stabilised for $C4mim_5LiCl_5^+$ as were found for $C4mim_5NaCl_5^+$. However the equivalent of conformation (a) was considerably different from the sodium example. The corresponding calculated conformation for $C4mim_5LiCl_5^+$ is shown in Figure 5-45. This shows that there is a considerably more natural tetrahedral structure around the metal cation and the fifth chlorine anion is further from the metal. Indeed the distance between the metal and the fifth chlorine is now 5.85 Å compared with 4.77 Å in the sodium example. Meanwhile chlorine anions around the metal which were seen to separate now have a Cl-M-Cl angle of 110.40 ˚ which is down from 118.95 ˚, this value is considerably closer to the tetrahedral angle of 109.47 ˚. The separated anion appears to be primarily held between three cations, one of which is adopting the FrM conformation. These changes are likely necessary due to the contraction associated with the smaller metal cation. The steric hindrance of a structure similar to the sodium example would be too large and is relieved by increasing the metal to chlorine distance and adopting a more natural configuration around the metal.

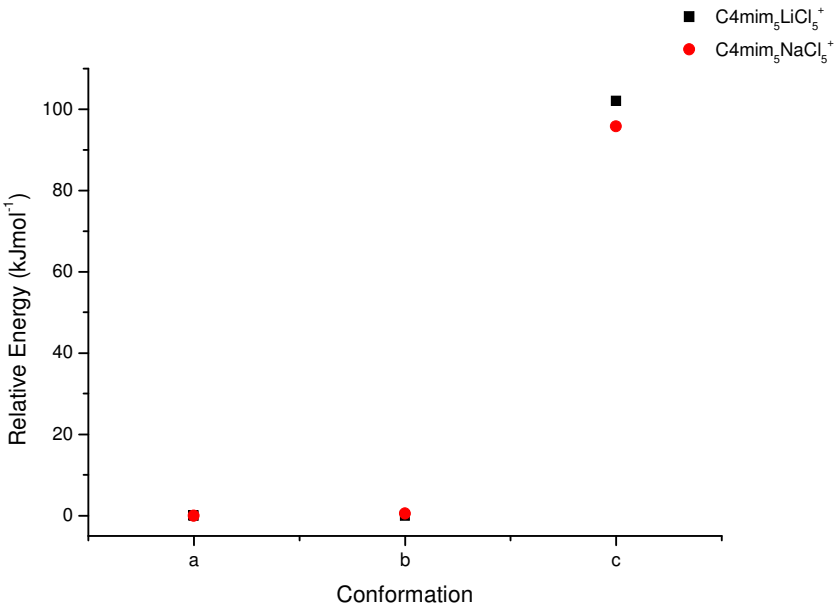

Figure 5-46 Relative energy differences of the $C4mim_5LiCl_5^+$ and $C4mim_5NaCl_5^+$ aggregates calculated using the CEP-31G* basis set.

The relative energies of the calculated structures are shown in Figure 5-46. This graph shows that despite the considerable changes to conformation (a), structures (a) and (b) remain approximately degenerate. Meanwhile the linear conformation (c) has a slightly larger relative energy than the sodium aggregate. This change continues the trend shown for the smaller aggregates with the relative energy difference between lithium and sodium aggregates decreasing as the aggregate size increases. Overall the series of aggregates incorporating a single lithium ion have shown very similar conformations to those observed with sodium. However there have been several changes primarily due to the decreased size of the metal ion and the associated increase in steric hindrance mainly caused by the large $C4mim^+$ cations.

5.2.3 KCl, CsCl and C4mimCl

The structures for aggregates observed with MS containing the group 1 alkali metals, lithium and sodium, were successfully calculated. Following from these calculations the series of aggregates was extended to include other group 1 elements, namely potassium and caesium. These would be expected to form similar structures to those seen for the previous metals however they form weaker bonds with chlorine and have

much larger ionic radii as was previously seen. As was stated in Section 3.2 it was necessary to use a different basis set for aggregates containing larger elements. For the following aggregates the LanL2DZ basis set was used on the heavy atoms and the D95V(d,p) basis set on the first row elements. In order to allow direct comparisons to be made, the majority of the sodium and lithium containing aggregates were repeated with the new basis sets and the values listed in the following section include this.

Table 5-3 Relative energy differences of the complete series of $C4mim_2LiCl_2^+$, $C4mim_2NaCl_2^+$, $C4mim_2KCl_2^+$ and $C4mim_2CsCl_2^+$ aggregates calculated using the LanL2DZ and D95V(d,p) basis sets.

Cation 1 Conf.	Cation 2 Conf.	Metal Position	Relative Energy ($kJmol^{-1}$) for $C4mim_2MCl_2^+$			
			Li^+	Na^+	K^+	Cs^+
FrM	FrM	Inside	0.0	0.0	0.0	0.0
FrM	FrB	Inside	1.0	1.1	1.4	1.3
FrB	FrB	Inside	1.5	2.1	2.3	2.3
FrM	MeS	Inside	17.2	17.3	18.6	19.7
FrM	BuS	Inside	14.4	16.2	17.6	18.5
FrB	MeS	Inside	16.7	18.3	19.8	20.8
FrB	BuS	Inside	15.0	17.1	18.4	19.8
FrM	Back	Inside	32.8	35.2	37.7	40.0
FrB	Back	Inside	30.8	33.8	36.5	38.5
MeS	MeS	Inside	29.1	32.6	34.9	37.4
MeS	BuS	Inside	30.6	35.2	39.9	43.7
BuS	BuS	Inside	32.2	36.9	41.4	45.0

Cation 1 Conf.	Cation 2 Conf.	Metal Position	Relative Energy (kJmol^{-1}) for C4mim$_2$*M*Cl$_2^+$			
			Li^+	Na^+	K^+	Cs^+
MeS	Back	Inside	47.5	53.2	59.2	63.9
BuS	Back	Inside	45.6	51.8	57.8	62.5
Back	Back	Inside	62.7	71.7	80.9	87.5
FrB	MeS	Outside	125.4	89.7	59.9	32.3
FrM	BuS	Outside	123.5	87.2	57.3	29.3
MeS	FrB	Outside	122.4	86.2	58.6	32.9
BuS	FrM	Outside	117.1	84.1	56.2	30.4

Structures corresponding to the nineteen different conformations of the C4mim$_2$*M*Cl$_2^+$ aggregates which were found for *M* = Li^+ and Na^+ were also found for *M* = K^+ and Cs^+. These structures are listed and the relative energy differences are shown in Table 5-3. The relative energy for the aggregates which have the metal ion acting at the centre exhibit very similar patterns with all of the alkali metals. They are grouped based on combinations of front, side and back. The energy penalty for moving from a front to a side conformation is about 19 and 20 kJmol^{-1} for K^+ and Cs^+ respectively. The difference between a front and a back conformation is about 37 and 39 kJmol^{-1} for the same metals. The relative energy differences consistently increase going down group 1. Going down this group causes a decrease in the strength of the metal-chlorine interaction and a relative strengthening of the C4mim$^+$ to Cl^- interaction. As this interaction is stronger, the changes in conformation are seen to have a greater affect on the relative energy of the aggregates and thus the relative energies are seen to increase with increasing ionic radius of the metal. The relative energies of the aggregates with the metal on the outside show a clear trend as the metal is varied. Going down this group, the relative intensity greatly decreases. This difference is positive for all metals compared with the lowest energy front-front

conformations. However, this decrease results in some of the inside conformations being less stable than the outside ones for the larger metals. There is a clear preference shown for multiple metal-chloride bonding which decreases with increasing metal size.

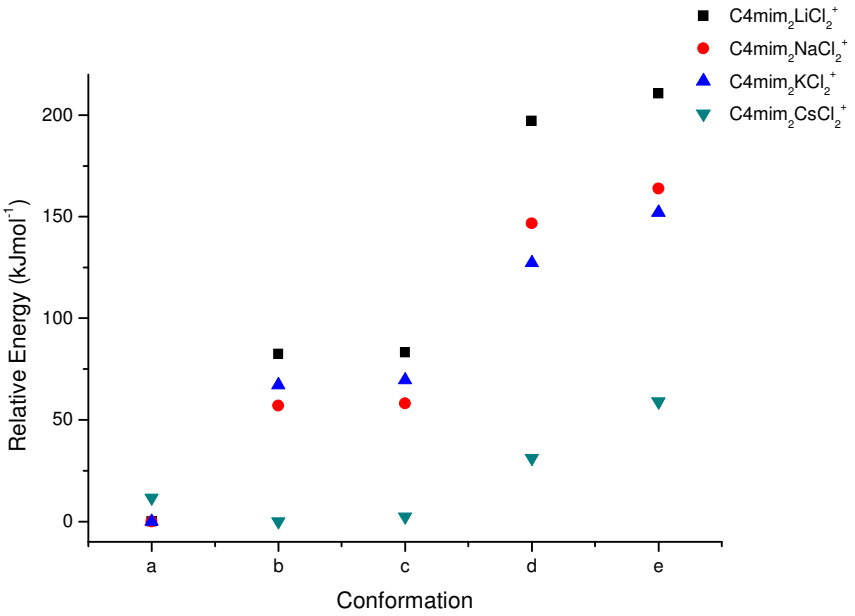

Figure 5-47 Relative energy differences of the $C4mim_3LiCl_3^+$, $C4mim_3NaCl_3^+$, $C4mim_3KCl_3^+$ and $C4mim_3CsCl_3^+$ aggregates calculated using the LanL2DZ and D95V(d,p) basis sets.

The series of $C4mim_3MCl_3^+$ aggregates was also extended to include K^+ and Cs^+. The structures found were equivalent to the ones previously shown for Na^+ and the relative energies of these aggregates are given in Figure 5-47. The series containing potassium follows a very similar trend to those seen previously for lithium and sodium. For conformations (d) and (e) the position of the K^+ aggregates falls in line with the previous observations, however, conformations (b) and (c) lie between the Na^+ and Li^+ series. This indicates that these aggregates are comparatively less stable than would be predicted relative to structure (a). This difference can be attributed to a structural change which occurred in conformation (a) which can be seen in Figure 5-48(a). It can be seen that the increased metal-chlorine distance and the resulting increase in the chlorine-chlorine distance has resulted in a favourable structural change. The separation between the chlorine ions is now sufficient to allow each of

the $C4mim^+$ cations to interact with two anions without significant steric hindrance. This gives this aggregate an added stability over the lithium and sodium equivalents and hence the relatively large relative energy values for conformations (b) and (c).

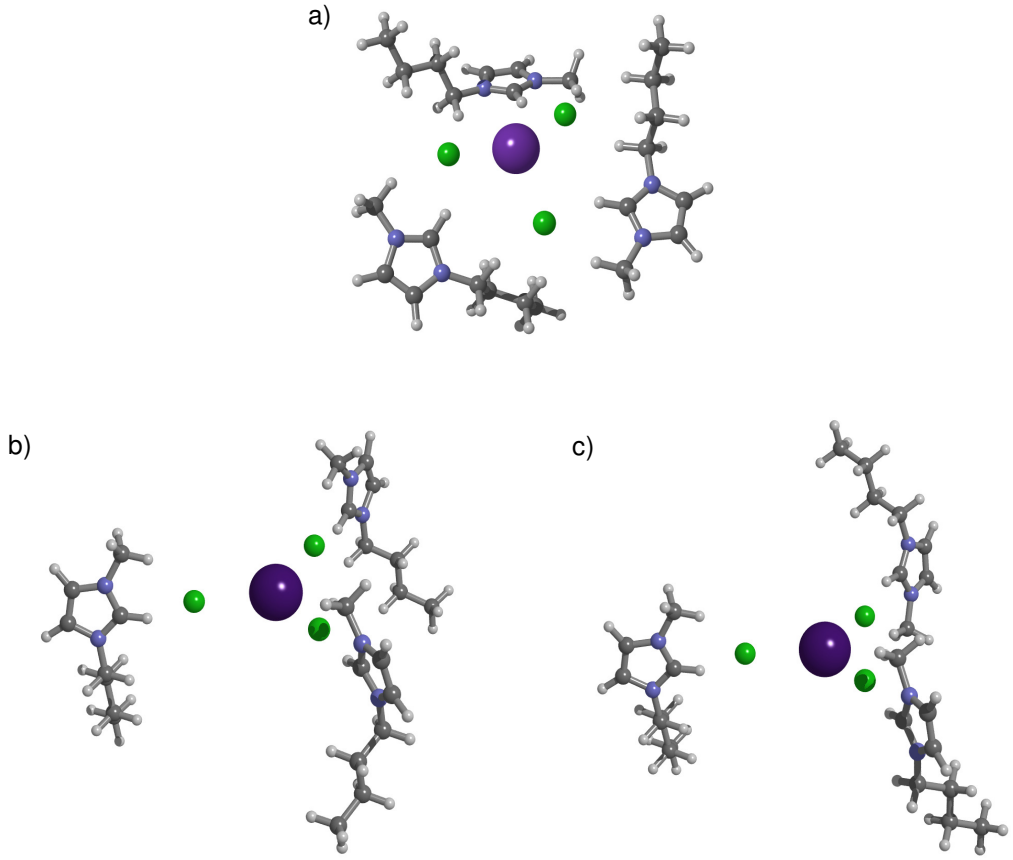

Figure 5-48 Conformation (a) of a) $C4mim_3KCl_3^+$ b) and c) $C4mim_3CsCl_3^+$ which were calculated using the B3LYP DFT method and the LanL2DZ and D95V(d,p) basis sets.

The relative energy values shown for $C4mim_3CsCl_3^+$ are very different from the previous examples. In this case the most stable conformation is (b) which is almost degenerate with (c). There is then an energy penalty of 12 $kJmol^{-1}$ for conformation (a) which was previously the most stable. Similar to what was previously seen conformations (d) and (e) are higher in energy but the gaps are smaller, however this is likely due to the decreased stability for conformation (a). Two different structures were found of conformation (a) for $C4mim_3CsCl_3^+$ and they can be seen in Figure 5-48(b) and Figure 5-48(c). Due to the increased size of the metal ion, the chlorine-chlorine distance has increased to a point where the $C4mim^+$ cations can no longer

bridge between them. The $C4mim^+$ cations are seen to only bind to a single anion and can adopt either of the two conformations shown above. These have relative energies of 11.6 $kJmol^{-1}$ and 11.7 $kJmol^{-1}$ respectively and were thus displayed under a single point in Figure 5-47. The lack of binding to multiple anions is likely the reason for the comparative instability of these aggregates and the relative increase in the stability of the linear conformations (b) and (c).

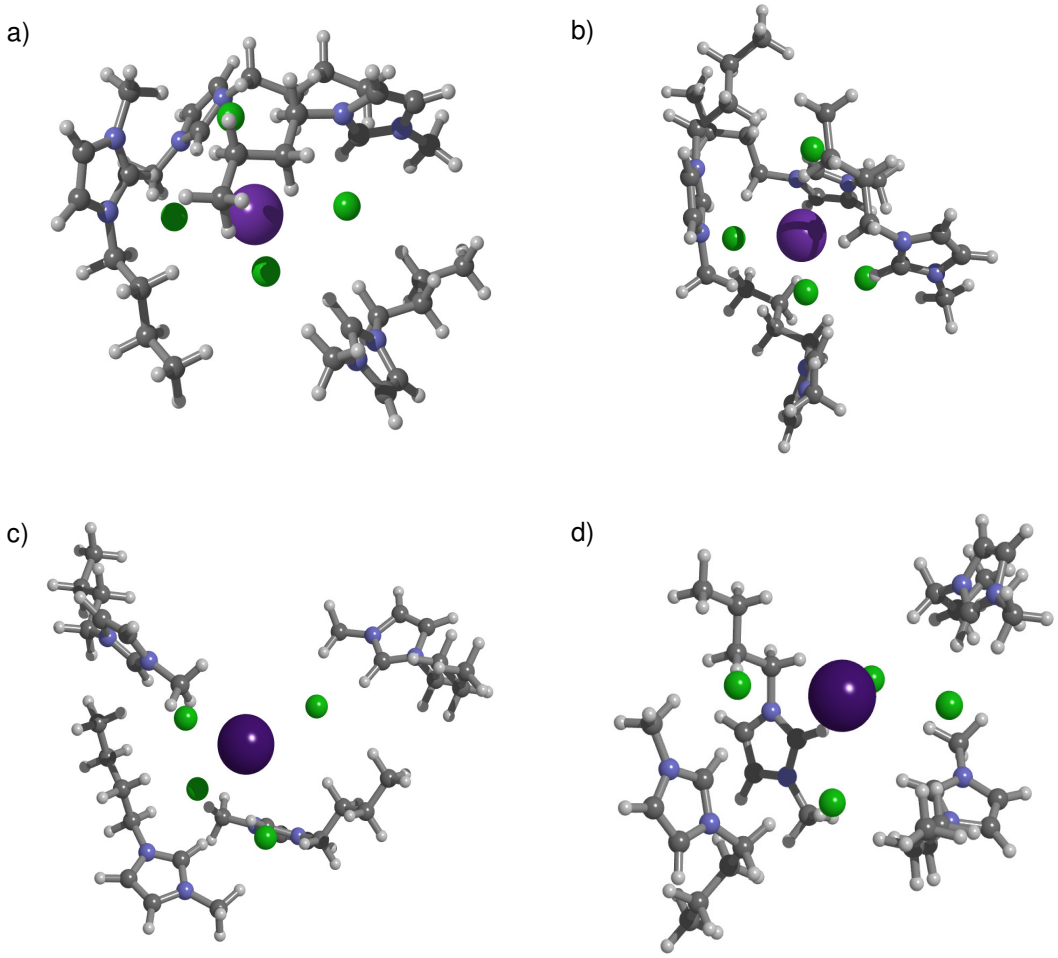

Figure 5-49 Conformation (a) of a) and b) $C4mim_4KCl_4^+$ c) $C4mim_4CsCl_4^+$ and d) conformation (g) of $C4mim_4CsCl_4^+$ which were calculated using the B3LYP DFT method and the LanL2DZ and D95V(d,p) basis sets.

The potassium and sodium series were extended to include the aggregates $C4mim_4KCl_4^+$ and $C4mim_4CsCl_4^+$. The calculated structures mimicked the stable conformations observed for $C4mim_4LiCl_4^+$ and $C4mim_4NaCl_4^+$. The larger size of the metal was most noticeable in the aggregates where it was acting as a core

surrounded by four C4mimCl ion pairs. Figure 5-49 shows the effect of this increase with two different structures of the potassium aggregate shown in Figure 5-49(a) and (b). The two conformations are similar in structure and only 2 $kJmol^{-1}$ apart in energy; as a result they have both been labelled as conformation (a). Conformation (a) of $C4mim_4CsCl_4^+$ can be seen in Figure 5-49(c), the increased metal-chlorine distance is very obvious here and there is little problem with steric hindrance between the $C4mim^+$ cations. A new conformation of $C4mim_4CsCl_4^+$ is displayed in Figure 5-49(d) and is labelled as conformation (g). This is very similar to conformation (a); there are still four chlorine anions around the metal. The geometry adopted by these anions is significantly different and the tetrahedral structure is deformed. Two of the chlorine anions make a Cl-Cs-Cl bond angle of 175.4 ° leaving a large gap visible at the top of the image. This deformation allows the $C4mim^+$ cations to interact with a larger number of anions following similar patterns to what has previously been observed in stable aggregates.

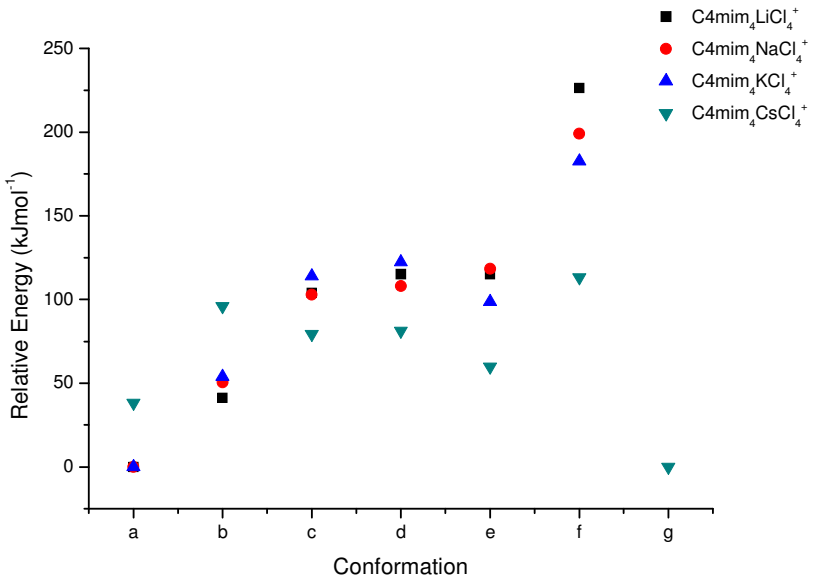

Figure 5-50 Relative energy differences of the $C4mim_4MCl_4^+$ aggregates where M = Li^+, Na^+, K^+ and Cs^+ calculated using the LanL2DZ and D95V(d,p) basis sets.

The relative energies of all of the $C4mim_4MCl_4^+$ aggregates are shown in Figure 5-50. From this it can again be seen that the potassium adducts follow a similar pattern to the sodium and lithium examples. However the caesium aggregates follow

a very different pattern. To start with, the new conformation (g) is now the most stable, this is not too surprising due to the similarities it shares with conformation (a). However there is a large energy difference of 38 $kJmol^{-1}$ between (g) and (a) which is probably in part due to the ability of the $C4mim^+$ cations to form a greater number of interactions with different anions. In Figure 5-47 it was seen that the caesium surrounded by three chlorine anions was less stable than the aggregates with two chlorine anions around the metal. This feature is continued for the $C4mim_4CsCl_4^+$ aggregate where conformation (b) is more unstable than conformations (c), (d) and (e). The $C4mim^+$ cations in conformation (b) are only able to bond with one of the chlorine ions which are directly interacting with the metal centre at a time. Meanwhile conformation (f) remains the least stable of the different structures however the energy penalty associated with this conformation is remarkably smaller than with the other metals. This penalty is indeed seen to decrease as the size of the metal ion increases going down the alkali metals. The trends which were observed for the lithium and sodium adducts have generally been found to persist through the potassium and caesium examples. However the increased size of the metal and the weakening of the metal-chlorine interaction play an increasingly large role. In particular, the increasingly large metal ions separate the chlorine ions to such a large degree that is not possible for the $C4mim^+$ aggregates to bridge between them and significant stability gains are lost.

5.2.4 $MgCl_2$, $ZnCl_2$ and C4mimCl

The MS experiments of mixed solutions of $MgCl_2$ and C4mimCl showed the preferential formation of the $C4mim_3MgCl_4^+$ aggregate. This ion was very prominent in all of the spectra shown from Figure 5-18 to Figure 5-20. Similar calculations to those shown above for the mixed IL and alkali metal aggregates were performed for $C4mim_3MgCl_4^+$. As was shown in the previous section the LanL2DZ and D95V(d,p) basis sets were used for the magnesium and zinc containing aggregates.

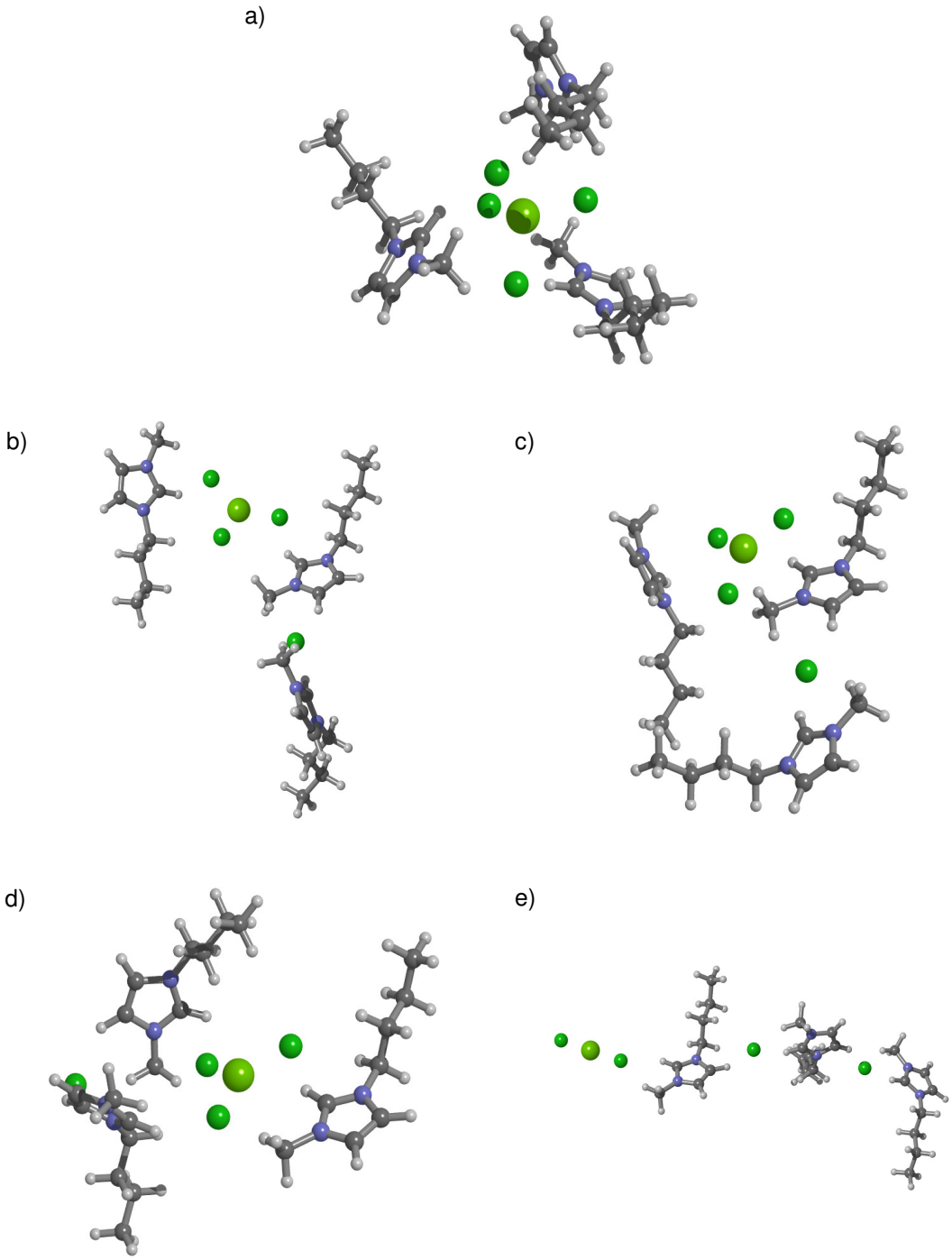

Figure 5-51 Stable calculated conformations of $C4mim_3MgCl_4^+$ which were calculated using the B3LYP DFT method and the LanL2DZ and D95V(d,p) basis sets.

Five minimum energy structures were found for this aggregate and these are shown in Figure 5-51. Unlike the previous examples, magnesium is divalent and therefore to

form singly charged cationic aggregates one more chlorine anion needs to be present compared with the number of $C4mim^+$ cations. As a result of this, the structures formed are generally considerably less crowded and it appears that the steric hindrance around the metal is reduced. Conformation (a) shows the metal cation surrounded by four anions with the three $C4mim^+$ cations forming a shell on the outside of the anions. This conformation is very similar to the aggregates formed with alkali metals surrounded by four chlorine anions. The $C4mim^+$ cations are seen to form multiple interactions with different anions with little restriction. Conformations (b), (c) and (d) are examples where the magnesium cation is surrounded by three anions. In conformation (b) two $C4mim^+$ cations bind to two of the metal bound anions through front position with the final C4mimCl ion pair at the MeS position of one of these cations. Conformation (c) is very similar to (b) however one of the cations now interacts with the anions via a top conformation and through the butyl chain. Conformation (d) is different in that the non-metal bound anion is held between two $C4mim^+$ cations though a BuS and MeS conformation. These cations then interact with the metal bound anions through a combination of front and top positions. The final conformation, (e), is a linear structure where the metal ion interacts directly with only two anions.

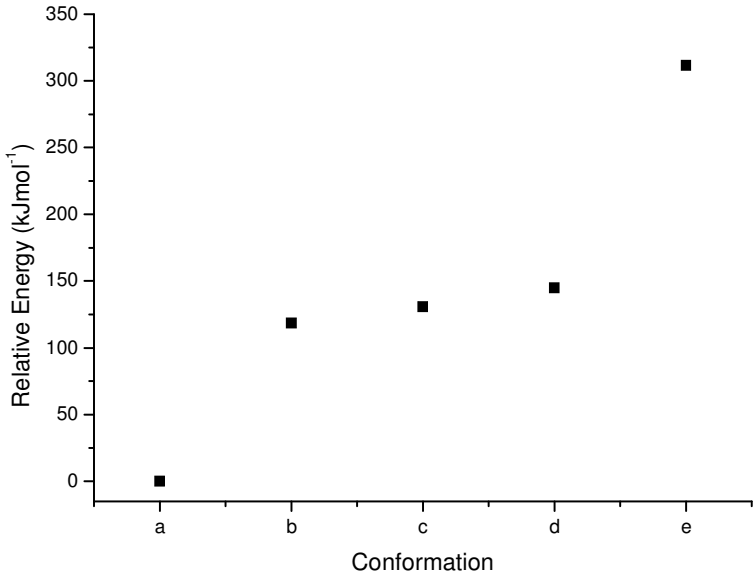

Figure 5-52 Relative energy differences of the $C4mim_3MgCl_4^+$ aggregates calculated using the LanL2DZ and D95V(d,p) basis sets.

The relative energies are displayed in Figure 5-52 for the set of $C4mim_3MgCl_4^+$ aggregates which were shown in Figure 5-51. This shows that the most stable conformation is (a) where the metal ion was acting as a core. This conformation will greatly benefit from the large number of strong metal-chlorine interactions and binding to multiple anions by the $C4mim^+$ cations. The $C4mim^+$ cations were seen to cause little steric repulsion while binding up to three anions. Conformations (b), (c) and (d) are close in energy however the penalty was increasing from 118 $kJmol^{-1}$ for (b) up to 145 $kJmol^{-1}$ for (d) relative to conformation (a). This change is likely due to the increasingly weak binding of the $C4mim^+$ cations to the chlorine anions. Meanwhile conformation (e) is 312 $kJmol^{-1}$ higher in energy than conformation (a). This comparatively large instability is probably down to the low number of metal-chlorine and $C4mim^+$-chlorine interactions. The list of stabilised structures does not include any case where the metal is bound to a single ion or a linear structure where the metal is between $C4mim^+$ cations in a chain like structure. These structures would both have required a chlorine anion to be bound to a single $C4mim^+$ on the outside of the aggregate; it is likely that this requirement is the cause of their absence.

The same calculations were repeated for the zinc containing aggregate $C4mim_3ZnCl_4^+$. Much like the $C4mim_3MgCl_4^+$ aggregate, the zinc equivalent was observed to be very prominent in mass spectra of $ZnCl_2$ and C4mimCl. The stabilised structures were very similar to those observed with magnesium which can be seen in Figure 5-51.

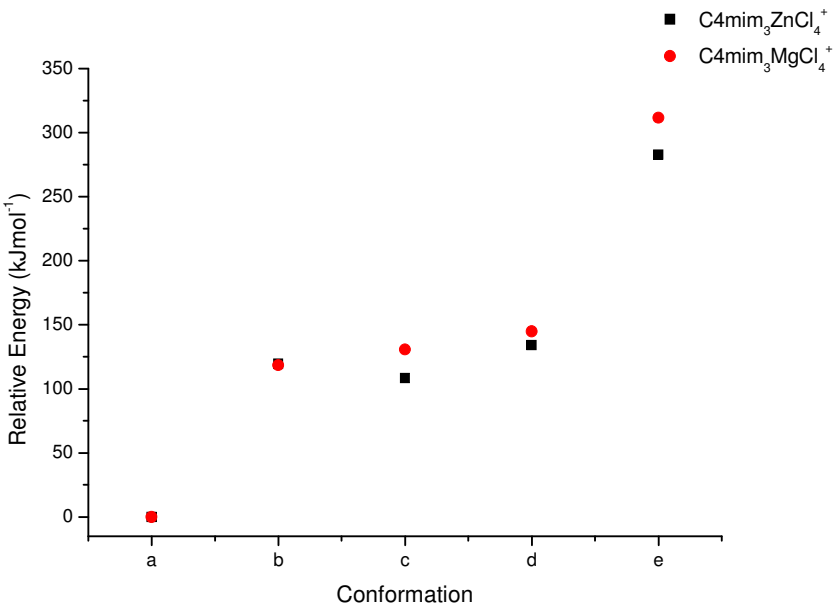

Figure 5-53 Relative energy differences of the $C4mim_3ZnCl_4^+$ and $C4mim_3MgCl_4^+$ aggregates calculated using the LanL2DZ and D95V(d,p) basis sets.

The calculated relative energy differences for $C4mim_3ZnCl_4^+$ are shown in Figure 5-53 along with the previously displayed values for $C4mim_3MgCl_4^+$. These series are seen to follow similar trends with conformation (a) being the most stable for each example. The energy then increases as there are fewer metal-chlorine interactions and a decrease in the number of $C4mim^+$-Cl interactions. The strong similarity between the two series can be explained in large part by consideration of the ionic radii of the metal ions. Zn^{2+} has an ionic radius of 74 pm while Mg^{2+} is 72 pm. As a result of this the spacing between the anions remains very consistent and the $C4mim^+$ cations are able to bridge and interact with the anions in very similar patterns. Overall many of the aggregates which have been found in MS have been studied by computational chemistry. They have revealed many possible conformations for each aggregate and a relative stability of each one. It was found that the metal ion will most commonly act as the core for the aggregate with the $C4mim^+$ cations arranged around the outside. The size of the aggregate and the strength of the metal-chlorine bonding have an effect on the stability of the different conformations which can be adopted. Additionally the $C4mim^+$ cations have been widely shown to prefer to bind

to more than one chlorine anion this is particularly favourable when multiple anions are bound in the front of the imidazolium ring.

5.3 References

(1) Ma, X. D.; Pawlik, M. *Journal of Colloid and Interface Science* **2005**, *289*, 48-55.

(2) Lang, P. F.; Smith, B. C. *Dalton Trans* **2010**, *39*, 7786-91.

(3) M. J. Frisch, G. W. T., H. B. Schlegel, G. E. Scuseria, M. A. Robb, J. R. Cheeseman, J. A. Montgomery, Jr., T. Vreven, K. N. Kudin, J. C. Burant, J. M. Millam, S. S. Iyengar, J. Tomasi, V. Barone, B. Mennucci, M. Cossi, G. Scalmani, N. Rega, G. A. Petersson, H. Nakatsuji, M. Hada, M. Ehara, K. Toyota, R. Fukuda, J. Hasegawa, M. Ishida, T. Nakajima, Y. Honda, O. Kitao, H. Nakai, M. Klene, X. Li, J. E. Knox, H. P. Hratchian, J. B. Cross, V. Bakken, C. Adamo, J. Jaramillo, R. Gomperts, R. E. Stratmann, O. Yazyev, A. J. Austin, R. Cammi, C. Pomelli, J. W. Ochterski, P. Y. Ayala, K. Morokuma, G. A. Voth, P. Salvador, J. J. Dannenberg, V. G. Zakrzewski, S. Dapprich, A. D. Daniels, M. C. Strain, O. Farkas, D. K. Malick, A. D. Rabuck, K. Raghavachari, J. B. Foresman, J. V. Ortiz, Q. Cui, A. G. Baboul, S. Clifford, J. Cioslowski, B. B. Stefanov, G. Liu, A. Liashenko, P. Piskorz, I. Komaromi, R. L. Martin, D. J. Fox, T. Keith, M. A. Al-Laham, C. Y. Peng, A. Nanayakkara, M. Challacombe, P. M. W. Gill, B. Johnson, W. Chen, M. W. Wong, C. Gonzalez, and J. A. Pople, *Gaussian 03, Revision E.01, Gaussian, Inc., Wallingford CT, 2004.*

Chapter 6: Addition of Discrete Solvent Molecules and Protonation

Attempts were made during the MS experiments to observe the addition of discrete solvent molecules and also to observe protonated aggregates. This proved difficult and the attempted methods were unable to achieve either of these goals. The methods which were attempted in order to achieve this will be detailed in this chapter and a selection of companion calculations will be presented in order to find any possible difficulties which may have prevented these observations.

6.1 Mass Spectrometry Techniques

6.1.1 Solvent Addition

A number of different techniques were used in attempts to solvate the gas-phase IL aggregates. In the first of these methods the experimental setup was modified to include a solvent bubbler on the sheath gas supply line. A diagram of such a piece of equipment is shown in Figure 6-1(a). The aim of this modification was to pick up solvent molecules and allow them to interact with the analyte ions within the atmospheric pressure source region of the LCQ instrument. In order to do this, the supply gas is passed through a small quantity of solvent in a sealed container. After leaving the chamber, the gas is then used directly as the sheath gas for ESI experimentation. The sheath gas will be in close proximity to the solvent spray and eventually the bare analyte ions and this would hopefully allow for ion molecule collisions to take place with the solvent molecules forming aggregates with the analyte. The IL aggregates were produced from a 5 mM solution of C4mimCl in a 90:10 mixture of methanol and water as was previously shown in Chapter 4. The apparatus was prepared as indicated in Figure 6-1(a) and successfully attached to the instrument. Water, methanol and acetonitrile were placed within the chamber at different times and examination of the sheath gas leaving the ESI needle showed the presence of solvent. Using this method it was not possible to observe aggregates containing solvent molecules and the spectra appeared identical to those in Chapter 4

without the addition of the solvent bubbler. It seems probable that any aggregates which were successfully bound to a solvent molecule in this region were dissociated prior to reaching the QIT. In an effort to reduce this effect the spray voltage, capillary voltage and capillary temperature were varied, however, the desired result was still not achieved. The capillary temperature previously set to 200 ˚C was progressively reduced as low as 60 ˚C and the spray voltage was reduced as low as 3 kV and while these alterations did reduce the quality of the spray, no solvent addition was observed.

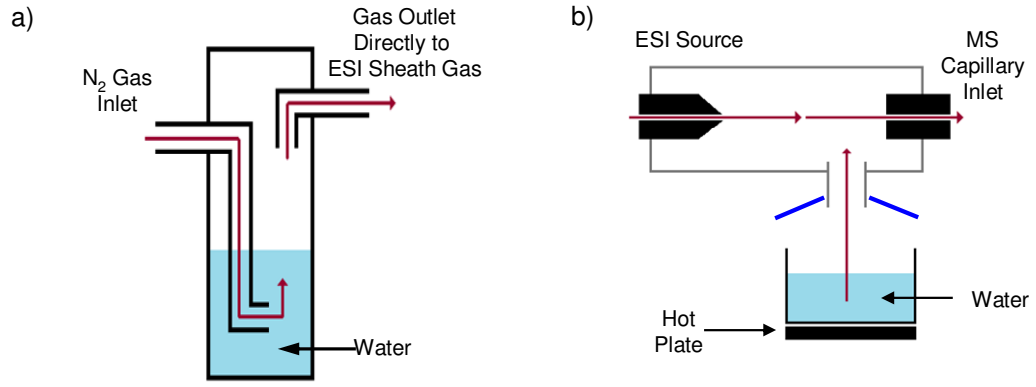

Figure 6-1 Schematic illustrations of apparatus used in experiments for solvent addition to gas-phase aggregates. a) Solvent bubbler added to sheath gas supply line b) Apparatus used to increase solvent concentration in source region.

A further method was attempted to induce ion-molecule collisions within the atmospheric pressure source region of the LCQ instrument. While the previous method had failed to produce the desired results it was hoped that increasing the overall concentration of solvent within this region would increase the probability of success. The standard LCQ ESI source head has a partially closed chamber formed around the source region with a single opening to atmosphere. This allowed for a water bath and hot plate to be placed directly under this opening and steam was allowed to rise to the MS, this is represented in Figure 6-1(b). A plastic funnel could be fashioned around the opening to crudely control the quantity of steam directed towards the ESI source represented in blue in Figure 6-1(b). As previously, the ions were produced from a 5 mM solution of C4mimCl in a 90:10 mixed solution of

methanol and water. This technique was likewise unsuccessful in achieving solvent addition and was only performed with water in the bath. The additional advantage of attempting this method was the ability to have an unperturbed sheath gas flow allowing for the ionisation to be carried out with the previously determined optimal gas pressure. As was previously performed, alterations were made to the source conditions however these did not induce the desired result.

Addition of solvent was further attempted in collaboration with the research group of Dr. Perdita Barran at the University of Edinburgh. The system has been previously detailed in publication for use in hydrogen deuterium exchange (HDX) experiments and was used to directly increase the solvent quantity in the QIT.[1] Briefly the buffer gas inlet line was modified on an LCQ to pass through a reservoir of deuterated methanol before reaching the LCQ. A software patch was applied from Thermo Scientific to allow for longer activation times and to increase the probability of collisions between solvent and aggregate. This method was likewise unable to produce aggregates containing a solvent molecule. The final method which was employed to attempt this experimentally was the addition of different quantities of water to the dilute IL solutions used for MS. As has been mentioned in previous chapters many of the experiments were already performed using 90:10 mixtures of methanol and water. Similar solutions were prepared with 5 mM C4mimCl in different mixtures of methanol and water. Solutions with lower quantities of water (1, 2, 3, 4 and 5 %) were prepared and mass spectra produced along with solutions with larger amounts of water (20, 50 and 100 %). However as with the previous examples there was no evidence of water inclusion within the aggregates.

6.1.2 Protonation

When examined using ESI-MS it is common for many different small molecules such as drug molecules or larger molecules such as proteins to undergo protonation. While small molecules will tend to bind with a single proton, larger protein molecules can bind with tens of protons. This leads to the formation of charged species which can be observed by MS however similar behaviour was not observed throughout the experiments with ILs performed in chapters 4 or 5. As was previously

observed, the charged species were either found to include an odd number of IL ions or include a metal ion. Attempts were made to induce this effect by the use of protonated solvents and the addition of formic, acetic and hydrochloric acids to the solutions for MS. The lack of an obvious protonatable site on the $C4mim^+$ cation will likely play a key role in preventing the formation of these aggregates. However, the ability of the proton to bind directly with the chlorine anion will be investigated through the use of computational calculations and these structures compared with those with the general formula $C4mim_{n+1}Cl_n^+$ in terms of structure and relative energy.

6.2 Computational Investigation

6.2.1 Solvent Addition

The Gaussian 03 suite of programs[2] was used to investigate water binding to the cation for the aggregates $C4mimCl(H_20)$ and $C4mim_{n+1}Cl_n(H_20)^+$ where n = 1 and 2. This allowed the preferential binding sites for a water molecule to be identified on the $C4mim^+$ cation and to ensure these remained constant as additional ion pairs were added to the systems. These calculations were performed using the previously seen LanL2DZ basis set which employed the use of an ECP. This basis set was used on the heavy atoms as before which in this case meant just the chlorine anion. The remaining light atoms were modelled using the D95V basis set which allowed for an efficient calculation which has been shown in previous chapters to be effective for investigating these systems. All of the structures which are presented were fully geometry optimised and checked for minimum energy status using frequency analysis. The structures which will be presented in this section will be limited to those which were successfully identified as minimum energy configurations. An extensive range of initial structures were attempted, yet the range of conformations found to be minimum energy structures were limited relative to the numbers of configurations previously identified for the pure IL ($C4mim_{n+1}Cl_n^+$) aggregates.

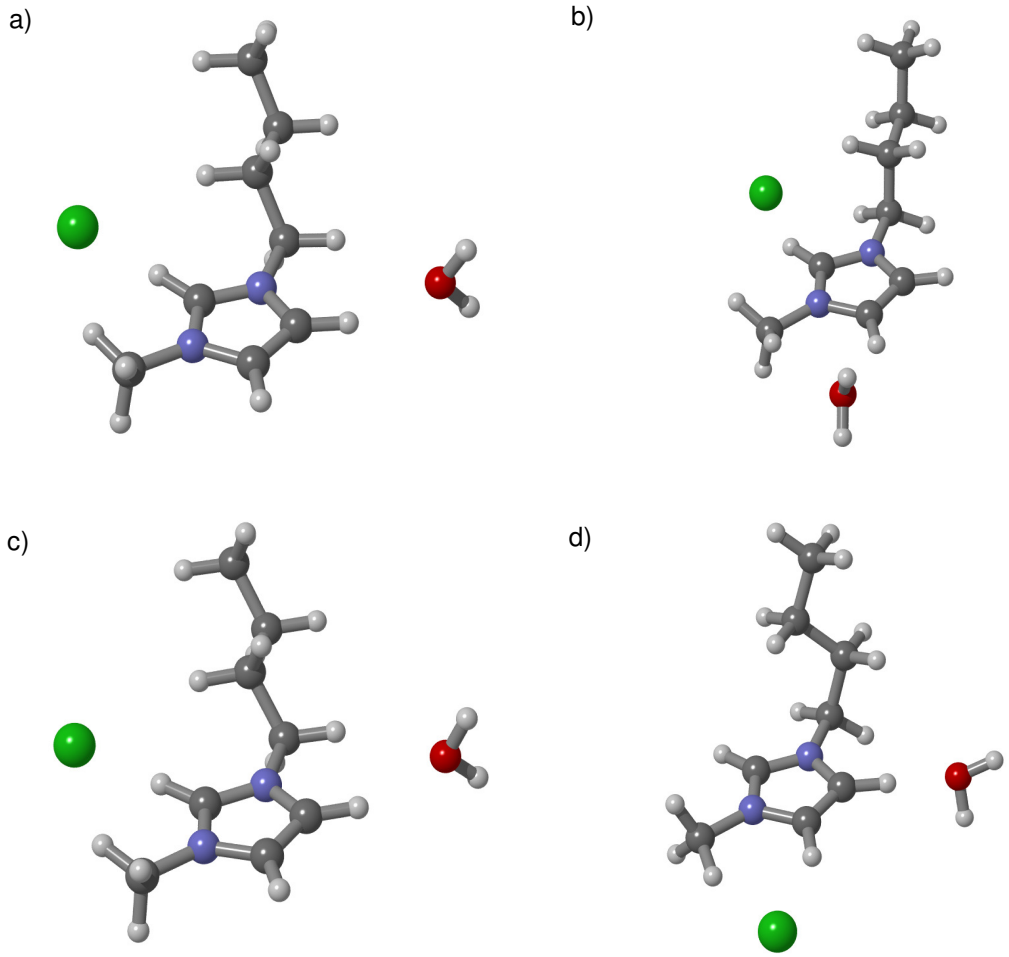

Figure 6-2 The stable calculated conformations of C4mimCl(H_20).

Only four different stable conformations were identified for the C4mimCl$(H_2O)^+$ cationic aggregate and these can be seen in Figure 6-2. In each example the water molecule was identified to position itself in a way which corresponded to the C4mimCl ion pair arrangements previously seen in Chapter 4. Additionally the water molecule was seen to have the oxygen atom oriented towards the electropositive imidazolium ring with both of the hydrogen atoms oriented away. In this way, conformation (a) shows the water molecule in the BuS conformation with the chlorine anion in the FrM position. In order to accommodate this, the butyl chain has been turned towards the front positions and away from the water molecule. A stable conformation was not observed with either a straight butyl chain or where it was turned towards the water molecule. This repulsion would suggest that the water is having an unfavourable effect on the aggregate and might be early evidence why

such interactions were not observed in the gas-phase. Conformation (b) shows the water molecule now in the MeS position and the chlorine anion adopting the FrB conformation. With the water molecule now on the methyl side of the imidazolium ring the butyl chain once again adopts its regular more linear conformation. Meanwhile conformation (c) shows the water molecule adopting a front conformation for the first time; in this case the water molecule can be observed in the FrM position. As a result of this, the chlorine anion is now seen to take up position in the BuS conformation. These three conformations (a, b and c) are similar to conformations which were previously observed in Section 4.2. They resemble the $C4mim_3Cl_2^+$ aggregate conformations where, around the central $C4mim^+$ cation, the two chlorine anions adopted either the FrM and BuS or FrB and MeS conformations. Additionally they are similar to conformations published for the interaction of a water molecule with the C2mimCl ion pair.[3] This work found a limited number of conformations which could be adopted for such an aggregate and these are similar to what is reported here. This publication does not explore different imidazolium based cations or larger aggregates of the IL but does show that the calculations which are reported here are in line with other investigations. Conformation (d) is different from the previous examples as both the water molecule and chlorine anion can be found in side positions. The water molecule has adopted the BuS conformation while the chlorine anion is in the MeS conformation. In the case of the aggregate $C4mim_4Cl_3^+$ and also in larger aggregates, anions were observed in both of these positions. However this is first time that species have been observed throughout this thesis with these positions occupied while the front positions are empty. As with conformation (a), the butyl chain in conformation (d) has been turned away from the water molecule. The torsional angle around the first and second carbon atoms in the butyl chain has reduced from 180 ˚ to approximately 60 ˚ which causes the chain to sit partially over the NCN group of the imidazolium ring.

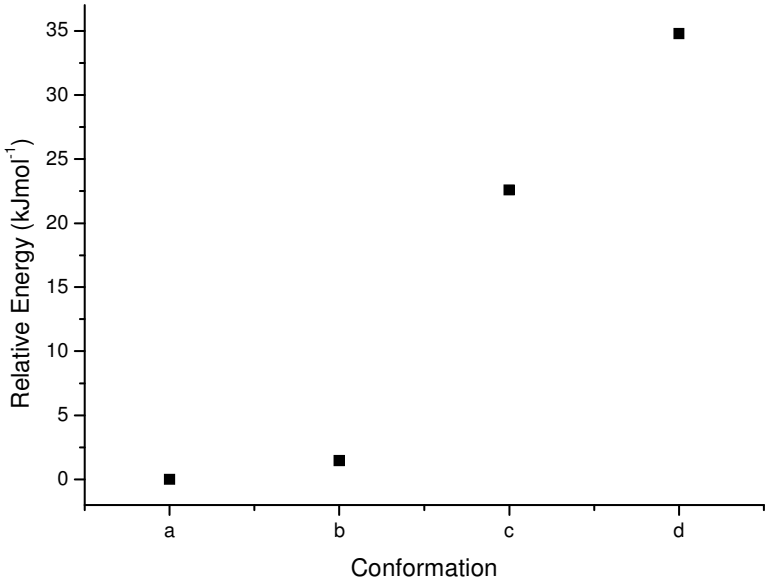

Figure 6-3 Relative energies for the calculated conformations of the C4mimCl(H_20) aggregate.

The relative energies for the conformations of C4mimCl$(H_2O)^+$ which are shown in Figure 6-2 are displayed in Figure 6-3. From this graph it can be seen that conformation (a) is the most stable followed by (b), (c) and (d) with increasing energy. Section 4.2 showed that switching between then FrM/BuS and FrB/MeS combinations gave an energy increase of 1.8 kJmol^{-1}. Switching from conformation (a) to conformation (b) is analogous to the previously observed alteration and this time has a similar energy penalty of 1.5 kJmol^{-1}. This shows that as long as the chlorine anion remains in the front positions these trends hold. However, when conformation (c) is considered, an energy penalty of 22.6 kJ mol^{-1} is found. Moving the water molecule to the front positions has caused the aggregate to significantly destabilise relative to conformations (a) and (b). This increased energy perhaps indicates why a conformation with the water molecule in the FrB position and the chlorine anion in the MeS was not observed. The most unstable of the conformations was (d) which has a relative energy 34.8 kJmol^{-1} when compared with conformation (a). This might have been expected due to the consistently observed instability of the side positions compared with the front positions. Additionally this type of conformation with species only in the side positions was not previously observed and

as such was likely to be unstable compared to the others following more conventional patterns.

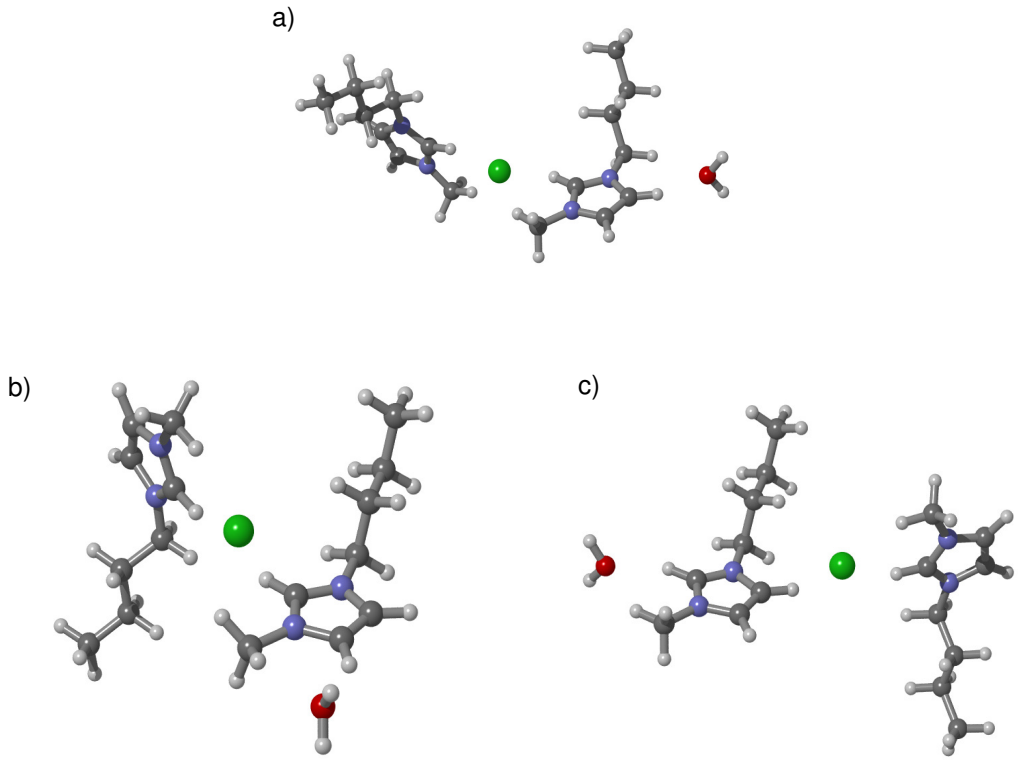

Figure 6-4 The stable calculated conformations of $C4mim_2Cl(H_20)^+$.

The information gained about the interaction of a water molecule with the C4mimCl ion pair was used to construct a range of possible initial structures for the $C4mim_2Cl(H_2O)^+$ aggregate. Three stable structures were calculated for this species and they are displayed in Figure 6-4. These are very similar to the conformations observed in Figure 6-2 with an additional $C4mim^+$ cation bound to each chlorine anion through the FrM conformation. Conformation (a) shows the water molecule in a BuS conformation and the chlorine in the FrM position. This is analogous to conformation (a) from Figure 6-2 however the butyl chain in proximity to the water molecule twisting towards the chlorine. Structure (b) has the water in the MeS conformation and the chlorine adopting the FrB conformation. Structures (a) and (b) incorporate the most stable and second most stable conformations which were previously calculated for the $C4mim_2Cl^+$ aggregate where each of the cations is

adopting front positions with the chlorine anion. Thus it is expected that these conformations will be similar in energy with a slightly lower in energy. Additionally from the study of C4mimCl$(H_2O)^+$ it might be expected that conformation (a) will be slightly lower in energy than (b). Meanwhile conformation (b) shows the water molecule adopting the FrM conformation and the chlorine in the BuS position. From consideration of the C4mimCl$(H_2O)^+$ aggregate this structure is likely to be less stable than (a) and (b). In addition to this, the two cations adopt FrM and BuS conformations with the chlorine anion. In Section 4.2 this configuration was seen to be 18.8 kJmol^{-1} less stable than the FrM-FrM combination and a similar energy difference might be expected here between conformations (a) and (c). A structure which is analogous to the unstable conformation (d) from Figure 6-2 was not found with increasing aggregate size.

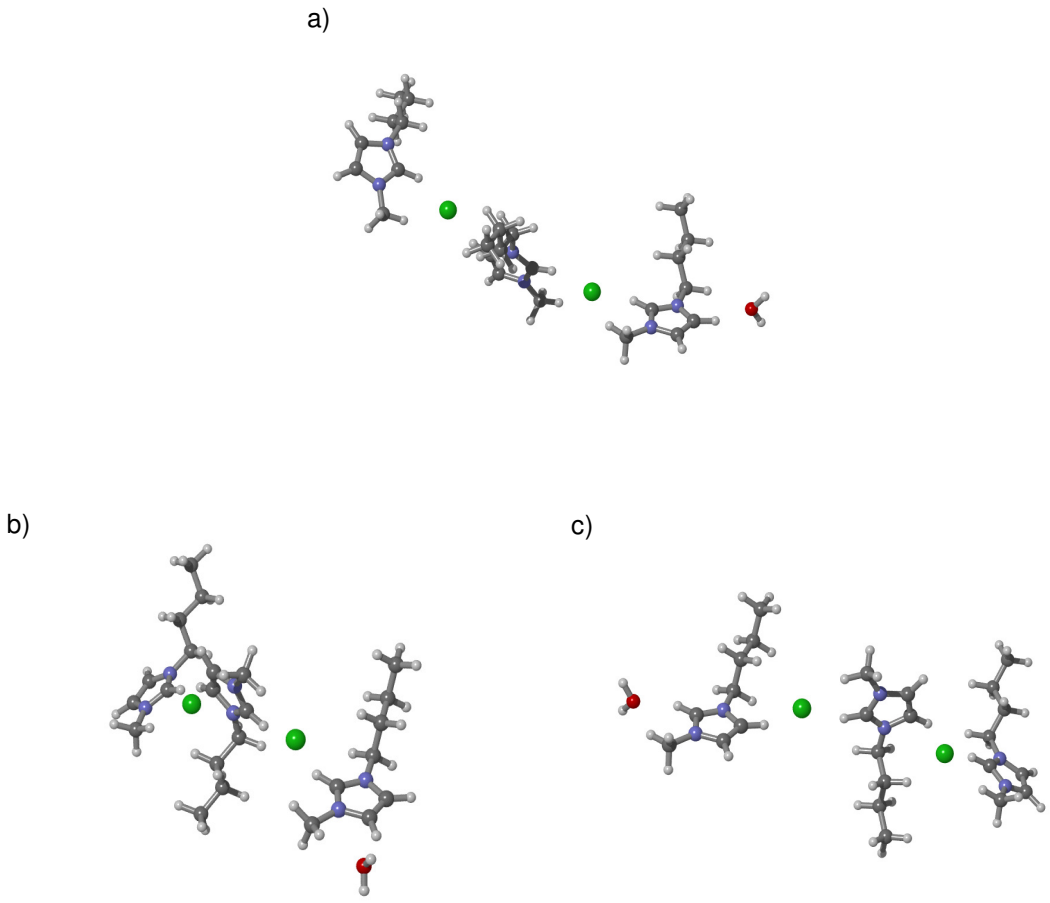

Figure 6-5 The stable calculated conformations of C4mim$_3$Cl$_2$(H$_2$0)$^+$.

Using the information obtained in producing Figure 6-4, the water containing aggregate was expanded by a further C4mimCl ion pair. The three calculated structures for the resulting $C4mim_3Cl_2(H_2O)^+$ aggregate can be seen in Figure 6-5. It can be observed that each of the new ion pairs bind to the old aggregates via the BuS conformation and the outer cations each adopt the FrM conformation. The conformations which are adopted by the water molecule and the water bound cations remain constant relative to the structures which were observed in Figure 6-4. As a result of this, the trends which might be expected in the relative energy for the $C4mim_2Cl(H_2O)^+$ aggregate should be repeated in the $C4mim_3Cl_2(H_2O)^+$ aggregate.

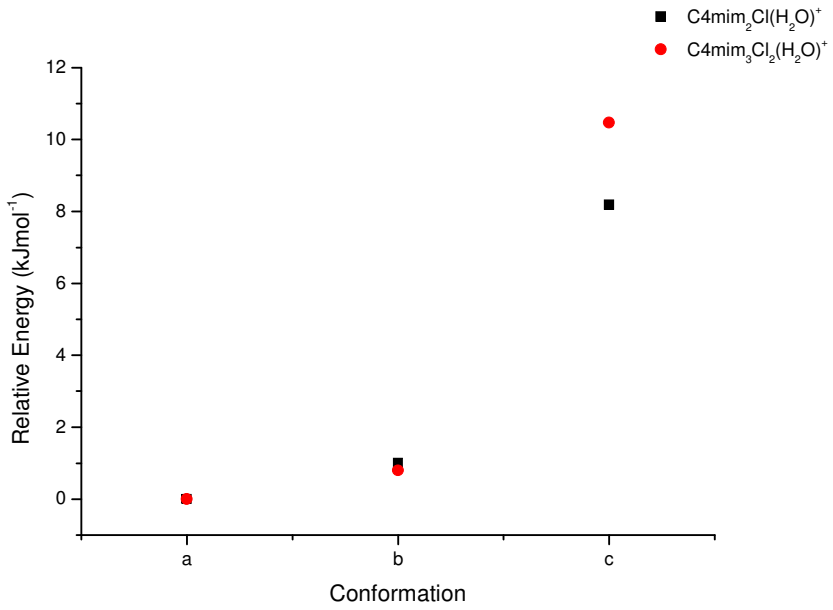

Figure 6-6 Relative energies for the calculated conformations of the $C4mim_2Cl(H_20)^+$ (black) and $C4mim_3Cl_2(H_20)^+$ (red) aggregates.

The relative energies for the three conformations of $C4mim_2Cl(H_20)^+$ and the three conformations of $C4mim_3Cl_2(H_20)^+$ were calculated and are shown in Figure 6-6. Examining the relative energies of the $C4mim_2Cl(H_20)^+$ aggregate, the hypothesised trends can be seen to be present. Conformation (a) is the most stable with a very small energy penalty to reach conformation (b) with a larger penalty to (c). In this case the energy difference between conformations (a) and (b) is only 1.0 $kJmol^{-1}$. This is lower than both the energy difference between conformations (a) and (b) for $C4mimCl(H_20)$ and also the difference between the FrM-FrM and FrM-FrB

conformations of $C4mim_3Cl_2(H_20)^+$. This is surprising as both conformations have these structural elements contained within them so a larger difference might have been expected. However with these calculations it can be difficult to accurately observe trends in energies varying by such small values. Meanwhile the change to conformation (c) is larger with a value of 8.2 $kJmol^{-1}$ relative to conformation (a). As was previously suggested, moving the water molecule to a front conformation and away from the side causes a significant energy increase. There is a clear favouritism for having the chlorine anion in such a position rather than the water molecules. Additionally, as noted above, considering the $C4mim^+$ geometries around the anion, a larger energy difference would have been predicted. So in both cases the presence of the water molecule has reduced the previously observed energy differences. When the $C4mim_3Cl_2(H_20)^+$ aggregate is considered, a similar trend is observed in the relative energies, as was previously stated this was to be expected due to the similarities in the structures which were calculated. For this aggregate the relative energy associated with conformation (c) is higher than the corresponding value for $C4mim_2Cl(H_20)^+$.

The binding energies of H_20 to $C4mim_2Cl^+$ have been calculated including an estimate of the BSSE as described in Section 4.2 and these energies revealed that the water bound aggregates were more stable than the unbound gas-phase species. Conformation (a) was found to be 29.3 $kJmol^{-1}$ more stable than the isolated species. Meanwhile the values for conformations (b) and (c) were 30.4 $kJmol^{-1}$ and 36.0 $kJmol^{-1}$ respectively. The calculations have shown that binding to water molecules is possible; however there are a limited number of conformations which can be adopted during this binding. These restrictions have reduced the probability of binding despite the energetic benefit in formation of these aggregates. These results thus suggest that while binding may be difficult to observe, its observation remains a possibility in future work.

6.2.2 Protonation

Attempts were made to calculate protonated structures of small C4mimCl aggregates. Structures were calculated for the $C4mimClH^+$ and $C4mim_2Cl_2H^+$ aggregates and

will be discussed in the following section. These calculations were performed with the B3LYP hybrid DFT method and the CEP-31G* basis set. Both of these were previously used for the calculation of $C4mim_{n+1}Cl_n^+$ aggregates for n = 1 to 5 and also ones which contained a lithium or sodium ion. For the $C4mimClH^+$ aggregate the H^+ was found to bind to the chlorine anion and no structures were observed with it bound the $C4mim^+$ cation.

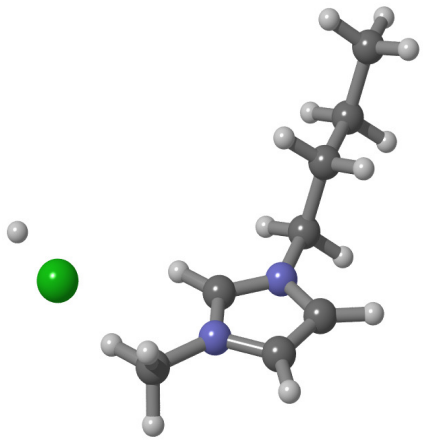

Figure 6-7 The stable FrM calculated conformation of $C4mimClH^+$.

The conformations of the $C4mimClH^+$ aggregate which were found followed the structures of C4mimCl observed in Section 4.2 and the relative energies followed the same trend. This meant that the front conformations were the most stable followed by the side conformations before finally the back was least stable. The low energy conformation is shown in Figure 6-7 where it can be seen that the $C4mim^+$ cation is adopting the FrM conformation and the H^+ sits on the opposite side of the chlorine anion. This aggregate was then expanded by a further ion pair and stable structures of the $C4mim_2Cl_2H^+$ aggregate were found.

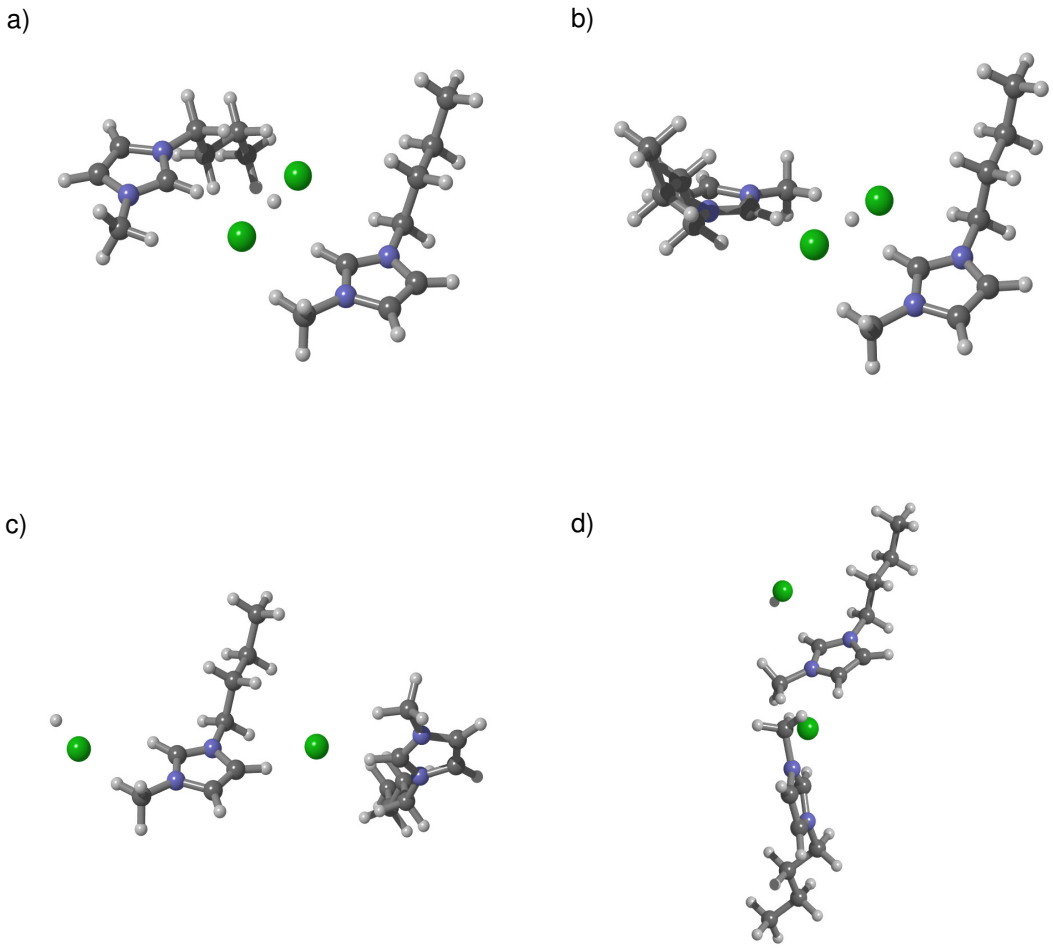

Figure 6-8 The stable calculated conformations of $C4mim_2Cl_2H^+$.

Four different stable structures were calculated for this aggregate and are displayed in Figure 6-8. From a brief study of these it can be seen that they fall into two categories. The first of these categories is represented by conformations (a) and (b) where the proton is at the centre of the aggregate. It is held between the two chlorine anions with the two $C4mim^+$ cations bridging between both of these anions on the outside of the aggregate. Meanwhile the second category is represented by conformations (c) and (d) where the aggregate is more of a linear chain like structure with the protons bound to a single chlorine anion at the outer edge of the aggregate. These structures are more closely related to the ones found for $C4mimClH^+$ including the example which is shown in Figure 6-7 and can be considered as simple

linear extensions as was previously seen for the water containing aggregates in Section 6.2.1. The difference between conformations (a) and (b) is the orientation of the two $C4mim^+$ cations relative to each other. In conformation (a) the two butyl chains can be seen oriented in the same direction, meanwhile they face in opposite directions for conformation (b). In order for the $C4mim^+$ cations to bind with both chlorine anions the imidazolium rings are required to be approximately in plane with each other which varies greatly from the previous examples with two $C4mim^+$ cations where the rings were more favourable closer to 90 ° relative to each other. Meanwhile the examples in (c) and (d) are very similar to the previous examples. It is worth noting that the previously seen preference for chlorine anions to bind in both the FrM and BuS or FrB and MeS positions around a $C4mim^+$ cation holds.

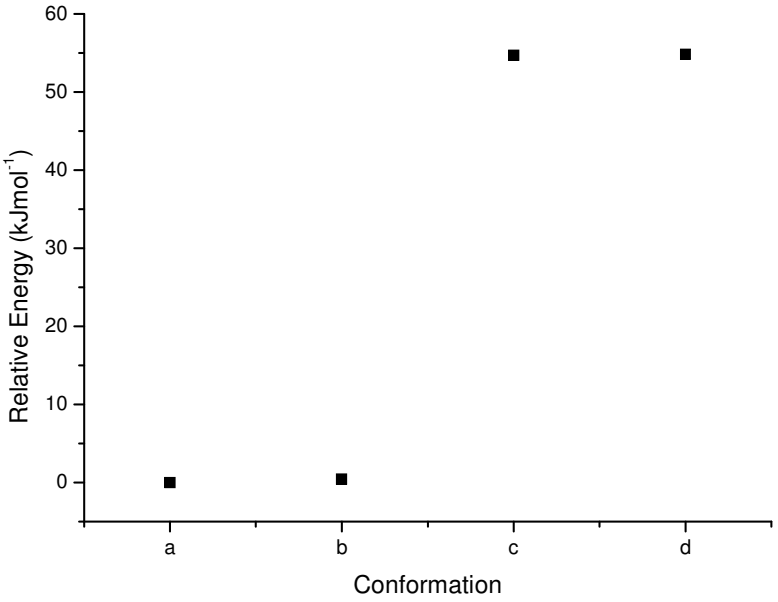

Figure 6-9 Relative energies for the calculated conformations of the $C4mim_2Cl_2H^+$ aggregate.

The relative energies for the previously calculated $C4mim_2Cl_2H^+$ aggregates are shown in Figure 6-9. This shows that conformation (a) is the most stable closely followed by (b) with (c) and (d) significantly higher in energy. The two categories of structure can clearly be seen and within each category the structures are approximately degenerate with each other. Conformations (a) and (b) were found to be only 0.5 $kJmol^{-1}$ apart which means they can treated as effectively degenerate.

The same is true for conformations (c) and (d) which were calculated to be only 0.1 $kJmol^{-1}$ different from each other. The difference between the most stable conformations in each category (a and c) was 54.7 $kJmol^{-1}$ which shows that the first category of structure is significantly favoured. The incorporation of the proton into the centre of the aggregate has allowed the two chlorine anions to come together in a way which was previously not possible. This in turn has allowed the $C4mim^+$ cations to bridge between the pair of chlorine anions. The ability to form such structural motifs was previously shown to be particularly stable when the metal chloride was present and it is not particularly surprising that such a structure has lead to the formation of an especially stable pair of structures in this case.

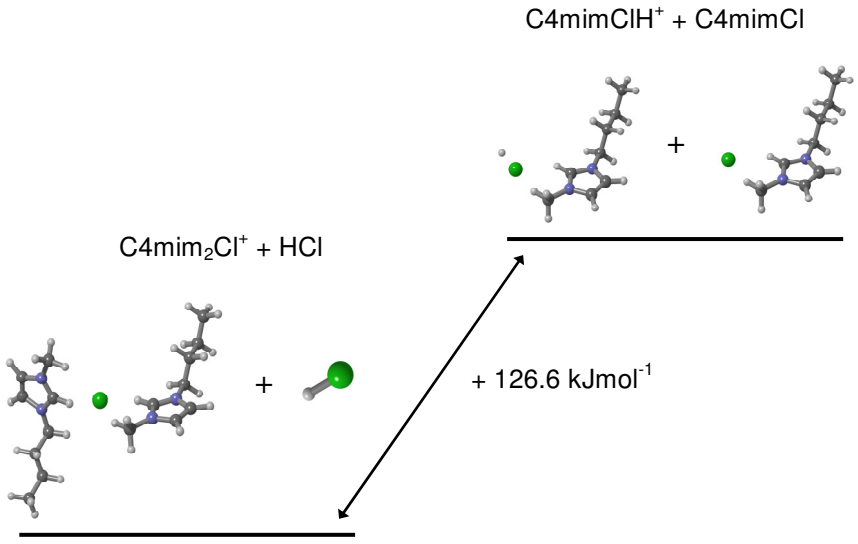

Figure 6-10 Relative energy comparison for the binding of $C4mim^+$ and H^+ to a C4mimCl ion pair.

The relative energy values were used to calculate whether the aggregates would be more stable with an extra $C4mim^+$ cation or with a proton bound to them. Figure 6-10 shows that when the ion pair is bound to the $C4mim^+$ cation it is 126.6 $kJmol^{-1}$ more stable than the corresponding case with the ion pair bound to the proton. This suggests why there was no evidence in the mass spectra of aggregates forming which include protonated aggregates. According to the calculated energies, the aggregates will preferentially incorporate an extra IL cation rather than include a proton. This trend was continued when the $C4mim_2Cl_2$ aggregate was considered; it was found

that binding a $C4mim^+$ cation was 43.9 $kJmol^{-1}$ more stable than the corresponding aggregate incorporating the proton. All of these calculations use the lowest energy conformations which were found, which means that the $C4mim_2Cl_2H^+$ aggregate has the proton bound at the centre to produce the stable structure incorporating the bridging cations. The presence of this stabilisation is the likely cause of the reduced difference between the binding of the IL cation and the H^+ to the aggregate. Despite this increased stabilisation the aggregate remains significantly more stable without the H^+ which corresponds well with the observations from MS.

6.3 References

(1) Esswein, S. T.; Florance, H. V.; Baillie, L.; Lippens, J.; Barran, P. E. *Journal of Chromatography A* **2010**, *1217*, 6709-6717.

(2) Frisch, M. J. T., G. W.; Schlegel, H. B.; Scuseria, G. E.; Robb, M. A.; Cheeseman, J. R.; Montgomery, Jr., J. A.; Vreven, T.; Kudin, K. N.; Burant, J. C.; Millam, J. M.; Iyengar, S. S.; Tomasi, J.; Barone, V.; Mennucci, B.; Cossi, M.; Scalmani, G.; Rega, N.; Petersson, G. A.; Nakatsuji, H.; Hada, M.; Ehara, M.; Toyota, K.; Fukuda, R.; Hasegawa, J.; Ishida, M.; Nakajima, T.; Honda, Y.; Kitao, O.; Nakai, H.; Klene, M.; Li, X.; Knox, J. E.; Hratchian, H. P.; Cross, J. B.; Bakken, V.; Adamo, C.; Jaramillo, J.; Gomperts, R.; Stratmann, R. E.; Yazyev, O.; Austin, A. J.; Cammi, R.; Pomelli, C.; Ochterski, J. W.; Ayala, P. Y.; Morokuma, K.; Voth, G. A.; Salvador, P.; Dannenberg, J. J.; Zakrzewski, V. G.; Dapprich, S.; Daniels, A. D.; Strain, M. C.; Farkas, O.; Malick, D. K.; Rabuck, A. D.; Raghavachari, K.; Foresman, J. B.; Ortiz, J. V.; Cui, Q.; Baboul, A. G.; Clifford, S.; Cioslowski, J.; Stefanov, B. B.; Liu, G.; Liashenko, A.; Piskorz, P.; Komaromi, I.; Martin, R. L.; Fox, D. J.; Keith, T.; Al-Laham, M. A.; Peng, C. Y.; Nanayakkara, A.; Challacombe, M.; Gill, P. M. W.; Johnson, B.; Chen, W.; Wong, M. W.; Gonzalez, C.; and Pople, J. A. In *Gaussian 03, Revision E.01*; Gaussian, Inc., Wallingford CT: 2004.

(3) Wang, Y.; Li, H. R.; Han, S. J. *Journal of Physical Chemistry B* **2006**, *110*, 24646-24651.

Chapter 7: Conclusions and Future Work

A two pronged strategy involving MS and computational chemistry has been used to investigate the formation and structure of IL aggregates in the gas-phase. The MS experiments were predominantly performed using an LCQ instrument fitted with an ESI source. Once it had proved possible to produce gas-phase aggregates of different ILs, CID was performed to investigate their fragmentation and stability. However a QTOF was also used and the LCQ with SSI and PADI sources was also employed for comparison. The calculations performed used *ab initio* techniques to investigate the structure and relative energies of the different aggregates and their stable conformations were determined. The calculations employed the Gaussian 03 suite of programs where the B3LYP hybrid DFT method was mainly used with a number of different basis sets. These techniques allowed for the investigation of the IL aggregates and also IL aggregates with a range of different metal ions, water and H^+ present.

In Chapter 4, the IL C4mimCl was the primary subject of investigation and its singly charged gas-phase aggregates were formed and characterised by MS. In order to perform ESI-MS with this IL it was necessary to dilute the sample in a volatile organic solvent, typically a 90:10 mixture of methanol and water. The IL was diluted to a concentration of 3 to 5 mM providing a sufficiently strong signal for the desired analysis. The series of aggregates $C4mim_{n+1}Cl_n^+$ for n = 1 to 10 were produced by MS and the instrumental settings and sample preparation was optimised to produce optimal results. These results showed high levels of formation of the aggregates with n = 1 and 4. The relatively new ionisation techniques SSI and PADI were used to investigate this IL for the first time with varying results. SSI proved very effective at aiding the formation of larger aggregates while PADI proved to be a very inefficient ionisation source with only the n = 1 aggregate formed even at 10 and 20 mM. A QTOF instrument was also used to study this IL forming the same series of aggregates but with an increased resolution. It was possible in many of these cases to observe aggregates containing sodium, potassium or iron ions which are not uncommon with an ESI source but which led to further investigation in Chapter 5.

CID was used to study many of the different aggregates and information about their fragmentation pathways and relative stabilities was gathered. This revealed the consistent loss of ion pairs from the aggregates and the increased stability of the n = 1 and 4 aggregates showing their magic number characteristics. Different ILs were also studied and revealed the formation of equivalent singly charged cationic aggregates with the general formula $Cation_{n+1}Anion_n^+$. The sample preparation for these IL was close to C4mimCl with similar solvents and concentrations used.

Knowledge of the interactions between individual ions along with contributions of the intermolecular forces is required to understand differences in physiochemical between ILs. This experimental work and the following computational study extend the available information about C4mimCl in the gas-phase and the interactions between the individual ions. The formation of aggregates covered the entire mass range of the instrument and it may be possible to observe larger aggregates by increasing the available mass range or to observe multiply charged aggregates. This work could readily be extended to include any number of ILs using this methodology. The initial work using two other ILs showed that this is possible and the CID technique could easily be applied in these cases allowing for the determination of fragmentation pathways and also the relative stability of different ILs. The inability to find suitable solvents for some ILs may hinder its application requiring refinement of the technique.

A large number of *ab initio* computational chemistry calculations were performed using the Gaussian 03 suite of programs. This was used to investigate the different stable conformations which could be adopted by the aggregates. The $C4mim_{n+1}Cl_n^+$ aggregates were studied for n = 1 to 4 in this way and many different stable conformations were found for each aggregate. From the literature it was known that the C4mimCl ion pair preferentially adopts the FrM and FrB conformations and these structural features were commonly found within the lowest energy conformations which were calculated. For the n = 1 to n =3 aggregates the lowest energy conformations have the ions arranged in a chain like structure where no ion was bound to more than two other ions. However more complicated conformations were found with ions making more than two interactions and for n = 4 two such

structures were now more stable than the chain like structure. The $C4mim^+$ cations were observed to be able to bind with multiple chlorine ions in the front region of the ion which later proved to be a key feature in aggregate structures by providing additional stability to the aggregates. These calculations further allowed the investigation of the binding energy of ion pairs with increasing aggregate size. When these calculated values were compared with the results obtained by MS a strong correlation was found between them. This showed that the techniques being employed could together help further the information known about these systems such as the additional stability of the $n = 1$ and 4 magic number aggregates.

These computational methods could easily be applied to the study of different ILs in order to determine the gas-phase structures of different aggregates. The C4mimCl IL was particularly suitable for this investigation due to the simplicity of the anion which reduced the computational cost compared with what would be have been incurred with many other anions. The use of molecular dynamics simulations would be more suitable for the study of larger aggregates or ILs with increasingly complex ion structure. Structural features were observed which were previously observed in supramolecular aggregates such as where one cation surrounded by three anions or vice versa. These observations show a consistency with larger systems and show that this technique can successfully be applied to learn about the structure of gas-phase IL aggregates.

In Chapter 5, C4mimCl aggregates incorporating different metal ions were studied for the first time with the combined MS and computational chemistry approach. The LCQ was used to produce a wide range of aggregates incorporating monovalent metal ions (Li^+, Na^+, K^+ and Cs^+) and divalent metal ions (Mg^{2+} and Zn^{2+}). The use of the 90:10 mixtures of methanol and water allowed for the strong signal intensity from the high concentration of methanol while the presence of the water overcame any solubility problems associated with the metal chloride salts. These aggregates were formed from mixed solutions of C4mimCl and the appropriate metal chloride salt. The mole fraction of IL was varied from zero to one in each case allowing the aggregates present to be tracked with changing concentration. The incorporation of increasing or decreasing amounts of metal ion could be followed with varying mole

fraction of IL. The suitable mole fraction of IL could be determined in order to produce aggregates containing a single metal ion allowing for CID experiments to be performed on these species. Where the metal ion was kept constant it was possible to observe differences in the relative stability of the aggregates for example the $C4mim_4NaCl_4^+$ aggregate was shown to be significantly less stable than the $C4mim_3NaCl_3^+$ aggregate, an observation later shown likely due to the increased steric hindrance between the $C4mim^+$ cations. By comparison of the results obtained using different metals, trends could be observed within the results, for example when the group one alkali metal aggregates were considered. In this case going down group one the relative stability of the $C4mim_3MCl_3^+$ aggregates was seen to decrease while the relative energies of the $C4mim_4MCl_4^+$ aggregates increased. The suggested explanation involved two competing influences, with each one prevailing on one occasion.

Contamination of ILs is a particular issue surrounding their practical use. An understanding of how different contaminants interact with the IL at a molecular level may allow IL design to better counteract or utilise their presence. This work may be extended to other ILs or by the inclusion of such species as catalysts which are increasingly incorporated into practical IL systems. Additionally such experimentation could potentially allow for improved design of the IL and catalyst based on their molecular level interactions.

A large number of the mixed aggregates which were studied using MS were also investigated using computational chemistry for the first time. As previously, many different stable conformations were located for each aggregate with the most stable examples based on the $C4mim^+$ cations adopting either FrM or FrB conformations. Exclusively, the lowest energy structures incorporated the metal ion as a core to the aggregate with the C4mimCl ion pairs arranged around this. For the larger aggregates which were studied with 4 and especially 5 C4mimCl ion pairs around a smaller metal ion it proved sterically difficult to accommodate the bulky cations within such a confined space and it became increasing favourable to move ion pairs to a second shell. As was previously mentioned, it was favourable for the IL cations to bond to multiple anions through their front region thus bridging between adjacent anions.

This was particularly in evidence while considering the aggregates containing metals. For aggregates with the smaller metal ions present this bridging was possible, however, with the larger metal ions present there was too large a distance between the anions to allow this to take place.

These calculations have proved successful for the investigation of the interaction between contaminant species and C4mimCl. They have revealed new information about the interactions made with these metal ions and this could help to tailor the IL structure to either favour or hinder their interaction. This could readily be extended to include different contaminants and ILs while working in conjunction with MS.

Chapter 6 discusses two observations which were not made by MS and attempts to rationalise these using calculations. Despite extensive experimentation it did not prove possible to observe aggregates containing water or protonated aggregates. The computational investigation showed that while there is a slight energy benefit to binding with the water molecules, the number of conformations where this is possible is comparatively limited compared with what was previously observed in Chapters 4 and 5. The calculations suggested that with further experimental study it might be possible to observe the water molecule binding in one of the side positions of the $C4mim^+$ cation. Meanwhile the calculated structures showed that while it seems not to be possible to bind a proton with the IL cation, it would be possible to bind it to the chlorine anions in an aggregate. Indeed, in the case of the $C4mim_2Cl_2H^+$ aggregate it seemed possible for the H^+ to act as a core with the chlorine anions at either side of it. This enabled the $C4mim^+$ cations to bridge between the anions producing a structure more stable than the linear chain alternative. However, the aggregates which contained an additional IL cation rather than a H^+ were more stable. This suggests an explanation why these aggregates were preferentially found in the MS experiments.

Overall, the strategy of combining the MS experiments with the *ab initio* computational calculations has allowed an increased insight into the structure and relative stability of IL aggregates in the gas-phase. In addition to this, the effect of incorporating different contaminant species such as metal ions or molecular solvents

has been further investigated using this combined approach allowing for a more detailed understanding of the interactions of C4mimCl ions.

The interest in ILs has grown rapidly in recent decades, particularly in the field of green chemistry, and the range of available ILs is ever increasing. The wide variety of ILs means that in order to maximise the benefit from their use it is very important to select the most appropriate IL. However it can be difficult to predict the properties of new ILs and how they will behave when used in conjunction with other species such as catalysts for synthesis. To achieve a better understanding of their behaviour, more needs to be known about the interactions between individual ions.

In this thesis, the combined approach of MS and computational chemistry has contributed to this knowledge. In the future, information gathered from this approach may be expanded and combined with data from other techniques such as NMR spectroscopy to help build a more complete understanding of the structure and interactions that exist within all ILs. This would allow for better predictions of how reactants, products, catalysts and other contaminant species will act. In turn this would allow for the design of ILs for a specific use.

Benefits of tailoring the design could include reduced toxicity, increased solubility, reduced effect of contamination, a broader electrochemical window, reduced viscosity and increased catalytic properties. Consequently, the ability to maximise the potential for every possible application would be gained. Specific examples could be to create new electrolytes for Li^+ batteries and to improve the immobilisation of transition metal catalysts.

Appendix A

Contents of Electronic Appendix

A number of folders are contained within the electronic appendix:

- **Ionic Liquid Aggregates:** The Cartesian coordinates for the stable structures presented within Chapter 4. The coordinates are included for aggregates $C4mim_2Cl^+$, $C4mim_3Cl_2^+$, $C4mim_4Cl_3^+$ and $C4mim_5Cl_4^+$.

- **Mixed Aggregates:** The Cartesian coordinates for the stable structures presented within Chapter 5. Coordinates are included for aggregates incorporating Li^+, Na^+, K^+, Cs^+, Mg^{2+} and Zn^{2+} with C4mimCl.

- **Water and Protonated Aggregates:** The Cartesian coordinates for the stable structures presented within Chapter 6. The coordinates are included for aggregates incorporating either a proton or a water molecule.

- **Thesis:** An electronic copy of this thesis is included.